Theoretical studies of multi-state and multi-mode nonadiabatic dynamics of isoelectronic molecular systems

Thesis submitted in partial fulfilment
of the requirements for the degree of

Doctor of Philosophy

by

V. Jhansi Rani

Reg. No. 17CHPH60

vadalajhansirani1994@gmail.com

School of Chemistry
University of Hyderabad
Hyderabad - 500 046, INDIA
May 2024

Declaration of Authorship

I hereby affirm that the content presented in the thesis titled "**Theoretical studies of multi-state and multi-mode nonadiabatic dynamics of isoelectronic molecular systems**" is the outcome of my research conducted at the School of Chemistry, University of Hyderabad, India. I conducted this research under the guidance and supervision of Prof. Susanta Mahapatra.

I certify that this thesis is original and does not contain any plagiarized content. As per the standard procedure in scientific research, appropriate acknowledgments have been included whenever the work discussed is based on the discoveries of other researchers.

16/05/2024

Date

Hyderabad 500046

V. Jhansi Rani

Signature of the candidate

Certificate

School of Chemistry
University of Hyderabad
Hyderabad-500 046
India

It is certified that the work contained in this thesis, titled "**Theoretical studies of multi-state and multi-mode nonadiabatic dynamics of isoelectronic molecular systems**"by **Vadala Jhansi Rani (Reg.No. 17CHPH60)**, has been carried out under my supervision and is not submitted elsewhere for a degree.

This thesis is entirely original and does not contain any plagiarized material. Furthermore, it has not been previously submitted, either in whole or in part, to this university or any other institution for the purpose of obtaining any degree or diploma.

Parts of this thesis have been published in the following publications:

1. **V. Jhansi Rani**, Arun Kumar Kanakati and S. Mahapatra*, J. Phys. Chem. A **126**, 6581 (2022), **Chap. 3**.
2. **V. Jhansi Rani**, Arun Kumar Kanakati and S. Mahapatra*, J. Chem. Phys. (under review) **Chap. 5**.

and presented in following conferences :

1. Current Trends in Theoretical Chemistry (CTTC-2021), 23-25 September, 2021 (virtual), organised by Bhabha Atomic Research center (BARC), mumbai, India (National).
2. 17th Indian Theoretical Chemistry Symposium (TCS-2016), 11-14 December, 2021, at Indian Institute of Science Education and Research (IISER) Kolkata, India (International).
3. National Conference on Molecular Modelling and Simulations (NCMMS 2022), from February 28-March 02, 2022 (virtual), at VIT Bhopal University, Bhopal, India (National).
4. Structure and Dynamics: Spectroscopy and Scattering (SDSS-2023), 5th-8th October, 2023, IACS, Kolkata, India (International).
5. 18th Indian TCS-2023, 07-10 December, at Indian Institute Of Technology (IIT) Madras, India (International).

Further, the student has passed the following courses towards fulfilment of coursework requirement for Ph.D.

Course code	Name	Credits	Pass/Fail
1. CY-801	Research Proposal	4	Pass
2. CY-802	Chemistry Pedagogi	4	Pass
3. CY-805	Instrumentation Methods-A	4	Pass
4. CY-806	Instrumentation Methods-B	4	Pass
5. CY-577	Computational Chemistry	2	Pass

16/05/2024

Date

Hyderabad 500046

Advisor: Prof. Susanta Mahapatra

Susanta Mahapatra
Senior Professor
School of Chemistry
University of Hyderabad
Hyderabad-500046, TS, India.

Dean
School of Chemistry
University of Hyderabad

Dean
School of Chemistry
University of Hyderabad
Hyderabad-500 046.

Acknowledgements

I want to start by sincerely thanking Prof. Susanta Mahapatra, my adviser, for all of his help, encouragement, and inspiration. I owe him since he allowed me to work in this lab on my own terms and taught me valuable lessons about approaching research problems. These things have strengthened and independent me. I am quite grateful to him. I knew nothing about him before I joined, but now that I know he is nature, kind-hearted, student favor, protective, and supportive, I'm glad to meet such a wonderful person and consider myself fortunate to be a part of this SM group. Thank you, sir, for everything.

It is also my pleasure and obligation to thank my senior, Dr. Arun Kumar Kanakati, who has been a pillar of support during my PhD journey. I was able to make it through this lab because of his encouragement and support. He is my "guru" in my opinion. He taught me the importance of using diligence and genuine effort to tackle scientific challenges and how to approach them. Naturally, I place a high value on the pleasant conversations and queries I had with him, as they gave me courage and many valuable life lessons that I will carry with me forever.

I express my gratitude to the current and past deans of the School of Chemistry for their unwavering support and motivation in fostering an exceptional work atmosphere over the years. The faculty members in our department who have guided and assisted me during my PhD journey are also deserving of my gratitude. I express my gratitude to Prof. Debashis Barik and Dr. Manju Sharma, members of my doctorate committee, for their insightful advice and support.

I am thankful for the financial support provided by the Department of Science Technology (DST) in New Delhi, Innovation in Science Pursuit for Inspired Research (INSPIRE), and the Centre for Modelling Simulation and Design (CMSD) for computing facilities.

I'm thankful to former and present group members, Dr. Rudraditya Sarkar, Dr. Sugata Goswami, Dr. N. Krishna Reddy, Dr. Arpita Dr. Arun Kumar kanakati, Dr. Jayakrushna , Daradi, Nitai, Ajay Rawat, Alamgir, Rani, Ajay, Dr. Manjusha, Dr Mohammed Shavez, and Megavath Arun for maintaining a friendly and supportive work environment.

I consider myself fortunate to have friends like Pooja, Nisha Di, and Bisnu Priya, who have made me feel very welcome on many occasions, I have enjoyed their company and when we are together, we forget about our struggles with our Ph.D and our families, we just enjoy cooking nice food and going out. They are my stress relievers, I am very grateful for their love, care and support. I am very thankful to them, their memories

will always have a special place in my heart.

Apart from my labmates, I would like to extend my special thanks to my school of chemistry friends, Kirthi, Prasanatha, Kamala, Shanti Akka, Geetha, Teja, Kumari, Sonali, Sneha, Manasa, Kalyani, Vemula Arun Kumar anna, Srinu, Sasi kanth, Vinod Kumar, Ramesh, Praveen, Shyam, Anand anna, Suman, Prachi di, Archana, Sampita, Nisha, Gujan and Sridhathri.

I am indebted to all my school and intermediate college teachers and all the integrated chemistry faculty members of Palamuru University (PU), Mahabubnagar, for providing gifted education. Thanks to non-teaching staff in PU they helped me in various matters. I thank all my integrated chemistry batchmates, Andela Vinod Kumar, Bupati Rama, Sindhu, Parvathi, Krishna Reddy, Mohan Lal, and Samatha, for their warm company on various occasions. I also have thanks to all my seniors and juniors at Palamuru University. Special thanks to Shiresha akka, Maheswari akka, Sandhya akka, Anusha akka, Uma akka, Shiva, Ranga, Chandhra Kanth, Sagar, vani, Mallika, Mounika, Sai, Sravani, Anitha and Aruna. I have shared many wonderful moments with them.

Also, I would like to thanks to my school and college friends in my village especially Krishna, Anasuya, Anjji anna. Parvathi, Shiva, Krishnamma, Kavsalya, Manjula, Vijaya, Parameshwari akka, Pushpa, Rajetha, Kavitha, Afsar begam, Sunitha, Laxmi, Lalitha, Shivalila, Divya, Pallavi, Swapna, Nagaraju, Raju, Eswar, Rajashekar.

I would like to thank my parents, Kamalamma and Arjun; my second parents, Padma and Shanker; my brothers, Vinay and Prasad; and my sisters, Mouni and Jyothsna, new family member Kalyan. I am very fortunate to have them. They never fail to express their love, support, and care. I am extremely grateful to God for having them in my life.

I have very big family relatives from my mother's side and Father's side, I have so many memories, and I will always be grateful to all of my chennammas (Ydhamma, Renuka, Parvathi, Baghamma, Sayamma), babhaies (Prakash, Krishnaiah, Madhu, Beemaiah, Nakulaiah), Mamas (Mahendhar, Manikham, Sridhar, Chandhraiah), athammas (Laxmi, Rani, Krishnaveni, Meramma) sisters (Prabha, Sandhya, Krishnaveni, Sravani, Shailu, Archana, Kavitha, Sunitha, Aruna, Ramana) and Brothers (Ramesh, Subhu, Madhu, Mahesh, Chakri) who shows so much love, I'm grateful to each and every one of you,

for their unwavering support, affection, and caring.

I want to thank my thatha (Balraju) and ammamma (Rangamma). I love them so much also, my nanamma (Pentamma) and thatha (Ramulu), I have so many memories with them. I will carry all these memories through out my life.

Finally, I'd like to express my gratitude to all of my well-wishers, friends, and family members who are missing here. I am quite grateful to have so many individuals in my life. Thank you to everyone.

May 2024   (**Vadala Jhansi Rani**)
Hyderabad - 500046

Contents

List of Figures

List of Tables

Abbreviations

aug-cc-pVDZ	augmented correlation-consistent polarized Valence Double-ζ
aug-cc-pVTZ	augmented correlation-consistent polarized Valence Triple-ζ
aug-cc-pVQZ	augmented correlation-consistent polarized Valence Quadrapule-ζ
ADT	adiabatic to diabatic transformation
B3LYP	Becke 3-Parameter, Lee, Yang and Parr
BO	Born-Oppenheimer
BH	Born-Haung
CASSCF	complete active space self consistent field
CCSD	coupled cluster singles and doubles
cc-pVDZ	correlation-consistent polarized Valence Double-ζ
CIs	conical intersections
DOF	degrees of freedom
DVR	discrete variable representation
EOM-CCSD	equation of motion-coupled cluster singles and doubles
EOMIP-CCSD	equation of motion ionization potential-coupled cluster singles and doubles
FC	Franck-Condon
FWHM	full width at the half maximum
HO	Harmonic oscillator
HOMO	highest occupied molecular orbital
IRREP	irreducible representation
JT	Jahn-Teller
LVC	linear vibronic coupling
MCTDH	multi-configuration time-dependent Hartree
MO	molecular orbital
MP2	Møller-Plesset perturbation theory
MRCI	multi-reference configuration interaction
OVGF	outer valence Greens function
PESs	potential energy surfaces
PJT	pseudo-Jahn-Teller
QVC	quadratic vibronic coupling
REMPI	resonance enhanced multiphoton ionization
SPFs	single particle functions
VC	vibronic coupling
VIEs	vertical ionization energies
VEEs	vertical excitation energies
WP	wave packet

Dedicated

to
"My dear family and invaluable supporters, your love and
encouragement fueled my journey through this thesis. I dedicate
this work to you with heartfelt thanks."

Chapter 1

Introduction

"Theoretical studies of multi-state and multi-mode nonadiabatic dynamics of iso-electronic molecular systems" is a topic of current interest, encompassing essential aspects of modern theoretical chemistry. It is crucial to provide the reader with an introduction that precisely outlines the discussion goals of this thesis.

The primary focus of this thesis is a theoretical investigation of the interactions between electronic and nuclear degrees of freedom (DOF) and their effects on chemical dynamics. It is widely recognized that the adiabatic approximation [1] fails in accounting for nuclear dynamics in polyatomic molecular systems. Vibronic coupling (VC), or the coupling of electronic and nuclear motion, is observed in all polyatomic molecules. As a consequence of this coupling, the Born-Oppenheimer (BO) approximation [1] breaks down when an electronic transition occurs during nuclear motion. In the presence of VC, conical intersections (CIs) of potential energy surfaces (PESs) are common [2–10]. The hallmark of CIs is often reflected in the molecular electronic spectrum and is characterized by the absence of radiative emission from excited molecular states. Due to their widespread use as a model for understanding the mechanics underlying photochemical reactions, CIs are also referred to as molecular funnels or diabolic points. This is due to their crucial role in the non-radiative de-excitation transitions of molecules from excited electronic states to their ground electronic states [11–18]. CIs are essential for understanding the mechanisms involved in photochemistry and photobiology. For example, CIs contribute to DNA stability concerning UV radiation [13, 14] through radiationless relaxation (DNA photo-stability). In an excited state, processes such as excited-state electron transfer (DNA photo-repair) [15, 16], excited-state energy transfer used in optoelectronics [19], photoisomerization of retinal in the rhodopsin protein (visual response) [17, 18], and proton transfer (green fluorescent protein) [20–22] can occur. A better understanding

of dynamics on various surfaces and new methodological innovations are required to explore these complex systems.

1.1 Potential Energy Surfaces

Within the framework of the Born–Oppenheimer approximation [1], the quantum dynamics is dictated by the configuration of the PESs in both the ground and excited electronic states, the inter-state couplings, and the nuclear masses. In classical mechanics, the study of photochemical reactions in polyatomic molecules often involves envisioning the motion of "billiard balls"along these PESs, particularly near the Franck-Condon (FC) region, and tracing their trajectories toward different reaction channels. These PESs play a pivotal role in comprehending molecular processes, characterized by intricate topographies including wells, barriers, avoided crossings, and conical intersections. Such complexities are challenging to predict or parameterize straightforwardly, necessitating the use of *ab initio* methods to compute PESs and couplings point by point. Typically, a decent number of grid points per coordinate are needed to adequately sample the relevant portion of the PES for a given reaction coordinate (of interest) [23] and it's schematic piture is shown in Fig. 1.1. Subsequently, all computed points on the PES must be fitted to an analytical function for practical use in dynamic simulations. However, the dearth of high-quality complete PESs and couplings remains a bottleneck for realistic calculations, a situation that is unlikely to change significantly in the near future.
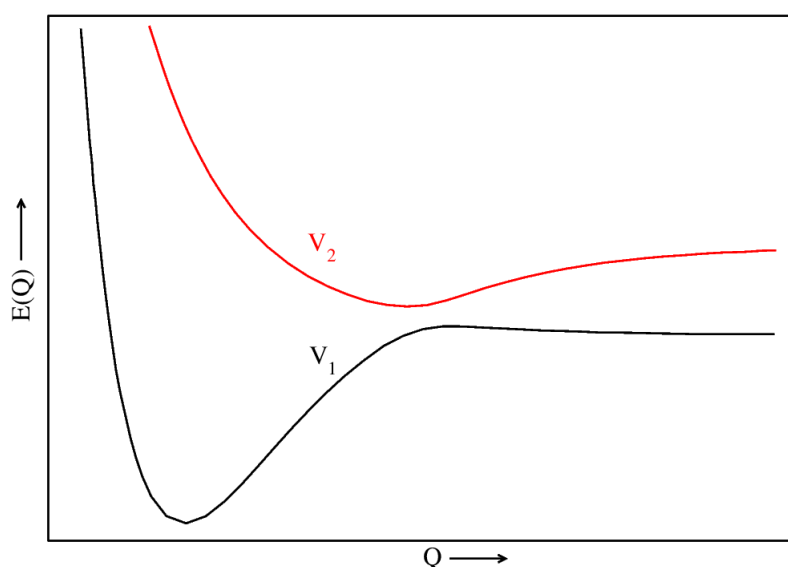
FIGURE 1.1: Schematic representation of potential energy curves

1.2 Current State of Research

Understanding the astrochemical evolution of celestial objects relies heavily on elucidating the organic content within vast molecular clouds and the chemical processes responsible for their production, such as those occurring in proto-planetary disks, comets, and asteroids [24]. In the present thesis, we primarily focus on three key molecular systems: acetaldehyde, oxirane, and aziridine, and their significance in both astrochemistry and the interstellar medium. While these molecules share an isoelectronic nature, they possess distinct molecular arrangements. Specifically, acetaldehyde (CH_3CHO) and oxirane/ethylene oxide (c-C_2H_4O/$(CH_2)_2O$) are structural isomers of C_2H_4O. Aziridine, on the other hand, can be synthesized by replacing the "oxygen-atom" with an NH group in the c-C_2H_4O ring. Theoretical investigations into the photoelectron spectra of acetaldehyde, oxirane, and aziridine are essential for understanding their electronic structures, photochemical reactivity, and potential applications in areas such as photochemistry and atmospheric chemistry. Additionally, vibronic coupling plays a crucial role and largely governs the mechanistic details of the spectroscopy and dynamics of the electronically excited states of these molecules.

Many complex organic molecules (COMs) were reported in stellar environments [25]. In interstellar conditions, COMs are ionized either *via* charge transfer reactions or an exposure to the cosmic radiation [26]. Ultra violet (UV) and vacuum ultra violet (VUV) radiations emitted by stars have the ability to rapidly ionize and dissociate these molecules [27]. One such COM that is predicted to have signature in the interstellar space is, acetaldehyde radical cation $CH_3COH^{·+}$. In a variety of interstellar conditions, its neutral counterpart has been discovered [28–32]. Therefore, the photochemistry and photophysics of $CH_3COH^{·+}$ are of fundamental interest and of potential astrochemical relevance.

Walsh *et al.*[33] through Rydberg series analysis of recorded absorption spectrum found the lowest adiabatic ionization potential of CH_3COH to be $\sim$82,505$\pm$5 cm^{-1} (10.2293$\pm$0.0007 eV). A value of $\sim$10.2295$\pm$0.0007 eV of the same was reported by Knowles *et al.* [34]. The photoelectron spectra of acetaldehyde were recorded using He I and He II radiations [35–47]. Photoionization mass spectrometry [48–50] and electron impact mass spectrometry [51] experiments have been carried out. Along with this, photoelectron-photoion coincidence studies [45, 52, 53] were reported. Yencha *et al.*[54] have recently reported threshold photoelectron (TPE) spectrum and total photoion yield (TPIY) spectrum of acetaldehyde. Velocity-map ion imaging experiment characterizing the wavelength dependent photo-fragmentation dynamics of the $CH_3COH^{·+}$ was reported in a most recent

work of Kapnas *et al.* [49]. From all these observations mentioned above, we could only find the limited information about the vibrational band structures and the electronic states involved in the spectrum. In addition to this, acetaldehyde belongs to the point group of low symmetry [55–57]. It governs the electronic states of this molecule will have the same spatial symmetry. Therefore, a detailed systematic theoretical investigation of the vibronic coupling between the electronic states considered here to understand the photoelectron spectroscopy of acetaldehyde (see Chapter 3).

Oxirane (ethylene oxide, dimethylene oxide, c-C_2H_4O/$(CH_2)_2O$) is a three-membered cyclic ring, with each carbon being fully hydrogenated. This is the smallest cyclic ether and it is related to cyclopropane (C_3H_6) through a replacement of one of the methylene (CH_2) groups of the alkane with an isoelectronic oxygen atom. The oxirane is noted for its reactivity making it (and its derivatives) key reagents in the synthesis of many products of industrial and biological significance [58–61] and it has been serving as a model for photochemistry from a long time [62–67]. The molecular reactivity has been ascribed largely to ring strain as happens in cyclopropane and interest in its electronic structure has a long history. Acetaldehyde [CH_3CHO (C_s)], oxirane [c-C_2H_4O (C_{2v}))] and vinyl alcohol [H_2CCHOH (C_s)] are the three stable isomers (i.e., molecules with the same chemical formula but with different connections of the atoms) of C_2H_4O [68]. Oxirane is a higher energy isomer of the molecules acetaldehyde and vinyl alcohol, only acetaldehyde has been first identified organic molecules in the interstellar medium (ISM) [69], although vinyl alcohol has been attempted to identify in cold dark clouds [70, 71], latter researches found the oxirane has been detected in the interstellar medium especially in the star-forming regions [61, 61, 72–76], these studies proved the existence of oxirane in ISM and it is confirmed by Dickens *et al.* [77]. Also, Coll *et al.* have suggested that oxirane molecule could be present in the Titan atmosphere [78]. To understand the formation of these three isomers of C_2H_4O particular pertinence to test the astrochemical evolution of the interstellar medium, since these molecules also play a key role in astrobiology [58, 59, 61, 69, 71]. Acetaldehyde and oxirane have been implicated in the formation of amino acids [59], underscoring their significance as complex organic molecules (COMs) [68]. Oxirane and acetaldehyde isomers are particularly noteworthy due to their potential contributions to amino acid synthesis [68]. The presence of oxirane in hot cores implies the existence of ring-shaped molecules with more than three carbon atoms, such as furan (c-C_4H_4O), which is closely associated with the sugars ribose and deoxyribose, the structural backbones of RNA and DNA, respectively [61, 74]. Observations by Occhiogrosso *et al.* [79] have revealed gaseous abundances of oxirane and acetaldehyde in high-mass star-forming regions. Their findings suggest that oxirane might be prevalent in the outer and cooler regions of hot cores where its isomer has been

previously detected, providing valuable insights compared to earlier studies that focused solely on oxirane formation [76, 80–82].

Heterocyclic complex organic molecules, incorporating heavier elements alongside carbon in their ring structures, hold significance in various fields, particularly in the study of the ISM [72–77]. Oxygen-bearing species within this category are of particular interest due to their implications for the presence of life [58–60]. Ribose, for instance, is intricately linked to the molecular architecture of DNA [59, 60]. Exploring simpler heterocyclic molecules than ribose leads us to oxirane [58–61]. Oxirane represents the smallest cyclic species containing oxygen, bonded to two carbon atoms. Conversely, acetaldehyde, a non-cyclic isomer of C_2H_4O, serves as a significant evolutionary tracer in various astronomical contexts [83]. Initially detected in the ISM by Gottlieb in 1973, oxirane has since been observed in diverse astrochemical environments, particularly notable is its presence in regions of star formation [76, 77, 81, 82]. The relatively higher abundance of acetaldehyde compared to oxirane aligns with the reported ratios between the two isomers, ranging from 1 to 9 according to Ikeda *et al.* [76]. A gas-grain chemical model was developed to explore the chemistry of oxirane in high-mass star-forming regions, successfully reproducing its observed abundances in such environments [79]. Despite their distinct chemical structures, the chemistry of oxirane appears intertwined with that of acetaldehyde, suggesting the potential utility of acetaldehyde as a tracer for oxirane in cold cores [80].

The He I and He II photoelectronc spectra of oxirane are studied experimentally and theoretically [46, 47, 84–91] in the past decades. However, there are so far no literature available on the multi-state and multi-mode dynamics of oxirane radical cation. But a couple of theoretical calculations on the electronic structure and vertical ionization energies of oxirane are available [85, 89, 91, 92]. Due to the limited information on the electronic spectrum of this molecule, we carried out a detailed theoretical calculations and quantum dynamical simulations of nuclear motion to understand the theoretical photoelectron spectrum of oxirane (see Chapter 4).

Three-membered cyclic molecules are geometrically strained and the atoms present on those molecules shows some interesting properties in molecular spectroscopy [93]. So the electronic and geometrical structural studies of strained molecules have lots of importance both in experimental as well as in theoretical studies. A large number of organic molecules are found in the Interstellar medium (ISM) [25]. Aziridine, CH_2NHCH_2, also called ethylenimine is a three-membered heterocycle having an amine group. The

CH_2NHCH_2 is a feasible interstellar molecular candidate since it contains a number small nitrogen compounds and epoxides have been discovered in the ISM [77] and as well as in the atmosphere of Titan since many small nitrogen derivates are already found [94]. The CH_2NHCH_2 is of potential astronomical importance because it may be a constituent of so-called hot cores, star-forming areas with relatively large abundances of complex organic compounds [95, 96]. Myers *et al.* reported on the search for interstellar pyrrole in 1980 [97]. They assumed, in some ways, that because of their favorable partition characteristics, oxirane and aziridine were ideal candidates for astronomical detection. The structure of aziridine can be simply deduced by replacing the oxygen atom by NH in c-C_2H_4O ring. We put forward aziridine to be a promising candidate for interstellar chemistry due to its abundant nitrogen and multi-faceted interstellar chemistry. Therefore, the study of photochemistry and photophysics of CH_2NHCH_2 has fundamental importance (see Chapter 5).

1.3 Our goal and outline of my thesis

The primary objective of this thesis is to examine the vibronic interactions in the photo-induced dynamics of polyatomic isoelectronic molecular systems, with a particular focus on acetaldehyde, oxirane/ethylene oxide, and aziridine/ethylene imine. Quantum dynamical approaches are employed for this investigation. Acetaldehyde and aziridine possess equilibrium geometries belonging to the C_s symmetry point group, while oxirane exhibits C_{2v} point group symmetry. The optimized equilibrium geometries of acetaldehyde, oxirane, and aziridine are illustrated in Fig. 1.2.

(a) Acetaldehyde　　　　　(b) Oxirane　　　　　(c) Aziridine
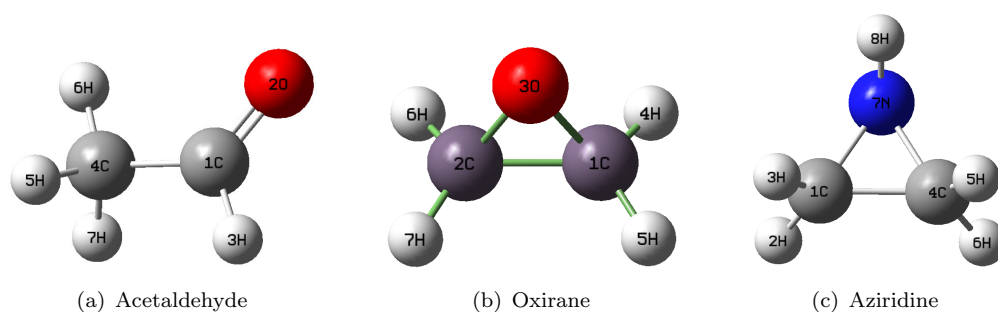
FIGURE 1.2: Schematic representation of the equilibrium minimum structure of the electronic ground state of acetaldehyde (a), oxirane (b) and aziridine (c) molecules.

The study investigates the multi-state and multi-mode vibronic coupling effects in the photo-ionization spectroscopy of acetaldehyde, oxirane, and aziridine. Ab initio electronic structure calculations are employed to understand complex vibronic spectra and ultrafast nonradiative decay dynamics through CIs, with nuclear motion for coupled

electronic states simulated using quantum dynamical calculations. The investigation delves into the intricate vibronic spectra, identifying prominent vibrational progressions in each electronic state, examining population transfer processes at CIs, analyzing nonradiative decay rates, and addressing spectrum broadening due to strong vibronic coupling. Theoretical conclusions are compared with available experimental data. A diabatic electronic representation is constructed and applied to manage PES crossings and mitigate the singularity in the adiabatic electronic representation of the nuclear kinetic coupling term. This framework constructs a model vibronic Hamiltonian using simple symmetry selection techniques, with essential coupling parameters derived from *ab initio* electronic structure data. A four-fold diabatization scheme is utilized to compute adiabatic and diabatic PESs and their coupling parameters. Vibronic bands are computed by solving both time-independent and time-dependent Schrödinger equations using the multi-configuration time-dependent Hartree (MCTDH) program module.

Chapter 2 furnishes a comprehensive theoretical foundation for the ongoing investigations. Specifically, it offers an overview of the BO approximation and underscores the necessity for a diabatic electronic basis. Furthermore, it delves into the basic linear vibronic coupling (LVC) method, supplemented by diagonal quadratic terms. Symmetry selection rules play a crucial role in determining the matrix elements, while the pertinent coupling parameters of the Hamiltonian are derived from *ab initio* electronic structure calculations. Additionally, this chapter elaborates on the quantum dynamics calculations, encompassing both time-independent and time-dependent approaches, which entail solving the quantum eigenvalue equation to compute vibronic spectra. The methodologies discussed herein utilize the MCTDH program module.

In Chapter 3, the multi-state and multi-mode vibronic dynamics in the seven energetically low-lying ($\widetilde{X}\ ^2A'$, $\widetilde{A}\ ^2A''$, $\widetilde{B}\ ^2A'$, $\widetilde{C}\ ^2A'$, $\widetilde{D}\ ^2A''$, $\widetilde{E}\ ^2A'$ and $\widetilde{F}\ ^2A'$) electronic states of acetaldehyde radical cation is investigated [98]. Adiabatic energies of these electronic states are calculated by *ab initio* quantum chemistry methods. A VC model of seven electronic states is constructed in a diabatic electronic basis to carry out the first principles nuclear dynamics study. The vibronic spectrum is calculated and compared with the experimental findings reported in the literature. The progressions of vibrational modes found in the spectrum are assigned. The findings reveal that, the $\widetilde{X}\ ^2A'$ and $\widetilde{F}\ ^2A'$ electronic states are energetically well separated from the other electronic states and the remaining states ($\widetilde{A}\ ^2A''$ to $\widetilde{E}\ ^2A'$) are energetically very close or even quasi-degenerate at the equilibrium geometry of the reference electronic ground state of acetaldehyde. The energetic proximity of $\widetilde{A}\ ^2A''$ to $\widetilde{E}\ ^2A'$ electronic states results into multiple multistate conical intersections. The impact of electronic nonadiabatic interactions due to

conical intersections on the vibronic structure of photoionization band and nonradiative internal conversion dynamics is discussed.

Chapter 4 explores the photoelectron spectrum of oxirane molecule and considering the first six low-lying $\widetilde{X}\ ^2B_1$, $\widetilde{A}\ ^2A_1$, $\widetilde{B}\ ^2B_2$, $\widetilde{C}\ ^2A_2$, $\widetilde{D}\ ^2A_1$ and $\widetilde{E}\ ^2B_1$ electronic states of c-$C_2H_4O^{·+}$. The standard VC theory is used to study the interactions between the electronic states and using the symmetry selection rules a model 6×6 diabatic electronic Hamiltonian is constructed. The parameters of the diabatic Hamiltonian are estimated by performing extensive *ab initio* electronic structure calculations, using the EOMIP-CCSD method. The nuclear dynamics calculations are performed to diabatic electronic states using both time-independent and time-dependent methods using the MCTDH framework. The calculated vibronic structures of the six diabatic electronic states are found to be in excellent agreement with the available experimental findings. The progressions are assigned in terms of vibrational modes. It is found that, extremely strong vibronic interactions among the $\widetilde{X}\ ^2B_1$-$\widetilde{A}\ ^2A_1$, $\widetilde{B}\ ^2B_2$-$\widetilde{C}\ ^2A_2$ and $\widetilde{D}\ ^2A_1$-$\widetilde{E}\ ^2B_1$ electronic states results into a highly overlapping vibronic bands and multiple multi-state conical intersections are formed among them. The impact of associated nonadiabatic effects on the vibronic structure and dynamics of these electronic states are examined at length. Also, interesting comparison is made with the results of the isomeric acetaldehyde radical cation.

Chapter 5 deals with the theoretical photoionization spectroscopy of the aziridine molecule. To start with, we have optimized the geometry of this molecule at the neutral (CH_2NHCH_2) electronic ground state at the DFT/aug-cc-pVTZ level of theory using the G09 program. The electronic structure calculations were restricted to the first six low-lying electronic states to account for the complete experimental photoelectron spectrum of the aziridine molecule. The first six low-lying electronic states ($\widetilde{X}\ ^2A'$, $\widetilde{A}\ ^2A'$, $\widetilde{B}\ ^2A''$, $\widetilde{C}\ ^2A''$, $\widetilde{D}\ ^2A'$, and $\widetilde{E}\ ^2A'$) of the PESs are calculated by both EOMIP-CCSD and MCQDPT *ab initio* quantum chemistry methods along the dimensionless normal displacement coordinates in which multiple conical intersections were observed between the electronic states. A (6×6) model vibronic Hamiltonian is constructed on a diabatic electronic basis, using the symmetry selection rules and Taylor series expansion. The C_s symmetry point group of the aziridine molecule enables the electronic states symmetry of either A' or A'' and these states are close in energy, due to which, the same symmetry electronic states avoid each other. To get a smooth diabatic PESs, a four-fold diabatization scheme was used, which is implemented in the GAMESS suite of programs. All the elements used in the diabatic VC model Hamiltonian are calculated in terms of the

normal modes of vibrational coordinates. Finally, the vibronic model Hamiltonian constructed for the coupled six electronic states was used to solve both time-independent and time-dependent Schrödinger equations using the MCTDH program module to get the dynamical observables. The theoretical vibronic band structure is found to be in good agreement with the available experimental results. At the end, we compared this results with Chapters 3 and 4 isoelectronic molecules.

Chapter 6 summarises the theoretical efforts, in my PhD (Jan. 2018 - May 2024), towards the understanding of the photo-induced dynamics of isoelectronic molecular systems. Additionally, it provides a summary of potential research topics and the future directions.

Chapter 2

Theoretical methodology

2.1 The Born-Oppenheimer approximation and Adiabatic electronic picture

The fundamental theoretical underpinnings of the current work are discussed in this chapter. The Born-Oppenheimer (BO) approximation [1] plays a crucial role in describing molecular chemistry. The division of electronic and nuclear motions is a fundamental tenet of this approximation. Considering that an electron's mass is significantly less (approximately 1836 times) than that of a nucleus, and electrons move swiftly, changes in nuclear locations can be regarded as unimportant when computing electronic wave functions. As a result, the BO approximation allows molecular processes to be calculated in two steps. The electronic problem is addressed in the first stage while the nuclei remain stationary. For each constant nuclear position, electronic energies are estimated using quantum chemistry methods, leading to the derivation of potential energy surfaces (PESs). The second stage involves performing nuclear dynamics on one or more predefined PESs.

In the entire molecular Hamiltonian, encompassing electronic q and nuclear Q coordinates, the time-independent molecular Schrödinger equation can be stated as:

$$\hat{H}(q,Q)\Psi(q,Q) = E\Psi(q,Q), \tag{2.1}$$

where $\Psi(q,Q)$ is an energy eigenfunction, E is the associated energy eigenvalue, and $\hat{H}(q,Q)$ is the molecular Hamiltonian, defined at the non-relativistic level of theory

$$\hat{H} = -\frac{\hbar^2}{2}\sum_{\alpha}\frac{\nabla_\alpha^2}{m_\alpha} - \frac{\hbar^2}{2m_e}\sum_{i}\nabla_i^2 + \sum_{\alpha}\sum_{\beta>\alpha}\frac{Z_\alpha Z_\beta e^2}{r_{\alpha\beta}} - \sum_{\alpha}\sum_{i}\frac{Z_\alpha e^2}{r_{i\alpha}} + \sum_{i}\sum_{j>i}\frac{e^2}{r_{ij}}. \tag{2.2}$$

Here, α and β refer to nuclei, and i and j refer to electrons. The first and second terms in Eq. 2.2 represent the operators for the kinetic energy of the nuclei and electrons, respectively. The third term accounts for the potential energy (PE) resulting from repulsions between the nuclei, denoted as $r_{\alpha\beta}$, the distance between nuclei α and β, each with atomic numbers Z_α and Z_β. The fourth term represents the PE arising from attractions between the electrons and the nuclei, with $r_{i\alpha}$ being the distance between electron i and nucleus α. The last term corresponds to the PE resulting from repulsions between the electrons, with r_{ij} representing the distance between electrons i and j. In abbreviated form, the above equation can be represented as follows:

$$\hat{H} \equiv \hat{T}_N + \hat{T}_e + \hat{V}_{NN} + \hat{V}_{eN} + \hat{V}_{ee}. \tag{2.3}$$

The following ansatz can be employed to expand the molecular wave function Ψ_i

$$\Psi_i(q, Q) = \sum_{i=1}^{N} \Phi_i(q, Q)\chi_i(Q). \tag{2.4}$$

Where $\Phi_i(q, Q)$ represents the electronic wave function and $\chi_i(Q)$ is the nuclear wave function, the ansatz given in Eq. 2.4 is exact for a complete set of eigenstates (i.e., $N \to \infty$). In many chemistry applications, N is constrained to a small number of closely related electronic states, and the impact of other electronic states is neglected. While nuclear wave functions are determined solely by the nuclear coordinate Q, electronic wave functions are influenced by both the electronic (q) and nuclear (Q) coordinates. The electron-nuclear interaction term $\hat{V}_{eN}$ (cf., Eq. 2.3) in the molecular Hamiltonian presents the primary obstacle to fully separating the electronic and nuclear wave functions. The electronic wave function, abbreviated as $\Phi_i(q, Q)$, in the BO approximation depends parametrically on the nuclear coordinates, denoted as $\Phi_i(q; Q)$. The fixed-nuclei electronic Schrödinger equation has been resolved by *ab initio* electronic structure processes in the BO approximation.

$$\hat{H}_e \Phi_i(q; Q) = V_i(Q)\Phi_i(q; Q), \tag{2.5}$$

The electronic Hamiltonian, denoted as $\hat{H}_e = \hat{T}_e + \hat{V}_{eN} + \hat{V}_{ee}$, features $V_i(Q)$ as the potential energy calculated by solving the eigenvalue equation 2.5, necessitating the nuclei to be in a fixed location. Parametrically altering the nuclear positions allows the acquisition of the PES, and solving Eq. 2.5 is performed for each case.

The coupled nuclear differential equation [1, 2] can be derived from the basis defined in Eq. 2.4 and the solution of the electronic Schrödinger equation 2.5.

$$\left[\hat{T}_N I + \hat{V}_j(Q) - E\right] \chi_j(Q) = \sum_{i=1}^{\infty} \hat{\Lambda}_{ij} \chi_i(Q). \tag{2.6}$$

In the preceding equation, the identity matrix is denoted as I. The quantity $\hat{\Lambda}_{ij}$ is defined as the components of the nonadiabatic coupling operator.

$$\hat{\Lambda}_{ij} = -\int dr \Phi_i^* [T_N, \Phi_j] \tag{2.7}$$

where $[A, B] = AB - BA$ represents the commutator of operators A and B. Utilizing the nuclear kinetic energy operator (KEO) in its generic form as a differential operator [99], the nonadiabatic operator $\hat{\Lambda}_{ij}$ in Q-space [2, 100] decomposes into a differential operator and a constant number.

$$\hat{\Lambda}_{ij} = \sum_{n=1}^{M} F_{ij}^{(n)} \nabla - G_{ij}, \tag{2.8}$$

with

$$F_{ij}^{(n)} = \langle \Phi_i | \nabla | \Phi_j \rangle; G_{ij} = \langle \Phi_i | \nabla^2 | \Phi_j \rangle \tag{2.9}$$

From Eq. 2.9, it is evident that the electronic states i and j are linked through derivative operators reflecting nuclear motion. The elements $F_{ij}^{(n)}$ and G_{ij} represent vector and scalar coupling, respectively. The presence of the nonadiabatic operator $(\hat{\Lambda}_{ij})$ adds complexity to the solution of the nuclear Schrödinger equation, especially for polyatomic molecules with multiple nuclear coordinates. The neglect of nonadiabatic operators $(\hat{\Lambda}_{ij}=0)$ corresponds to the adiabatic approximation. This approximation is grounded on the assumption that the KEO of the nuclei can be treated as a perturbation to electronic motion. A more practical approximation, the Born-Huang approximation [101], is derived by exclusively ignoring the off-diagonal terms of the nonadiabatic operators $\hat{\Lambda}_{ij}$. Employing the Hellmann-Feynman theorem [102–105], the vector coupling term is denoted as [2]:

$$F_{ij}^{(n)} = \frac{\langle \Phi_i(q; Q) | \nabla_n H_e(q; Q) | \Phi_j(q; Q) \rangle}{V_i(Q) - V_j(Q)} \tag{2.10}$$

In many instances, the adiabatic approximation proves inadequate, particularly when multiple electronic states are closely spaced in energy. The failure of the adiabatic approximation becomes pronounced when two electronic states are degenerate at the point of conical intersection (CI) $(i = j)$. In such cases, the derivative coupling terms for the electronic wave function ($F_{ij}^{(n)}$ in Eq. 2.9) become divergent, causing the breakdown of the adiabatic approximation near the CI. As a consequence of this singularity, electronic

states and their energies cease to be analytical functions of nuclear coordinates, leading to alterations in their electronic characteristics. A degeneracy cusp becomes evident on their energy surfaces [106].

Numerically solving the nuclear Schrödinger equation using the adiabatic electronic basis is impeded by the singularity of the aforementioned derivative coupling. To circumvent this issue, a diabatic electronic basis is introduced, involving a proper unitary transformation that converts the divergent kinetic coupling of the adiabatic electronic basis into a smoother potential coupling [2, 107–109]. Consequently, the nuclear Schrödinger equation is formulated on the diabatic electronic basis, as expressed in Eq. 2.6:

$$\left[\hat{T}_N I + \hat{U}_j(Q) - E\right]\chi_j(Q) = \sum_{i=1(i\neq j)}^{\infty} \hat{U}_{ij}(Q)\chi_i(Q), \tag{2.11}$$

with

$$\hat{U}_{ij}(Q) = \langle\phi_i(q;Q)|\hat{H}_e(q;Q)|\phi_j(q;Q)\rangle. \tag{2.12}$$

The electronic wave function for a diabatic system is expressed as $|\phi_i(q;Q)\rangle$, where integral operations are performed on electronic coordinates q. The divergent kinetic coupling presented in Eq. 2.6 is transformed into a smoother potential coupling in $\hat{U}_{ij}$, marking the primary distinction between Eqs. 2.6 and 2.11. On a diabatic basis, the divergent kinetic coupling can ideally be completely eliminated as a function of the Q basis, enabling the wave function and energy to recover analytic continuation. The diabatic electronic states are characterized by the diagonal elements $\hat{U}_j(Q)$ of the U matrix, while the coupling between them is defined by the off-diagonal elements $\hat{U}_{ij}(Q)$. As a result of analytical continuation, the states become smooth throughout the entire nuclear coordinate space, preserving the electronic nature of the states in this representation. The preceding discussion highlighted that, despite its greater realism, the adiabatic electronic representation is unsuitable for investigating dynamics. Consequently, albeit not entirely novel, the diabatic electronic representation is reinstated for all pertinent applications, ranging from atom-to-atom collisions to molecular spectroscopy [2, 108, 110].

2.2 Diabatic electronic representation

Consider the following diabatic electronic Hamiltonina featuring two states:

$$\hat{H}_e^d(Q) = \begin{bmatrix} \hat{U}_{11}(Q) & \hat{U}_{12}(Q) \\ \hat{U}_{21}(Q) & \hat{U}_{22}(Q) \end{bmatrix}. \tag{2.13}$$

In this context, the diabatic PESs are denoted by $\hat{U}_{11}(Q)$ and $\hat{U}_{22}(Q)$, while the coupling surface is described by $\hat{U}_{12}(Q)=\hat{U}_{21}(Q)$. All matrix elements depend on the set of nuclear coordinates Q. Employing a similarity transformation [2, 107–113] through an appropriate unitary matrix $\mathbf{S}$, it becomes feasible to obtain the adiabatic electronic Hamiltonian

$$\hat{H}_e^{ad}(Q) = \mathbf{S}^\dagger \hat{H}_e^d(Q)\mathbf{S}. \tag{2.14}$$

It is yielded by the transformation matrix and it is responsible for adiabatic-to-diabatic conversion.

$$\mathbf{S} = \begin{pmatrix} \cos\theta(Q) & \sin\theta(Q) \\ -\sin\theta(Q) & \cos\theta(Q) \end{pmatrix}. \tag{2.15}$$

where $\theta(Q)$, denoting the adiabatic-to-diabatic transfermation angle, is defined as [2],

$$\theta(Q) = \frac{1}{2}\tan^{-1}\left[\frac{2\hat{U}_{12}(Q)}{\hat{U}_{22}(Q) - \hat{U}_{11}(Q)}\right], \tag{2.16}$$

and $\Phi^{ad} = \mathbf{S}^\dagger\Phi^d$, ($\dagger$ denotes the adjoint). The expression for the adiabatic PESs is given by

$$V_{1,2}(Q) = \frac{1}{2}\left[(\hat{U}_{11} + \hat{U}_{22}) \pm \sqrt{(\hat{U}_{11} - \hat{U}_{22})^2 + (2\hat{U}_{12})^2}\right]. \tag{2.17}$$

This equation indicates the potential for their intersection. The difference between the potentials (V_1 and V_2) is determined by

$$\Delta V = V_1 - V_2 = \pm\sqrt{(\hat{U}_{11} - \hat{U}_{22})^2 + (2\hat{U}_{12})^2}. \tag{2.18}$$

The degeneracy (crossing) of the two adiabatic curves occurs when the square root of the two terms in the argument in Eq. 2.18 independently disappears, leading to the conditions

$$\hat{U}_{11}(Q) = \hat{U}_{22}(Q) \tag{2.19}$$
$$\hat{U}_{12}(Q) = 0. \tag{2.20}$$

To satisfy two equations simultaneously, only one independent parameter is possible, typically the inter-nuclear distance, denoted as Q. There is usually no compelling reason for a single variable to fulfill two distinct equations. Consequently, in one dimension, the potentials cannot cross, adhering to the "non-crossing rule". This principle is particularly pronounced for diatomics with a single degree of freedom (DOF), where two adiabatic curves related to the same symmetry of electronic states rarely intersect but exhibit avoided crossings [114].

In contrast, for molecules with three or more atoms (polyatomic systems), there are sufficient independent DOFs adaptable to meeting the conditions described in Eqs. 2.19 and 2.20. Consequently, degeneracies or surface crossings are expected to be common in polyatomic systems [4]. These crossings often manifest as isolated regions where the PESs can touch in two-dimensional space, referred to as "conical intersections"(CIs). Eq. 2.17 illustrates the double cone topography formed by the intersection of the two adiabatic PESs (V_1 and V_2) at the vertex [4, 5, 115].

In cases where there are more than two dimensions (N), the space housing all the intersections that constitute CIs is an (N-2)-dimensional space, with Eqs. 2.19 and 2.20 serving as two constraints.

2.3 The diabatic model Hamiltonian

2.3.1 Vibronic model Hamiltonian

This approach serves as the foundation for all theoretical investigations presented in this thesis. We assume the existence of a pre-established diabatic basis. In this configuration, the nuclear KEO resides in the diagonal elements of the matrix, while the off-diagonal components of the PE operator in the matrix delineate the coupling between electronic states. Unlike the adiabatic basis, where PESs exhibit non-crossing and discontinuity (singularity) at avoided crossings, in the diabatic basis, the PESs remain smooth when intersecting curves. The establishment of a suitable coordinate system is crucial before expressing components of the diabatic Hamiltonian. While an internal coordinate system, encompassing bond length and bond angle, is ideal for describing PESs, it becomes impractical for larger molecular systems. This choice leads to a highly complex representation of the nuclear KEO, challenging to analyze numerically for extensive systems.

Recognizing the need for a more efficient approach, especially for small amplitude nuclear motion, we adopt the normal coordinate representation of nuclear vibrations. In these coordinates, the nuclear KEO assumes a more straightforward form. Consequently, the electronic ground state of the associated neutral species is utilized to construct the vibronic Hamiltonian for the final states of the ionized species. Henceforth, electronic states and vibrational modes are denoted by n, m, and i, j, respectively. Diagonalizing the force field produces the mass-weighted normal coordinate (q_i), which is then transformed into dimensionless form [99] by

$$Q_i = (\omega_i/\hbar)^{\frac{1}{2}} q_i. \tag{2.21}$$

In this context, ω_i represents the harmonic frequency of the ith vibrational mode. For the convenience of this thesis, we adopt the convention $\hbar = 1$ (in atomic units). These vibrational frequencies delineate the normal displacement coordinates of the equilibrium geometry mentioned earlier at $\mathbf{Q} = 0$. The vibronic Hamiltonian, elucidating the photo-induced molecular process, can be articulated as follows expressed as [2]

$$\hat{H} = H_0 \mathbf{1_n} + \Delta H. \tag{2.22}$$

In the presented equation, $H_0 = \mathcal{T}_N + \mathcal{V}_0$ signifies the unperturbed Hamiltonian for the electronic ground state at equilibrium geometry. Expressed in terms of the dimensionless normal displacement coordinates of the vibrational modes, the KE and PE operators for the reference Hamiltonian H_0, within the harmonic approximation, are provided by

$$\mathcal{T}_N = -\frac{1}{2} \sum_i \omega_i \left[\frac{\partial^2}{\partial Q_i^2} \right], \tag{2.23}$$

$$\mathcal{V}_0 = \frac{1}{2} \sum_i \omega_i Q_i^2. \tag{2.24}$$

The term $\mathbf{1}_n$ in Eq. 2.22 represents the $n{\times}n$ diagonal unit matrix, where the value of n corresponds to the number of electronic states considered in the investigation of nuclear dynamics, and it can vary. The quantity ΔH denotes the change in electronic energy upon ionization from the reference Hamiltonian (H_0). The components of this electronic Hamiltonian (ΔH) elucidate the diabatic PESs ($\hat{U}_{nn}$) and their coupling PESs ($\hat{U}_{nm}$) with neighboring electronic states. The elements of $\hat{U}_{nm}$ play a crucial role in introducing nonadiabatic effects in molecules. All these factors are expanded in terms of Q_i in a Taylor series expansion.

$$\hat{U}_{nn} = E_n + \sum_i \kappa_i^{(n)} Q_i + \frac{1}{2!} \sum_{i,j} \gamma_{ij}^{(n)} Q_i Q_j + \cdots \tag{2.25}$$

$$\hat{U}_{nm} = \sum_i \lambda_i^{(nm)} Q_i + \cdots, (n \neq m) \tag{2.26}$$

with

$$\kappa_i^{(n)} = \left(\frac{\partial \hat{U}_{nn}}{\partial Q_i} \right) \Bigg|_{\mathbf{Q}=0} \tag{2.27}$$

$$\lambda_i^{(nm)} = \left(\frac{\partial \hat{U}_{nm}}{\partial Q_i} \right) \Bigg|_{\mathbf{Q}=0} \tag{2.28}$$

$$\gamma_{ij}^{(n)} = \frac{1}{2} \left[\frac{\partial^2 \hat{U}_{nn}}{\partial Q_i \partial Q_j} \right] \Bigg|_{\mathbf{Q}=0}. \tag{2.29}$$

In a molecular system, the vertical ionization energies (VIEs) are denoted by E_n, representing the vertical energy difference between the ground electronic state energy and the energy of the nth electronically interacting framework at $Q = 0$. The $\kappa_i^{(n)}$, illustrating the forces acting in an electronic state (n) and defining the structural modification relative to the potential of the ground state along the ith vibrational mode, and $\gamma_{ij}^{(n)}$, accountable for the frequency variation between the excited and ground states, are the linear and quadratic intra-state coupling constants for the nth electronic state, contributing to the Duschinsky rotation. For the coupling between the nth and mth electronic states, the linear inter-state coupling constant is denoted by $\lambda_i^{(nm)}$. Symmetry considerations eliminate numerous variables in Eqs. 2.25 and 2.26, particularly for highly symmetric molecules. To adhere to the symmetry selection criteria for non-vanishing linear terms, the condition is expressed as:

$$\Gamma_n \otimes \Gamma_{Q_i} \otimes \Gamma_m \supset \Gamma_A, \tag{2.30}$$

where Γ_n and Γ_{Q_i} are irreducible representations (IRREPs) of the nth electronic state and the ith vibrational mode. Similarly, non-vanishing quadratic terms satisfy

$$\Gamma_n \otimes \Gamma_{Q_i} \otimes \Gamma_{Q_j} \otimes \Gamma_m \supset \Gamma_A. \tag{2.31}$$

Similarly, these conditions extend to higher-order terms.

2.4 Four-fold way diabatization scheme

In this section, we will emphasize the diabatization based on electronic wavefunctions (i.e., properties of adiabatic wavefunctions) [116]. Other than this, there two more commonly employed diabatization methods are available in the literature. The first one is, diabatization based on derivative couplings (quasi-diabatization) and it is originally proposed by Simah and by Baer [112, 117]. The second method is based on the potetntial energies and it is a simpler approach compared to the other two methods, which is inherently more appropriate and relies only on PESs themselves [2, 118–120]. Among the three methods, the diabatization based on electronic wavefunctions (i.e., four-fold diabatization) method offers several advantages as follows; (1). It captures higher-order effects beyond linear couplings between the electronic states and nuclear motion. (2). It provides a more accurate description of nonadiabatic effects, such as avioded crossings and conical intersections. (3). It can be applied to a wide range of molecular systems, including large and complex molecules (i.e., when the molecules are having same spatial symmetry couplings). A schematic representation of the adiabatic and diabatic (after

four-fold diabatization) potential energy cuts are shown in Fig. 2.1.

Originally, the Nakamura and Truhlar proposed the fourfold-way diabatization scheme in unique path and they are briefly discussed in Refs. [116, 121–124]. The fourfold-way has several significant advantages main advantage is we can calculate the diabatic potentials and couplings at a particular geometry those are independent of any path leading to that geometry, and ability to create N diabatic electronic states that span the same space as N selected adiabatic states (for example, the N lowest) is a key characteristic of fourfold-way diabatization. In short, the main theme of this method is discussed below. The density matrix acts as the foundation for the fourfold-way method [116], it was first proposed to diabatize complete-active-space (CAS) self-consistent-field (CASSCF) wave functions. However, CASSCF is not quantitatively correct since it contains only a small portion of the dynamical correlation. To add dynamical correlation the approach was improved for the diabatization of multi-configuration quasi-degenerate per-turbation theory (MC-QDPT) [125–127]. In order to obtain diabatic states the multi-electron wave functions are defined in terms of diabatic molecular orbitals (DMOs) rather than the more common canonical molecular orbitals (CMOs) because the DMOs change smoothly with geometry. In contrast, continuous nuclear-coordinate pathways along CMOs are not required to be smooth. In the initial algorithms used DMOs derived from the CASSCF wave function to express the CASSCF diabatic states, and the eigenvectors of the MC-QDPT effective Hamiltonian were used to create a density matrix, from which the MC-QDPT diabatic states were derived in terms of DMOs.

In this thesis we have used the fourfold-way diabatization to calculate the VC between the electronic states of the same spatial symmetry, at the level of the multi-configuration quasi-degenerate perturbation theory (MCQDPT) [125–127], GAMESS program module [128] is used for this purpose. This kind of VC typically happens in molecules that belong to the equilibrium point group of low symmetry [55–57]. The fourfold method generates diabatic molecular orbitals (DMOs) that vary gradually. Normal configuration state functions (CSFs) written in terms of canonical (adiabatic) MOs are transformed into orthogonal diabatic CSFs (CSFs written in terms of DMOs), which is a novel process. So, we firstly derived CASSCF DMOs and then represented the adiabatic MCQDPT wave functions in terms of the CASSCF DMOs, and latter using the direct diabatization we can derive the energy of diabatic states and diabatic couplings. The following represents the way inter-state couplings occur when using this specific approach.

$$u^{nm} = u_0^{nm} + \sum_{i \epsilon a'} \lambda_i^{nm} Q_i + \frac{1}{2!} \sum_{i \epsilon a'} \gamma_i^{nm} Q_i^2 \qquad (2.32)$$
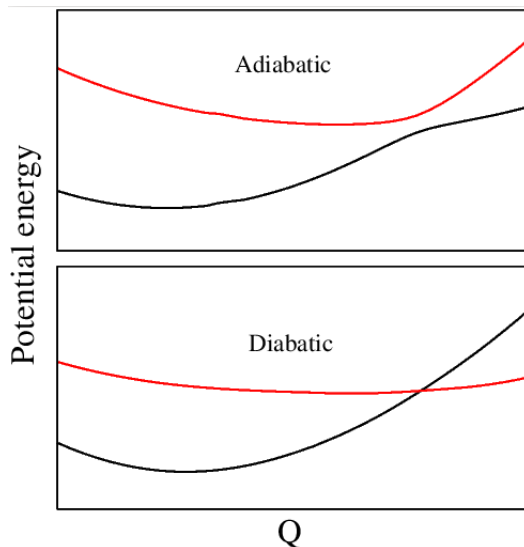
FIGURE 2.1:   Schematic representation of adiabatic and diabatic potential energy curves.

where u_0^{nm} is the calculated electronic couplings of the diabatic electronic states taken into account by the model at the ground state reference geometry ($\mathbf{Q}$=0). The u_0^{nm} is a constant at a distorted geometry for the coupled PESs, and the a' defines the totally symmetric vibrational mode (in the case of C_s symmetry point group). That is, the same spatial symmetry states couples through the totally symmetric vibrational mode.

2.5   Nuclear dynamics and electronic spectrum modelling

The nuclear dynamics of molecular systems are significantly influenced by the VC. Some approaches, like the surface hoping method [129], incorporate VC effects in a traditional treatment of dynamics. However, the goal of the present study is to provide a comprehensive quantum consideration of nuclear motion. The nuclear Schrödinger equation must be solved in order to do complete quantum dynamics simulations. This is easily accomplished in both time-independent and time-dependent techniques. A simple way is to build the total wave function from time-independent basis functions with time-dependent coefficients. Due to exponential escalation in computational time and memory requirements, this approach is only practical for a limited set of DOFs. The MCTDH method, developed by Meyer, Manthe, and Cederbaum in 1990 [130], is one approach to overcoming this issue. The time-dependent Schrödinger equation can be solved using this effective approach, which is based on a multi-configurational wave function ansatz.

A time-independent and time-dependent quantum mechanical approach is used to conduct a first-principles investigation of nuclear dynamics. The vibronic spectrum is determined via Fermi's golden rule (spectral intensity equation) in the time-independent

technique [2, 131]

$$P(E) = \sum_n |\langle \Psi_n^f | \hat{T} | \Psi_0^i \rangle|^2 \delta(E - E_n^f + E_0^i). \tag{2.33}$$

In the above equation, the quantity $\hat{T}$ denotes the transition dipole matrix corresponding to the photoionization mechanism, while E represents the energy of the external radiation. The initial and final vibronic states are denoted by $|\Psi_0^i\rangle$ and $|\Psi_\nu^f\rangle$ with respective energies ε_0^i and ε_ν^f. Within a diabatic electronic framework, the initial state is expressed as

$$|\Psi_0^i\rangle = |\Phi_0^i\rangle |\chi_0^i\rangle, \tag{2.34}$$

where, $|\Phi_0^i\rangle$ and $|\chi_0^i\rangle$ denoting the diabatic electronic and nuclear components of the initial wavefunction, respectively, the nuclear segment of the wave function takes the form of a direct product of the eigenfunctions of the reference Hamiltonian, $\mathcal{H}_0$. As a result, the final vibronic state of can be expressed as follows:

$$|\Psi_n^f\rangle = \sum_m |\Phi^m\rangle |\chi_n^m\rangle. \tag{2.35}$$

The variables m and ν in the aforementioned equation denote electronic states and vibrational modes, respectively. The spectral intensity described by Eq. 2.33 can now be expressed as

$$P(E) = \sum_{n,m} |\tau^m \langle \chi_n^m | \chi_0 \rangle|^2 \delta(E - E_n^f + E_0^i), \tag{2.36}$$

where,

$$\tau^m = \langle \Phi^m | \hat{T} | \Phi^0 \rangle, \tag{2.37}$$

represent the elements of the transition dipole matrix. When Eq. 2.36 is restructured, these elements are perceived as a weakly fluctuating function of nuclear coordinates. Within the framework of the generalized Condon approximation in a diabatic electronic basis, these elements remain constant throughout the current investigation [132].

2.5.1   Time-independent approach

The Hamiltonian (cf., Eq. (2.22)) is represented in the direct product HO basis of the reference state to solve the time-independent Schrödinger equation of vibronically coupled states. On this approach, the vibrational wave function, $|\chi_n^m\rangle$, is given by

$$|\chi_n^m\rangle = \sum_{n_1, n_2, ..., n_k} a_{n_1, n_2..., n_k}^m |n_1\rangle |n_2\rangle ... |n_k\rangle. \tag{2.38}$$

In the above equation, quantum number n_l that corresponds to the lth vibrational mode is given, and the total number of such modes is given by the variable k. The summing

covers all possible quantum number and diabatic state combinations. Depending on the excitation strength of each vibrational mode, the vibrational basis is appropriately truncated, $\left(\kappa^2/2\omega^2\right)$ and $\left(\lambda^2/2\omega^2\right)$ for the totally symmetric and non-totally symmetric vibrational modes, respectively. When the Hamiltonian matrix is stated in a direct product HO basis, it develops a sparse structure. This sparse matrix is tridiagonalized using the Lanczos technique [133], before being diagonalized. The location of the vibronic energy levels is determined by this matrix eigenvalues, and the intensity is determined by squaring the first element of the eigenvector matrix [134]. The vibronic eigenvalue spectrum produced using the above-described prescription is convolved with a line shape function to produce the spectral envelope, making it easier to compare with the experiment.

$$P_\Gamma(E) = P(E) \otimes \mathcal{L}_\Gamma(E) \tag{2.39}$$

For example, the $\mathcal{L}_\Gamma(E)$ can be taken as Lorentzian function with full width at the half maximum (FWHM) Γ

$$\mathcal{L}_\Gamma(E) = \frac{1}{\pi} \frac{\Gamma/2}{E^2 + (\Gamma/2)^2}. \tag{2.40}$$

2.5.2 Time-dependent approach

In a time-dependent context, the expression for $P(E)$ as defined in Eq. 2.33 undergoes transformation into the Fourier transform of the time autocorrelation function of the wavepacket propagating on the final electronic states

$$
\begin{aligned}
P(E) &\approx 2Re \sum_{m=1}^{N} \int_0^\infty e^{iEt/\hbar} \langle \chi_0 | \tau^\dagger e^{-i\hat{H}t/\hbar} \tau | \chi_0 \rangle dt, \tag{2.41} \\
&\approx 2Re \sum_{m=1}^{N} \int_0^\infty e^{iEt/\hbar} C^m(t) dt, \tag{2.42}
\end{aligned}
$$

where, $C^m = \langle \Psi^m(0) | \Psi^m(t) \rangle$, represents the time autocorrelation function of the WP initially prepared on the mth electronic state. Finally, the composite spectrum is computed by averaging the component spectra acquired by applying WP to each electronic state.

2.6 The Multi-configuration time-dependent Hartree method

Despite the straightforward implementation and good numerical precision, the traditional approach, which is the straightforward numerical solution of the time-dependent Schrödinger equation (TDSE), the computing effort grows exponentially with the number of electronic and nuclear DOFs. The time-dependent Hartree (TDH) technique,

which describes the wave function as a Hartree product of time-dependent single-particle-functions (SPFs), is an alternative to the traditional method, or the Dirac-Frenkel variational principle [135, 136] is used to solve the TDSE in order to derive the orbitals and the time-dependent expansion coefficients.

$$\langle \delta \Psi \left| \hat{H} - i\frac{\partial}{\partial t} \right| \Psi \rangle. \tag{2.43}$$

The TDH, is a single reference approach, frequently performs badly and misses a major portion of the correlation between distinct DOFs [137]. The numerically accurate approach correctness and the TDH method effectiveness have been traded off in the development of the MCTDH method [130, 138, 139]. The ability of MCTDH to cover a whole range of approximations between TDH (single reference) and numerically precise (similar to the entire CI treatment in electronic structure theory) is made possible by the flexibility in the number of DOFs and in selecting the number of SPFs. Importantly, the variational aspect means that small sets of SPFs are frequently enough to produce effective results in many situations, which makes the MCTDH technique desirable, especially when the number of DOFs are more.

The following ansatz defines the MCTDH wave function [130, 138, 139], which permits the combination of several DOFs in its multi-set formulation:

$$
\begin{aligned}
\Psi(Q_1, Q_2, ..., Q_f, t) &= \Psi(q_1, q_2, ..., t) \tag{2.44} \\
&= \sum_m \sum_{j_l=1}^{n_l^{(m)}} \sum_{\cdots} \sum_{j_p=1}^{n_k^{(m)}} A_{j_l,...,j_p}^{(m)}(t) \prod_{k=1}^{p} \phi_{jk}^{(m,k)}(q_k, t)|m\rangle, \tag{2.45} \\
&= \sum_m \sum_J A_J^{(m)} \Phi_J^{(m)} |m\rangle. \tag{2.46}
\end{aligned}
$$

The electronic state indices in the aforementioned equation are m, f, and p, the number of vibrational DOFs, and MCTDH particles count, respectively. The DOFs are combined to create the particles. The particle coordinate, for instance, can be specified as, $q_k=[Q_1, Q_2, ...]$. The $\phi_{jk}^{(m,k)}$ are the n_k time-dependent expansion functions (SPFs) for each DOF k connected to the electronic state m, and the $A_{j_l,...,j_p}^{(m)}$ stands for the MCTDH expansion coefficients. The latter is the multidimensional function of the set of particle coordinates. Since $p < f$, the computational overhead for systems with many degrees of freedom has been dramatically decreased. The coordinates of a particle in one- or multi-dimensions are used to define the variables for the p sets of SPFs. The SPFs indicated by the composite index $J=(j_l, ..., j_p)$ are combined to form $\Phi_J^{(m)}$, which

is a f-dimensional Hartree product. In order to represent the SPFs practically, a time-independent primitive basis set must be used as the foundation.

$$\phi_{jk}^{(m,k)}(q_k,t) = \sum_{l=1}^{N_k} c_{lj_k}^{(k)}(t)\chi_l^{(k)}(q_k). \tag{2.47}$$

A discrete variable representation (DVR) grid is commonly used in place of the primitive basis functions. Only in the case when $n_k < N_k(k = 1,...,f)$ does MCTDH outperform the numerically accurate technique. The approach evaluates the WP on the grid using DVR, the rapid Fourier transform algorithm, and robust integrators. Readers are directed to the URL for more technical information https://www.pci.uni-heidelberg.de/cms/mctdh.html.

We give a quick description of the memory required for the MCTDH calculations here because memory consumption is frequently the limiting factor in quantum dynamical calculations. In comparison to the N^f numbers needed to describe the traditional approach, the MCTDH wave functions necessitate

$$memory \sim fnN + n^f, \tag{2.48}$$

Here, f, n, and N represent the total number of DOFs, SPFs, and total number of grid points or primitive basis functions, respectively. The first part in the sum (fnN) accounts for the space needed to store the SPFs, and the second term (n^f), accounts for the storage of the coefficient vector [140]. The base can be further lowered by putting DOFs together in combined modes or logical coordinates [140]. The number of effective DOFs, d, is reduced (i.e., d DOFs are combined). There are therefore $p = f/d$ particles; the grid size grows to $\tilde{N} = N^d$, and the number of combined SPFs grows to $\tilde{n} = dn$. The amount of RAM required shifts to

$$memory \quad \sim \quad p\tilde{n}\tilde{N} = \tilde{n}^p \tag{2.49}$$

$$\sim \quad fnN^d + \tilde{n}^{f/d}, \tag{2.50}$$

It results in significant memory savings when the problem's dimension is high [140, 141]. The readers are advised to consult the original research articles for further information on this method and algorithm [130, 138, 139, 142]. All of the quantum dynamical calculations in this thesis will be performed using the Heidelberg MCTDH software package [142].

Chapter 3

Multi-state and multi-mode vibronic coupling effects in the photo-ionization spectroscopy of acetaldehyde

This chapter focuses on the photo-ionization spectroscopy of the acetaldehyde molecular system. The analysis encompasses the examination of the first seven low-lying electronic states of $CH_3COH^{.+}$, and the construction of potential energy surfaces (PESs) along dimensionless normal displacement coordinates. A vibronic coupling model is then developed on a diabatic basis, and the photoelectron spectrum of CH_3COH is calculated and studied. Before delving into the specifics, a brief introduction is provided, elucidating the motivation behind this chapter's work. It is noted that numerous complex organic molecules (COMs) have been identified in stellar environments [25], where they undergo ionization through charge transfer reactions or exposure to cosmic radiation [26]. Ultraviolet (UV) and vacuum ultraviolet (VUV) radiations emitted by stars can effectively ionize and dissociate these molecules [27]. One such COM speculated to leave a signature in interstellar space is the acetaldehyde radical cation, $CH_3COH^{.+}$. Its neutral counterpart has been detected under various interstellar conditions [28–32]. Consequently, understanding the photochemistry and photophysics of $CH_3COH^{.+}$ holds fundamental interest and potential astrochemical significance.

The analysis of Rydberg series in the recorded absorption spectrum indicated that the lowest adiabatic ionization potential of CH_3COH is approximately $\sim$82,505$\pm$5 cm^{-1} (equivalent to 10.2293$\pm$0.0007 eV), as reported by Walsh *et al.* [33]. A similar value of

$\sim$10.2295$\pm$0.0007 eV was reported by Knowles *et al.* [34]. Various experimental techniques have been employed to study the photoelectron spectra of acetaldehyde, including experiments using He I and He II radiations [35–47], photoionization mass spectrometry [48–50], and electron impact mass spectrometry [51]. Additionally, studies involving photoelectron-photoion coincidence have been documented [45, 52, 53]. Yencha *et al.* [54] recently reported the threshold photoelectron (TPE) spectrum and total photoion yield (TPIY) spectrum of acetaldehyde. In a recent study, Kapnas *et al.* [49] conducted a velocity-map ion imaging experiment to characterize the wavelength-dependent photo-fragmentation dynamics of CH_3COH^{+}.

Among the experiments mentioned above, He I, He II and TPE spectra of acetaldehyde show a strong 0-0 component near 10.29 eV in the first band [35–47, 54]. This is attributed to originate from a non-bonding type of parent orbital, which can be assigned to the oxygen "lone pair" [n_O ($10a'$)] orbital. Excitation of three ionic vibrational modes at 1260 cm^{-1} (C-H rocking/CH$_3$ deformation), 1100 cm^{-1} (C-C stretching) and 700 cm^{-1} (CH$_3$ rocking) was reported in this band [37]. A few diffuse bands corresponding to the higher excited states of the cation were also observed at higher vertical ionization energy (VIE). The second ($\widetilde{A}$) band at $\sim$13.10 eV showed two vibrational structures, with progressions of CO stretching (ν_4, $\sim$1270 cm^{-1}) and CCO bend/deformation (ν_{10}, $\sim$460 cm^{-1}) vibrational modes. The $\widetilde{A}$ state originates from ionization of an electron from the $\pi_{C=O}$ ($2a''$) bonding molecular orbital of CH$_3$COH. No vibrational structure was observed in the third, fourth, fifth and seventh band originating from the $\widetilde{B}$, $\widetilde{C}$, $\widetilde{D}$ and $\widetilde{F}$ electronic states, respectively. On the other hand, vibrational progression of $\sim$1200 cm^{-1} due to CO stretching mode was reported in the sixth electronic band due to $\widetilde{E}$ electronic state occurring at a VIE of $\sim$16.32 eV. The latter state is formed from an ionization of a σ-type of CO orbital. Among the six electronic bands, the first and the last bands are energetically well separated from the other bands and the remaining bands are very close in energy. Therefore, in case of the latter bands vibronic coupling of the electronic states is anticipated to play an important role to shape up their observed structure. In addition to this, the $\widetilde{B}$, $\widetilde{C}$ and $\widetilde{E}$ electronic states of CH_3COH^{+} possess the same spatial symmetry, A'. The electronic structure data presented later in the text reveal avoided crossings among them. Therefore, although not strictly governed by the selection rule, coupling among them is expected to have impact on the dynamics. Such couplings are rare and treated in different ways by various practitioners in the literature [55–57, 116, 121–124, 143]. Generally, this type of vibronic coupling often occurs in molecules belonging to equilibrium point group of low symmetry [55–57]. The vibronic coupling between the electronic states of same spatial symmetry in the present case is calculated by applying the fourfold-way diabatization scheme proposed by Truhlar *et al.*

[116, 121–124] at the level of multi-configuration quasi-degenerate perturbation theory (MCQDPT) [125–127].

To the best of our knowledge, a study of the multi-state and multi-mode quantum dynamics of $CH_3COH^{.+}$ has not been reported till date. However, some theoretical calculations on the electronic structure and spectroscopic data of CH_3COH were reported [37, 144–149]. Also, while dealing with the ionized species as a reference molecule there are some challenges and difficulties to consider in the theoretical calculations. That is, spin and spin-contamination, relativistic effect, and spin-orbit coupling. Therefore, the main goal of the present work is to study the nuclear dynamics in the mentioned seven electronic states of $CH_3COH^{.+}$ from first principles by constructing a theoretical model through rigorous *ab initio* quantum chemistry calculations. A vibronic coupling model is developed in a diabatic electronic basis with the aid of the adiabatic electronic energies calculated *ab initio*. The latter calculations are carried out by the equation of motion ionization potential coupled cluster singles and doubles (EOMIP-CCSD) method [150, 151]. Time-independent and time-dependent quantum mechanical methods are employed to carry out nuclear dynamics calculations. A matrix diagonalization method using the Lanczos algorithm [133] is employed for the time-independent calculations. For the time-dependent calculations wave packet (WP) propagations are carried out. The multi-configuration time-dependent Hartree (MCTDH) method developed at Heidelberg is employed for the purpose [139, 152–154]. A comparison is made between the theoretical and experimental results and discussed in detail.
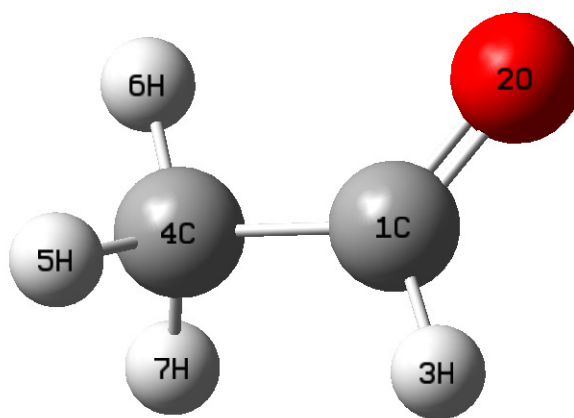
FIGURE 3.1: Schematic representation of the optimized equilibrium structure of CH_3COH in its electronic ground state.

3.1 *Ab initio* calculations

The reference electronic ground state geometry of CH_3COH molecule is optimized at the density functional theory (DFT) level with Becke 3-parameter, Lee-Yang-Parr (B3LYP) functional employing the 6-311++g(d,p) basis set. Gaussian-09 program module is used for the calculation [155]. The optimized equilibrium geometry belongs to the C_s symmetry point group and $^1A_1$ ground electronic term. The optimized equilibrium geometry of CH_3COH is plotted in Fig. 3.1 and the corresponding geometry parameters are given in Table 3.1.

TABLE 3.1: Geometry parameters (distances in Angstroms, angles in degrees) of the equilibrium structure of the electronic ground state of CH_3COH.

parameters	This work	Experiment [156]
R(C1-O2)	1.206	1.216
R(C1-H3)	1.112	1.114
R(C1-C4)	1.504	1.501
R(C4-H5,C4-H6,C4-H7)	1.090	
∠(O2-C1-H3)	120.07	
∠(O2-C1-C4)	124.79	123.92
∠(H3-C1-C4)	115.13	117.47
∠(C1-C4-H5,C1-C4-H7)	109.47	
∠(C1-C4-H6)	110.93	

Harmonic frequency (ω_i) of the vibrational modes at the equilibrium geometry is calculated at the same level of theory by diagonalizing both kinematic ($\mathbf{G}$) and *ab initio* force constant ($\mathbf{F}$) matrix [99]. The resulting eigenvectors yield the mass-weighted normal coordinates of the vibrational modes. The latter are transformed to their dimensionless form Q_i by multiplying with $\sqrt{\omega_i}$ (in atomic units, $\hbar=1$). The normal modes, their symmetry labels and the harmonic vibrational frequencies are given in Table 3.2. The vibrational frequencies and the optimized parameters (cf., Table 3.1) are in good agreement with the available literature data [144, 156–159].

The potential energy surfaces of the electronic states of $CH_3COH^{.+}$ are constructed along the dimensionless normal displacement coordinates ($\mathbf{Q}$) of the reference electronic ground state of the neutral CH_3COH for the nuclear dynamics study. The adiabatic energies of these electronic states of $CH_3COH^{.+}$ are calculated by the EOMIP-CCSD method using the 6-311++g(d,p) basis set. The calculations are carried out with CFOUR suite of programs [160]. The VIEs are calculated along the dimensionless normal displacement coordinate of each vibrational mode at the reference equilibrium geometry ($\mathbf{Q}_0$) by various methods [viz., outer valence Green's function (OVGF) [161], EOMIP-CCSD,

and complete active space self-consistent field multi-reference configuration interaction (CASSCF-MRCI) [162–165]] are given in Table 3.3 . The available literature data are also given in the table for comparison. It can be seen from the table that our theoretical results compare well with the available experimental data. The data given in the Table 3.3 show that both $\widetilde{X}$ and $\widetilde{F}$ states are energetically far apart from the other electronic states. The remaining ($\widetilde{A}$ to $\widetilde{E}$) electronic states are vertically very close in energy. Among the latter electronic states, the $\widetilde{C}$ and $\widetilde{D}$ states are quasi-degenerate at the Franck-Condon region. Due to the energetic proximity of $\widetilde{A}$, $\widetilde{B}$, $\widetilde{C}$, $\widetilde{D}$ and $\widetilde{E}$ electronic states, nonadiabatic interactions among them appear to be crucial to govern the mechanistic details of the nuclear dynamics.

TABLE 3.2: The vibrational modes of the electronic ground state of the CH_3COH are designated by their symmetry and their harmonic frequency (in cm^{-1}).

modes	This work	Theory [144]	Experiment [157]	Experiment [158]	Experiment [159]	Nature of mode
a'						
ν_1	3134	3118	3005	3014	3138	CH_3 d-str.
ν_2	3020	3035	2917	2923	3056	CH_3 s-str.
ν_3	2870	2868	2822	2716	2841	CH str.
ν_4	1807	1812	1743	1743	1774	CO str.
ν_5	1460	1483	1441	1433	1457	CH_3 d-deformation
ν_6	1420	1426	1390	1395	1411	CH bend
ν_7	1377	1377	1352	1352	1400	CH_3 s-deformation
ν_8	1127	1138	1113	1114	1145	CC str.
ν_9	885	879	877	867	906	CH_3 rock
ν_{10}	510	507	509	509	521	CCO deformation
a''						
ν_{11}	3074	3106	2967	2964	3072	CH_3 d-str.
ν_{12}	1469	1461	1420	1448	1469	CH_3 d-deformation
ν_{13}	1132	1125	1107	1111	1129	CH_3 rock
ν_{14}	776	776	763	764	780	CH bend
ν_{15}	152	140	150	150	186	CH_3 torsion

TABLE 3.3: Seven lowest VIEs (in eV) of the $CH_3COH^{.+}$ at various level of theory.

State	OVGF	EOMIP-CCSD	CASSCF-MRCI [14,11] active space	Experiment[54]	Experiment[166]
$\widetilde{X}^2A'$	10.37	10.03	10.23	10.228	10.3(10.20)
$\widetilde{A}^2A''$	13.31	13.26	13.38	13.093	13.2(12.61)
$\widetilde{B}\ ^2A'$	14.39	14.36	14.51	13.93	14.2
$\widetilde{C}^2A'$	15.39	15.29	15.57	15.20	15.4
$\widetilde{D}^2A''$	15.56	15.70	15.90	15.5	15.4
$\widetilde{E}^2A'$	16.66	16.59	16.79	16.37	16.5
$\widetilde{F}^2A'$		19.81	20.13	19.4	19.4

3.2 Multi-state and multi-mode vibronic Hamiltonian

In this section, a coupled states vibronic Hamiltonian is constructed to study the nuclear dynamics in the first seven electronic states of $CH_3COH^{.+}$. The Hamiltonian is constructed in a diabatic electronic basis and in terms of the dimensionless normal displacement coordinates (Q) of the vibrational modes employing the symmetry selection rule. The equilibrium geometry of CH_3COH has C_s point group symmetry and the states belong to either A' or A'' electronic term. Symmetry allowed coupling between A' and A'' symmetry states is caused by five a'' vibrational modes ($A' \times A'' \times a'' \supset A'$) in first-order. Although not governed by symmetry rule, the vibrational modes of a' symmetry act both as tuning and coupling modes among the states of same symmetry. The fifteen vibrational modes of the reference CH_3COH molecule belong to the following symmetry species of the C_s symmetry point group

$$\Gamma_{vib} = 10a' + 5a''. \tag{3.1}$$

The vibronic model Hamiltonian of the $\widetilde{X}$, $\widetilde{A}$, $\widetilde{B}$, $\widetilde{C}$, $\widetilde{D}$, $\widetilde{E}$ and $\widetilde{F}$ electronic states of $CH_3COH^{.+}$ can be symbolically written as [167]

$$\mathcal{H} = \mathcal{H}_0 \mathbf{1_7} + \Delta\mathcal{H}. \tag{3.2}$$

In the above equation, $\mathcal{H}_0 = \mathcal{T}_N + \mathcal{V}_0$, is the unperturbed Hamiltonian of the reference electronic ground state of CH_3COH. Within the harmonic approximation its elements are given by

$$\mathcal{T}_N = -\frac{1}{2} \sum_{i\epsilon a',a''} \omega_i \frac{\partial^2}{\partial Q_i^2}, \tag{3.3}$$

$$\mathcal{V}_0 = \frac{1}{2} \sum_{i\epsilon a',a''} \omega_i Q_i^2. \tag{3.4}$$

The quantity $\mathbf{1_7}$ in Eq. 3.2 is a 7×7 diagonal unit matrix. The quantity $\Delta\mathcal{H}$ represents the change in electronic energy upon ionization. In a diabatic electronic basis it is given by

$$\Delta\mathcal{H} = \begin{pmatrix} \varepsilon^{\widetilde{X}} + u^{\widetilde{X}} & u^{\widetilde{X}\widetilde{A}} & 0 & 0 & u^{\widetilde{X}\widetilde{D}} & 0 & 0 \\ & \varepsilon^{\widetilde{A}} + u^{\widetilde{A}} & u^{\widetilde{A}\widetilde{B}} & u^{\widetilde{A}\widetilde{C}} & 0 & u^{\widetilde{A}\widetilde{E}} & u^{\widetilde{A}\widetilde{F}} \\ & & \varepsilon^{\widetilde{B}} + u^{\widetilde{B}} & u^{\widetilde{B}\widetilde{C}} & u^{\widetilde{B}\widetilde{D}} & u^{\widetilde{B}\widetilde{E}} & 0 \\ & & & \varepsilon^{\widetilde{C}} + u^{\widetilde{C}} & u^{\widetilde{C}\widetilde{D}} & u^{\widetilde{C}\widetilde{E}} & 0 \\ & & & & \varepsilon^{\widetilde{D}} + u^{\widetilde{D}} & u^{\widetilde{D}\widetilde{E}} & u^{\widetilde{D}\widetilde{F}} \\ & h.c. & & & & \varepsilon^{\widetilde{E}} + u^{\widetilde{E}} & 0 \\ & & & & & & \varepsilon^{\widetilde{F}} + u^{\widetilde{F}} \end{pmatrix} . \tag{3.5}$$

The diagonal elements of the matrix in Eq. 3.5 represent the diabatic energies of the electronic states of $CH_3COH^{\cdot+}$ and the off-diagonal elements represent the coupling between various electronic states. We note that, in Eq. 3.5 some of the coupling (off-diagonal) terms are approximated to zero between the same symmetry electronic states. This is primarily because a large energy gap between these states and the absence of avoided crossings among them (see later in the text). The quantity ε^n is the VIE of the nth electronic state. The elements u^n and u^{nm} are expanded in a Taylor series in Q in the following way,

$$u^n = \sum_{i\epsilon a'}\kappa_i^n Q_i + \frac{1}{2!}\sum_{i,j\epsilon a',a''}\gamma_{ij}^n Q_i Q_j + \frac{1}{3!}\sum_{i\epsilon a'}\rho_i^n Q_i^3 + \frac{1}{4!}\sum_{i\epsilon a''}\xi_i^n Q_i^4 \; ; \;\; n \in \widetilde{X} - \widetilde{F}, \quad (3.6)$$

$$u^{nm} = \sum_{i\epsilon a''}\lambda_i^{nm} Q_i + \sum_{i\epsilon a''}\beta_i^{nm} Q_i^3 + \sum_{i\epsilon a''}\eta_i^{nm} Q_i^5 \; ; \;\; n, m \in \widetilde{X} - \widetilde{F}. \quad (3.7)$$

In Eq. 3.6 the linear, quadratic, cubic, and quartic intrastate coupling parameters are defined by κ_i^n, γ_{ij}^n, ρ_i^n, and ξ_i^n, respectively, for the nth electronic state along the ith vibrational mode. The quantity u^{nm} denotes the diabatic coupling between the n and m electronic states via the vibrational modes of a'' symmetry. Quantities λ_i^{nm}, β_i^{nm} and η_i^{nm} represent the linear, cubic and fifth order inter-state coupling parameters, respectively. The higher-order coupling parameters (ξ_i^n, η_i^{nm}) describe the anharmonicity of the potentials. It is noted that the potentials along the a' and a'' symmetry vibrational modes are expanded up to third and fourth-order, respectively. That is, third-order expansion is enough to represent the *ab initio* points well along the a' modes and to account the anharmonicity of the *ab initio* potentials along the a'' (ν_{12} and ν_{15}) modes the fourth-order expansion is required along these modes. The adiabatic form of the diabatic electronic Hamiltonian of Eq. 3.5 is fit to the *ab initio* calculated adiabatic electronic energies by a non-linear least squares method to derive the coupling parameters introduced above. Also, the parameters which are involved in Eq. 3.7 are evaluated from a separate two-state model calculations. Tables A1 to A3 of the Appendix A provide the estimated entire set of parameters.

As we can see from the Fig. 3.2 that the electronic states of same spatial A' symmetry (viz., $\widetilde{B}$-$\widetilde{C}$, $\widetilde{B}$-$\widetilde{E}$ and $\widetilde{C}$-$\widetilde{E}$ states) clearly show an avoided crossing between them. The same spatial symmetry states can also be coupled through totally symmetric (a') vibrational modes. That is, the coupling modes simultaneously modulate the energy gap between the uncoupled electronic states. Especially for these states the vibrionic coupling mechanism operates only by virtue of strong electron correlation effects [55]. This is a rare situation encountered in the vibronic coupling literature with polyatomic molecules belonging to low symmetry point groups [55–57]. The coupling parameters

between the above mentioned same spatial symmetry electronic states ($\widetilde{B}$-$\widetilde{C}$, $\widetilde{B}$-$\widetilde{E}$ and $\widetilde{C}$-$\widetilde{E}$) were obtained from the corresponding adiabatic electronic states using the diabatization method of Truhlar and coworkers [116, 121–124]. The adiabatic electronic states were calculated using the MCQDPT [125–127] method, a 6-311++g(d,p) basis set and employing five roots with equal weights (A') in the state averaged-CASSCF (SA-CASSCF) calculation as a reference. An active space of 17 electrons in 13 orbitals [i.e., (17,13)] was used. To account for the effect of intruder states in the energies of the states, an intruder state avoidance shift [168] of 0.02 was used. All these calculations are carried out using GAMESS program package [128].

In particular, for the electronic couplings between the states of same spatial symmetry, we used the fourfold-way diabatization scheme [116, 121–124] at the MCQDPT level of theory. The fourfold-way produces smoothly varying diabatic MOs (DMOs). The transformation of the usual configuration state functions (CSFs) written in terms of canonical (adiabatic) MOs into orthogonal diabatic CSFs (CSFs written in terms of DMOs) is unique. That is, we first obtained CASSCF DMOs, then the adiabatic MCQDPT wave functions were expressed in terms of the CASSCF DMOs and the latter are used for direct diabatization to obtain the energies of diabatic states and diabatic couplings. Using the above ansatz, for the $\widetilde{B}$-$\widetilde{C}$, $\widetilde{B}$-$\widetilde{E}$ and $\widetilde{C}$-$\widetilde{E}$ inter-state couplings Eq. 3.7 takes the following form:

$$u^{nm} = u_0^{nm} + \sum_{i \epsilon a'} \lambda_i^{nm} Q_i + \frac{1}{2!} \sum_{i \epsilon a'} \gamma_i^{nm} Q_i^2 \; ; \;\; nm \in \widetilde{B} - \widetilde{C}, \widetilde{B} - \widetilde{E}, \text{ and } \widetilde{C} - \widetilde{E}, \quad (3.8)$$

where u_0^{nm} is a electronic couplings of the diabatic electronic states considered in the model and calculated at the ground state reference geometry ($\mathbf{Q}$=0). The u_0^{nm} is a constant at a distorted geometry for the $\widetilde{B}$-$\widetilde{C}$ (~ 0.04 eV), $\widetilde{B}$-$\widetilde{E}$ (~ 0.02 eV) and $\widetilde{C}$-$\widetilde{E}$ (~ 0.05 eV) coupled surfaces.

The diagonal bilinear (γ_{ij} in Eq. 3.6) coupling parameters along six totally symmetric (ν_4, ν_5, ν_7, ν_8, ν_9 and ν_{10}) vibrational modes are also calculated. For this purpose a two-dimensional fit of the *ab initio* calculated adiabatic electronic energies is carried out by using the Levenberg Marquardt algorithm [169]. The estimated diagonal bilinear coupling parameters are given in Table A4 of the Appendix A.

3.3 Potential energy surfaces

In Fig. 3.2, we show one dimensional cuts of the adiabatic PESs of $\widetilde{X}$, $\widetilde{A}$, $\widetilde{B}$, $\widetilde{C}$, $\widetilde{D}$, $\widetilde{E}$, and $\widetilde{F}$ electronic states of the $CH_3COH^{\cdot+}$ along the dimensionless normal displacement coordinates (Q) of the totally symmetric (a') vibrational modes (ν_1-ν_{10}). In each panel, the computed *ab initio* adiabatic electronic energies are shown by points and those obtained from the vibronic model of Sec. 3.2 are shown by solid lines. The *ab initio* electronic energies are in good agreement with those determined from the model (cf., Eq. 3.6). The vibrational modes of a' symmetry tune the electronic energy minimum
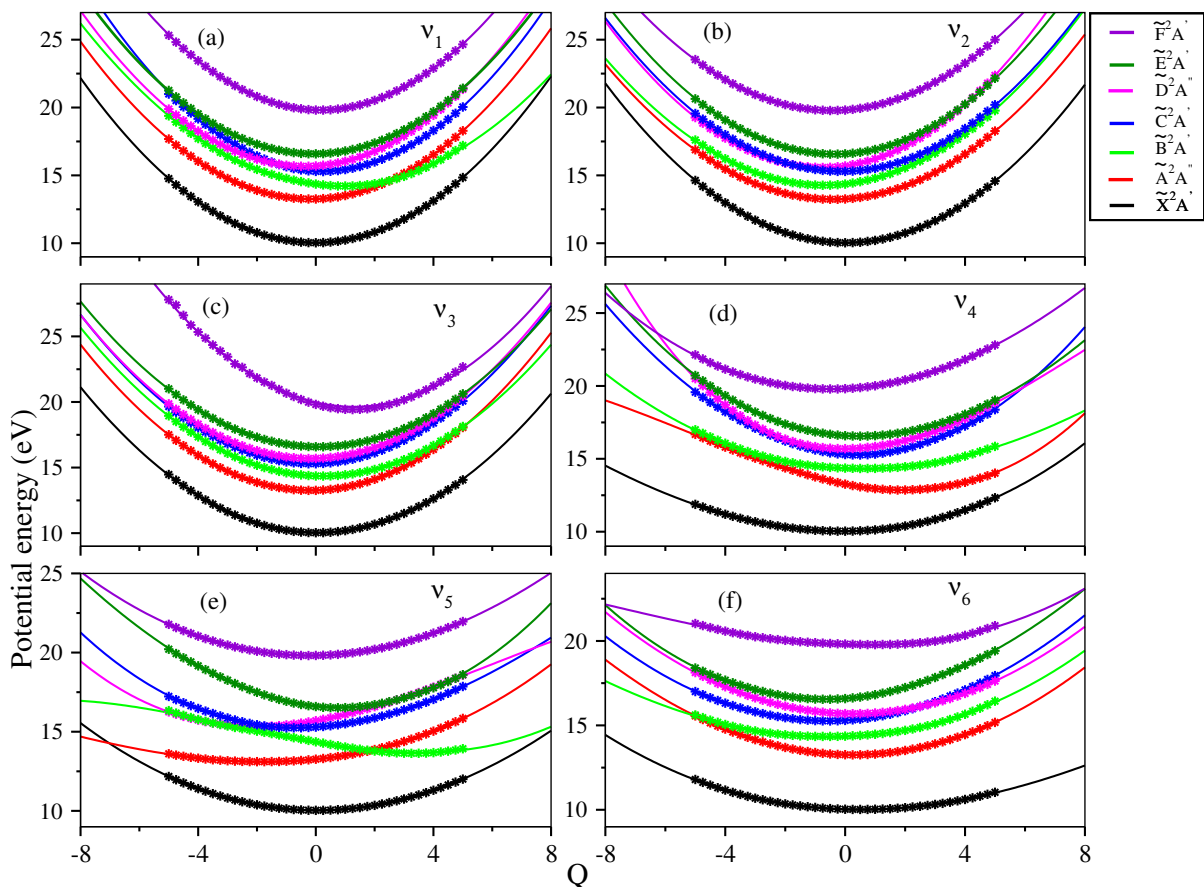
FIGURE 3.2: One dimensional cut of the adiabatic PESs of the lowest electronic state $\widetilde{X}$, $\widetilde{A}$, $\widetilde{B}$, $\widetilde{C}$, $\widetilde{D}$, $\widetilde{E}$ and $\widetilde{F}$ of $CH_3COH^{\cdot+}$ plotted along the normal displacement coordinate of the a' vibrational modes, ν_1-ν_{10}. The solid lines were obtained from the theoretical model of Eq. 3.2 and the calculated *ab initio* potential energies are shown by the asterisks.

away from the reference geometry of the electronic ground state of CH_3COH (at $\mathbf{Q}$=0), and therefore, modify the energy gap between the electronic states. As can be seen from Fig. 3.2 as well as from the data given in Table 3.3 that the $\widetilde{X}$ and $\widetilde{F}$ states are vertically far apart in energy from the remaining electronic states. The data presented in Table A1 of the Appendix A indicate the existence of both strong and weak intra-state couplings in the first seven electronic states of $CH_3COH^{\cdot+}$. The excitation strength of
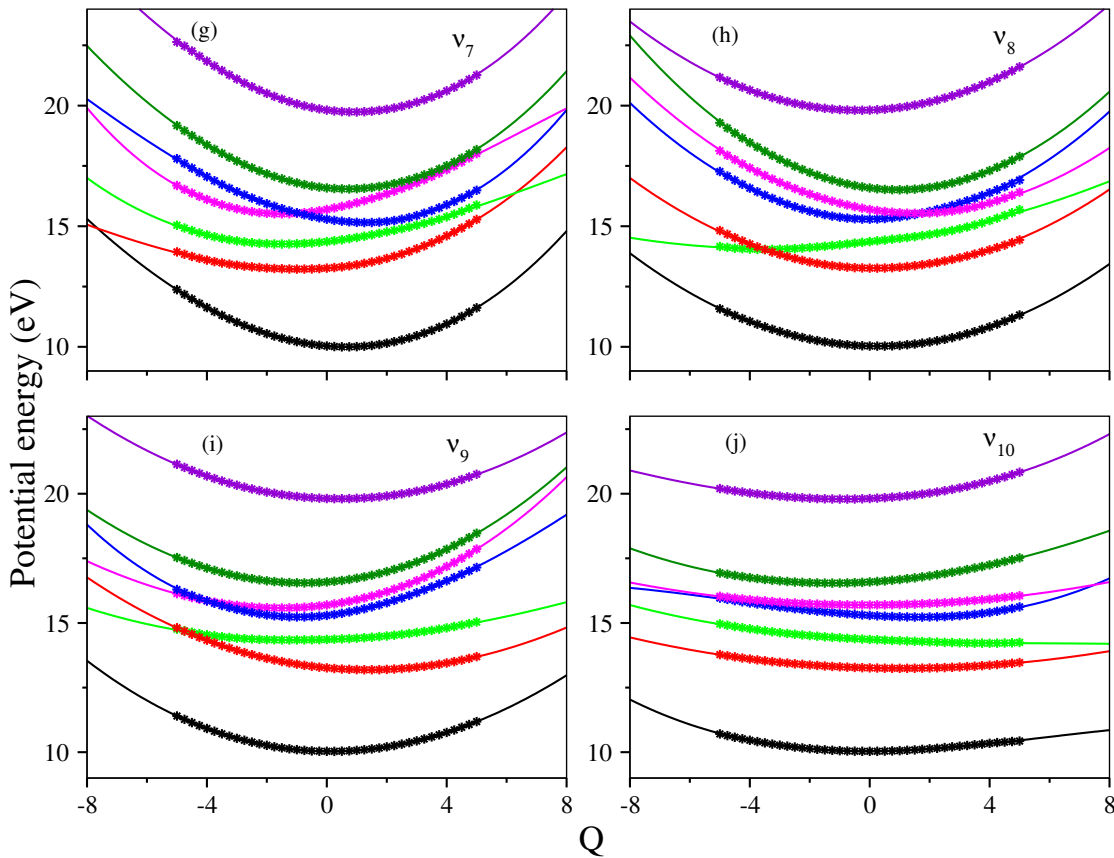
FIGURE 3.2: Continued.

the condon active a' vibrational modes is estimated from the Huang-Rhys parameter, $\kappa_i^2/2\omega_i^2$. The positional and directional shift of the energy minimum of an electronic state relative to the reference electronic configuration is determined by this parameter. The amount of shift of the minimum of an electronic state increases with an increasing value of this parameter and the direction of the shift is determined by the sign of "κ_i". Due to a shift of the energetic minimum of the electronic states, they undergo curve crossings along suitable vibrational modes (cf., Fig. 3.2). These curve crossings acquire the topography of CIs of PESs in higher dimensional nuclear coordinate space. Also, in the above mentioned seven electronic states ($\widetilde{X}$ to $\widetilde{F}$), the A' symmetry states ($\widetilde{B}$, $\widetilde{C}$ and $\widetilde{E}$) exhibit strong avoided crossings (cf., Fig. 3.2). As discussed in Sec. 3.2 that, the four-fold diabatization scheme is used to remove the avoided crossings between the states of same spatial symmetry. The resulting diabatic potential energy curves are plotted along the normal displacement coordinate of vibrational modes, ν_4-ν_9 and are shown in Fig. A1 of the Appendix A. It can be seen from this figure that the avoided crossings of the adiabatic representation (cf., Fig. 3.2) are removed using this diabatization scheme. Along with these a' vibrational modes, in Fig. A2 we also show the one-dimensional adiabatic potential energy cuts of the $\widetilde{X}$ to $\widetilde{F}$ states along the a'' symmetry vibrational modes. It can be seen from this figure that, along ν_{12} and ν_{15} vibrational modes the

electronic states strongly repel each other. This leads to the double-minimum potentials at the distorted nuclear geometries (cf., panels (b) and (e) of Fig. A2).

In order to understand the nuclear dynamics in coupled electronic states, we examined the static aspects of the electronic PESs within a second-order vibronic coupling model. The equilibrium minimum of states and minimum energy on the seam of CIs of different electronic states are calculated. For this, a constrained optimization procedure based on the Lagrange multiplier is used and numerical tools available in MATHEMATICA [170] are employed for the purpose. The results are given in Table 3.4.

TABLE 3.4: Estimated the diagonal entries represent the equilibrium minimum of the given state and off-diagonal entries represent the minimum of various CIs of the electronic states of the $CH_3COH^{.+}$ within a second-order model. All quantities are given in eV.

	$\widetilde{X}$	$\widetilde{A}$	$\widetilde{B}$	$\widetilde{C}$	$\widetilde{D}$	$\widetilde{E}$	$\widetilde{F}$
$\widetilde{X}$	9.98	12.92	-	-	16.85	-	-
$\widetilde{A}$	-	12.51	13.49	16.34	-	22.53	25.21
$\widetilde{B}$	-	-	12.92	14.99	14.87	45.29	-
$\widetilde{C}$	-	-	-	14.94	15.16	16.69	-
$\widetilde{D}$	-	-	-	-	14.77	16.22	20.41
$\widetilde{E}$	-	-	-	-	-	16.21	-
$\widetilde{F}$	-	-	-	-	-	-	19.29

It can be seen from the table that the minimum of the $\widetilde{X}$ and $\widetilde{F}$ states are energetically well separated from all other states and their intersection minimum with other states is also very high in energy (cf., Table 3.4). The equilibrium minimum of the $\widetilde{A}$ and $\widetilde{B}$ states occurs at ~12.51 eV and ~12.92 eV, respectively. These two states are very close in energy, the $\widetilde{A}$-$\widetilde{B}$ CI located ~0.98 eV and ~0.57 eV above the minimum of the $\widetilde{A}$ and $\widetilde{B}$ electronic states, respectively. The intersection between $\widetilde{A}$ state with higher electronic states occurs at very high energies. The $\widetilde{B}$-$\widetilde{C}$ intersection minimum occurs ~2.07 eV, ~0.05 eV above the minimum of the $\widetilde{B}$ and $\widetilde{C}$ electronic states, respectively. The $\widetilde{C}$ state minimum is very close to the $\widetilde{B}$-$\widetilde{C}$ intersection minimum. Also, $\widetilde{B}$-$\widetilde{D}$ intersection minimum is lower in energy than the $\widetilde{B}$-$\widetilde{C}$ intersection minimum. The $\widetilde{B}$-$\widetilde{D}$ intersection minimum is ~1.95 eV and ~0.1 eV higher in energy than the minimum of the $\widetilde{B}$ and $\widetilde{D}$ electronic states, respectively. The $\widetilde{C}$-$\widetilde{D}$ CI is about ~0.22 eV higher in energy than the minimum of the $\widetilde{C}$ state and the minimum of the $\widetilde{D}$ state is ~0.39 eV lower in energy than the minimum of the $\widetilde{C}$-$\widetilde{D}$ intersection seam. The energetic minimum of $\widetilde{C}$ and $\widetilde{D}$ electronic states occurs at ~14.94 eV and ~14.77 eV, respectively. The minimum of the $\widetilde{D}$ state is slightly below to that of the $\widetilde{C}$ electronic state. This is because of strong

vibrionic coupling between them and it causes a shift of the minimum of the $\widetilde{D}^2A''$ state at a distorted geometry. The minimum energy of $\widetilde{D}$-$\widetilde{E}$ intersection seam is ~1.45 eV and ~0.01 eV higher than the minimum of the $\widetilde{D}$ and $\widetilde{E}$ states, respectively.

The coupling of $\widetilde{A}$ and $\widetilde{D}$ states with all other states is reasonably strong along the ν_{15} vibrational mode of a'' symmetry and it is mild along ν_{11}-ν_{14} modes of same symmetry (cf., Table A3 of the Appendix A). Along with these, the coupling of $\widetilde{B}$-$\widetilde{C}$, $\widetilde{B}$-$\widetilde{E}$ and $\widetilde{C}$-$\widetilde{E}$ states coupling is also strong along ν_6-ν_{10} vibrational modes of a' symmetry (cf., Table A3 of the Appendix A). The $\widetilde{A}$-$\widetilde{B}$, $\widetilde{B}$-$\widetilde{C}$, $\widetilde{C}$-$\widetilde{D}$ and $\widetilde{D}$-$\widetilde{E}$ electronic states are energetically very close. The equilibrium minimum of these states is closer to the minimum of various CIs (cf., Table 3.4). Therefore, nonadiabatic coupling among them is expected to play a major role in the nuclear dynamics on these states.

3.4   Results and discussion

The vibronic band structure of the cationic ground $\widetilde{X}$, and excited electronic states $\widetilde{A}$, $\widetilde{B}$, $\widetilde{C}$, $\widetilde{D}$, $\widetilde{E}$ and $\widetilde{F}$ of acetaldehyde calculated with the aid of the diabatic model Hamiltonian (cf., Eq. 3.2) constructed in Sec. 3.2 is discussed in this section. For a better assessment of nonadiabatic coupling effects, these calculations were performed both in absence and presence of coupling among the electronic states as mentioned above. From the coupled states dynamics, time-dependence of diabatic electronic population, the decay rate of electronic states and internal conversion processes are also studied. Theoretical results are discussed and compared with the available experimental [47] photoelectron spectroscopy results.

3.4.1   Vibronic structure of the electronic states of CH₃COH·⁺

3.4.1.1   Uncoupled states calculations

In this section, we discuss the vibrational energy level spectrum of the uncoupled $\widetilde{X}$, $\widetilde{A}$, $\widetilde{B}$, $\widetilde{C}$, $\widetilde{D}$, $\widetilde{E}$ and $\widetilde{F}$ electronic states of CH₃COH·⁺ calculated by the matrix diagonalization method [167]. These calculations are performed with eight relevant a' vibrational modes (ν_3-ν_{10}) and the diabatic vibronic model Hamiltonian of Eq. 3.2 constructed in Sec. 3.2 using the parameters of Tables A1 and A2 of the Appendix A. The results obtained are shown in Fig. 3.3. The HO basis functions used along each vibrational mode are given in Table A5 of the Appendix A. For each electronic state, the Hamiltonian is diagonalized using 10,000 Lanczos iterations to generate the corresponding vibronic spectrum and these spectral bands are shown in Fig. 3.3. In this figure, the spectral envelopes were obtained by convoluting the stick line spectrum with a Lorentzian function of 40 meV full width at the half maximum. The energy eigenvalue of the low-lying
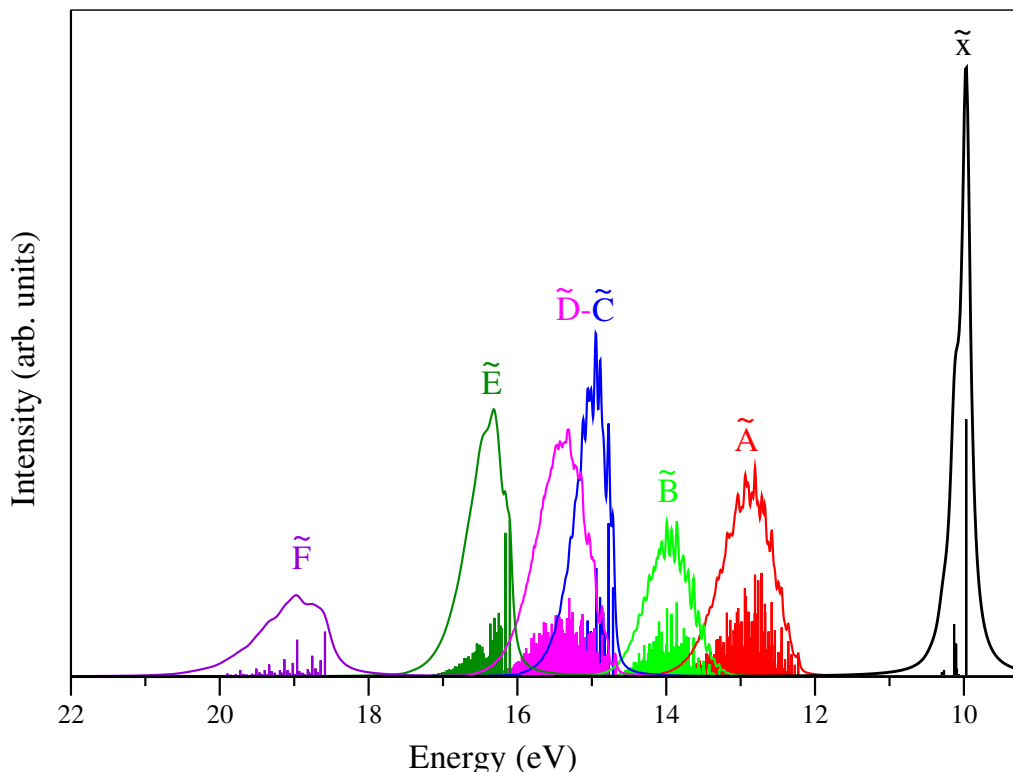
FIGURE 3.3: The $\widetilde{X}$, $\widetilde{A}$, $\widetilde{B}$, $\widetilde{C}$, $\widetilde{D}$, $\widetilde{E}$ and $\widetilde{F}$ photoionization bands of CH_3COH calculated with the a' vibrational modes and the time-independent matrix diagonalization method (see text for details). The relative intensity is plotted as a function of the energy of the vibronic levels.

vibronic levels of the uncoupled $\widetilde{X}$, $\widetilde{A}$, $\widetilde{B}$, $\widetilde{C}$, $\widetilde{D}$, $\widetilde{E}$ and $\widetilde{F}$ states are given in Table A6 of Appendix A along with their assignments. These assignments are done by examining the nodal pattern of their wave functions calculated with a block-improved relaxation method using the MCTDH program modules [140, 152, 171, 172]. The results in the Table A6 of Appendix A demonstrate that, the fundamental of a' vibrational modes (ν_3-ν_{10}) is excited in each of the given electronic state of $CH_3COH^{\cdot+}$. Along with this, excitation of several overtones and combination energy levels can also be found. The first ionization band due to the $\widetilde{X}$ electronic state of $CH_3COH^{\cdot+}$ is shown in Fig. 3.3. The dominant progression in this band is formed by ν_6, ν_7 and ν_8 vibrational modes, and the corresponding vibrational progressions are observed at ~ 1135 cm^{-1}, ~ 1360 cm^{-1} and ~ 1034 cm^{-1}, respectively. The vibrational mode ν_9 (~ 861 cm^{-1}) is weakly excited in this state. It can be seen from Table A6 of Appendix A that progressions of totally symmetric vibrational modes obtained in the uncoupled state situation compare quite well with the available experimental findings in the literature [37].

Owing to energetic proximity, the second and third vibronic bands due to $\widetilde{A}$ and $\widetilde{B}$ electronic states of $CH_3COH^{\cdot+}$ are highly overlapping. It can be seen from Fig. 3.3 that

the low-lying vibronic levels of the $\widetilde{B}$ state mix with the high-lying vibronic levels of the $\widetilde{A}$ state. The vibronic band structure of the $\widetilde{A}$ state reveals dominant excitation of ν_4, ν_5, ν_9 vibrational modes, and moderate excitation of ν_7, ν_{10} modes (cf., Table A6). Peaks are $\sim$1837 cm^{-1}, $\sim$1123 cm^{-1}, $\sim$760 cm^{-1} and $\sim$1074 cm^{-1}, $\sim$357 cm^{-1} spaced in that order, respectively. In case of the $\widetilde{B}$ state ν_5, ν_7 and ν_8 vibrational modes form extended progression with line spacing of $\sim$1268 cm^{-1}, $\sim$1075 cm^{-1} and $\sim$668 cm^{-1}, respectively.

The fourth vibronic band result from the $\widetilde{C}$ and $\widetilde{D}$ electronic states of CH$_3$COH$^{\cdot+}$. It can be seen from Fig. 3.3 that the vibronic band structures of the $\widetilde{C}$ and $\widetilde{D}$ states are highly overlapping because of their energetic proximity. The individual vibronic band structures of $\widetilde{C}$ and $\widetilde{D}$ states reveal dominant excitation of ν_7, ν_9 and ν_{10} ; and ν_5, ν_7, ν_8 and ν_9 vibrational modes, respectively. The peaks are spaced $\sim$1380 cm^{-1}, $\sim$955 cm^{-1}, $\sim$468 cm^{-1} and $\sim$1486 cm^{-1}, $\sim$1350 cm^{-1}, $\sim$1087 cm^{-1} and $\sim$847 cm^{-1}, respectively, corresponding to the frequency of the vibrational modes mentioned above.

The fifth vibrionic band resulting from the $\widetilde{E}$ state of CH$_3$COH$^{\cdot+}$ reveals dominant excitation of ν_5, ν_8 and ν_{10} vibrational modes, respectively. The sixth vibronic band solely originates from the $\widetilde{F}$ electronic state as it is energetically well separated from the other states. The dominant vibrational progressions in this band are formed by ν_3, ν_7 and ν_{10} vibrational modes and the peaks are $\sim$3117 cm^{-1}, $\sim$1436 cm^{-1} and $\sim$488 cm^{-1} spaced in energy, respectively. In addition to the fundamental vibrational progressions as discussed above, overtones and numerous combination levels are also excited in each band (cf., Table A6 of Appendix A).

The nodal pattern of the vibrational wave functions is examined further to confirm their assignments. In Fig. A3 (a-i) of the Appendix A a few vibrational wave functions of the $\widetilde{X}$ state are shown. The probability density of the wave function is plotted in this figure along suitable dimensionless normal displacement coordinates. In panels (a-c), the wave functions of the fundamental of ν_7, ν_6 and ν_8 are shown, respectively. The wave function acquires a node along the relevant normal coordinate, as can be seen from these figures. The wave functions for the initial overtone (two nodes along the respective modes) peaks of the excited vibrational modes are shown in panels (d-f). Along with this some of the combination peaks are also shown in Fig. A3 (g-i) of the Appendix A. Similarly, for the other states vibrational wave functions are shown in Figs. A3-A9 of the Appendix A.

3.4.1.2 Coupled two-states dynamics

Several coupled two-states calculations are performed and discussed in this section to assess the impact of nonadiabatic coupling on the vibronic structure of an individual state. Despite its relatively strong coupling with the $\widetilde{A}$ and $\widetilde{D}$ states, the spectrum of the $\widetilde{X}$ state remains unchanged in the coupled states situation. This is because the $\widetilde{X}$ state is vertically well apart from the other electronic states (cf., Table 3.4), and the minimum of the seam of crossings with them is significantly higher in energy than its equilibrium minimum (cf., Table 3.4). As a result, very little electronic population flows to the $\widetilde{A}$ state (cf., Fig. A10 (a)) when the dynamics is started on the $\widetilde{X}$ state. On the other hand, a large fraction of population is transferred to the $\widetilde{X}$ state when the WP is initially prepared on the $\widetilde{A}$ state (cf., Fig. A10 (b)). This is because the $\widetilde{A}$ state minimum is closer to the minimum of $\widetilde{X}$-$\widetilde{A}$ intersection seam (cf., Table 3.4). This results into a broad and structureless vibronic spectrum of the $\widetilde{A}$ state.

In contrast, the coupling between $\widetilde{A}$-$\widetilde{B}$, $\widetilde{B}$-$\widetilde{C}$, $\widetilde{C}$-$\widetilde{D}$, and $\widetilde{D}$-$\widetilde{E}$ states has significant impact on their individual vibronic structures. When the WP is initially prepared on the $\widetilde{A}$ state in the $\widetilde{A}$-$\widetilde{B}$ coupled states situation minimal population flows to the $\widetilde{B}$ state (cf., Fig. A10 (c)). Because the minimum energy of the $\widetilde{A}$-$\widetilde{B}$ intersection seam occurs at ~13.49 eV, which is ~0.98 eV and ~0.57 eV above the minimum of the $\widetilde{A}$ and $\widetilde{B}$ electronic states (cf., Table 3.4), respectively. On the other hand, nonadiabatic coupling between $\widetilde{A}$-$\widetilde{B}$ states (cf., Table A3) has strong impact on the vibronic band structure of the $\widetilde{B}$ state and its electronic population dynamics. A large fraction of the population (~50%) is transferred to the $\widetilde{A}$ state (within ~25 fs) when the WP is initially prepared on the $\widetilde{B}$ state (cf., Fig. A10 (d)).

The population dynamics of the coupled $\widetilde{B}$-$\widetilde{C}$ states is shown in panels (e) and (f) of Fig. A10 of the Appendix A. When the WP is excited to the $\widetilde{B}$ state, very little amount of the population flows to the $\widetilde{C}$ state (cf., Fig. A10 (e)). On the other hand, for an initial excitation to the $\widetilde{C}$ state a large fraction of population moves to the $\widetilde{B}$ state (cf., Fig. A10 (f)). This is because the $\widetilde{B}$-$\widetilde{C}$ intersection minimum is ~2.07 eV and ~0.05 eV above the minimum of the $\widetilde{B}$ and $\widetilde{C}$ states, respectively (cf., Table 3.4). Also, these states are strongly coupled through the vibrational modes of a' symmetry (cf., Table A3). Due to this the energy spectrum of the $\widetilde{C}$ state is broad and structureless.

The spectra of $\widetilde{C}$ and $\widetilde{D}$ states are highly overlapping and form a single broad band (cf., Fig. 3.3). Strong nonadiabatic coupling between these states leads to an interchange of the energetic minimum of $\widetilde{C}$ and $\widetilde{D}$ states. The energetic minimum of $\widetilde{C}$ and

$\widetilde{D}$ states occurs at ~14.94 eV and ~14.77 eV, respectively (cf., Table 3.4). Also, their intersection minimum located ~0.22 eV and ~0.39 eV above the equilibrium minimum of the $\widetilde{C}$ and $\widetilde{D}$ electronic states (cf., Table 3.4), respectively. As a result, a significant amount of population exchange takes place between them. For illustration, panels (g) and (h) of Fig. A10 of the Appendix A, respectively, show the time-dependence of the diabatic electronic population for an initial excitation to the $\widetilde{C}$ and $\widetilde{D}$ states in the $\widetilde{C}$-$\widetilde{D}$ coupled states situation. Panels (g) and (h) of Fig. A10 show a considerable portion of the population flows into both the electronic states. Within ~50 fs, a sharp population depletion occurs, followed by the population moving back and forth between these states.

The population dynamics of the coupled $\widetilde{D}$-$\widetilde{E}$ states is quite similar to the coupled $\widetilde{A}$-$\widetilde{B}$ states. When the WP is initially excited to the $\widetilde{D}$ state, a minimal population is transferred to the $\widetilde{E}$ state (cf., Fig. A10 (i)). However, a significant fraction of the population (~90%, within the ~22 fs time) is transferred to the $\widetilde{D}$ state in case of initial excitation to the $\widetilde{E}$ state (cf., Fig. A10 (j)). This is because of strong coupling between $\widetilde{D}$ and $\widetilde{E}$ states and the $\widetilde{D}^2 A''$-$\widetilde{E}^2 A'$ intersection minimum is only ~0.01 eV above the minimum of the $\widetilde{E}$ state (cf., Table 3.4).

3.4.1.3 Coupled $\widetilde{X}$-$\widetilde{A}$-$\widetilde{B}$-$\widetilde{C}$-$\widetilde{D}$-$\widetilde{E}$-$\widetilde{F}$ states calculations

In this section the vibronic structure of the photoionization band of CH_3COH in the energy range between ~10-22 eV is examined. Seven coupled electronic states ($\widetilde{X}$ to $\widetilde{F}$) are considered and the dynamical calculations are carried out with the model Hamiltonian (Eq. 3.2) described in Sec. 3.2 including twelve vibrational DOFs (eight ν_3-ν_{10} of a' symmetry and four ν_{12}-ν_{15} of a'' symmetry) using the MCTDH program module [139, 152]. The TDSE is solved for the purpose. The initial WP for each of the seven electronic states ($\widetilde{X}$ to $\widetilde{F}$) is prepared separately in these calculations. The vibrational mode combinations and the size of the basis functions sizes are given in Table B7 of Appendix A. In each calculation, the WP is propagated for 200 fs. The photoionization band of each electronic state is generated by Fourier transformation of the autocorrelation function $C(t)$ of the WP evolving on that state. The autocorrelation function is multiplied by an exponential damping factor, e^{-t/τ_r} (with τ_r=33 fs) prior to Fourier transformation. The composite theoretical band is obtained by combining the results of seven calculations with equal weightage. The results are shown in panel (b) of Fig. 3.4 and compared with the experimental spectrum of Bieri *et al.* [47] (shown in Fig. 3.4(a)). In panel (c) of Fig. 4 the uncoupled state spectrum is presented again to reveal the impact of nonadiabatic coupling on the composite vibronic spectrum given in panel (b). It can be seen from the figure that the first band due to the $\widetilde{X}$ state is far apart from the other bands. The second and third bands due to $\widetilde{A}$ and $\widetilde{B}$ electronic states are
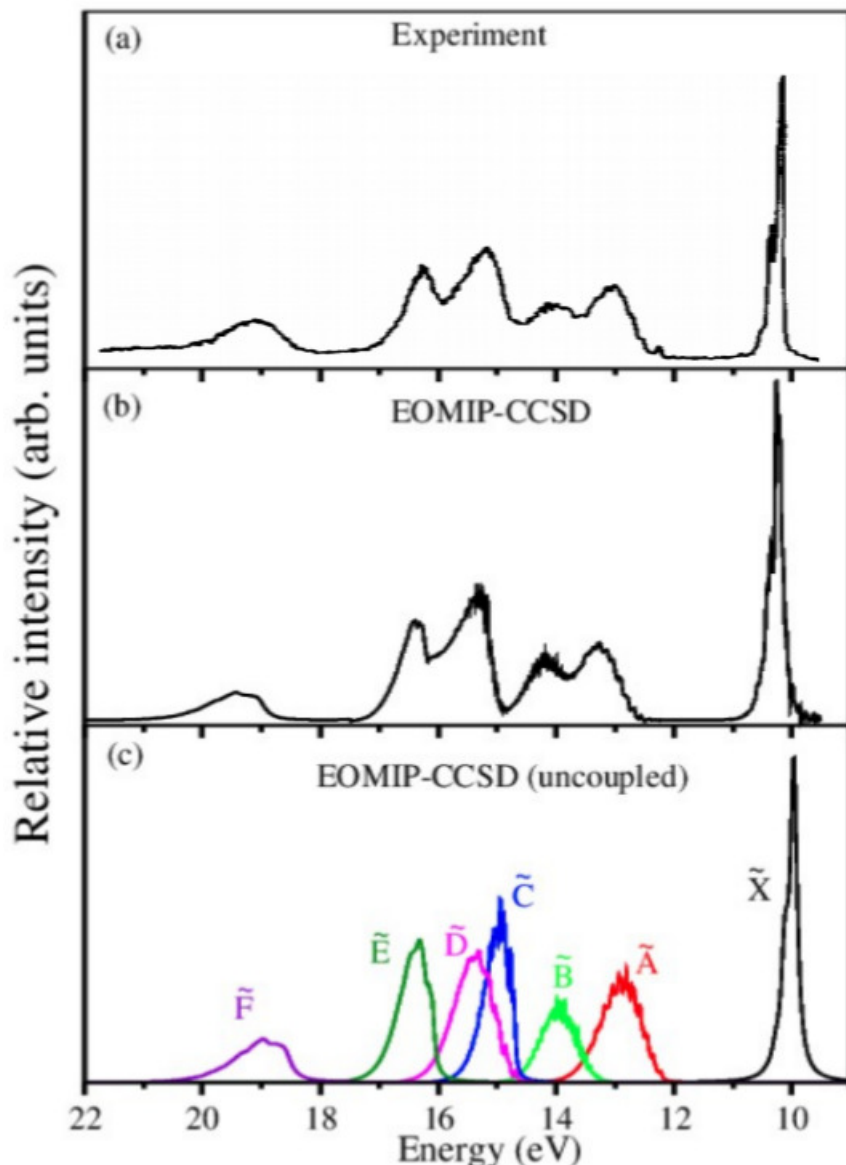
FIGURE 3.4: Comparison of the experimental [47] (shown in panel (a)) and theoretical coupled states (shown in panel (b)) and uncoupled states (shown in panel (c)) photo-ionization spectrum of CH_3COH, respectively. The theoretical spectrum (cf., panel (b)) is obtained with seven coupled electronic states and twelve vibrational modes and calculated by propagating wave packets using the MCTDH program modules (see text for details).

close to each other. The highly overlapping $\widetilde{C}$ and $\widetilde{D}$ electronic states form the fourth band, and the fifth band is due to the $\widetilde{E}$ electronic state. The $\widetilde{F}$ electronic state forms the sixth band, and it is well separated from the other bands. We note that the vibronic band structures are unaffected upon inclusion of the bilinear coupling parameters given in Table A4 of the Appendix A. So, to save space and for brevity we do not show the corresponding spectrum in Fig. 3.4.

3.4.2 Diabatic electronic population

The diabatic electronic populations of $\widetilde{X}$, $\widetilde{A}$, $\widetilde{B}$, $\widetilde{C}$, $\widetilde{D}$, $\widetilde{E}$ and $\widetilde{F}$ electronic states of $CH_3COH^{\cdot+}$ recorded in the coupled states dynamics discussed in Sec. 3.4.1.3 are shown in Fig. 3.5. Panels (a-g) of Fig. 3.5 show the results obtained by populating the $\widetilde{X}$, $\widetilde{A}$, $\widetilde{B}$, $\widetilde{C}$, $\widetilde{D}$, $\widetilde{E}$, and $\widetilde{F}$ electronic states, respectively. Panel (a) shows the results obtained when the WP is prepared on the $\widetilde{X}$ state initially. It can be seen that a small amount ($\sim 20\%$) of it is transferred to the $\widetilde{A}$ state. This is because of their intersection minimum is situated ~ 2.94 eV above the $\widetilde{X}$ state minimum. A minimal amount of population moves to the other excited states. Contrary to the above, a large fraction population
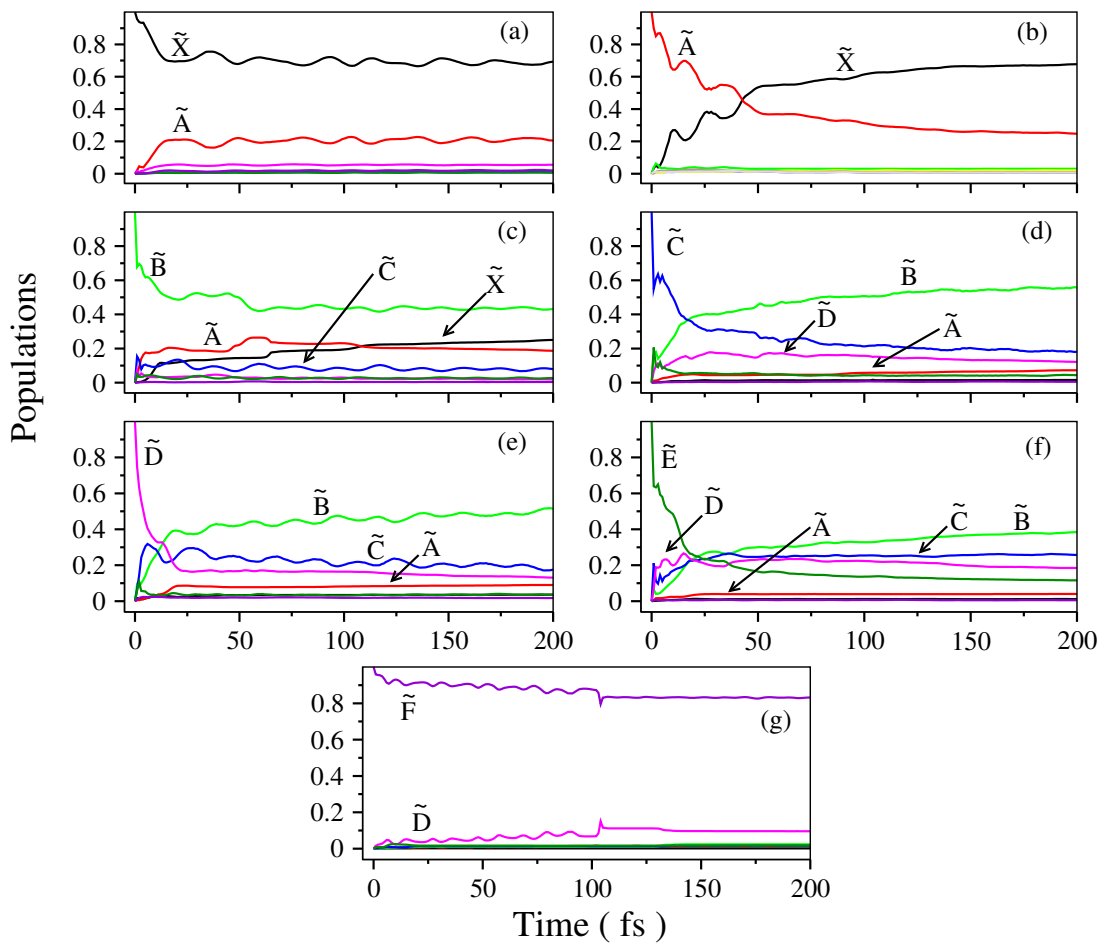
FIGURE 3.5: Electronic population dynamics in the coupled seven $\widetilde{X}$-$\widetilde{A}$-$\widetilde{B}$-$\widetilde{C}$-$\widetilde{D}$-$\widetilde{E}$-$\widetilde{F}$ electronic states of the $CH_3COH^{\cdot+}$. The population diagrams obtained by locating the initial (at t = 0) WP separately on each of the $\widetilde{X}$, $\widetilde{A}$, $\widetilde{B}$, $\widetilde{C}$, $\widetilde{D}$, $\widetilde{E}$ and $\widetilde{F}$ electronic states are shown in the panels (a)-(g), respectively.

is transferred to the $\widetilde{X}$ state, when the WP is initially prepared on the $\widetilde{A}$ state (cf., Fig. 3.5(b)). The population curve of the $\widetilde{A}$ state yields a decay rate of ~ 50 fs of this state. The minimum of the $\widetilde{A}$ state is closer to the minimum of $\widetilde{X}$-$\widetilde{A}$ intersection seam (cf., Table 3.4). In addition to this, the $\widetilde{X}$-$\widetilde{A}$ states are strongly coupled through the vibrational modes of a'' symmetry (cf., Table 3.4), which causes the fast decay of the

population of the $\widetilde{A}$ state.

The population dynamics of the $\widetilde{B}$ state shown in Fig. 3.5(c), reveals a $\sim$50% decreases on a time scale of $\sim$25 fs. Afterwards, the population decreases up to $\sim$40% within $\sim$50 fs, and it remains constant thereafter. In this case about $\sim$20% population flows to the $\widetilde{A}$ electronic state and $\sim$10% population flows to the $\widetilde{X}^2A'$ and $\widetilde{A}^2A''$ states within $\sim$24 fs. The energetic minimum of the $\widetilde{X}^2A'$-$\widetilde{B}\,^2A'$ and $\widetilde{A}^2A''$-$\widetilde{B}\,^2A'$ intersection seams occur at $\sim$12.94 eV and $\sim$13.49 eV, respectively. The $\widetilde{A}$-$\widetilde{B}$ intersection seam is located $\sim$0.98 eV and $\sim$0.57 eV above the minimum of the $\widetilde{A}$ and $\widetilde{B}$ electronic states, respectively. The minimum of the $\widetilde{A}^2A''$-$\widetilde{B}\,^2A'$ intersections is closer to the $\widetilde{B}$ state minimum as compared to the minimum of $\widetilde{X}^2A'$-$\widetilde{B}\,^2A'$ intersections. Furthermore, the coupling between the $\widetilde{X}$ and $\widetilde{A}$ is reasonably strong. Because of this, somewhat more population flows to the $\widetilde{X}$ state as compared to the $\widetilde{A}$ state after $\sim$100 fs through $\widetilde{A}^2A''$-$\widetilde{B}\,^2A'$ and $\widetilde{X}^2A'$-$\widetilde{A}^2A''$ CIs.

The initial excitation to the $\widetilde{C}$ electronic state (Fig. 3.5(d)) results more population flow to the $\widetilde{B}$ state. After $\sim$13 fs, the population of these two states becomes equal ($\sim$40%). After $\sim$50 fs, the $\widetilde{C}$ state population goes down to $\sim$20%. In contrast, the $\widetilde{B}$ state is nearly $\sim$60% populated and the remaining population is transferred to the $\widetilde{A}^2A''$ and $\widetilde{D}^2A''$ states (cf., Fig. 3.5(d)). The $\widetilde{B}$-$\widetilde{C}$ intersection minimum is $\sim$0.05 eV above the $\widetilde{C}$ state minimum and strong inter-state coupling between them plays a crucial role in the population dynamics. Moreover, the $\widetilde{C}$ and $\widetilde{D}$ states are quasi-degenerate and coupling between them leads to the population transfer to the $\widetilde{D}$ state. A decay rate of $\sim$23 fs can be estimated from the initial population decay of the $\widetilde{C}$ state.

Panels (e) and (f) of Fig. 3.5 show electron population dynamics when the WP is initially prepared on the $\widetilde{D}$ and $\widetilde{E}$ electronic states, respectively. As can be seen from these panels that the population dynamics of these electronic states is more complex and involved. Due to the strong nonadiabatic coupling among the $\widetilde{A}$, $\widetilde{B}$, $\widetilde{C}$, $\widetilde{D}$ and $\widetilde{E}$ electronic states (cf., Table A3), most of the population flows to the $\widetilde{B}$ and $\widetilde{C}$ electronic states in the former case (cf., Fig. 3.5(e)), and to the $\widetilde{B}$, $\widetilde{C}$, and $\widetilde{D}$ electronic states, in the latter case (cf., Fig. 3.5(f)). As a result of the energetic proximity of the states, the minimum energy of various intersection seams (cf., Table 3.4) and vibronic coupling between them leads to a substantial population transfer. Decay rate of 13 fs and 19 fs of the $\widetilde{D}^2A''$ and $\widetilde{E}^2A'$ states, respectively, follows from the initial fast decay of the corresponding populations.

In Fig. 3.5(g) the population dynamics for an initial transition of the WP to the $\widetilde{F}$ is presented. It can be seen that, except $\widetilde{D}$ state, virtually no population flows to other electronic states in this case. Only a minimal amount of population flows to the $\widetilde{D}$ state. Since the $\widetilde{F}$ state energetically far apart from all other states, the CIs of the $\widetilde{F}$ state with all other states occur at high energies and thus can not be accessed by the WP while it is evolving on the $\widetilde{F}$ state.

3.5 Summary

A theoretical account of multi-state and multi-mode vibronic coupling in the photo-ionization spectroscopy of CH_3COH is presented in this chapter. A standard vibronic coupling model Hamiltonian is developed with seven energetically low-lying electronic states of $CH_3COH^{\cdot+}$ in a diabatic electronic basis and in terms of dimensionless normal displacement coordinates of the electronic ground state of CH_3COH. The electronic ground state of CH_3COH is optimized at the DFT level with B3LYP functional employing 6-311++g(d,p) basis set. Extensive *ab initio* quantum chemistry calculations of adiabatic electronic energy are performed with EOMIP-CCSD method to parameterize the vibronic Hamiltonian. From the electronic structure results, it is found that both $\widetilde{X}$ and $\widetilde{F}$ states are far apart in energy from the other states at the Franck-Condon zone. The remaining ($\widetilde{A}$ to $\widetilde{E}$) electronic states are vertically very close in energy. Among these electronic states $\widetilde{C}$ and $\widetilde{D}$ states are quasi-degenerate. Due to the energetic proximity of the $\widetilde{A}$, $\widetilde{B}$, $\widetilde{C}$, $\widetilde{D}$ and $\widetilde{E}$ electronic states vibronic coupling among them plays the key role to govern the details of the nuclear dynamics. The standard vibronic coupling theory and elementary symmetry selection rules are used to assess the coupling among seven ($\widetilde{X}$ to $\widetilde{F}$) electronic states. Coupling between electronic states of same spatial symmetry, ($\widetilde{B}$-$\widetilde{C}$, $\widetilde{B}$-$\widetilde{E}$ and $\widetilde{C}$-$\widetilde{E}$) via a' vibrational modes is also treated in this chapter.

The nuclear dynamical calculations are carried out by both time-independent and time-dependent quantum mechanical methods. Individual vibronic bands are systematically analyzed. The results are compared with the available experimental findings. It is observed that, the first and sixth vibronic bands due to $\widetilde{X}$ and $\widetilde{F}$ electronic states are well separated from the other bands. The fundamental vibrational progression formed by ν_7 ($\sim$1360 cm^{-1}), ν_8 ($\sim$1034 cm^{-1}) and ν_9 ($\sim$861 cm^{-1}) vibrational modes in the first ($\widetilde{X}$) band compares well with the available experimental findings. Due to the energetic proximity, $\widetilde{A}$ and $\widetilde{B}$ electronic states form highly overlapping second and third bands of CH_3COH^+. The latter also holds for the vibronic band structures of the $\widetilde{C}$ and $\widetilde{D}$ electronic states. The fifth vibronic band is due to the $\widetilde{E}$ electronic state and it

overlaps with the high-lying vibronic levels of $\widetilde{D}$ state. The assignment of the peaks is also confirmed by utilizing block-improved relaxation method to examine the nodal pattern of the vibrational wave functions. The final theoretical results are found to be in good agreement with the experimental data.

Chapter 4

Vibronic coupling effects in the six low-lying electronic states of oxirane radical cation: Theoretical photoelectron spectrum of oxirane

In this chapter, the theoretical photoelectron spectrum of oxirane molecule is presented. Oxirane (ethylene oxide, dimethylene oxide, c-C_2H_4O/$(CH)_2O$) is a three-membered cyclic ring, with each carbon being fully hydrogenated. This is the smallest cyclic ether and it is related to cyclopropane (C_3H_6) through a replacement of one of the methylene (CH_2) groups of the alkane with an isoelectronic oxygen atom. The oxirane is noted for its reactivity making it (and its derivatives) key reagents in the synthesis of many products of industrial and biological significance [58–61] and it has been serving as a model for photochemistry from a long time [62–67]. The molecular reactivity has been ascribed largely to ring strain as happens in cyclopropane and interest in its electronic structure has a long history. Acetaldehyde [CH_3CHO (C_s)], oxirane [c-C_2H_4O (C_2v)] and vinyl alcohol [H_2CCHOH (C_s)] are the three stable isomers (i.e., molecules with the same chemical formula but with different connections of the atoms) of C_2H_4O [68]. Oxirane is a higher energy isomer of the molecules acetaldehyde and vinyl alcohol. Only acetaldehyde has been first identified organic molecules in the interstellar medium (ISM) [69], although vinyl alcohol have been attempted to identify in cold dark clouds [70, 71]. Latter researches found the oxirane has been detected in the interstellar medium especially in the star-forming regions [61, 61, 72–76]. These studies proved the existence

of oxirane in ISM and it is confirmed by Dickens *et al.* [77]. Also, Coll *et al.* have suggested that oxirane molecule could be present in the Titan atmosphere [78]. To understand the formation of these three isomers of C_2H_4O in particular relevant to test the astrochemical evolution of the interstellar medium, since these molecules also play a key role in astrobiology [58, 59, 61, 69, 71]. Acetaldehyde and oxirane have been implicated in the formation of amino acids [59], underscoring their significance as complex organic molecules (COMs) [68]. Oxirane and acetaldehyde isomers are particularly noteworthy due to their potential contributions to amino acid synthesis [68]. The presence of oxirane in hot cores implies the existence of ring-shaped molecules with more than three carbon atoms, such as furan (c-C_4H_4O), which is closely associated with the sugars ribose and deoxyribose, the structural backbones of RNA and DNA, respectively [61, 74]. Observations by Occhiogrosso *et al.* [79] have revealed gaseous abundances of oxirane and acetaldehyde in high-mass star-forming regions. Their findings suggest that oxirane might be prevalent in the outer and cooler regions of hot cores where its isomer has been previously detected, providing valuable insights compared to earlier studies that focused solely on oxirane formation [76, 80–82].

Heterocyclic complex organic molecules, incorporating heavier elements alongside carbon in their ring structures, hold significance in various fields, particularly in the study of the ISM [72–77]. Oxygen-bearing species within this category are of particular interest due to their implications for the presence of life [58–60]. Ribose, for instance, is intricately linked to the molecular architecture of DNA [59, 60]. Exploring simpler heterocyclic molecules than ribose leads us to oxirane [58–61]. Oxirane represents the smallest cyclic species containing oxygen, bonded to two carbon atoms. Conversely, acetaldehyde, a non-cyclic isomer of C_2H_4O, serves as a significant evolutionary tracer in various astronomical contexts [83]. Initially detected in the ISM by Gottlieb in 1973, oxirane has since been observed in diverse astrochemical environments, particularly notable is its presence in regions of star formation [76, 77, 81, 82]. The relatively higher abundance of acetaldehyde compared to oxirane aligns with the reported ratios between the two isomers, ranging from 1 to 9 according to Ikeda *et al.* [76]. A gas-grain chemical model was developed to explore the chemistry of oxirane in high-mass star-forming regions, successfully reproducing its observed abundances in such environments [79]. Despite their distinct chemical structures, the chemistry of oxirane appears intertwined with that of acetaldehyde, suggesting the potential utility of acetaldehyde as a tracer for oxirane in cold cores [80].

Ionization and excitation energies of a series of saturated three-membered rings, including cyclopropane, ethylenimine, and oxirane, are computed using the novel semi-empirical approach HAM/3. The obtained results are meticulously compared with experimental data, predominantly electron spectra. Notably, peculiar intensity relationships were identified within the electron impact energy loss spectrum of oxirane [84]. Additionally, a comprehensive *ab initio* examination is conducted to analyze the geometries, force constants, and vibrational frequencies across various saturated three-membered-ring compounds. These investigations are carried out utilizing minimal, split-valence, and split-valence-polarized basis sets [85].

The He I and He II photoelectron spectra of oxirane are reported previously experimentally and some theoretical studies are reported [46, 47, 84–91]. The photoelectron spectrum, ionization potentials computed in different ways presented and correlation corrections are in good agreement with the photo-electron spectrum of oxirane [86]. The spectra obtained for several oxygen and nitrogen-containing molecules using filtered 30.4 nm radiation have been meticulously recorded. Notably, the 58.4 nm spectra have been effectively eliminated from consideration in all instances. To enhance the signal for high ionization potential species, photoelectrons were pre-accelerated by an average of 6 V prior to analysis, as detailed by Potts *et al.* [46]. In the case of oxirane, the relative band intensities in the He I and He II photoelectron spectra are elucidated through a theoretical framework. However, for oxirane, there exists a discrepancy between the assignment of the two bands in the 15-18 eV range based on intensity considerations and the sequence of the corresponding *ab initio* eigenvalues, as noted by Schweig *et al.* [87]. Various experimental techniques, including time-resolved photoionization mass spectrometry (PIMS), ion cyclotron resonance spectroscopy (ICR), and photoelectron spectroscopy, have been employed to investigate the formation of the oxirane molecular ion and its subsequent ion–molecule reactions leading to the products $C_2H_5O^+$ and $C_3H_5O^+$, as described by Corderman *et al.* [88]. Proton affinities and photoelectron spectra have been measured for oxirane, the photoelectron spectra assigned by using *ab initio* STO-431G calculations and structural correlation with some three-membered-ring heterocycles [89]. He I and He II photoelectron spectra of some fundamental organic molecules are reported by Kimura *et al.* and Bieri *et al.* [47, 90]. For oxirane vertical ionization potentials are reported by using many-body Green's function method [91].

In this study, the molecular orientation is established with the C_2 axis aligned along the z-axis, while the molecule is positioned within the xz-plane. It is worth noting that previous studies have sometimes defined the molecular plane as yz and xz, resulting in

the interchange of state symmetry labels b_1 and b_2. With this consideration, our findings regarding molecular orbital (MO) configurations and state symmetries align with those of Aue *et al.* [89] and Kimura *et al.* [90]. To date, there is a dearth of literature addressing the multi-state and multi-mode quantum dynamics of c-$C_2H_4O^{.+}$. However, several theoretical investigations have delved into the electronic structure and vertical ionization energies (VIEs) of c-C_2H_4O [85, 89, 91, 92]. Consequently, our primary objective is to address these gaps in the existing knowledge by conducting comprehensive electronic structure calculations and quantum dynamical simulations of nuclear motion.

Bieri *et al.* [47] reported the photoelectron spectrum 9 to 22 eV energy range with six vibronic bands. Among the six electronic bands first two bands are from the $\widetilde{X}\ ^2B_1$ and $\widetilde{A}\ ^2A_1$ electronic states, the $\widetilde{B}\ ^2B_2$ and $\widetilde{C}\ ^2A_2$ states combine and will form third band, remaining $\widetilde{D}\ ^2A_1$ and $\widetilde{E}\ ^2B_1$ states are very close in energy, they together form fourth band. The overlapping electronic band structure observed in these bands motivates us to investigate vibronic coupling within the energetically low-lying six electronic states and nuclear dynamics in c-$C_2H_4O^{.+}$. In the subsequent analysis, vibronic coupling within the lowest six electronic states of c-$C_2H_4O^{.+}$ is explored. These six states originate from ionization of the last occupied valence MOs of neutral c-C_2H_4O. The configuration of these six MOs is as follows: (core) $(1b_1)^2(5a_1)^2(6a_2)^2(3b_2)^2(6a_1)^2(2b_1)^2$. Ionization from the highest occupied MO and the inner orbitals results in the formation of the $\widetilde{X}\ ^2B_1$, $\widetilde{A}\ ^2A_1$, $\widetilde{B}\ ^2B_2$, $\widetilde{C}\ ^2A_2$, $\widetilde{D}\ ^2A_1$ and $\widetilde{E}\ ^2B_1$ electronic states of c-$C_2H_4O^{.+}$.

The diabatic vibronic coupling model is employed to study the nuclear dynamics of the aforementioned six electronic states. The electronic PESs are computed *ab initio* using the EOMIP-CCSD [150, 151] method. The coupling strengths of all vibrational modes across the six electronic states are calculated, and all vibrational modes are included in the study based on their coupling strength. Initially, the nuclear dynamics study is conducted using both time-independent and time-dependent quantum mechanical methods. Time-independent calculations are performed via a matrix diagonalization method [167]. This approach enables us to pinpoint the specific locations of the vibronic energy levels and assign their progressions accordingly. Subsequently, time-dependent calculations are carried out through WP propagation employing the MCTDH method developed at Heidelberg [139, 152–154]. This effort enables the computation of broad-band electronic spectra and facilitates the study of mechanistic details regarding radiative and nonradiative decay processes of excited electronic states. These results are good agreement with the available experimental findings.

In addition to this, we have compared the present results with our recent results of acetaldehyde isomer [98]. Oxirane and acetaldehyde have C_{2v} and C_s symmetry point groups, respectively. So, their electronic state characters are different. However, for both the isomers of photoelectron spectrum are reported between 9 to 20 eV energy range. But, within this energy range six and seven low-lying ionic states are found in oxirane and acetaldehyde, respectively, and discussed in this chapter in detail.

4.1 Electronic structure calculations

The electronic ground state equilibrium geometry optimization, harmonic vibrational frequencies (ω_i), and mass-weighted normal mode coordinates (q_i) of the reference c-C_2H_4O molecule is calculated at the second-order Møller-Plesset (MP2) perturbation method employing the augmented correlation consistent polarized valence triple zeta (aug-cc-pVTZ) basis set of Dunning [173] using the Gaussian-09 program [155]. The equilibrium geometry of c-C_2H_4O possesses C_{2v} point group symmetry and the electronic ground term symbol is $^1A_1$. Fig. 4.1 shows the schematic representation of optimized equilibrium geometry of c-C_2H_4O with atom numbering and its corresponding optimized parameters are given in Table 4.1.
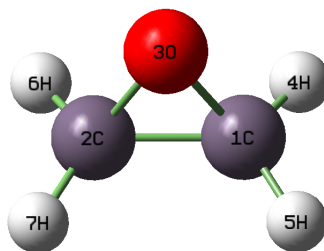
FIGURE 4.1: Optimized equilibrium geometry of the reference c-C_2H_4O molecule.

TABLE 4.1: Optimized geometry parameters (distances in Angstrom, angles in degrees) of the equilibrium structure of the electronic ground state of c-C_2H_4O.

parameters	This work	Expt. [174]
R(C1-O3)	1.436	1.436
R(C1-C2)	1.462	1.472
R(C1-H4)	1.082	1.082
∠(C1-O3-C2)	61.2	61.7
∠(H1-C2-H3)	116.4	116.7
∠(H3-C1-O3)	114.7	-
∠(H1-C1-C2)	119.3	-

The mass-weighted normal coordinates (q_i) of the vibrational modes are transformed to the dimensionless form (Q_i) by, $Q_i = \sqrt{\omega_i/\hbar}\, q_i$ [99]. Where ω_i is the harmonic

vibrational frequency of the ith normal mode and $\hbar=1$ (in atomic units). The harmonic frequencies of the vibrational modes and their symmetry are given in Table 4.2 along with the available literature data [174–176].

TABLE 4.2: Symmetry of vibrational modes, their designation and harmonic frequencies (in cm^{-1}) of the ground electronic state of the c-C_2H_4O.

Symmetry	modes	This work	Expt. [175]	Expt. [176]	Nature of mode
a_1	ν_1	3157	2983	3018	CH$_2$ s-str.
	ν_2	1549	1505	1498	CH$_2$ scissors
	ν_3	1308	1273	1270	ring stretch
	ν_4	1150	1093	1148	CH$_2$ wag
	ν_5	901	888	877	ring deformation
b_1	ν_6	3261	3096	3065	CH$_2$ s-str.
	ν_7	1169	1156	1142	CH$_2$ wag
	ν_8	823	805	821	ring deformation
b_2	ν_9	3150	3011	3006	CH$_2$ a-str.
	ν_{10}	1515	1468	1472	CH$_2$ scissors
	ν_{11}	1164	1169	1151	CH$_2$ twist
	ν_{12}	846	827	840	CH$_2$ rock
a_2	ν_{13}	3247	3078	-	CH$_2$ a-str.
	ν_{14}	1179	1168	-	CH$_2$ twist
	ν_{15}	1052	1014	-	CH$_2$ rock

It can be seen from the Tables 4.1 and 4.2 that, the theoretical results are in good accord with the available literature data.

To study the nuclear dynamics, the PESs of the six states are calculated along the dimensionless normal displacement coordinates (Q) of the reference electronic ground state. The potential energies of these electronic states of c-$C_2H_4O^{.+}$ are calculated by EOMIP-CCSD method using the aug-cc-pVTZ basis set. The EOMIP-CCSD calculations are performed using CFOUR suite of program [160]. The PESs are calculated along the dimensionless normal coordinate of each vibrational mode. The VIEs calculated by EOMIP-CCSD and OVGF [177] methods at the equilibrium geometry of the reference state are given in Table 4.3 along with the available literature data for comparison.

TABLE 4.3: VIEs of c-$C_2H_4O^{\cdot+}$ (in eV) calculated the energetically lowest $\widetilde{X}\ ^2B_1$, $\widetilde{A}\ ^2A_1$, $\widetilde{B}\ ^2B_2$, $\widetilde{C}\ ^2A_2$, $\widetilde{D}\ ^2A_1$ and $\widetilde{E}\ ^2B_1$ electronic states of the reference equilibrium geometry and compared with the available experimental data.

State symmetry	OVGF This work	EOMIP-CCSD This work	Expt. [89]	Expt. [86]	Expt. [47]
$\widetilde{X}\ ^2B_1$	11.12	10.60	10.56	10.57	10.57
$\widetilde{A}\ ^2A_1$	11.85	11.83	11.85	11.7	11.85
$\widetilde{B}\ ^2B_2$	14.09	13.99	13.73	13.7	14.0
$\widetilde{C}\ ^2A_2$	14.22	14.14	14.16	14.2	14.0
$\widetilde{D}\ ^2A_1$	16.63	16.60	16.52	16.6	16.6
$\widetilde{E}\ ^2B_1$	17.64	17.70	17.20	17.4	17.4

It can be seen from the Table 4.3 that, our theoretical results are in very good agreement with the available experimental data. From these data one can see that at the vertical configuration, $Q = 0$, among the six electronic states, $\widetilde{X}\ ^2B_1$-$\widetilde{A}\ ^2A_1$, $\widetilde{B}\ ^2B_2$-$\widetilde{C}\ ^2A_2$ and $\widetilde{D}\ ^2A_1$-$\widetilde{E}\ ^2B_1$ states are close in energy (cf., Table 4.3) in pair wise manner. The energetic closeness of these states results into a strong vibronic coupling and multiple multi-state CIs among them (cf., Fig. 4.2). Therefore, the vibronic coupling appears to be an important mechanism for the detailed nuclear dynamics on these states.

4.2 The Vibronic model Hamiltonian

Using the standard vibronic coupling theory [167] and symmetry selection rules a coupled six ($\widetilde{X}\ ^2B_1$ to $\widetilde{E}\ ^2B_1$) electronic states of cationic oxirane (c-$C_2H_4O^{\cdot+}$) vibronic model 6×6 matrix Hamiltonian is developed in a diabatic electronic basis [167] in terms of Q_i of the reference electronic ground state of neutral c-C_2H_4O molecule. The equilibrium geometry of c-C_2H_4O belongs to the C_{2v} symmetry point group, the symmetry of the electronic states is A_1, B_1, B_2 and A_2. According to the symmetry selection rules, the coupling modes are of b_1, b_2 and a_2 symmetry. The fifteen vibrational modes transform to the following irreducible representations

$$\Gamma_{vib} = 5a_1 + 3b_1 + 4b_2 + 3a_2. \tag{4.1}$$

The c-$C_2H_4O^{\cdot+}$ vibronic model Hamiltonian of the six low-lying $\widetilde{X}\ ^2B_1$, $\widetilde{A}\ ^2A_1$, $\widetilde{B}\ ^2B_2$, $\widetilde{C}\ ^2A_2$, $\widetilde{D}\ ^2A_1$ and $\widetilde{E}\ ^2B_1$ states can be symbolically written as [167],

$$
\mathcal{H} = \mathcal{H}_0 \mathbf{1_6} +
\begin{pmatrix}
U_{\widetilde{X}} & U_{\widetilde{X}\widetilde{A}} & U_{\widetilde{X}\widetilde{B}} & U_{\widetilde{X}\widetilde{C}} & U_{\widetilde{X}\widetilde{D}} & 0 \\
 & U_{\widetilde{A}} & U_{\widetilde{A}\widetilde{B}} & U_{\widetilde{A}\widetilde{C}} & 0 & U_{\widetilde{A}\widetilde{E}} \\
 & & U_{\widetilde{B}} & U_{\widetilde{B}\widetilde{C}} & U_{\widetilde{B}\widetilde{D}} & U_{\widetilde{B}\widetilde{E}} \\
 & & & U_{\widetilde{C}} & U_{\widetilde{C}\widetilde{D}} & U_{\widetilde{C}\widetilde{E}} \\
 & h.c. & & & U_{\widetilde{D}} & U_{\widetilde{D}\widetilde{E}} \\
 & & & & & U_{\widetilde{E}}
\end{pmatrix}
\tag{4.2}
$$

In the above equation, $\mathbf{1_6}$ denotes the 6×6 unit matrix, and $\mathcal{H}_0$ denotes the Hamiltonian of the reference ground electronic state of c-C_2H_4O, within the harmonic approximation, the latter reads

$$
\mathcal{H}_0 = -\frac{1}{2} \sum_{i \epsilon a_1, b_1, b_2, a_2} \omega_i \frac{\partial^2}{\partial Q_i^2} + \frac{1}{2} \sum_{i \epsilon a_1, b_1, b_2, a_2} \omega_i Q_i^2.
\tag{4.3}
$$

In Eq. 4.2, the second term (in RHS side) represents the electronic potential matrix in a diabatic electronic basis. The diagonal elements (U_n where, $n = \widetilde{X}\ ^2B_1$ to $\widetilde{E}\ ^2B_1$) of this matrix describe the diabatic potential energies of the electronic states and off-diagonal elements (U_{nm}) represent the coupling between them. These elements (diagonal and off-diagonal) are expanded in a standard Taylor series around the reference equilibrium geometry of the c-C_2H_4O at $Q=0$ in the following way

$$
U_n = E_0^n + \sum_{i \epsilon a_1} \kappa_i^n Q_i + \frac{1}{2!} \sum_{i \epsilon a_1, b_1, b_2, a_2} \gamma_i^n Q_i^2 + \frac{1}{3!} \sum_{i \epsilon a_1} \rho_i^n Q_i^3 + \frac{1}{4!} \sum_{i \epsilon a_1, b_1, b_2, a_2} \delta_i^n Q_i^4
$$
$$
+ \frac{1}{6!} \sum_{i \epsilon b_1, b_2, a_2} \sigma_i^n Q_i^6 + \frac{1}{8!} \sum_{i \epsilon b_1} \xi_i^n Q_i^8 \ ; \quad n \in \widetilde{X} - \widetilde{E},
\tag{4.4}
$$

$$
U_{nm} = \sum_{i \epsilon b_1, b_2, a_2} \lambda_i^{nm} Q_i \ ; \quad n, m \in \widetilde{X} - \widetilde{E}.
\tag{4.5}
$$

In the above equations E_0^n refers to the VIEs of the electronic state ($n = \widetilde{X}\ ^2B_1$, $\widetilde{A}\ ^2A_1$, $\widetilde{B}\ ^2B_2$, $\widetilde{C}\ ^2A_2$, $\widetilde{D}\ ^2A_1$, $\widetilde{E}\ ^2B_1$) and Q_i represent the dimensionless normal displacement coordinate of the electronic ground state of neutral c-C_2H_4O molecule. The specific form of the various coupling terms, i.e., diagonal (U_n) and off-diagonal (U_{nm}) matrix elements, is dictated by symmetry selection rules. In these expansions (cf., Eqs. 4.4 and 4.5), the terms κ_i^n (linear-), γ_{ij}^n (quadratic-), ρ_i^n (cubic-), δ_i^n (quartic-), σ_i^n (sixth-order), and ξ_i^n (eighth-order) denotes the intrastate coupling parameters of the nth electronic state along the ith vibrational mode. We noticed that up to a fourth-order Taylor series expansion is enough for the totally symmetric vibrational modes, and the sixth- and

eighth-order expansion is used only for the asymmetric modes. The quantity λ_i^{nm} denotes the linear inter-state coupling constants between the n and m electronic states. Due to anharmonicity of the potential energy curves along the coupling coordinates (i.e., b_1, b_2 and a_2) higher-order expansions are used. Especially, $\widetilde{B}\ ^2B_2$ and $\widetilde{C}\ ^2A_2$ electronic states strongly repel to each other along the b_1 symmetry vibrational modes. This coupling leads to the $\widetilde{B}\ ^2B_2$-state as double-minimum potential at the distorted geometry, this is known as pseudo-Jahn–Teller (PJT) effect in the literature [178]. So, to reproduce the *ab initio* points well for $\widetilde{B}\ ^2B_2$ and $\widetilde{C}\ ^2A_2$ electronic states along the b_1 symmetry vibrational modes eighth-order expansion is necessary. Along with the linear inter-state (λ_i^{nm}) coupling parameters, we also estimated the higher-order coupling parameters along the suitable coupling vibrational modes. But the magnitude of these parameters are of the order of 10^{-5} or less. Therefore, we restricted the linear expansion in Eq. 4.5. The coefficients of the Taylor series expansions were evaluated by non-linear least squares fitting of the 6×6 diabatic potential energy matrix to the *ab initio* energies. The estimated complete set of parameters are given in Table 4.5 and Tables B1 to B4 of the Appendix B.

4.3 Potential energy curves

One-dimensional potential energy cuts of c-$C_2H_4O^{·+}$ along the dimensionless normal displacement coordinates of five totally symmetric (a_1) vibrational modes, ν_1, ν_2, ν_3, ν_4 and ν_5, of the $\widetilde{X}\ ^2B_1$, $\widetilde{A}\ ^2A_1$, $\widetilde{B}\ ^2B_2$, $\widetilde{C}\ ^2A_2$, $\widetilde{D}\ ^2A_1$ and $\widetilde{E}\ ^2B_1$ electronic states are shown in Fig. 4.2. In each panel of Fig. 4.2, the points represent the *ab initio* electronic structure data and the solid lines represent the results obtained from present vibronic model defined in section 4.2. It can be seen from the Fig. 4.2 that the calculated *ab initio* points are well reproduced by the present theoretical vibronic coupling model. The calculated parameters derived from the fittings are tabulated in Table 4.5 and Tables B1 to B4 of Appendix B. To fit the totally symmetric and coupled vibrational modes (b_1, b_2 and a_2 symmetry), up to a fourth-order and higher-order (sixth and eighth) Taylor series expansion of the Hamiltonian is used to represent the *ab initio* points extremely well. The totally symmetric vibrational modes tune the energy gap between the electronic states by tuning the electronic energy minimum and form the intersections between them. It is noticed that all six electronic states strongly interact with each other (cf., Fig. 4.2) and $\widetilde{B}\ ^2B_2$-$\widetilde{C}\ ^2A_2$ states are quasi-degenerate at the Franck-Condon geometry (cf., Table 4.3). Also, the existence of strong to weak intra-state coupling of the six ($\widetilde{X}\ ^2B_1$ to $\widetilde{E}\ ^2B_1$) electronic states of c-$C_2H_4O^{·+}$ can be seen from the data given in Table 4.5. Poisson Parameter or excitation strength ($\kappa_i^2/2\omega_i^2$) of the intra-state coupling of the a_1 vibrational modes (ν_1 to ν_5) are estimated and are included in the Table 4.5. From
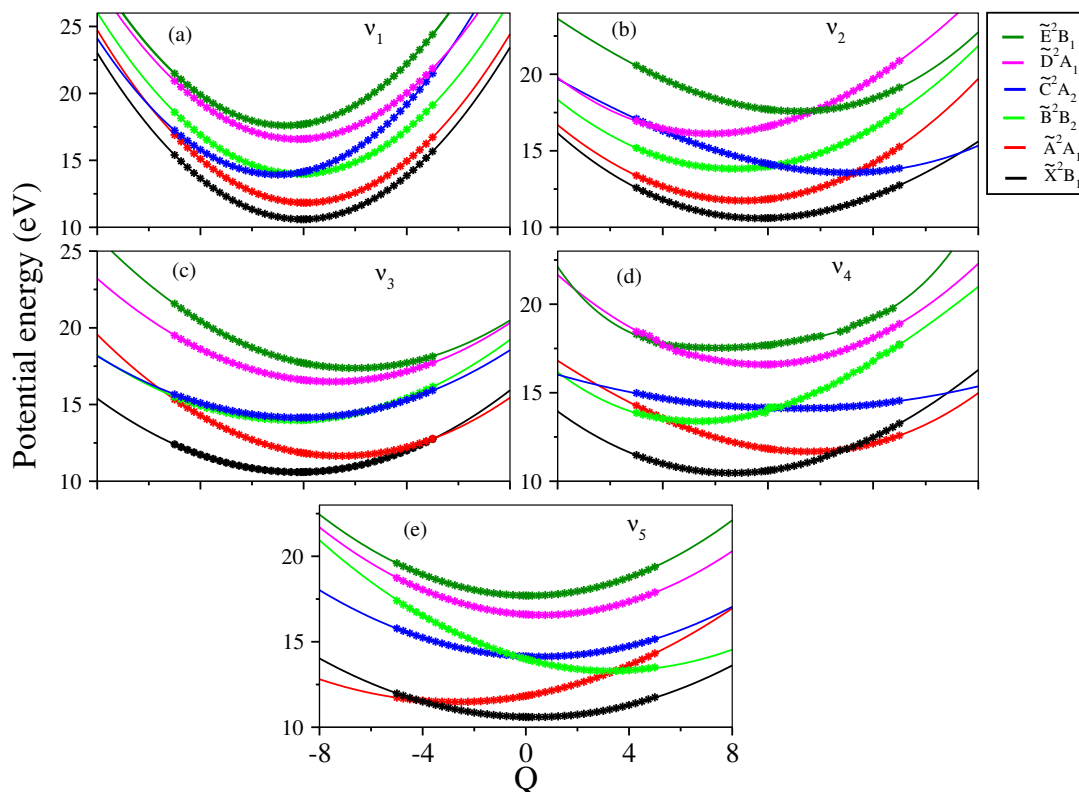
FIGURE 4.2: One dimensional viewgraph of the multi-dimensional potential energy surfaces of the lowest six $\widetilde{X}$, $\widetilde{A}$, $\widetilde{B}$, $\widetilde{C}$, $\widetilde{D}$ and $\widetilde{E}$ electronic state of c-$C_2H_4O^{\cdot+}$ plotted along the dimensionless normal coordinate (Q_i) of the totally symmetric vibrational modes, ν_1-ν_5. The potential energies obtained from the theoretical model and calculated *ab initio* are shown as solid lines and points, respectively.

these parameters, one can measure the directional and positional shift of the energetic minimum of a particular electronic state with respect to the reference neutral ground electronic configuration of c-C_2H_4O. With an increase in the value of these parameters leads to the shifting of the minimum of the electronic state in the opposite direction of the sign of "k". It can be seen from the Fig. 4.2 that all the six electronic states are interacting with each other and due to the shifting of the minimum of electronic states they undergo curve crossings (cf., Fig. 4.2). These curve crossing evolves into CIs in a multi-dimensional space and play crucial role in the nuclear dynamics.

The static points (i.e., energetic minima and minimum of the seam of CIs) are calculated using a QVC model and utilizing the model Hamiltonian parameters given in the Tables 4.2- 4.5, with the help of a minimization algorithm employing Lagrange multipliers. The numerical tools available in MATHEMATICA [170] are used for this purpose. The results are given in a matrix array in Table 4.4.

TABLE 4.4: Estimated equilibrium minimum (diagonal entries) and minimum of the seam of various conical intersections (off-diagonal entries) of the electronic states of c-$C_2H_4O^{\cdot+}$ within a quadratic coupling model. All quantities are given in eV.

	$\widetilde{X}\ ^2B_1$	$\widetilde{A}\ ^2A_1$	$\widetilde{B}\ ^2B_2$	$\widetilde{C}\ ^2A_2$	$\widetilde{D}\ ^2A_1$	$\widetilde{E}\ ^2B_1$
$\widetilde{X}\ ^2B_1$	10.44	11.14	13.02	13.38	35.25	20.77
$\widetilde{A}\ ^2A_1$	-	11.05	12.79	13.31	22.79	17.95
$\widetilde{B}\ ^2B_2$	-	-	12.46	13.68	17.22	18.04
$\widetilde{C}\ ^2A_2$	-	-	-	13.29	16.07	30.77
$\widetilde{D}\ ^2A_1$	-	-	-	-	15.96	16.99
$\widetilde{E}\ ^2B_1$	-	-	-	-	-	16.94

In this table the diagonal elements represent the energetic minimum of electronic states and the off-diagonal elements represents the minimum of the seam of CIs.

For example, it can be seen from Table 4.5 that, among the five totally symmetric modes ν_4 is the strong Condon active mode in the $\widetilde{X}$ state with a positive k value. As a re-

TABLE 4.5: *Ab initio* calculated linear (κ_i) and quadratic (γ_i) coupling parameters for the $\widetilde{X}\ ^2B_1$, $\widetilde{A}\ ^2A_1$, $\widetilde{B}\ ^2B_2$, $\widetilde{C}\ ^2A_2$, $\widetilde{D}\ ^2A_1$ and $\widetilde{E}\ ^2B_1$ electronic states of c-$C_2H_4O^{\cdot+}$. All quantities are in eV and the dimensionless Poisson parameters $\left(\kappa_i^2/2\omega_i^2\right)$ are given in the parentheses.

		$\widetilde{X}$		$\widetilde{A}$		$\widetilde{B}$	
Sym.	Mode	κ_i	γ_i	κ_i	γ_i	κ_i	γ_i
a_1	ν_1	0.0256 (0.0021)	0.0034	-0.0195(0.0012)	0.0068	0.0509 (0.0084)	-0.0018
	ν_2	0.0488 (0.0323)	-0.0268	0.1885(0.4818)	0.0069	0.2499 (0.8469)	-0.0011
	ν_3	0.0335 (0.0213)	-0.0039	-0.2571(1.2570)	0.0150	0.0632 (0.0759)	-0.0144
	ν_4	0.1991 (0.9756)	-0.0011	-0.2021(1.0052)	-0.0155	0.4414 (4.7952)	0.0008
	ν_5	-0.0258 (0.0267)	-0.0109	0.2593(2.6946)	-0.0164	-0.4002 (6.4187)	0.0056

		$\widetilde{C}$		$\widetilde{D}$		$\widetilde{E}$	
Sym.	Mode	κ_i	γ_i	κ_i	γ_i	κ_i	γ_i
a_1	ν_1	0.4244 (0.5878)	0.0260	0.0930 (0.0282)	-0.0076	0.2904 (0.2752)	0.0279
	ν_2	-0.3556 (1.7148)	-0.0867	0.4264 (2.4655)	-0.0072	-0.1990 (0.5370)	-0.0205
	ν_3	0.0238 (0.0108)	-0.0306	-0.1806 (0.6203)	-0.0005	-0.3402 (2.2009)	0.0100
	ν_4	-0.0437 (0.0470)	-0.0941	0.0395 (0.0384)	0.0256	0.1671 (0.6872)	-0.0725
	ν_5	-0.0609 (0.1486)	-0.0058	-0.0875 (0.3068)	0.0259	-0.0210 (0.0177)	0.0313

sult, the shift of the energetic minimum of the ground state of the c-$C_2H_4O^{\cdot+}$ along this normal mode is in the negative direction (cf., panel (d) of Fig. 4.2). Similarly, the largest shift of the energy minima of $\widetilde{A}$ to $\widetilde{E}$ states can be found along ν_1, ν_2, ν_3, ν_4 and ν_5 vibrational modes (cf., Fig. 4.2), respectively, and these electronic states can undergo curve crossings along these normal coordinates. The latter result into CIs in multi-dimension and play a crucial role in shaping up the electronic spectrum and internal conversion dynamics. It can be seen from Table 4.4 that, the equilibrium minimum of the $\widetilde{X}\ ^2B_1$-$\widetilde{A}\ ^2A_1$, $\widetilde{B}\ ^2B_2$-$\widetilde{C}\ ^2A_2$ and $\widetilde{D}\ ^2A_1$-$\widetilde{E}\ ^2B_1$ states are relatively close in energy, the $\widetilde{X}\ ^2B_1$-$\widetilde{A}\ ^2A_1$ intersection minimum occurs ∼0.7 eV and ∼0.09 eV above the minimum of the $\widetilde{X}\ ^2B_1$ and $\widetilde{A}\ ^2A_1$ electronic states, respectively. Therefore, the $\widetilde{A}\ ^2A_1$ state minimum is close to the $\widetilde{X}\ ^2B_1$-$\widetilde{A}\ ^2A_1$ intersection minimum. The intersection between

$\widetilde{X}$ ^{2}B$_1$ state with $\widetilde{B}$ ^{2}B$_2$-$\widetilde{E}$ ^{2}B$_1$ electronic states are high in energy. The $\widetilde{A}$ ^{2}A$_1$-$\widetilde{B}$ ^{2}B$_2$ intersection minimum occurs $\sim$1.74 eV and $\sim$0.33 eV above the minimum of the $\widetilde{A}$ ^{2}A$_1$ and $\widetilde{B}$ ^{2}B$_2$ electronic states, respectively. Also the $\widetilde{B}$ ^{2}B$_2$-$\widetilde{C}$ ^{2}A$_2$ intersection minimum occurs $\sim$1.22 eV, $\sim$0.39 eV above the minimum of the $\widetilde{B}$ ^{2}B$_2$ and $\widetilde{C}$ ^{2}A$_2$ electronic states, respectively. The $\widetilde{C}$ ^{2}A$_2$-$\widetilde{D}$ ^{2}A$_1$ intersection minimum occurs $\sim$2.78 eV above the minimum of the $\widetilde{C}$ ^{2}A$_2$ state and the minimum of $\widetilde{D}$ ^{2}A$_1$ state is $\sim$0.11 eV above the $\widetilde{C}$ ^{2}A$_2$-$\widetilde{D}$ ^{2}A$_1$ intersection minimum. The $\widetilde{D}$ ^{2}A$_1$ state minimum is close to the $\widetilde{C}$ ^{2}A$_2$-$\widetilde{D}$ ^{2}A$_1$ intersection minimum. The $\widetilde{D}$ ^{2}A$_1$-$\widetilde{E}$ ^{2}B$_1$ intersection minimum occurs $\sim$1.03 eV and $\sim$0.05 eV above the minimum of the $\widetilde{D}$ ^{2}A$_1$ and $\widetilde{E}$ ^{2}B$_1$ states, respectively. The $\widetilde{E}$ ^{2}B$_1$ state minimum is very close to the $\widetilde{D}$ ^{2}A$_1$-$\widetilde{E}$ ^{2}B$_1$ intersection minimum. The strong interactions between the six electronic states are expected to have strong impact on the nuclear dynamics study.

The linear inter-state couplings (coupling between the two different electronic states) of $\widetilde{X}$ ^{2}B$_1$ to $\widetilde{E}$ ^{2}B$_1$ states are fairly strong along the vibrational modes of b_1, b_2 and a_2 symmetry (cf., Table B4 of the Appendix B). The ν_7 and ν_8 modes of b_1 symmetry have strong inter-state coupling and the ν_6 has moderate coupling, between $\widetilde{X}$ ^{2}B$_1$-$\widetilde{A}$ ^{2}A$_1$, $\widetilde{X}$ ^{2}B$_1$-$\widetilde{D}$ ^{2}A$_1$ and $\widetilde{B}$ ^{2}B$_2$-$\widetilde{C}$ ^{2}A$_2$ electronic states, respectively. Also the coupling is small between $\widetilde{A}$ ^{2}A$_1$-$\widetilde{E}$ ^{2}B$_1$ and $\widetilde{D}$ ^{2}A$_1$-$\widetilde{E}$ ^{2}B$_1$ states along b_1 symmetry vibrational mode. Along the b_2 symmetry modes, the inter-state coupling between $\widetilde{X}$ ^{2}B$_1$-$\widetilde{C}$ ^{2}A$_2$ and $\widetilde{A}$ ^{2}A$_1$-$\widetilde{B}$ ^{2}B$_2$ states is coupled by only ν_{12} vibrational mode. The $\widetilde{B}$ ^{2}B$_2$-$\widetilde{D}$ ^{2}A$_1$ and $\widetilde{C}$ ^{2}A$_2$-$\widetilde{E}$ ^{2}B$_1$ states coupling is strong along ν_9, ν_{10} and ν_{11} vibrational modes of b_2 symmetry. In case of a_2 symmetry, the $\widetilde{X}$ ^{2}B$_1$-$\widetilde{B}$ ^{2}B$_2$ coupling is large along both ν_{13} and ν_{15} vibrational modes, and $\widetilde{A}$ ^{2}A$_1$-$\widetilde{C}$ ^{2}A$_2$ coupling is large along the ν_{15} vibrational mode. The $\widetilde{C}$ ^{2}A$_2$-$\widetilde{D}$ ^{2}A$_1$ coupling is strong along the ν_{13} and ν_{14} vibrational modes (cf., Table B4 of the Appendix B).

The vibrational modes of b_1 symmetry couples the $\widetilde{X}$ ^{2}B$_1$-$\widetilde{A}$ ^{2}A$_1$, $\widetilde{X}$ ^{2}B$_1$-$\widetilde{D}$ ^{2}A$_1$, $\widetilde{A}$ ^{2}A$_1$-$\widetilde{E}$ ^{2}B$_1$, $\widetilde{B}$ ^{2}B$_2$-$\widetilde{C}$ ^{2}A$_2$ and $\widetilde{D}$ ^{2}A$_1$-$\widetilde{E}$ ^{2}B$_1$ states. Among these $\widetilde{B}$ ^{2}B$_2$-$\widetilde{C}$ ^{2}A$_2$ states are quasi-degenerate (cf., Table 4.3) and they strongly couple each other (cf., Table B4 of the Appendix B). Because of this strong nonadiabatic (or inter-state) coupling, the $\widetilde{B}$ ^{2}B$_2$ and $\widetilde{C}$ ^{2}A$_2$ states strongly repel to each other along the b_1 symmetry coupling vibrational mode. The topography of these coupling surfaces are shown in Fig. 4.3. It can be seen from this figure that the lower adiabatic potential energy surfaces exhibit a symmetric double-well along the ν_7 mode with two symmetric minimum at distorted geometry compared to the Franck-Condon C_{2v} geometry, at Q=0. This symmetry breaking effect [179], known as PJT effect [178], occurs due to strong nonadiabatic coupling through b_1 symmetry vibrational modes (cf., Table B4 of the Appendix B) between the energetically

close-lying $\widetilde{B}\ ^2B_2$ and $\widetilde{C}\ ^2A_2$ electronic states. Therefore, the vibronic coupling through
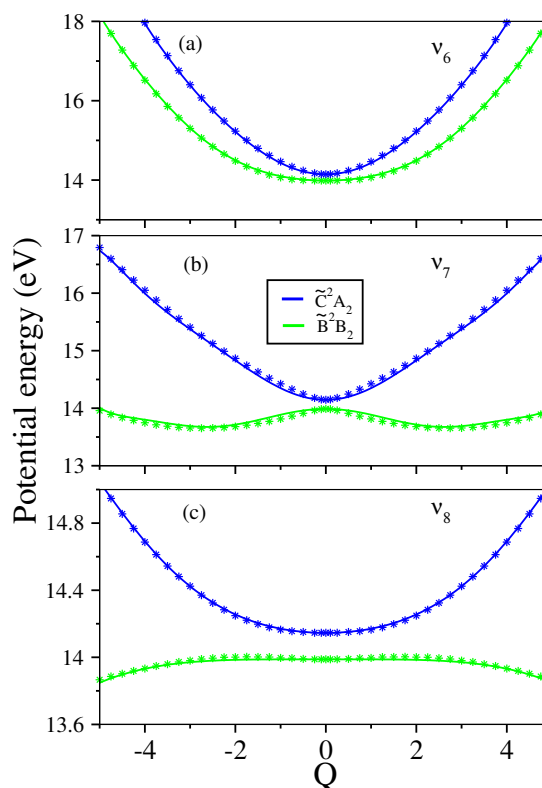
FIGURE 4.3: One dimensional viewgraph of the multi-dimensional potential energy surfaces of the lowest $\widetilde{B}$ and $\widetilde{C}$ electronic states of c-$C_2H_4O^{\cdot+}$ plotted along the dimensionless normal coordinate (Q_i) of the asymmetric vibrational mode of b_1 symmetry, ν_6-ν_8. The potential energies obtained from the theoretical model and calculated *ab initio* are shown as solid lines and points, respectively.

b_1 symmetry vibrational modes stabilizes the c-$C_2H_4O^{\cdot+}$ in its $\widetilde{B}\ ^2B_2$ state at various distorted geometries (cf., Fig. 4.3 (b)).

As discussed in the introduction, oxirane and acetaldehyde molecules are more stable isomers of C_2H_4O and their point group of symmetries are C_{2v} and C_s, respectively. The topography of PES of both oxirane and acetaldehyde radical cations are different. According to the low-symmetry point group (C_s) of acetaldehyde, several electronic states have same symmetry. Because of this, in acetaldehyde the same symmetry states strongly repel each other (cf., Fig. 2 of Ref. [98]). These states are diabatized using four-fold way diabatization scheme proposed by Truhlar and co-workers [116, 121–124] at the level of multi-configuration quasi-degenerate perturbation theory (MCQDPT) citeNakano1993,Nakano1993mcscf,Granovsky2011. In case of acetaldehyde, among the seven ($\widetilde{X}\ ^2B_1$, $\widetilde{A}\ ^2A_1$, $\widetilde{B}\ ^2B_2$, $\widetilde{C}\ ^2A_2$, $\widetilde{D}\ ^2A_1$ and $\widetilde{E}\ ^2B_1$) electronic states $\widetilde{A}\ ^2A_1$ to $\widetilde{E}\ ^2B_1$ states are very close to each other (see Fig. 2 of Ref. [98]) and these states exhibit strong

vibronic coupling between them.

4.4 Results and discussion

In the following, vibronic band structures of the $\widetilde{X}\ ^2B_1$, $\widetilde{A}\ ^2A_1$, $\widetilde{B}\ ^2B_2$, $\widetilde{C}\ ^2A_2$, $\widetilde{D}\ ^2A_1$ and $\widetilde{E}\ ^2B_1$ electronic states of c-$C_2H_4O^{\cdot+}$ are calculated by both in absence and presence of coupling with their neighboring electronic states, and compared with the available experimental photoelectron spectroscopy results of c-C_2H_4O [47, 86]. The decay rates of six electronic states and internal conversion dynamics are calculated in terms of change of electronic population in time. The vibronic energy level structure of the uncoupled and coupled electronic states reveal nonadiabatic coupling effect on the energy level band structures. To find specific location of the energy levels of the uncoupled electronic states, we have used the time-independent matrix diagonalization method. Finally, the effect of electronic state coupling on the vibronic structure and relaxation dynamics is examined by time-dependent quantum mechanical method. For all these calculations we used the MCTDH program package developed at the Heidelberg University [139, 152–154].

4.4.1 The uncoupled electronic states spectrum of c-$C_2H_4O^{\cdot+}$

The vibrational energy level spectrum of the uncoupled $\widetilde{X}\ ^2B_1$, $\widetilde{A}\ ^2A_1$, $\widetilde{B}\ ^2B_2$, $\widetilde{C}\ ^2A_2$, $\widetilde{D}\ ^2A_1$ and $\widetilde{E}\ ^2B_1$ electronic states is calculated by including five totally symmetric vibrational modes (ν_1–ν_5) by a matrix diagonalization approach [167] using the Lanczos algorithm [133] and are shown in Fig. 4.4. For this purpose, we used the vibronic model Hamiltonian discussed in Sec. 4.2 and the parameters from the Tables 4.5 and B1 to B4 of Appendix B. The Appendix B provides the HO basis functions utilized for each mode in these computations, as detailed in Table B5. Following this, the Hamiltonian of each state, represented in the HO basis, undergoes diagonalization through 10,000 Lanczos iterations. The resulting theoretical stick spectrum, derived from the diagonalization of the Hamiltonian matrix, is then convolved with a Lorentzian line shape function possessing a full width at half maximum (FWHM) of 40 meV. This convolution process yields the spectral envelopes depicted in Fig. 4.4. The low energy vibronic levels of uncoupled $\widetilde{X}\ ^2B_1$, $\widetilde{A}\ ^2A_1$, $\widetilde{B}\ ^2B_2$, $\widetilde{C}\ ^2A_2$, $\widetilde{D}\ ^2A_1$ and $\widetilde{E}\ ^2B_1$ states are given in Table B6 of the Appendix B along with their assignments. The time-independent calculations performed to understand the vibronic energy level spectrum of c-$C_2H_4O^{\cdot+}$, and it helps to identify the dominant progressions of various vibrational modes and to interpret the vibrational modes contributions in the spectral broadening measured in the experiment. Thereafter, the nodal pattern of the respective vibronic wave functions is examined by calculating
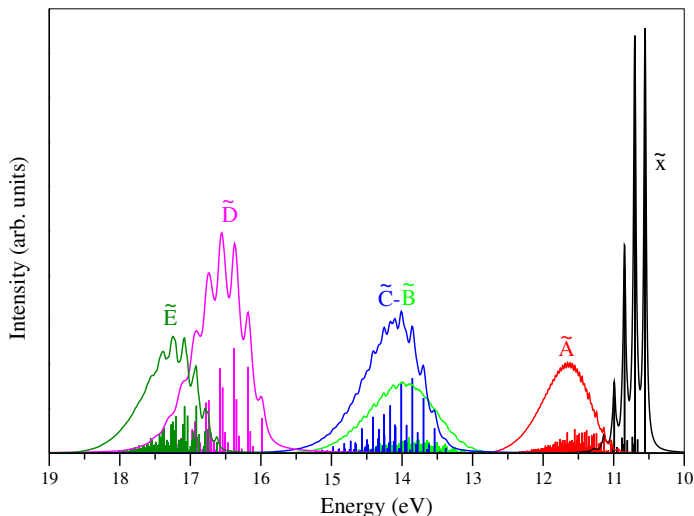
FIGURE 4.4: The stick vibronic spectrum and the convoluted envelope of the $\widetilde{X}\ ^2B_1$, $\widetilde{A}\ ^2A_1$, $\widetilde{B}\ ^2B_2$, $\widetilde{C}\ ^2A_2$, $\widetilde{D}\ ^2A_1$ and $\widetilde{E}\ ^2B_1$ electronic states of c-$C_2H_4O^{\cdot+}$ calculated with the a_1 vibrational modes. The intensity in arbitrary units is plotted as a function of the energy of the vibronic levels.

them using block-improved relaxation method as implemented in the MCTDH program module [139, 152].

It can be seen from the data given in Table B6 of Appendix B that, fundamental of totally symmetric vibrational modes (ν_1–ν_5), are excited in each of the given electronic state of the c-$C_2H_4O^{\cdot+}$. In each electronic state, the vibrational modes excitation/progressions depend on their coupling strength ($\kappa_i{}^2/2\omega_i{}^2$). Along with this, several overtones and combination energy levels of respective strongly excited modes are also found. The first vibronic band originates from the $\widetilde{X}\ ^2B_1$ electronic state. The dominant progressions in this band are formed by ν_2, ν_4 and ν_5 vibrational modes, and the peaks are ~1446 cm^{-1}, ~1172 cm^{-1} and ~856 cm^{-1} spaced in energy, respectively. The vibrational mode ν_1 (~3170 cm^{-1}) is weakly excited in this state. These uncoupled-state vibrational progressions (cf., Table B6 of the Appendix B) are compared with the available literature data of the totally symmetric modes [86]. One can see from the present results that our results are in well agreement with the available experimental findings in the literature [86]. The second vibronic band is formed by the $\widetilde{A}\ ^2A_1$ electronic state and it is close to $\widetilde{X}\ ^2B_1$ electronic state (cf., Fig. 4.4). The dominant progressions in this band are formed by ν_3, ν_4 and ν_5 vibrational modes, moderate excitation along the ν_1 and ν_2 modes are found (cf., Table 4.5). Peaks are spaced ~1366 cm^{-1}, ~1136 cm^{-1}, ~832 cm^{-1}, ~3184 cm^{-1} and ~1576 cm^{-1} in that order, respectively.

The third vibronic band is formed by the strongly overlapping of $\widetilde{B}$ $^2B_2$ and $\widetilde{C}$ $^2A_2$ electronic states. This is because of the quasi-degeneracy of the $\widetilde{B}$ $^2B_2$ and $\widetilde{C}$ $^2A_2$ electronic states, which leads to a strong mixing of vibronic energy levels of $\widetilde{B}$ $^2B_2$ and $\widetilde{C}$ $^2A_2$ states. The $\widetilde{B}$ $^2B_2$ state vibronic band structure reveals dominant excitation of ν_2, ν_4 and ν_5 ; moderate excitation of ν_1 and ν_3 vibrational modes (cf., Table 4.5). Peaks are spaced $\sim$1620 cm^{-1}, $\sim$1152 cm^{-1} and $\sim$923 cm^{-1}; $\sim$3149 cm^{-1} and $\sim$1248 cm^{-1}, respectively, in that order. In case of $\widetilde{C}$ $^2A_2$ state, extended progressions of ν_1, ν_2 and ν_5 vibrational modes with line spacing of $\sim$3260 cm^{-1}, $\sim$1267 cm^{-1} and $\sim$877 cm^{-1}, respectively, are found.

The fourth and fifth vibronic bands are formed by the $\widetilde{D}$ $^2A_1$ and $\widetilde{E}$ $^2B_1$ electronic states (cf., Fig. 4.4). At the equilibrium configuration both $\widetilde{D}$ $^2A_1$ and $\widetilde{E}$ $^2B_1$ states are energetically close (cf., Tables 4.3 and 4.4). Due to this, the individual vibronic bands (vibronic energy levels) of $\widetilde{D}$ $^2A_1$ and $\widetilde{E}$ $^2B_1$ states strongly overlap and forms the fourth vibronic band in the experimental spectrum (this will be discussed in more detail in next section). The individual vibronic band structures of $\widetilde{D}$ $^2A_1$ and $\widetilde{E}$ $^2B_1$ states reveals the dominant excitation of ν_2, ν_3, ν_5 and ν_2, ν_3, ν_4, respectively. Peak spacing of $\sim$1590 cm^{-1}, $\sim$1305 cm^{-1}, $\sim$1000 cm^{-1} and $\sim$1524 cm^{-1}, $\sim$1347 cm^{-1}, $\sim$1006 cm^{-1} in that order, respectively, is found. For all vibrational band structures we have mentioned only the dominant progressions of fundamentals. Apart from the fundamentals, their overtones and several combination levels are also excited in each band and are given in Table B6 of the Appendix B.

In addition to determining the energetic positions and analyzing the excitation strengths, the assignment of peaks is further validated by scrutinizing the nodal patterns of the vibrational wave functions. These wave functions are computed using a block improved-relaxation method, as implemented in the MCTDH program module [140, 171, 172]. In Fig. B1 (a)-(i) in Appendix B, specifically, depict several vibrational eigenfunctions of the $\widetilde{X}$ $^2B_1$ state. This figure illustrates the probability density of the wave function plotted in a suitable reduced dimensional of normal coordinate space. The panels (a)-(c) display the wave functions corresponding to the fundamental vibrations of ν_2, ν_4 and ν_5, respectively. These plots reveal the wave function emergence of a node along each respective normal coordinate. In panels (d)-(f) shown the wave functions for the overtone peaks of the excited vibrational modes. Additionally, panels (g)-(i) of Fig. B1 of Appendix B display some combination peaks. Similarly, for all the states of the vibrational wave functions are shown in Figs. B2-B6 of Appendix B.

Subsequently, the calculations for coupled-state nuclear dynamics are conducted employing the coupled-state Hamiltonian outlined in Sec. 4.2. The time-dependent quantum mechanical method is employed for this endeavor. Finally, the theoretical outcomes are compared with the existing experimental photoelectron spectrum data of the c-C_2H_4O molecule.

4.4.2 Vibronic structure of the coupled two-electronic states dynamics of c-$C_2H_4O^{.+}$

To explore the influence of nonadiabatic coupling on the vibronic characteristics of individual states, we conducted several coupled two-state calculations, focusing on neighboring states, as detailed in this section. The outcomes are depicted in Fig. B7 of Appendix B. Despite the significant coupling with the $\widetilde{A}\ ^2A_1$ state (as indicated in Table B4), the overall nature of the $\widetilde{X}\ ^2B_1$ state spectrum remains unchanged (cf., panel (a) of Fig. B8). This is attributed to the substantial vertical separation of the $\widetilde{X}\ ^2B_1$ state from others (as illustrated in Table 4.4), with the minima of the intersection seams lying notably above its equilibrium minimum (as shown in Table 4.4, i.e., the energetic minimum of the intersection seam occurs ~0.7 eV and ~0.09 eV above the minimum of the $\widetilde{X}\ ^2B_1$ and $\widetilde{A}\ ^2A_1$ states, respectively). Consequently, the WP initially prepared on the $\widetilde{X}\ ^2B_1$ state does not venture into the vicinity of the $\widetilde{X}\ ^2B_1$-$\widetilde{A}\ ^2A_1$ crossing seam, resulting in minimal electronic population flow to the $\widetilde{A}\ ^2A_1$ state (cf., panel (a) of Fig. B8). In contrast, for the $\widetilde{A}\ ^2A_1$ state, the WP accesses the $\widetilde{X}\ ^2B_1$-$\widetilde{A}\ ^2A_1$ intersection seam, leading to over ~80% of electronic population transferring to the $\widetilde{X}\ ^2B_1$ state within ~25 fs (see panel (b) of Fig. B8). This substantial population exchange contributes to a significant increase in spectral line density and broadening of the vibronic spectrum of the $\widetilde{A}\ ^2A_1$ state (see panel (b) of Fig. B7).

In contrast to the aforementioned scenario, the coupling between the $\widetilde{A}\ ^2A_1$-$\widetilde{B}\ ^2B_2$, $\widetilde{B}\ ^2B_2$-$\widetilde{C}\ ^2A_2$, $\widetilde{C}\ ^2A_2$-$\widetilde{D}\ ^2A_1$ and $\widetilde{D}\ ^2A_1$-$\widetilde{E}\ ^2B_1$ states significantly influences their respective vibronic structures. When considering the coupled states $\widetilde{A}\ ^2A_1$-$\widetilde{B}\ ^2B_2$, minimal electronic population flows from the $\widetilde{A}\ ^2A_1$ to the $\widetilde{B}\ ^2B_2$ state when the WP is initially localized on the $\widetilde{A}\ ^2A_1$ state (cf., panel (c) of Fig. B8). The energetic minimum of the intersection seam occurs ~1.74 eV and ~0.33 eV above the minimum of the $\widetilde{A}\ ^2A_1$ and $\widetilde{B}\ ^2B_2$ electronic states, respectively (see Table 4.4). While no coupling effect is observed in the $\widetilde{A}\ ^2A_1$ band (cf., panel (c) of Fig. B7), the impact of coupling on the $\widetilde{B}\ ^2B_2$ state is substantial. This coupling effect is evident in both the vibronic structure and electronic population dynamics of the $\widetilde{B}\ ^2B_2$ state (cf., panel (d) of Fig. B7). When the WP is initially prepared on the $\widetilde{B}\ ^2B_2$ state, it accesses the $\widetilde{A}\ ^2A_1$-$\widetilde{B}\ ^2B_2$ intersection

seam, resulting in ~45% of the electronic population transferring to the $\widetilde{A}\,^2A_1$ state (see panel (g) of Fig. B8).

In the case of the $\widetilde{B}\,^2B_2$-$\widetilde{C}\,^2A_2$ coupled states, they exhibit quasi-degeneracy in terms of energy (cf., Table 4.4). When the WP is initially localized on the $\widetilde{B}\,^2B_2$ state, only a small amount of electronic population transfers to the $\widetilde{C}\,^2A_2$ state (see panel (e) of Fig. B8). The energetic minimum of the intersection seam is ~1.22 eV and 0.39 eV above the minimum of the $\widetilde{B}\,^2B_2$ and $\widetilde{C}\,^2A_2$ electronic states, respectively (cf., Table 4.4), and the corresponding band structure is depicted in panel (e) of Fig. B7. The impact of coupling is notable in the dynamics of the $\widetilde{C}\,^2A_2$ state. Both the vibronic structure and electronic population dynamics of the $\widetilde{C}\,^2A_2$ state reflect this coupling effect (cf., panel (f) of Fig. B7). When the WP is initially prepared on the $\widetilde{C}\,^2A_2$ state, it accesses the $\widetilde{B}\,^2B_2$-$\widetilde{C}\,^2A_2$ intersection seam, resulting in ~60% of the electronic population transferring to the $\widetilde{B}\,^2B_2$ state within ~20 fs (see panel (f) of Fig. B8).

In the scenario involving the $\widetilde{C}\,^2A_2$-$\widetilde{D}\,^2A_1$ coupled states, the intersection seam energetic minimum is ~2.78 eV and ~0.11 eV above the estimated equilibrium minimum of the $\widetilde{C}\,^2A_2$ and $\widetilde{D}\,^2A_1$ states, respectively (cf., Table 4.4). The coupling strength between these states is also notably strong (see Table B4 in Appendix B). Consequently, there is a substantial exchange of population between them. To illustrate the time-dependent behavior of the diabatic electronic population when transitioning to the $\widetilde{C}\,^2A_2$ and $\widetilde{D}\,^2A_1$ states in the $\widetilde{C}\,^2A_2$-$\widetilde{D}\,^2A_1$ coupled state scenario, panels (g) and (h) of Fig. B8 in Appendix B depict this situation, respectively. It is evident from these panels that a lesser amount of population is transferred to the $\widetilde{D}\,^2A_1$ state, with a significant fraction flowing to the $\widetilde{C}\,^2A_2$ electronic state. This disparity arises because the equilibrium minimum of the $\widetilde{D}\,^2A_1$ states is energetically very close to the minimum of the $\widetilde{C}\,^2A_2$-$\widetilde{D}\,^2A_1$ CIs (see Table 4.4). A rapid decay of population occurs within ~15 fs. The vibronic band structures of the coupled $\widetilde{C}\,^2A_2$-$\widetilde{D}\,^2A_1$ states are illustrated in panels (g) and (h) of Fig. B7 in Appendix B.

In the scenario involving coupled $\widetilde{D}\,^2A_1$-$\widetilde{E}\,^2B_1$ states, the intersection seams energetic minimum occurs ~1.03 eV and ~0.05 eV above the estimated equilibrium minimum of the $\widetilde{D}\,^2A_1$ and $\widetilde{E}\,^2B_1$ states, respectively (cf., Table 4.4). Consequently, there is minimal population transfer to the $\widetilde{E}\,^2B_1$ state when the WP is initially launched on the $\widetilde{D}\,^2A_1$ state (cf., panel (i) of Fig. B8), and the corresponding vibronic band structure is depicted in panel (i) of Fig. B7 in Appendix B. Due to the fairly strong vibronic coupling between the $\widetilde{D}\,^2A_1$ and $\widetilde{E}\,^2B_1$ states, and their intersection seams proximity

to the minimum of the $\widetilde{E}\ ^2B_1$ state (cf., Table 4.4), there is a notable impact on the dynamics of the $\widetilde{E}\ ^2B_1$ state. Within a short time frame of $\sim$25 fs, the population of the $\widetilde{E}\ ^2B_1$ state sharply decreases to around $\sim$0.3, while that of the $\widetilde{D}\ ^2A_1$ state increases to about $\sim$0.7 (cf., panel (j) of Fig. B8) when the WP is initially located on the $\widetilde{E}\ ^2B_1$ state.

4.4.3 Coupled six-state dynamics of c-$C_2H_4O^{.+}$

The vibronic coupling between the six $\widetilde{X}\ ^2B_1$-$\widetilde{A}\ ^2A_1$-$\widetilde{B}\ ^2B_2$-$\widetilde{C}\ ^2A_2$-$\widetilde{D}\ ^2A_1$-$\widetilde{E}\ ^2B_1$ electronic states are included in the coupled state spectrum calculations. From the latter one can understand the features identified in the recorded broad band vibronic spectrum of c-$C_2H_4O^{.+}$ and is discussed in this section. The vibronic spectrum of the six coupled electronic states of c-$C_2H_4O^{.+}$ is shown in Fig. 4.5. The dynamics calculations are
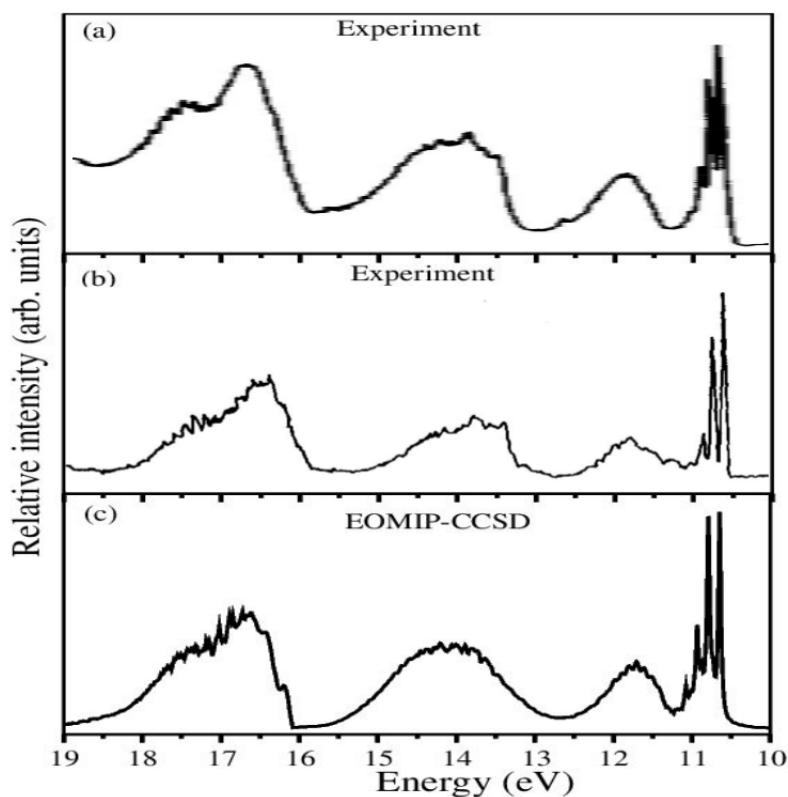
FIGURE 4.5: Vibronic band structure of the coupled $\widetilde{X}\ ^2B_1$-$\widetilde{A}\ ^2A_1$-$\widetilde{B}\ ^2B_2$-$\widetilde{C}\ ^2A_2$-$\widetilde{D}\ ^2A_1$-$\widetilde{E}\ ^2B_1$ electronic states of c-$C_2H_4O^{.+}$. Relative intensity (in arbitrary units) is plotted as a function of the energy of the vibronic states of c-$C_2H_4O^{.+}$. Available experimental spectrum reproduced from Refs. [47] and [86] are shown in panel (a) and (b), respectively. The present theoretical result is shown in panel (c).

carried out by propagating the WPs on the coupled electronic states using the Heidelberg MCTDH suite of program modules [139, 152]. The totally symmetric vibrational modes, ν_1-ν_5 and non-totally symmetric vibrational modes, ν_6-ν_{15} are included in these

calculations. That is, all fifteen DOFs are considered. Six WP calculations are conducted, with each initial excitation of the WP performed separately for each of the six electronic states. The specifics of the vibrational mode combinations and the sizes of the basis functions are outlined in Table B7 of Appendix B. In each calculation, the WP is propagated for a duration of 200 fs. The time autocorrelation function is damped using an exponential function with a relaxation time of 33 fs, after which it is Fourier transformed to obtain the spectrum. The results obtained from the calculations for the six electronic states are then combined with equal weightage to generate the composite theoretical bands. The results are shown in panel (c) of Fig. 4.5 along with the available two different experimental [47, 86] band structures shown in panels (a) and (b) of Fig. 4.5. It can be seen from the figure that the vibronic spectrum of the first and second bands originate solely from the $\widetilde{X}$ $^2B_1$ and $\widetilde{A}$ $^2A_1$ electronic states. The third band is very broad and structureless (cf., Fig. 4.5) and it originates from the strongly overlapping $\widetilde{B}$ $^2B_2$ and $\widetilde{C}$ $^2A_2$ electronic states. The energetic minimum of $\widetilde{B}$ $^2B_2$ and $\widetilde{C}$ $^2A_2$ states is quasi-degenerate (cf. Table 4.3), and have strong nonadiabatic coupling between them leads to this vibronic band structure. This is already discussed more elaborately in Sec. 4.4.2. The fourth band is formed by combination of $\widetilde{D}$ $^2A_1$ and $\widetilde{E}$ $^2B_1$ electronic states. The composite theoretical band structures (cf., Fig. 4.5 (c)) and the available experimental results are given in Fig. 4.5 (a and b). It can be seen from this figure that the theoretical results are in good accord with the available experimental findings [47, 86].

From this coupled-state dynamical calculations of the oxirane isomer we note that, the photoelectron band structures of both oxirane and acetaldehyde isomers of C_2H_4O are different. That is, in case of oxirane isomer the first and second bands are from by the $\widetilde{X}$ $^2B_1$ and $\widetilde{A}$ $^2A_1$ states separately (cf., Fig. 4.5). The remaining third and fourth bands are formed from the $\widetilde{B}$ $^2B_2$-$\widetilde{C}$ $^2A_2$ and $\widetilde{D}$ $^2A_1$-$\widetilde{E}$ $^2B_1$ states, respectively (cf., Fig. 4.5). In case of acetaldehyde isomer, first and last bands are well separated from the other bands and are formed from the solely $\widetilde{X}^2A^{'}$ and $\widetilde{F}^2A^{'}$ electronic states (cf., Fig. 4 of Ref. [98]). Interestingly, the $\widetilde{A}$ to $\widetilde{E}$ states are energetically close to each other in the latter isomer and all these states combinely forms the four vibronic bands (cf., Fig. 4 of Ref. [98]). Because these two isomers having different molecular arrangements and different molecular symmetry.

4.5 Coupled states diabatic electronic population dynamics

Time-dependent diabatic electronic populations of the $\widetilde{X}$ $^2B_1$, $\widetilde{A}$ $^2A_1$, $\widetilde{B}$ $^2B_2$, $\widetilde{C}$ $^2A_2$, $\widetilde{D}$ $^2A_1$ and $\widetilde{E}$ $^2B_1$ electronic states of c-$C_2H_4O^{\cdot+}$ in the coupled states dynamics are presented and discussed in this section. This is to understand and unravel the effect of vibronic coupling on the dynamics of a given state. Diabatic electronic populations of the $\widetilde{X}$ $^2B_1$, $\widetilde{A}$ $^2A_1$, $\widetilde{B}$ $^2B_2$, $\widetilde{C}$ $^2A_2$, $\widetilde{D}$ $^2A_1$ and $\widetilde{E}$ $^2B_1$ electronic states are shown in panels (a–f) of Fig. 4.6. Diabatic electronic population for an initial excitation of the WP to
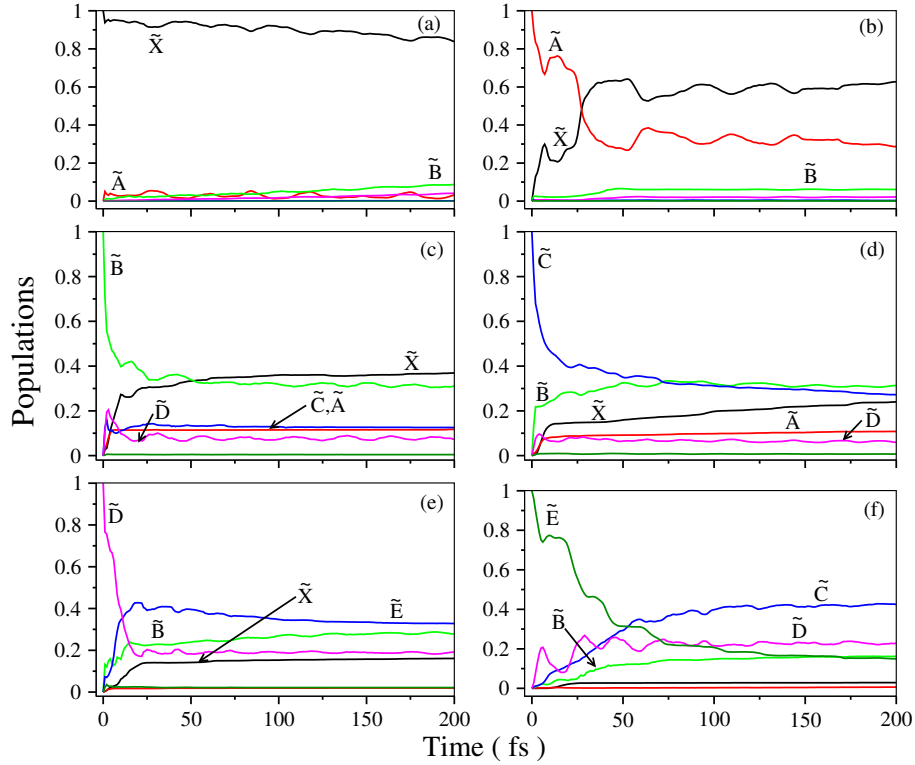
FIGURE 4.6: Time-dependence of diabatic electronic populations in the coupled $\widetilde{X}$ $^2B_1$-$\widetilde{A}$ $^2A_1$-$\widetilde{B}$ $^2B_2$-$\widetilde{C}$ $^2A_2$-$\widetilde{D}$ $^2A_1$-$\widetilde{E}$ $^2B_1$ state nuclear dynamics of c-$C_2H_4O^{\cdot+}$. The initial wave packet is located on each of the six electronic states separately and the population results are shown in panels (a) to (f).

the $\widetilde{X}$ $^2B_1$ state is shown in panel (a) of Fig. 4.6. It can be seen from this figure that, a very small amount of population flows to the other higher energy excited electronic states, this is due to the minimum of the seam of CI the $\widetilde{X}$ $^2B_1$ state with all other states are higher in energy and the WP can not access these states. At the same time, a quite large amount of population flows to the $\widetilde{X}$ $^2B_1$ state, when the WP is initially prepared on the $\widetilde{A}$ $^2A_1$ state (cf., panel (b) of Fig. 4.6). It can be seen that these population profiles that reveals strong vibronic coupling between $\widetilde{X}$ $^2B_1$ and $\widetilde{A}$ $^2A_1$ states. A decay rate of $\sim$41 fs is estimated from the $\widetilde{A}$ $^2A_1$ state population. The energetic minimum of the $\widetilde{X}$ $^2B_1$-$\widetilde{A}$ $^2A_1$ CIs occurs $\sim$0.7 eV and $\sim$0.09 eV above the minimum of the $\widetilde{X}$ $^2B_1$

and $\widetilde{A}\ ^2A_1$ states, respectively. Therefore, the location of the energetic minimum of the $\widetilde{A}\ ^2A_1$ state is relatively close to the minimum of the $\widetilde{X}\ ^2B_1$-$\widetilde{A}\ ^2A_1$ CIs and drives the population dynamics to the $\widetilde{X}\ ^2B_1$ state as shown in the panel (b) of Fig. 4.6.

It can be seen from the panels (c-f) of Fig. 4.6 that, the time-dependent diabatic electronic population of the $\widetilde{A}\ ^2A_1$, $\widetilde{B}\ ^2B_2$, $\widetilde{C}\ ^2A_2$, $\widetilde{D}\ ^2A_1$ and $\widetilde{E}\ ^2B_1$ electronic states of c-$C_2H_4O^{\cdot+}$ seems to be more interesting to understand the nonadiabatic dynamics in the current scenario. The population for an initial excitation of the WP to the $\widetilde{B}\ ^2B_2$ state is shown in Fig. 4.6 (c), and most of the population flows to the $\widetilde{X}\ ^2B_1$, $\widetilde{A}\ ^2A_1$, $\widetilde{C}\ ^2A_2$ and $\widetilde{D}\ ^2A_1$ states. This is due to the minimum of the $\widetilde{A}\ ^2A_1$-$\widetilde{B}\ ^2B_2$ CIs located ~1.74 eV, ~0.33 eV, above the minimum of the $\widetilde{A}\ ^2A_1$ and $\widetilde{B}\ ^2B_2$ states, respectively. The minimum of the $\widetilde{X}\ ^2B_1$-$\widetilde{B}\ ^2B_2$ CIs located ~2.58 eV above the minimum of the $\widetilde{X}\ ^2B_1$ state and ~0.58 eV above the minimum of the $\widetilde{B}\ ^2B_2$ state (cf., Table 4.4). The coupling between $\widetilde{X}\ ^2B_1$ state with $\widetilde{A}\ ^2A_1$, $\widetilde{B}\ ^2B_2$, $\widetilde{C}\ ^2A_2$ and $\widetilde{D}\ ^2A_1$ states is strong (cf., Table B4 of Appendix B). Because of the strong vibronic coupling, when the WP is initially prepared on the $\widetilde{B}\ ^2B_2$ state most of the population is transferred to the $\widetilde{X}\ ^2B_1$, $\widetilde{A}\ ^2A_1$, $\widetilde{C}\ ^2A_2$ and $\widetilde{D}\ ^2A_1$ electronic states. And there is a strong vibronic coupling between $\widetilde{X}\ ^2B_1$ and $\widetilde{B}\ ^2B_2$ states along the ν_{13} and ν_{14} ν_{15} modes of a_2 symmetry (cf., Table B4). So, the population flows to the $\widetilde{X}\ ^2B_1$ state slowly increases at longer time scale and the decay rate of $\widetilde{B}\ ^2B_2$ state is estimated to be ~6 fs.

When the WP is initially prepared on the $\widetilde{C}\ ^2A_2$ state and the corresponding population profile is shown in the Fig. 4.6 (d). In this case, the major portion of the population flows to the $\widetilde{B}\ ^2B_2$ state via the energetically low-lying $\widetilde{B}\ ^2B_2$-$\widetilde{C}\ ^2A_2$ CIs minimum. The minimum of the $\widetilde{B}\ ^2B_2$ and $\widetilde{C}\ ^2A_2$ CIs located ~1.22 eV and ~0.39 eV above the minimum of the $\widetilde{B}\ ^2B_2$ and $\widetilde{C}\ ^2A_2$ states, respectively (cf., Table 4.4). Also, there is a strong nonadiabatic coupling between the $\widetilde{B}\ ^2B_2$-$\widetilde{C}\ ^2A_2$ states along the ν_6, ν_7 and ν_8 vibrational modes of b_1 symmetry (cf., Table B4 of the Appendix B). However, the coupling between $\widetilde{X}\ ^2B_1$-$\widetilde{C}\ ^2A_2$, $\widetilde{A}\ ^2A_1$-$\widetilde{C}\ ^2A_2$ and $\widetilde{C}\ ^2A_2$-$\widetilde{D}\ ^2A_1$ states are also relatively strong enough (cf., Table B4 of the Appendix B) to drive the population to the $\widetilde{X}\ ^2B_1$, $\widetilde{A}\ ^2A_1$ and $\widetilde{D}\ ^2A_1$ states as well. A decay rate of ~12 fs is estimated from the $\widetilde{C}\ ^2A_2$-state population.

The population for an initial excitation of the WP to the $\widetilde{D}\ ^2A_1$ state is shown in Fig. 4.6 (e). Surprisingly in this case most of the population flows to the higher excited $\widetilde{E}\ ^2B_1$ state and the decay rate of ~11 fs for the $\widetilde{D}\ ^2A_1$ state. This is mainly because of the minimum of the $\widetilde{D}\ ^2A_1$-$\widetilde{E}\ ^2B_1$ CIs is located ~1.03 eV and ~0.05 eV above the minimum

of the $\widetilde{D}$ $^2A_1$ and $\widetilde{E}$ $^2B_1$ states, respectively (cf., Table 4.4). It can be seen from panel (e) of Fig. 4.6 that, in addition to the $\widetilde{E}$ $^2B_1$ state the population is transferred to the $\widetilde{B}$ $^2B_2$ and $\widetilde{X}$ $^2B_1$ electronic states. This is because of strong nonadiabatic coupling of $\widetilde{D}$ $^2A_1$-$\widetilde{E}$ $^2B_1$, $\widetilde{X}$ $^2B_1$-$\widetilde{D}$ $^2A_1$ and $\widetilde{B}$ $^2B_2$-$\widetilde{D}$ $^2A_1$ electronic states (cf., Table B4 of the Appendix B).

The electron population dynamics becomes more complex and involved when the WP is initially prepared on the $\widetilde{E}$ $^2B_1$ electronic state and it is shown in the panel (f) of Fig. 4.6. Most of the population flows to the $\widetilde{C}$ $^2A_2$ electronic state and a small amount of population is transferred to the $\widetilde{B}$ $^2B_2$ and $\widetilde{D}$ $^2A_1$ electronic states. This is because of strong vibronic coupling between $\widetilde{C}$ $^2A_2$-$\widetilde{D}$ $^2A_1$, $\widetilde{C}$ $^2A_2$-$\widetilde{E}$ $^2B_1$ and $\widetilde{D}$ $^2A_1$-$\widetilde{E}$ $^2B_1$ electronic states. Among these, $\widetilde{C}$ $^2A_2$-$\widetilde{D}$ $^2A_1$ coupling is relatively stronger than the $\widetilde{C}$ $^2A_2$-$\widetilde{E}$ $^2B_1$ and $\widetilde{D}$ $^2A_1$-$\widetilde{E}$ $^2B_1$ states (cf., Table B4 of Appendix B). So, due to this $\widetilde{C}$ $^2A_2$ state acquires more population. A decay rate of $\sim$54 fs is estimated from the decay of population of $\widetilde{E}$ $^2B_1$ state.

4.6 Summary

In summary, a detailed theoretical study of the vibronic coupling in the photo-ionization spectroscopy of c-C_2H_4O is discussed in this chapter. The multi-state multi-mode vibronic coupling in the first six energetically low-lying electronic states of this c-$C_2H_4O^{\cdot+}$ is considered in this study. We calculated the electronic PESs using the extensive *ab initio* quantum chemistry calculations with EOMIP-CCSD method. The PESs of the $\widetilde{X}$ $^2B_1$, $\widetilde{A}$ $^2A_1$, $\widetilde{B}$ $^2B_2$, $\widetilde{C}$ $^2A_2$, $\widetilde{D}$ $^2A_1$ and $\widetilde{E}$ $^2B_1$ electronic states of c-C_2H_4O radical cation are plotted along the dimensionless normal displacement coordinates. A vibronic model Hamiltonian of the coupled manifold of $\widetilde{X}$ $^2B_1$, $\widetilde{A}$ $^2A_1$, $\widetilde{B}$ $^2B_2$, $\widetilde{C}$ $^2A_2$, $\widetilde{D}$ $^2A_1$ and $\widetilde{E}$ $^2B_1$ electronic states is constructed in a diabatic electronic basis. The standard vibronic coupling theory and the elementary symmetry selection rules are used for this purpose. The nuclear dynamics calculations are treated with the developed Hamiltonian parameters using both time-independent matrix diagonalization and time-dependent WP propagation methods. To treat the nuclear dynamics in full dimension we have included all the fifteen $(5a_1 + 3b_1 + 4b_2 + 3a_2)$ vibrational modes. The vibronic band structures of $\widetilde{X}$ $^2B_1$, $\widetilde{A}$ $^2A_1$, $\widetilde{B}$ $^2B_2$, $\widetilde{C}$ $^2A_2$, $\widetilde{D}$ $^2A_1$ and $\widetilde{E}$ $^2B_1$ electronic states are discussed and assigned. Vibrational modes responsible for a particular band structure is identified. It is found that, the impact of nonadiabatic coupling between $\widetilde{X}$ $^2B_1$-$\widetilde{A}$ $^2A_1$, $\widetilde{B}$ $^2B_2$-$\widetilde{C}$ $^2A_2$ and $\widetilde{D}$ $^2A_1$-$\widetilde{E}$ $^2B_1$ states is stronger as compared to other possible electronic states combination. The decay rates of $\widetilde{X}$ $^2B_1$, $\widetilde{A}$ $^2A_1$, $\widetilde{B}$ $^2B_2$, $\widetilde{C}$ $^2A_2$, $\widetilde{D}$ $^2A_1$ and

$\widetilde{E}$ ^{2}B$_1$ states are also calculated. The $\widetilde{X}$ ^{2}B$_1$-$\widetilde{A}$ ^{2}A$_1$, $\widetilde{B}$ ^{2}B$_2$-$\widetilde{C}$ ^{2}A$_2$ and $\widetilde{D}$ ^{2}A$_1$-$\widetilde{E}$ ^{2}B$_1$ coupling has a significant effect on the vibronic structure of the second, third and fourth vibronic bands and are shown in the Fig. 4.5.

It is found that, $\widetilde{B}$ ^{2}B$_2$ and $\widetilde{C}$ ^{2}A$_2$ electronic states undergo the PJT effect along the b_1 symmetry vibrational mode. This leads to a symmetric double well potential topography and the minimum at a distorted geometry as compared to the FC geometry (at Q=0) of the adiabatic $\widetilde{B}$ ^{2}B$_2$ state. Among the three b_1 symmetry vibrational modes (ν_6, ν_7, ν_8), ν_7 mode has strong coupling between the $\widetilde{B}$ ^{2}B$_2$ and $\widetilde{C}$ ^{2}A$_2$ states, along ν_6 and ν_8 modes and coupling is moderate. Finally it is concluded that, $\widetilde{X}$ ^{2}B$_1$-$\widetilde{A}$ ^{2}A$_1$, $\widetilde{B}$ ^{2}B$_2$-$\widetilde{C}$ ^{2}A$_2$ and $\widetilde{D}$ ^{2}A$_1$-$\widetilde{E}$ ^{2}B$_1$ electronic states are energetically close, they have strong nonadiabatic coupling between them and all of these couplings played a major role in the nuclear dynamics. The calculated theoretical results are shown to be in good accord with the available experimental results. In addition to this, the interesting c-C$_2$H$_4$O results are compared with that of acetaldehyde isomer [98].

Chapter 5

Photoionization of Aziridine: Nonadiabatic Dynamics of the first six low-lying electronic states of the Aziridine radical cation

In this chapter, the nonadiabatic dynamics of the first six low-lying electronic states of the aziridine radical cation is investigated using the vibronic coupling theory. A brief introduction and the motivation behind this chapter is discussed in the following. Three-membered cyclic molecules are geometrically strained and the atoms present in these molecules show some interesting properties in molecular spectroscopy [93]. So the electronic and geometrical structural studies of strained molecules have lots of importance both in experimental as well as in theoretical studies. A large number of organic molecules are found in the Interstellar medium (ISM) [25]. The aziridine (CH_2NHCH_2), also called ethylene imine is a three-membered heterocycle having an amine group. The CH_2NHCH_2 is a feasible interstellar molecular candidate since it contains a number of small nitrogen compounds and epoxides have been discovered in the ISM [77] as well as in the atmosphere of Titan since many small nitrogen derivates are already found [94]. The CH_2NHCH_2 is of potential astronomical importance because it may be a constituent of so-called hot cores, star-forming areas with relatively large abundances of complex organic compounds [95, 96]. Myers *et al.* reported on the fruitless search for interstellar pyrrole in 1980 [97]. They assumed, in some ways, that because of their favorable partition characteristics, oxirane and aziridine were ideal candidates for astronomical detection. The structure of aziridine can be simply deduced by replacing the oxygen atom by NH in c-C_2H_4O ring. We put forward aziridine to be a promising candidate

for interstellar chemistry due to its abundant nitrogen and multi-faceted interstellar chemistry. Therefore, the study of photochemistry and photophysics of CH_2NHCH_2 has fundamental importance.

High-resolution photoelectron (PE) spectrum of CH_2NHCH_2 was recorded by Basch *et al.* [86] in 1969. The objective of their work was to comprehend the electronic structures and electronic spectra of small molecules. They employed computations of contracted Gaussian-type orbitals (GTO), gas-phase optical spectroscopy, and condensed-phase optical spectroscopy. In this study, the gaseous molecule was exposed to monochromatic light with an energy of 21.22 eV to obtain the PE spectrum. The ejected electrons kinetic energy was examined using the 1270 electron velocity analyzer described by Turner [180]. Rademacher *et al.* [181] utilized quantum mechanical calculations and ultraviolet He (I) photoelectron spectroscopy to examine the electronic structure of substituted aziridines. They analyzed the experimental data through *ab initio* calculations, performed with 3-21G and 6-31G* basis sets in GAUSSIAN 82. The initial vibrational mode studies of aziridine were conducted by Potts *et al.* [182] and Mitchell *et al.* [183]. Subsequently, Coulombeau *et al.* [184] recorded neutron inelastic scattering spectra, particularly identifying the A'' ring deformation at $820\ cm^{-1}$. Nagom *et al.* [185] recorded high-resolution Fourier transformation spectra of aziridine, reassigning all fundamental bands using experimental data and findings from *ab initio* calculations. Theoretical calculations on electronic structure, vertical ionization energies (VIEs), and infrared spectrum were also reported [186–189]. Bieri *et al.* [47] captured the CH_2NHCH_2 PE spectrum using He I and II ionization sources, attributing the four bands in the 8-18 eV energy range to the ionization of six valence molecular orbitals (MOs) of CH_2NHCH_2. However, the above-mentioned studies are done at a very preliminary level of computation, and there remains many aspects to explore on these to understand the photoelectron spectroscopy of CH_2NHCH_2 molecule. Also, multi-state and multi-mode dynamics of this molecule is still missing in the literature. So, we took up this problem trying to understand the microscopic details of the photoelectron spectrum of CH_2NHCH_2 molecule using vibronic coupling theory [167].

The main goal of our present work is to study the photoelectron spectrum of the CH_2NHCH_2 molecule using the vibronic coupling theory. Going beyond the BO- approximation, we develop the vibronic coupling model Hamiltonian for the six energetically low-lying electronic states (i.e., $\widetilde{X}\ ^2A'$, $\widetilde{A}\ ^2A'$, $\widetilde{B}\ ^2A''$, $\widetilde{C}\ ^2A''$, $\widetilde{D}\ ^2A'$, and $\widetilde{E}\ ^2A'$) of $CH_2NHCH_2^+$, to investigate nonadiabatic nuclear dynamics. The *ab initio* electronic structure calculations are performed using EOMIP-CCSD and MCQDPT methods in CFOUR [150][151] and GAMESS [116, 121–124] program packages, respectively. The

vibronic coupling model Hamiltonian is developed within a diabatic electronic basis. We employ a four-fold diabatization scheme for evaluating the model Hamiltonian parameters between the same symmetry electronic states. The diabatic electronic matrix is expanded in terms of dimensionless normal displacement coordinates and basic symmetry selection rules using a Taylor series expansion. Quantum dynamical calculations are performed using the MCTDH approach [130, 138, 152, 190], developed at Heidelberg university, in both time-independent and time-dependent frameworks. Finally, the calculated vibronic band structures are interpreted and analyzed. The results are in good accord with available experimental recordings [47].

5.1 Computational details

5.1.1 *Ab initio* calculations

The equilibrium geometry of the reference electronic ground state of CH_2NHCH_2 is optimized using the density functional theory (DFT) with Becke 3-parameter, Lee, Yang, and Parr (B3LYP) functionals employing the augmented correlation-consistent polarized valence triple zeta (aug-cc-pVTZ) basis set of Dunning [191], implemented in the Gaussian-09 program module [155]. The resulting optimized equilibrium geometry exhibits C_s point group symmetry, as depicted in Fig. 5.1, which includes atom numbering and atomic labels. The optimized equilibrium geometry parameters are presented in Ta-
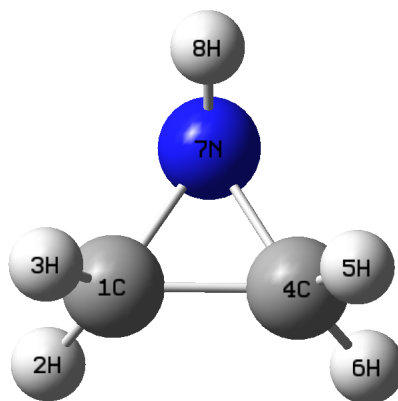
FIGURE 5.1: Schematic diagram of the optimized equilibrium ground electronic geometry of CH_2NHCH_2.

ble 5.1. Comparison with available experimental results and previous theoretical data from the literature demonstrates good agreement with our calculated theoretical geometry parameters [187, 192].

TABLE 5.1: The optimized equilibrium geometry parameters of the electronic ground state of CH_2NHCH_2 are presented, including the bond length (R) and bond angle ($\angle$) measured in Angstroms ($\widetilde{A}^2 A''$) and degrees (^{0}), respectively. Both theoretical data and experimental results reported in the literature are provided for comparison.

Parameters	This work	Theoretical[187]	Experimental [192]
R (C1-N7, C2-N7)	1.47	1.47	1.47
R (C1-C4)	1.48	1.48	1.48
R (C1-H3,C4-H5)	1.08	1.09	1.08
R (C1-H2,C4-H6)	1.08	1.08	1.08
R (N7-H)	1.01	1.02	1.01
$\angle$ (C1N7C4)	60.4	60.3	60.3
$\angle$ (H3C1N7, H5C4N7)	118.6	118.9	118.3
$\angle$ (H2C1N7, H6C4N7)	114.7	114.5	114.3
$\angle$ (H2C1C4, H6C4C1)	119.8	119.9	119.3
$\angle$ (H3C1C4, H5C4C1)	118	118	117.8
$\angle$ (H3C1H2, H5C4H6)	114.8	114.7	115.7
θ^a	69.6	67.4	67.5

[a] Angle between N-H bond and plane of the molecular ring.

The aziridine molecule is a three-membered heterocyclic ring with an amine group, having the molecular formula C_2H_4NH and comprising eighteen vibrational degrees of freedom (DOF). Harmonic vibrational frequencies (ω_i) of this molecule are calculated using the Gaussian-09 program module [155] at the same level of theory. The vibrational frequencies are transformed from mass-weighted normal displacement coordinates to dimensionless normal displacement coordinates Q_i by multiplying with $\sqrt{\omega_i/\hbar}$ (with $\hbar$ in atomic units). The harmonic vibrational frequencies of the eighteen modes, their symmetry, and mode designations are presented in Table 5.2, along with available literature data [182, 185, 185] for comparison. The data in Table 5.2 show good agreement between our calculated theoretical harmonic frequencies and the existing literature data [182, 185, 185].

The vertical ionization energies (VIEs) of the equilibrium geometry of the reference electronic ground state are computed using OVGF, EOMIP-CCSD, and MCQDPT methods employing the aug-cc-pVTZ basis set. The calculated VIEs are listed in Table 5.3, along with available theoretical and experimental results [47, 181, 193, 194]. Our theoretical VIEs reveal good agreement with the literature data [47, 181, 193, 194]. Table 5.3 also highlights that, at the Frank-Condon configuration, the energies of electronic states are in close agreement with the available literature data, and pairwise states exhibit the same symmetry. This suggests that vibronic coupling between these electronic states may play a significant role in driving the nuclear dynamics within these electronic states.

TABLE 5.2: The designation of vibrational modes, their harmonic frequencies (in cm^{-1}) and symmetry, of the ground electronic state of CH_2NHCH_2.

Symm.	modes	This work	Theory[185]	Expt.[182]	Expt.[185]	Assignment
	ν_1	3504.99	3514.1/3527.4	3338 $(3346)^b$	3337.4	$N-H$ str.
	ν_2	3194.2	3194.2/3231.2	3079	3079.6	CH_2 asymmetric-str.
	ν_3	3110.48	3108.1/3157.2	3015	3002.8	CH_2 symmetric-str.
	ν_4	1524.37	1526.7/1543.9	1481 $(1483)^b$	1482.9	CH_2 scissor.
A'	ν_5	1295.39	1294.4/1315	1210	1266.7	Ring str.
	ν_6	1237.25	1239.1/1253.3	1131 $(1096)^b$	1210.2	CH_2 twist.
	ν_7	1114.43	1116.6/1125.9	1090	1089.4	CH_2 wagging.
	ν_8	1006.29	1006/1018.6	998	997.1592	$N-H$ bending.
	ν_9	868.39	870.3/889.8	856	855.94	Ring deformation.
	ν_{10}	778.95	778.7/784.3	773	772.3571	CH_2 rocking.
	ν_{11}	3181.46	3180.9/3217.4	3079	3083.73	CH_2 asymmetric-str .
	ν_{12}	3105.61	3103.1/3148.8	3015 $(3003)^b$	3015.6	CH_2 symmetric-str.
	ν_{13}	1497.55	1499.8/1511.9	1462	1462.2	CH_2 scissor
A''	ν_{14}	1267.29	1237.4/1276.8	1268	1237	CH_2 twist
	ν_{15}	1154.98	1154.8/1165	1237	1130.4	$N-H$ bending
	ν_{16}	1123.46	1124.7/1123.4	1095 $(1131)^b$	1130.4	CH_2 wagging
	ν_{17}	918.56	919.4/920.5	904	904.0429	CH_2 rocking
	ν_{18}	851.94	857.3/865.8	817	-	Ring deformation

^{b} See reference [183]

TABLE 5.3: The VIEs (in eV) of the energetically lowest six electronic states of the $CH_2NHCH_2^+$ calculated at the reference equilibrium geometry of CH_2NHCH_2.

Electronic States	OVGF	EOMIP-CCSD	GAMESS(13,08)	Theory[193, 194]	Expt.[181]	Expt.[47]
$\widetilde{X}\ ^2A'$	9.961	9.83	9.14	9.68	9.84	9.86
$\widetilde{A}\ ^2A'$	12.249	12.26	11.52	12.05	11.94	11.9
$\widetilde{B}\ ^2A''$	12.450	12.43	12.10	12.22	12.72	12.7
$\widetilde{C}\ ^2A''$	13.648	13.63	13.21	13.37	13.53	13.6
$\widetilde{D}\ ^2A'$	16.136	16.21	15.39	15.87	15.90	16.0
$\widetilde{E}\ ^2A'$	17.635	17.69	16.84	17.49	17.35	17.5

The PESs of the first six low-lying electronic states ($\widetilde{X}\ ^2A'$, $\widetilde{A}\ ^2A'$, $\widetilde{B}\ ^2A''$, $\widetilde{C}\ ^2A''$, $\widetilde{D}\ ^2A'$, and $\widetilde{E}\ ^2A'$) of $CH_2NHCH_2^+$ are computed along the dimensionless normal displacement coordinates of the reference electronic ground state of CH_2NHCH_2. Diabatic and adiabatic energies are determined using the EOMIP-CCSD and MCQDPT methods with the aug-cc-pVTZ basis set, utilizing the CFOUR and GAMESS suite of programs, respectively. Additionally, VIEs are calculated along the dimensionless normal displacement coordinates of individual vibrational modes for nuclear geometries, ranging from $Q_i = \pm0.10, \pm0.25$ to ±5.0 with a spacing of 0.25.

5.1.2 Vibronic coupling model Hamiltonian

The vibronic coupling model Hamiltonian of the coupled $\widetilde{X}\,^2A'$, $\widetilde{A}\,^2A'$, $\widetilde{B}\,^2A''$, $\widetilde{C}\,^2A''$, $\widetilde{D}\,^2A'$, and $\widetilde{E}\,^2A'$ electronic states of $CH_2NHCH_2^+$ is developed here in a diabatic electronic basis following standard vibronic coupling theory [167]. Dimensionless normal displacement coordinates of vibrational modes, and elementary symmetry selection rules are employed in the construction [99]. The electronic reference geometry of CH_2NHCH_2 has C_s point group symmetry, and hence the electronic states of this molecule belongs to A' and A'' electronic terms. Irreducible representation (IRREP) of the eighteen vibrational modes of CH_2NHCH_2 reads as

$$\Gamma_{vib} = 10a' + 8a''. \tag{5.1}$$

Coupling between the states n and m by the vibrational mode Q is governed by the following selection rule

$$\Gamma_n \otimes \Gamma_Q \otimes \Gamma_m \supset \Gamma_A. \tag{5.2}$$

In the above equation Γ_n and Γ_m represents the IRREP of n and m electronic states, respectively, and Γ_Q represent the IRREP of the Qth vibrational mode. The Eq.(5.2) states that, the direct product of the above-mentioned IRREPs should transform into a totally symmetric representation which is shown as Γ_A. Therefore, the symmetry allowed coupling occur between the A' and A'' symmetry states with a'' vibrational modes $(A' \otimes a'' \otimes A'' \supset A')$.

The total Hamiltonian for the first six coupled $\widetilde{X}\,^2A'$, $\widetilde{A}\,^2A'$, $\widetilde{B}\,^2A''$, $\widetilde{C}\,^2A''$, $\widetilde{D}\,^2A'$ and $\widetilde{E}\,^2A'$ electronic states of $CH_2NHCH_2^+$ can be symbolically written as

$$\mathcal{H} = \mathcal{H}_0 \mathbf{1_6} + \Delta\mathcal{H} \tag{5.3}$$

In the above equation, $\mathcal{H}_0$ is the unperturbed Hamiltonian of the reference electronic ground state of the CH_2NHCH_2. Its elements within the harmonic approximation are given below

$$\mathcal{H}_0 = \mathcal{T}_N + \mathcal{V}_0 \tag{5.4}$$

where,

$$\mathcal{T}_N = -\frac{1}{2} \sum_{i \,\epsilon\, a',\, a''} \omega_i \frac{\partial^2}{\partial Q_i^2} \tag{5.5}$$

$$\mathcal{V}_0 = \frac{1}{2} \sum_{i \,\epsilon\, a',\, a''} \omega_i Q_i^2 \tag{5.6}$$

In the above Eq.(5.4), $\mathcal{T}_N$ and $\mathcal{V}_0$ represents the kinetic energy and potential energy of the reference CH_2NHCH_2 molecule, respectively. In Eq.(5.3), the quantity $\mathbf{1}_6$ represents a (6×6) diagonal unit matrix and the quantity $\Delta\mathcal{H}$ defines the change in electronic energy upon ionization from CH_2NHCH_2 to $CH_2NHCH_2^+$ electronic states. It can be defined in the following way

$$
\Delta\mathcal{H} = \begin{pmatrix}
E^{\widetilde{X}} + W^{\widetilde{X}} & W^{\widetilde{X}\widetilde{A}} & W^{\widetilde{X}\widetilde{B}} & W^{\widetilde{X}\widetilde{C}} & W^{\widetilde{X}\widetilde{D}} & W^{\widetilde{X}\widetilde{E}} \\
& E^{\widetilde{A}} + W^{\widetilde{A}} & W^{\widetilde{A}\widetilde{B}} & W^{\widetilde{A}\widetilde{C}} & W^{\widetilde{A}\widetilde{D}} & W^{\widetilde{A}\widetilde{E}} \\
& & E^{\widetilde{B}} + W^{\widetilde{B}} & W^{\widetilde{B}\widetilde{C}} & W^{\widetilde{B}\widetilde{D}} & W^{\widetilde{B}\widetilde{E}} \\
& & & E^{\widetilde{C}} + W^{\widetilde{C}} & W^{\widetilde{C}\widetilde{D}} & W^{\widetilde{C}\widetilde{E}} \\
& h.c. & & & E^{\widetilde{D}} + W^{\widetilde{D}} & W^{\widetilde{D}\widetilde{E}} \\
& & & & & E^{\widetilde{E}} + W^{\widetilde{E}}
\end{pmatrix} \quad (5.7)
$$

In the above matrix, the diagonal elements represent the diabatic electronic energies of $CH_2NHCH_2^+$, and the off-diagonal elements represent the coupling between the various excited electronic states. The quantity E^n defines the VIEs of the nth electronic state (where $n(m) = \widetilde{X}, \widetilde{A}, \widetilde{B}, \widetilde{C}, \widetilde{D}$, and $\widetilde{E}$). The elements of both W^n and W^{nm} are expanded in a Taylor series expansion around the equilibrium geometry of the reference electronic ground state at $Q = 0$ in the following way

$$
\begin{aligned}
W^n = \sum_{i\epsilon a'}\kappa_i^n Q_i + \frac{1}{2!}\sum_{i,j\epsilon a',a''}\gamma_{ij}^n Q_i^2 + \frac{1}{3!}\sum_{i\varepsilon a'}\eta_i^n Q_i^3 + \frac{1}{4!}\sum_{i\varepsilon a',a''}\delta_i^n Q_i^4 + \frac{1}{5!}\sum_{i\varepsilon a'}\alpha_i^n Q_i^5 \\
+ \frac{1}{6!}\sum_{i\varepsilon a',a''}\zeta_i^n Q_i^6 + \frac{1}{7!}\sum_{i\varepsilon a'}\beta_i^n Q_i^7 + \frac{1}{8!}\sum_{i\varepsilon a''}\mu_i^n Q_i^8 \; ; \quad n \in \widetilde{X} \text{ to } \widetilde{E},
\end{aligned} \quad (5.8)
$$

$$
W^{nm} = \sum_{i\epsilon a''}\lambda_i^{(1)} Q_i + \frac{1}{3!}\sum_{i\epsilon a''}\lambda_i^{(3)} Q_i^3 + \frac{1}{5!}\sum_{i\varepsilon a''}\lambda_i^{(5)} Q_i^5 + \frac{1}{7!}\sum_{i\varepsilon a''}\lambda_i^{(7)} Q_i^7 \; ; \quad n, m \in \widetilde{X} \text{ to } \widetilde{E}. \quad (5.9)
$$

In Eq.(5.8), the quantities κ_i^n, γ_{ij}^n, η_i^n, δ_i^n, α_i^n, ζ_i^n, β_i^n and μ_i^n are the linear, quadratic, cubic, quartic, fifth, sixth, seventh and eighth order intra-state coupling parameters, respectively, of the nth electronic state along the ith vibrational mode. In Eq.(5.9), the elements $\lambda_i^{(n)}$ defines the inter-state coupling parameters of nth-order.

In particular, for the electronic couplings between the states of same spatial symmetry (i.e., A' or A''), we used the fourfold-way diabatization scheme [116, 121–124] at the MCQDPT level of theory using the GAMESS suite of program. The fourfold-way produces smoothly varying diabatic molecular orbitals (DMOs). The transformation of the usual configuration state functions (CSFs) written in terms of canonical (adiabatic) MOs into orthogonal diabatic CSFs (CSFs written in terms of DMOs) is unique. That

is, we first obtained CASSCF DMOs, then the adiabatic MCQDPT wave functions were expressed in terms of the CASSCF DMOs and the latter are used for direct diabatization to obtain the energies of diabatic states and the couplings between them. The following equation is used to evaluate the inter-state couplings between the same spatial symmetry electronic states.

$$u^{nm} = u_0^{nm} + \sum_{i\epsilon a'} \lambda_i^{'(1)} Q_i + \frac{1}{2!}\sum_{i\epsilon a'} \lambda_i^{'(2)} Q_i^2 + \frac{1}{3!}\sum_{i\epsilon a'} \lambda_i^{'(3)} Q_i^3 \; ; \;\; n, m \in \widetilde{X} \text{ to } \widetilde{E}. \quad (5.10)$$

Where u_0^{nm} is a electronic couplings of the diabatic electronic states considered in the model and calculated at the ground state reference geometry ($\mathbf{Q}=0$). The u_0^{nm} is a constant at a distorted geometry for the $\widetilde{X}\,^2A'$-$\widetilde{A}\,^2A'$ ($\sim$ -0.027 eV), $\widetilde{X}\,^2A'$-$\widetilde{D}\,^2A'$ ($\sim$ -0.021 eV), $\widetilde{X}\,^2A'$-$\widetilde{E}\,^2A'$ ($\sim$ -0.013 eV), $\widetilde{A}\,^2A'$-$\widetilde{D}\,^2A'$ ($\sim$ -0.08 eV), $\widetilde{A}\,^2A'$-$\widetilde{E}\,^2A'$ ($\sim$ -0.032 eV), $\widetilde{B}\,^2A''$-$\widetilde{C}\,^2A''$ ($\sim$ -0.04 eV) and $\widetilde{D}\,^2A'$-$\widetilde{E}\,^2A'$ ($\sim$ -0.042 eV) coupled surfaces.

The Hamiltonian parameters of the Eqs. (5.8)-(5.9) are given in Tables 5.4-5.5 and C1-C6 of the Appendix C. The same spatial symmetry couplings are mentioned in Table C7 of Appendix C. The diagonal bilinear (γ_{ij} in Eq.(5.8) coupling parameters along the six totally symmetric (ν_4, ν_5, ν_6, ν_7, ν_9 and ν_{10}) vibrational modes are also calculated with the EOMIP-CCSD method. For this purpose, a two-dimensional fit of the *ab initio* calculated adiabatic electronic energies is carried out by using the Levenberg Marquardt algorithm [169]. The estimated diagonal bilinear coupling parameters are given in Table C8 of Appendix C.

5.2   Results and discussion

In this section, we present the results of our theoretical calculations. We begin with a comprehensive analysis of the PESs of the first six low-lying electronic states of $CH_2NHCH_2^+$. Subsequently, we focus into the vibronic band structures of the $\widetilde{X}\,^2A'$, $\widetilde{A}\,^2A'$, $\widetilde{B}\,^2A''$, $\widetilde{C}\,^2A''$, $\widetilde{D}\,^2A'$ and $\widetilde{E}\,^2A'$ electronic states, computed using the diabatic model Hamiltonian (cf., Eq. 5.3) developed in Sec. 5.1.2. These calculations are carried out both with and without electronic state couplings to gain deeper insights into nonadiabatic effects. Moreover, we analyze the decay rates of electronic states and internal conversion processes, examining the dynamics of coupled states and the time evolution of diabatic electronic populations. Finally, we discuss and compare our theoretical findings with available experimental results [47].

5.2.1 Potential energy surfaces

One-dimensional potential energy cuts of the $\widetilde{X}\ ^2A'$, $\widetilde{A}\ ^2A'$, $\widetilde{B}\ ^2A''$, $\widetilde{C}\ ^2A''$, $\widetilde{D}\ ^2A'$, and $\widetilde{E}\ ^2A'$ electronic states of the $CH_2NHCH_2^+$ are computed using both the EOMIP-CCSD and MCQDPT methods along the dimensionless normal displacement coordinates (Q) of the totally symmetric, a' vibrational modes ($\nu_1 - \nu_{10}$). These plots are presented in Figs. 5.2 and 5.3, respectively. Corresponding coupling parameters are provided in
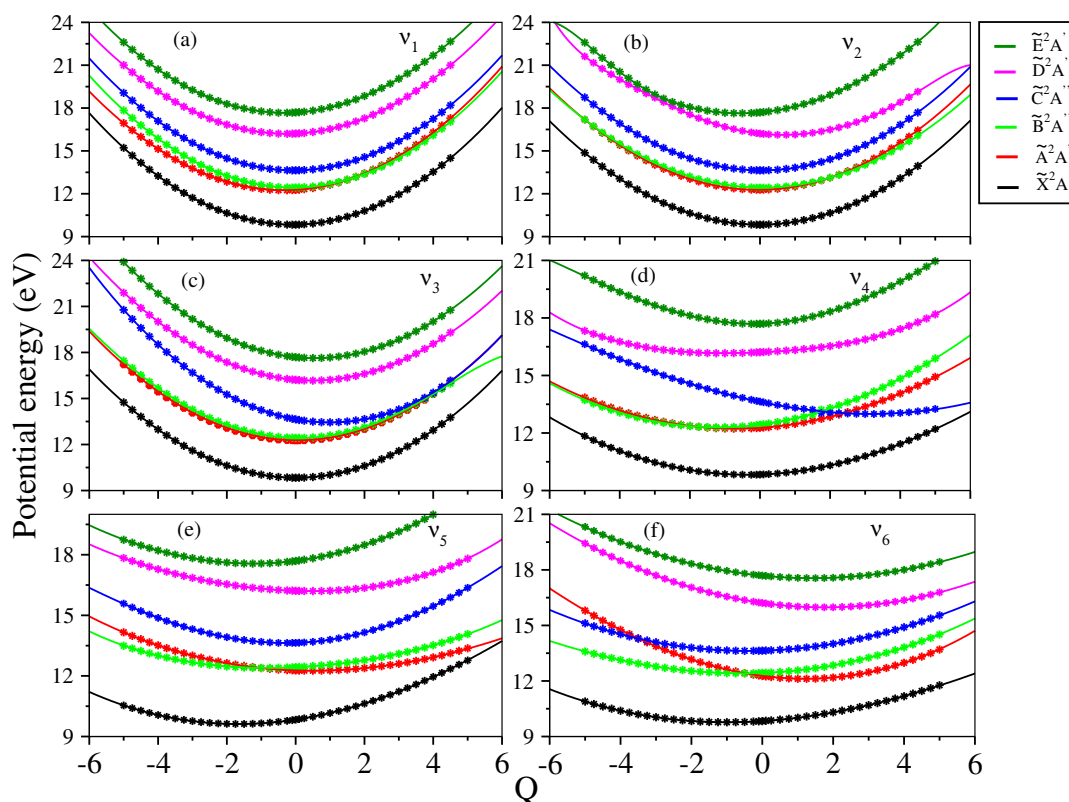
FIGURE 5.2: One-dimensional cuts of the multi-dimensional adiabatic PESs of six low-lying electronic states $\widetilde{X}\ ^2A'$, $\widetilde{A}\ ^2A'$, $\widetilde{B}\ ^2A''$, $\widetilde{C}\ ^2A''$, $\widetilde{D}\ ^2A'$, and $\widetilde{E}\ ^2A'$ are plotted along the dimensionless normal displacement coordinate of the totally symmetric a$'$ vibrational modes, $\nu_1 - \nu_{10}$, for the $CH_2NHCH_2^+$ ion. The asterisk points represent the *ab initio* calculated result using the EOMIP-CCSD method, while the solid lines depict the electronic energies obtained from the vibronic model.

Tables 5.4-5.5 and C1-C7 of Appendix C. For brevity, only the PESs (computed using the EOMIP-CCSD method) along the non-totally symmetric (a'') vibrational modes ($\nu_{13} - \nu_{15}$ and ν_{18}) are shown in Fig. 5.4. In each panel of Figs. 5.2-5.4, data points represent the *ab initio* electronic energies, while solid lines represent the Hamiltonian model defined in Section 5.1.2. These comparisons demonstrate the accuracy of our model Hamiltonian in reproducing the *ab initio* electronic structure data. Notably, we find that up to eighth- and seventh-order Taylor expansions of the electronic Hamiltonian along both a' and a'' vibrational modes are necessary to accurately represent the *ab initio* points.
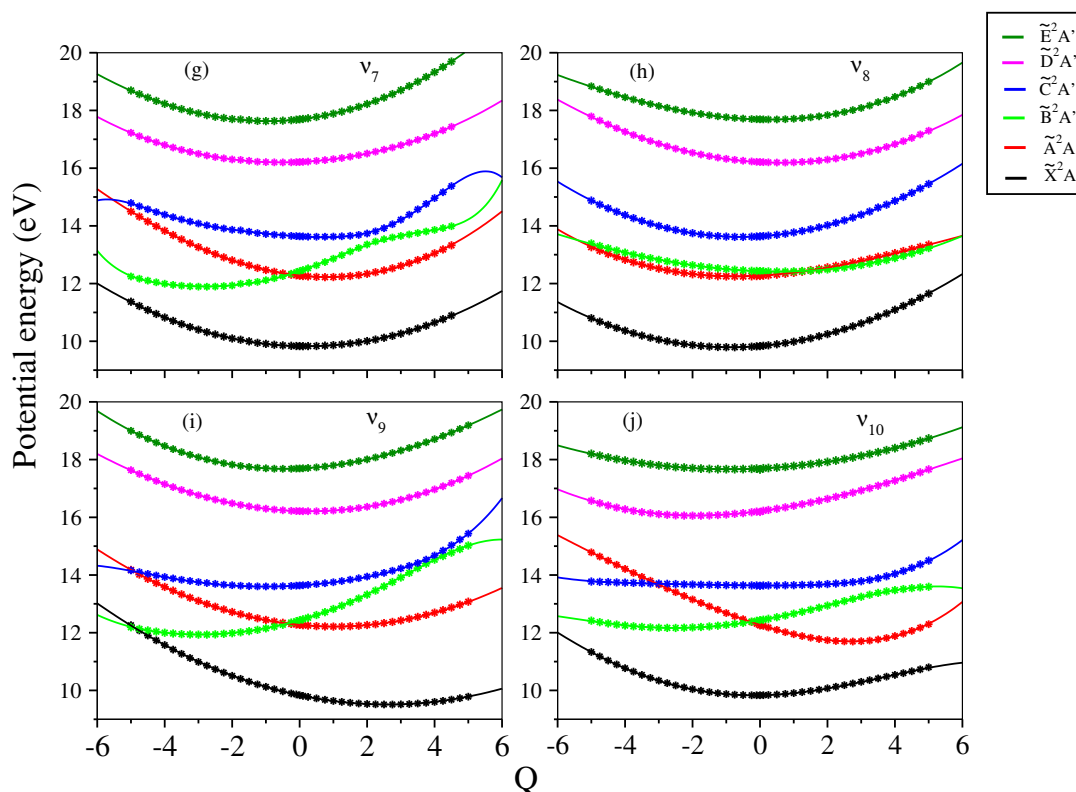
FIGURE 5.2: continued

The symmetric and asymmetric modes serve as tuning and coupling modes, respectively. Symmetric modes adjust the electronic energy minimum of $CH_2NHCH_2^+$ states relative to the equilibrium minimum of the electronic ground state of CH_2NHCH_2 (Q=0), thus modifying the vertical energy gap between electronic states. The electronic states, depicted in Figs. 5.2-5.4 and detailed in Table 5.3, demonstrate that the $\widetilde{X}\,^2A'$ state is slightly separated in energy from the other five excited electronic states. Conversely, the $\widetilde{A}\,^2A'$, $\widetilde{B}\,^2A''$ and $\widetilde{C}\,^2A''$ states exhibit close energetic proximity to each other (cf., Table 5.3). This proximity can result in multiple CIs in multi-dimensional space, as seen in Figs. 5.2 and 5.3 along the vibrational modes of ν_4, ν_6, ν_7, ν_9, and ν_{10}. At the Frank-Condon geometry, both $\widetilde{D}\,^2A'$ and $\widetilde{E}\,^2A'$ electronic states are well-separated, and these two states are energetically distant from their lower electronic states (cf., Table 5.3). However, $\widetilde{D}\,^2A'$ and $\widetilde{E}\,^2A'$ states intersect at longer distortion points along the ν_2, ν_4, and ν_5 vibrational modes (cf., Figs. 5.2 and 5.3). Using a second-order coupling model and parameters from Tables 5.2-5.5, the energies of various stationary points, including state minima and the energetic minimum of the seam of CIs, are calculated employing a minimization algorithm with Lagrange multipliers. MATHEMATICA software [170] is utilized for this purpose. The results are tabulated in a matrix array in Table 5.6, where diagonal entries correspond to specific electronic state minima, and off-diagonal entries indicate intersections with neighboring electronic states (i.e., minima of the intersection

seam).
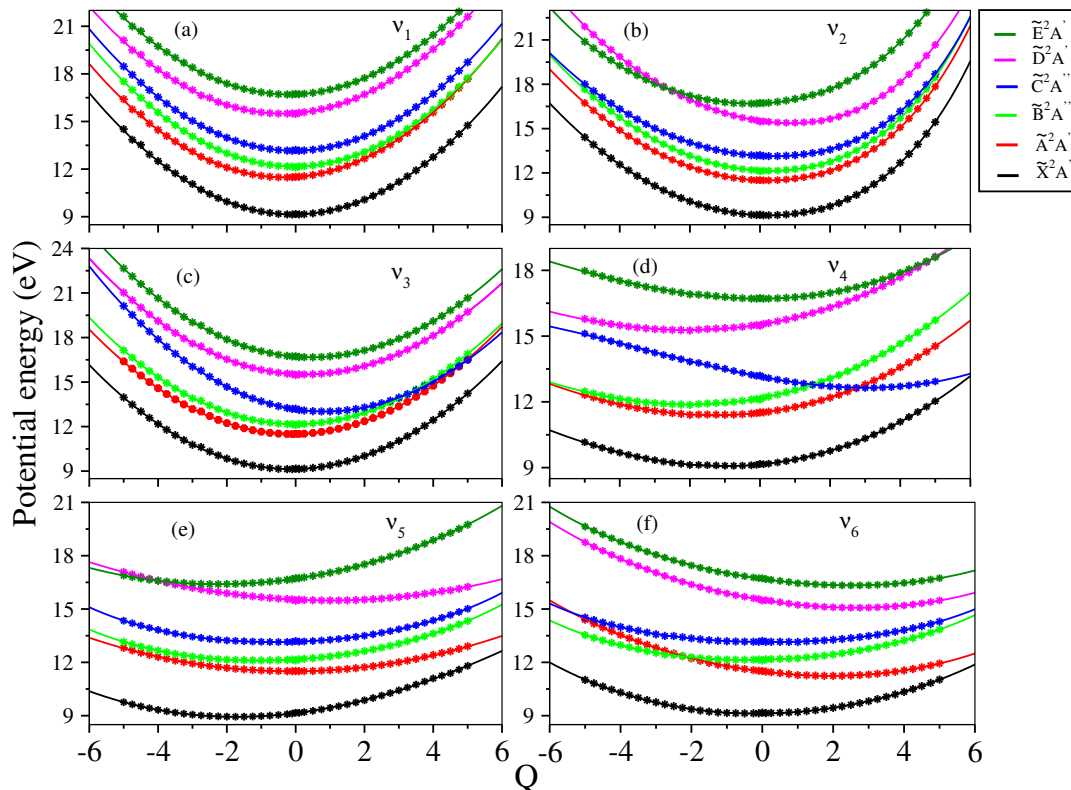
FIGURE 5.3: One-dimensional cuts of the multi-dimensional PESs of six low-lying electronic states $\widetilde{X}$ $^2A'$, $\widetilde{A}$ $^2A'$, $\widetilde{B}$ $^2A''$, $\widetilde{C}$ $^2A''$, $\widetilde{D}$ $^2A'$, and $\widetilde{E}$ $^2A'$ are plotted along the dimensionless normal displacement coordinate of the totally symmetric a$'$ vibrational modes, $\nu_1 - \nu_{10}$, for the $CH_2NHCH_2^+$ ion. The asterisk points represent the *ab initio* calculated result using the MCQDPT method, while the solid lines depict the electronic energies obtained from the vibronic model.

It can be seen from the Table 5.6 that, the minimum of the $\widetilde{X}$ $^2A'$ state is separated from all other excited electronic states (i.e., $\widetilde{A}$ $^2A'$-$\widetilde{E}$ $^2A'$). The intersection of the $\widetilde{X}$ $^2A'$ state with the latter states occur at high energies. Using the EOMIP-CCSD (MCQDPT) electronic structure data the $\widetilde{X}$ $^2A'$-$\widetilde{A}$ $^2A'$ intersection minimum is found at $\sim$11.10 eV (9.99 eV) and the minimum of the $\widetilde{A}$ $^2A'$ state appears at $\sim$11.10 eV (9.98 eV), and it is almost near degenerate with the $\widetilde{X}$ $^2A'$-$\widetilde{A}$ $^2A'$ intersection minimum (cf., Table 5.6). The $\widetilde{B}$ $^2A''$ state minimum is found at $\sim$10.79 eV (10.37 eV), with the EOMIP-CCSD electronic structure data this state energy is lower than the $\widetilde{A}$ $^2A'$ state minimum. This is due to at larger distortion points (away from the FC geometry) both $\widetilde{A}$ $^2A'$ and $\widetilde{B}$ $^2A''$ states minimum interchange, and also there is a strong vibronic coupling between them (cf., Table C5-C6 of Appendix C). On the other hand, in the case of MCQDPT electronic structure data and the corresponding static energies of $\widetilde{A}$ $^2A'$, $\widetilde{B}$ $^2A''$ and $\widetilde{C}$ $^2A''$ electronic excited states, we have discarded the ν_9 vibrational mode due to large negative γ value (it is greater than its corresponding frequency value). The energies of these three
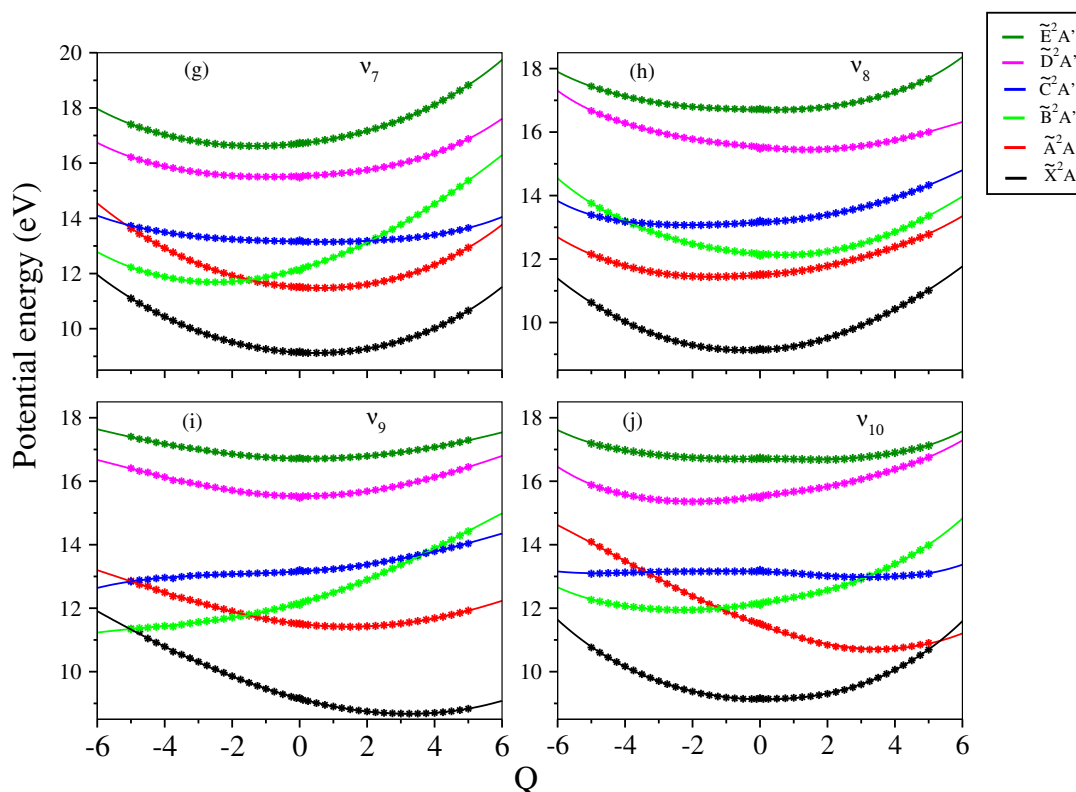
FIGURE 5.3: continued

states are in increasing order, which is inconsistent with the static energies derived from the EOMIP-CCSD data (cf., Table 5.6). However, the minimum energy values and their corresponding CI minimum points are close to each other in energy. The $\widetilde{D}\ ^2A'$ and $\widetilde{E}\ ^2A'$ electronic states exhibit well-separated minimum energies compared to the other electronic states. However, the intersection minimum between the $\widetilde{D}\ ^2A'$ and $\widetilde{E}\ ^2A'$ states is nearly degenerate with the minimum energy of the $\widetilde{E}\ ^2A'$ state (cf., Table 5.6). Additionally, the $\widetilde{A}\ ^2A'$-$\widetilde{B}\ ^2A''$-$\widetilde{C}\ ^2A''$ states demonstrate similar energy levels, with their intersection minima also closely situated. These observations indicate that these three states may significantly influence the nuclear dynamics.

The results presented above, along with the potential energy curves shown in Figs. 5.2 and 5.3, indicate that the $\widetilde{X}\ ^2A'$, $\widetilde{D}\ ^2A'$ and $\widetilde{E}\ ^2A'$ electronic states are energetically well separated from the other electronic states. Notably, the $\widetilde{A}\ ^2A'$, $\widetilde{B}\ ^2A''$ and $\widetilde{C}\ ^2A''$ electronic states exhibit close energy levels, with their respective equilibrium minima situated closer to various intersection minima (cf., Table 5.6). Moreover, these three states intersect each other, leading to the formation of several conical intersections in multidimensional space (cf., panels (d)-(j) of Figs. 5.2 and 5.3]. The low symmetry (C_s) point group of the CH_2NHCH_2 molecule results in the generation of low-lying electronic states with the same symmetry terms simultaneously (cf., Table 5.3). In the
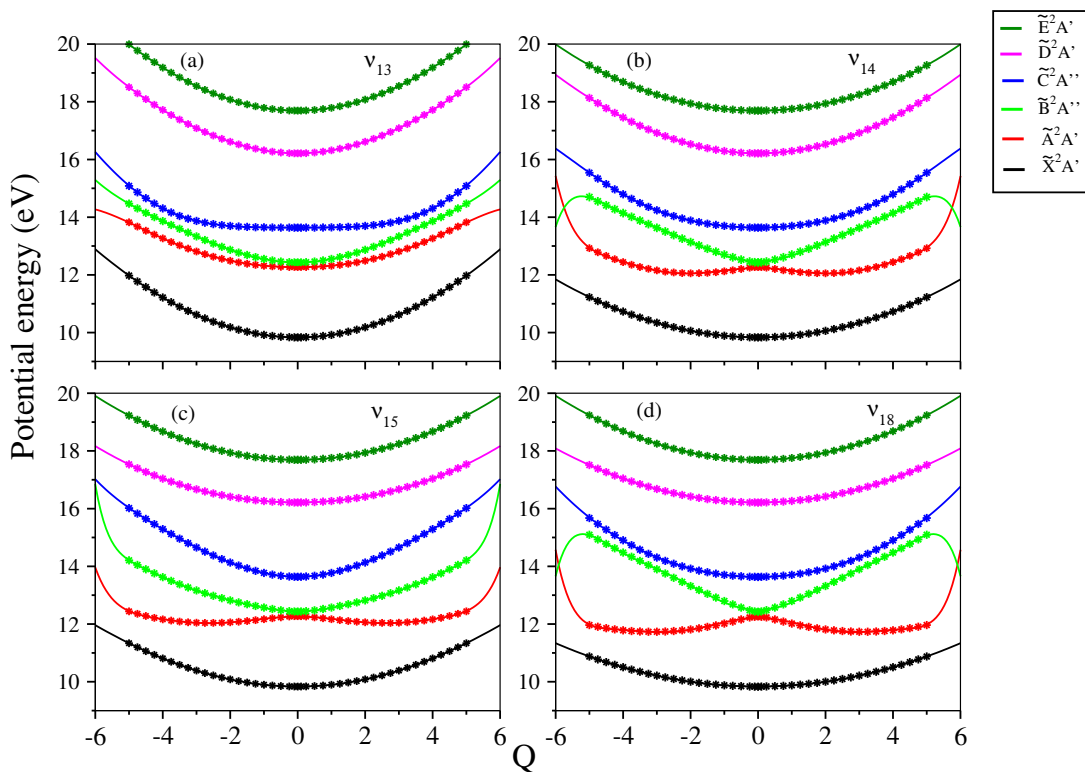
FIGURE 5.4: One-dimensional cuts of the multi-dimensional PESs of six low-lying electronic states $\widetilde{X}\ ^2A'$, $\widetilde{A}\ ^2A'$, $\widetilde{B}\ ^2A''$, $\widetilde{C}\ ^2A''$, $\widetilde{D}\ ^2A'$, and $\widetilde{E}\ ^2A'$ are plotted along the dimensionless normal displacement coordinate of the a'' vibrational modes, $\nu_{13} - \nu_{15}$, and ν_{18} for the $CH_2NHCH_2^+$ ion. The asterisk points represent the *ab initio* calculated result using the EOMIP-CCSD method, while the solid lines depict the electronic energies obtained from the vibronic model.

adiabatic picture, these states would typically avoid each other (cf., Fig. 5.2). Initially, we computed the PESs using the EOMIP-CCSD method and observed avoided crossings between electronic states with the same spatial symmetry (cf., Fig. 5.2). As detailed in Sec. 5.1.2, we employed a four-fold diabatization scheme to eliminate these avoided crossings among states with the same spatial symmetry. For this purpose, we utilized the MCQDPT level of theory within the GAMESS suite of programs. The resulting diabatic PESs are plotted along the dimensionless normal displacement coordinates of totally symmetric, a' vibrational modes (ν_1-ν_{10}) and are depicted in Fig. 5.3. Notably, these diabatized PESs effectively remove the avoided crossings observed in the adiabatic representation (cf., Fig. 5.2).

Based on the aforementioned findings and the potential energy curves presented in Figs. 5.2-5.4, it is evident that the $\widetilde{X}\ ^2A'$, $\widetilde{D}\ ^2A'$ and $\widetilde{E}\ ^2A'$ electronic states exhibit clear energetic separation from the other electronic states. Conversely, the $\widetilde{A}\ ^2A'$, $\widetilde{B}\ ^2A''$ and $\widetilde{C}\ ^2A''$ states demonstrate close energy levels, resulting in the formation of multiple CIs in higher-dimensional space. Additionally, the coupling between these states is notably

strong (cf., Tables C5-C6 of Appendix C). Furthermore, strong couplings are observed between states sharing the same spatial symmetry ($\widetilde{B}$ $^2A''$ and $\widetilde{C}$ $^2A''$) (cf., Table C7 of Appendix C). Moreover, one-dimensional adiabatic potential energy curves of the $\widetilde{X}$ $^2A'$ to $\widetilde{E}$ $^2A'$ states along the a'' symmetry vibrational modes are depicted. Notably, along the vibrational modes ν_{13}-ν_{15} and ν_{18}, the $\widetilde{A}$ $^2A'$, $\widetilde{B}$ $^2A''$ and $\widetilde{C}$ $^2A''$ electronic states exhibit strong repulsion, with the lower $\widetilde{A}$ $^2A'$ state forming double-minimum potentials at distorted geometries. This phenomenon is known as pseudo-Jahn-Teller type potentials [167, 178]. Therefore, nonadiabatic coupling among all these states is expected to play a significant role in the nuclear dynamics.

5.2.2 Vibronic structure of the CH$_2$NHCH$_2^+$

5.2.2.1 Uncoupled states calculations

In this section, we discuss the vibrational energy levels spectrum of $\widetilde{X}$ $^2A'$, $\widetilde{A}$ $^2A'$, $\widetilde{B}$ $^2A''$, $\widetilde{C}$ $^2A''$, $\widetilde{D}$ $^2A'$ and $\widetilde{E}$ $^2A'$ electronic states of CH$_2$NHCH$_2^+$, and are calculated using the matrix diagonalization method [167], which is implemented in the MCTDH [140, 152, 171, 172] program module. Here, we focus on the individual ($\widetilde{X}$ $^2A'$ to $\widetilde{E}$ $^2A'$) electronic state spectra without considering the interactions between them. These calculations are based on the strength of each a' vibrational mode coupling within a state and a diabatic vibronic model Hamiltonian (Eq. 5.3) constructed in Sec. 5.1.2. We used both EOMIP-CCSD and MCQDPT electronic structure data parameters for these calculations, and the associated results are presented in panels (a) and (b) of Fig. 5.5, respectively. The HO basis functions in each state used along each required (i.e., based on the couplling strength) mode are given in Table C9 of Appendix C. For each $\widetilde{X}$ $^2A'$, $\widetilde{A}$ $^2A'$, $\widetilde{B}$ $^2A''$, $\widetilde{C}$ $^2A''$, $\widetilde{D}$ $^2A'$ and $\widetilde{E}$ $^2A'$ electronic states, the Hamiltonian is diagonalized using 10,000 Lanczos iterations to generate the corresponding spectral bands and vibronic band structures (lines) they are shown in Fig. 5.5. Spectral envelopes in the Fig. 5.5 are created by convoluting the spectra with Lorentzian functions of 40 meV full width at the half maximum.

The energy eigenvalues of the uncoupled $\widetilde{X}$ $^2A'$, $\widetilde{A}$ $^2A'$, $\widetilde{B}$ $^2A''$, $\widetilde{C}$ $^2A''$, $\widetilde{D}$ $^2A'$ and $\widetilde{E}$ $^2A'$ electronic states are calculated using both EOMIP-CCSD and MCQDPT Hamiltonian parameters. The low-lying vibronic levels for each state, along with their assignments, are provided in Tables C10 and C11 of Appendix C. Peak assignments are determined by analyzing the nodal patterns of the wave functions, calculated using a block-improved relaxation method, and it is implemented in MCTDH program modules [140, 152, 171, 172]. The results presented in Tables C10 and C11 of Appendix C illustrate that the excitation of fundamental a' vibrational modes (ν_1–ν_{10}) depends

TABLE 5.4: The linear (κ_i) and quadratic (α_i) coupling parameters for the $\widetilde{X}\ ^2A'$, $\widetilde{A}\ ^2A'$, $\widetilde{B}\ ^2A''$, $\widetilde{C}\ ^2A''$, $\widetilde{D}\ ^2A'$, and $\widetilde{E}\ ^2A'$ electronic states of the $CH_2NHCH_2^+$ are calculated using the EOMIP-CCSD method. All values are provided in eV, with dimensionless Poisson parameters $\left(\kappa_i{}^2/2\omega_i{}^2\right)$ given in parentheses.

Symm.	Modes	$\widetilde{X}\ ^2A'$		$\widetilde{A}\ ^2A'$		$\widetilde{B}\ ^2A''$	
		κ_i	γ_i	κ_i	γ_i	κ_i	γ_i
a'	ν_1	0.0412 (0.0045)	0.0096	0.1447 (0.0554)	-0.0036	0.0332 (0.0029)	0.0087
	ν_2	0.0042 (0.00006)	0.0080	0.0223 (0.0016)	0.0064	-0.0225 (0.0016)	-0.0258
	ν_3	-0.0047 (0.00007)	0.0047	-0.0179 (0.0011)	0.0018	-0.0430 (0.0062)	-0.0010
	ν_4	0.0642 (0.0577)	-0.0109	0.1194 (0.1995)	-0.0203	0.2320 (0.7534)	0.0004
	ν_5	0.2556 (1.2663)	-0.0144	-0.0595 (0.0686)	-0.0421	0.0797 (0.1231)	-0.0647
	ν_6	0.1220 (0.3162)	-0.0342	-0.2497 (1.3248)	0.0454	0.0728 (0.1126)	-0.0237
	ν_7	-0.0230 (0.0138)	-0.0247	-0.1238 (0.4014)	0.0067	0.4019 (4.2303)	-0.0149
	ν_8	0.0978 (0.3072)	-0.0132	0.0648 (0.1349)	-0.0420	-0.0395 (0.0501)	-0.0552
	ν_9	-0.2462 (2.6145)	-0.0129	-0.1114 (0.5353)	0.0006	0.3341 (4.8146)	0.0131
	ν_{10}	0.0190 (0.0193)	0.0150	-0.3713 (7.3904)	-0.0087	0.2079 (2.3170)	-0.0267
a''	ν_{11}	-	0.0060	-	-0.0302	-	0.0365
	ν_{12}	-	0.0028	-	-0.0297	-	0.0179
	ν_{13}	-	-0.0103	-	-0.0792	-	0.0519
	ν_{14}	-	-0.0456	-	-0.3453	-	0.2805
	ν_{15}	-	-0.0182	-	-0.3057	-	0.1151
	ν_{16}	-	0.0068	-	-0.0467	-	0.0273
	ν_{17}	-	-0.0236	-	-0.0790	-	0.0385
	ν_{18}	-	-0.0222	-	-0.4310	-	0.4482

Symm.	Modes	$\widetilde{C}\ ^2A''$		$\widetilde{D}\ ^2A'$		$\widetilde{E}\ ^2A'$	
		κ_i	γ_i	κ_i	γ_i	κ_i	γ_i
a'	ν_1	0.0213 (0.0012)	0.0067	0.1123 (0.0334)	-0.0096	0.1428 (0.0540)	0.0034
	ν_2	-0.0161 (0.0008)	0.0087	-0.2673 (0.2277)	0.0271	0.2175 (0.1507)	-0.0167
	ν_3	-0.4089 (0.5621)	0.0189	-0.1821 (0.1115)	-0.0025	-0.2259 (0.1716)	0.0193
	ν_4	-0.3783 (2.0032)	-0.0854	0.0786 (0.0865)	-0.1078	0.0494 (0.0341)	0.0751
	ν_5	0.0567 (0.0623)	0.0377	-0.0519 (0.0522)	-0.0448	0.2151 (0.8968)	0.0143
	ν_6	0.0541 (0.0621)	-0.0182	-0.2685 (1.5318)	-0.0019	-0.1888 (0.7574)	-0.0191
	ν_7	-0.0781 (0.1597)	-0.0743	0.0507 (0.0673)	-0.0441	0.1287 (0.4338)	-0.0022
	ν_8	0.0705 (0.1596)	-0.0024	-0.0622 (0.1243)	-0.0189	-0.0269 (0.0232)	-0.0273
	ν_9	0.0741 (0.2368)	-0.0397	-0.0316 (0.0431)	-0.0020	0.0503 (0.1091)	0.0045
	ν_{10}	-0.0139 (0.0103)	-0.0819	0.1526 (1.2483)	-0.0248	0.0555 (0.1651)	-0.0347
a''	ν_{11}	-	-0.0438	-	0.0374	-	-0.0085
	ν_{12}	-	-0.0207	-	0.0348	-	0.0225
	ν_{13}	-	-0.1821	-	0.0189	-	0.0066
	ν_{14}	-	-0.0443	-	0.0015	-	-0.0353
	ν_{15}	-	0.1179	-	-0.0441	-	-0.0205
	ν_{16}	-	-0.0980	-	-0.0253	-	-0.0598
	ν_{17}	-	-0.0478	-	-0.0407	-	-0.0407
	ν_{18}	-	0.0386	-	-0.0022	-	0.0188

TABLE 5.5: The linear (κ_i) and quadratic (α_i) coupling parameters for the $\widetilde{X}\ ^2A'$, $\widetilde{A}\ ^2A'$, $\widetilde{B}\ ^2A''$, $\widetilde{C}\ ^2A''$, $\widetilde{D}\ ^2A'$, and $\widetilde{E}\ ^2A'$ electronic states of the $CH_2NHCH_2^+$ are calculated using the MCQDPT method. All values are provided in eV, with dimensionless Poisson parameters $\left(\kappa_i^2/2\omega_i^2\right)$ given in parentheses.

Symm.	Modes	$\widetilde{X}\ ^2A'$ κ_i	γ_i	$\widetilde{A}\ ^2A'$ κ_i	γ_i	$\widetilde{B}\ ^2A''$ κ_i	γ_i
a'	ν_1	0.0305 (0.0025)	0.0015	0.1428 (0.0540)	0.0052	0.0209 (0.0011)	0.0025
	ν_2	-0.1019 (0.0331)	-0.0125	-0.0922 (0.0271)	-0.0121	-0.1230 (0.0482)	0.0007
	ν_3	0.0477 (0.0076)	0.0104	0.0328 (0.0036)	0.0108	-0.0014 (0.000006)	0.0036
	ν_4	0.1501 (0.3154)	-0.0334	0.1859 (0.4837)	-0.0354	0.2910 (1.1853)	-0.0344
	ν_5	0.2394 (1.1109)	-0.0293	0.0116 (0.0026)	-0.0528	0.1211 (0.2843)	-0.0467
	ν_6	0.0201 (0.0086)	-0.0093	-0.2482 (1.3089)	-0.0272	0.0409 (0.0355)	-0.0454
	ν_7	-0.0643 (0.1083)	-0.0099	-0.0823 (0.1774)	-0.0053	0.3617 (3.4263)	-0.0090
	ν_8	0.0606 (0.1180)	0.0108	0.0874 (0.2454)	-0.0608	-0.0697 (0.1560)	-0.0212
	ν_9	-0.2813 (3.4131)	-0.0329	-0.1195 (0.6159)	-0.0305	0.2984 (3.8406)	-0.0498
	ν_{10}	-0.0193 (0.0200)	0.0125	-0.3931 (8.2837)	-0.0165	0.1526 (1.2483)	-0.0378
a''	ν_{11}	-	0.0161	-	-0.0128	-	0.0390
	ν_{12}	-	0.0088	-	-0.0181	-	0.0220
	ν_{13}	-	-0.0195	-	-0.0725	-	0.0489
	ν_{14}	-	-0.0576	-	-0.2610	-	0.2381
	ν_{15}	-	-0.0370	-	-0.2817	-	0.0712
	ν_{16}	-	-0.0079	-	-0.0554	-	0.0057
	ν_{17}	-	-0.0293	-	-0.0749	-	0.0318
	ν_{18}	-	0.0049	-	-0.4073	-	0.4210

Symm.	Modes	$\widetilde{C}\ ^2A''$ κ_i	γ_i	$\widetilde{D}\ ^2A'$ κ_i	γ_i	$\widetilde{E}\ ^2A'$ κ_i	γ_i
a'	ν_1	0.0226 (0.0013)	0.0007	0.1668 (0.0737)	-0.0112	0.0840 (0.0187)	-0.0116
	ν_2	-0.1383 (0.0609)	-0.0665	-0.3607 (0.4146)	-0.0118	0.0770 (0.0189)	-0.0292
	ν_3	-0.3463 (0.4032)	0.0259	-0.1119 (0.0421)	0.0024	-0.1834 (0.1131)	0.0091
	ν_4	-0.2990 (1.2514)	-0.1216	0.2514 (0.8847)	-0.0558	0.0039 (0.0002)	-0.0640
	ν_5	0.0668 (0.0865)	-0.0567	-0.0884 (0.1515)	-0.0691	0.2773 (1.4905)	-0.0359
	ν_6	-0.0167 (0.0059)	-0.0736	-0.3233 (2.2209)	-0.0340	-0.2781 (1.6433)	-0.0461
	ν_7	-0.0169 (0.0075)	-0.1139	0.0488 (0.0624)	-0.0773	0.1270 (0.4224)	-0.0398
	ν_8	0.0718 (0.1656)	-0.0860	-0.0887 (0.2527)	-0.0712	-0.0029 (0.0003)	-0.0783
	ν_9	0.0703 (0.2132)	-0.0750	-0.0078 (0.0026)	-0.0262	-0.0153 (0.0101)	-0.0546
	ν_{10}	-0.0408 (0.0892)	-0.1232	0.1240 (0.8242)	-0.0539	-0.0148 (0.0117)	-0.0854
a''	ν_{11}	-	-0.0289	-	0.0294	-	0.0126
	ν_{12}	-	-0.0028	-	0.0595	-	0.0189
	ν_{13}	-	-0.2015	-	0.0225	-	-0.0053
	ν_{14}	-	-0.0416	-	-0.0147	-	-0.0457
	ν_{15}	-	0.1295	-	-0.0501	-	-0.0271
	ν_{16}	-	-0.1023	-	-0.0398	-	-0.0686
	ν_{17}	-	-0.0493	-	-0.0467	-	-0.0501
	ν_{18}	-	0.0617	-	-0.0170	-	-0.0073

on the excitation strength within each $\widetilde{X}\ ^2A'$, $\widetilde{A}\ ^2A'$, $\widetilde{B}\ ^2A''$, $\widetilde{C}\ ^2A''$, $\widetilde{D}\ ^2A'$ and $\widetilde{E}\ ^2A'$ electronic state of $CH_2NHCH_2^+$. Additionally, the excitation of several overtones and combinations of energy levels is observed. Specifically, in the initial $\widetilde{X}\ ^2A'$ electronic state of $CH_2NHCH_2^+$ spectral bands are formed in Fig. 5.5, around $\sim$1288 cm^{-1}, $\sim$1127 cm^{-1} and $\sim$815 cm^{-1} ($\sim$1341 cm^{-1}, $\sim$1174 cm^{-1} and $\sim$820 cm^{-1}) due to the excitation of ν_5, ν_6 and ν_9 (ν_4, ν_5 and ν_9) vibrational modes, respectively, with the EOMIP-CCSD (MCQDPT) methods. Weak excitation of vibrational modes ν_1 and ν_2 (ν_1 and ν_6) in the $\widetilde{X}\ ^2A'$ state is also observed, as indicated in Table 5.4 (5.5).

TABLE 5.6: The diagonal elements of the following table represent the minimum equilibrium energy (in eV) of each electronic state, while the off-diagonal elements represent the minimum energy (in eV) of the intersection seam formed with its neighboring electronic state of the $CH_2NHCH_2^+$. These energies are calculated within the Second-order coupling model and using the adiabatic (diabatic) electronic energies determined via the EOMIP-CCSD(MCQDPT) method.

	$\widetilde{X}\ ^2A'$	$\widetilde{A}\ ^2A'$	$\widetilde{B}\ ^2A''$	$\widetilde{C}\ ^2A''$	$\widetilde{D}\ ^2A'$	$\widetilde{E}\ ^2A'$
$\widetilde{X}\ ^2A'$	9.16 (8.27)	11.10 (9.99)	10.91 (10.53)	12.63 (12.20)	17.80 (14.60)	25.90 (16.89)
$\widetilde{A}\ ^2A'$	-	11.10 (9.98)	12.05 (11.32)	12.69 (12.37)	16.03 (14.24)	18.69 (16.38)
$\widetilde{B}\ ^2A''$	-	-	10.79 (10.37)	12.82 (12.41)	16.81 (14.56)	22.19 (16.33)
$\widetilde{C}\ ^2A''$	-	-	-	12.60 (12.20)	17.57 (14.36)	33.43 (19.29)
$\widetilde{D}\ ^2A'$	-	-	-	-	15.58 (14.18)	17.58 (16.03)
$\widetilde{E}\ ^2A'$	-	-	-	-	-	17.17 (16.02)

Due to the close energy levels of the $\widetilde{A}\ ^2A'$, $\widetilde{B}\ ^2A''$, and $\widetilde{C}\ ^2A''$ electronic states (cf., Tables 5.3 and 5.6), the second, third, and fourth vibronic bands in $CH_2NHCH_2^+$ exhibit strong overlap. In Fig. 5.5, it is evident that the vibronic levels of $\widetilde{A}\ ^2A'$, $\widetilde{B}\ ^2A''$, and $\widetilde{C}\ ^2A''$ states intertwine, with the low-lying vibronic levels of $\widetilde{A}\ ^2A'$ and $\widetilde{B}\ ^2A''$ combining with the higher levels of $\widetilde{C}\ ^2A''$. The primary excitation in the vibronic band structure of the $\widetilde{A}\ ^2A'$ state arises from the ν_6, ν_9, ν_{10} vibrational modes in both methods (cf., Tables C10 and C11). The peak spacings are approximately $\sim$1450 cm^{-1}, $\sim$871 cm^{-1} and $\sim$1098 cm^{-1} ($\sim$1161 cm^{-1}, $\sim$758 cm^{-1} and $\sim$948 cm^{-1}) in the respective order. In the case of the $\widetilde{B}\ ^2A''$ state, ν_7, ν_9 and ν_{10} vibrational modes contribute to an extended progression in both the EOMIP-CCSD and MCQDPT methods, with line spacings of $\sim$1048 cm^{-1}, $\sim$900 cm^{-1} and $\sim$720 cm^{-1} ($\sim$1203 cm^{-1}, $\sim$504 cm^{-1} and $\sim$698 cm^{-1}), respectively. Similarly, the emergence of the $\widetilde{C}\ ^2A''$ state vibronic band is associated with the ν_4, ν_7 and ν_9 (ν_3, ν_4 and ν_8) vibrational modes, with line widths of $\sim$1289 cm^{-1}, $\sim$1035 cm^{-1} and $\sim$721 cm^{-1} ($\sim$3199 cm^{-1}, $\sim$1252 cm^{-1} and $\sim$600 cm^{-1}), respectively.
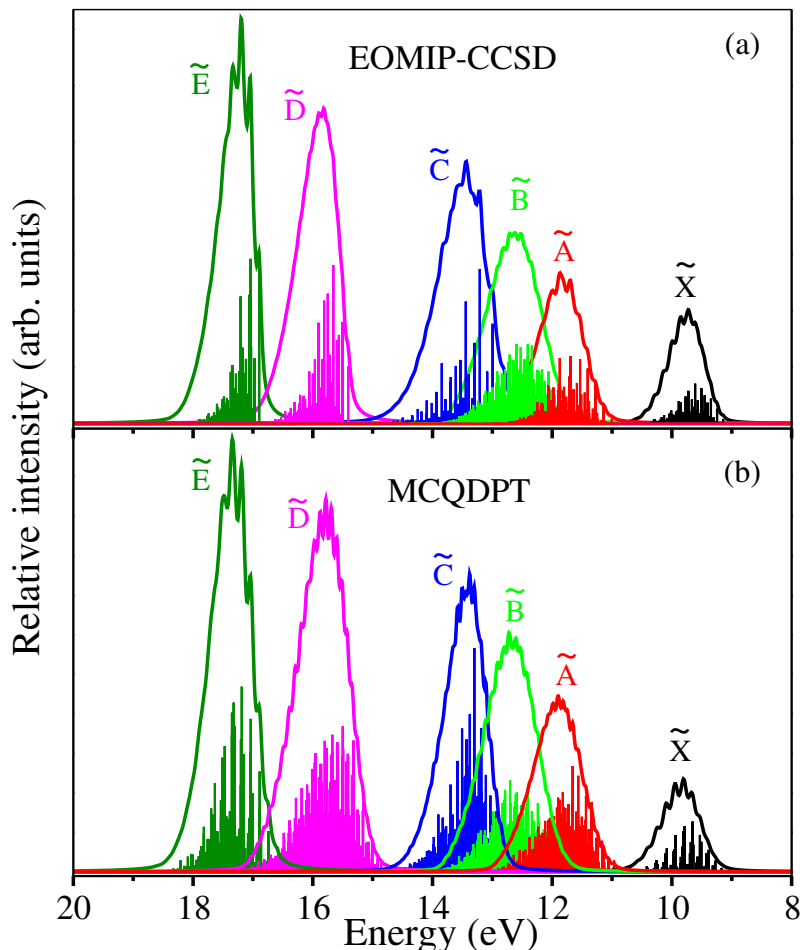
FIGURE 5.5: The photoionization bands of the $\widetilde{X}\ ^2A'$, $\widetilde{A}\ ^2A'$, $\widetilde{B}\ ^2A''$, $\widetilde{C}\ ^2A''$, $\widetilde{D}\ ^2A'$, and $\widetilde{E}\ ^2A'$ states of the CH_2NHCH_2 are calculated using the a' vibrational modes and the time-independent matrix diagonalization method (details provided in the text). The relative intensity is plotted as a function of the energy of the vibronic levels.

The fifth and sixth vibronic bands arise from the $\widetilde{D}\ ^2A'$ and $\widetilde{E}\ ^2A'$ electronic states of the $CH_2NHCH_2^+$. In Fig. 5.5, it's evident that the vibronic band structures of the $\widetilde{D}\ ^2A'$ and $\widetilde{E}\ ^2A'$ states are slightly separated in energy from each other and also distinctly separated from the other bands (of $\widetilde{X}\ ^2A'$, $\widetilde{A}\ ^2A'$, $\widetilde{B}\ ^2A''$, and $\widetilde{C}\ ^2A''$), as shown in Fig. 5.5. The fifth vibronic band, attributed to the $\widetilde{D}\ ^2A'$ state, predominantly originates (contributes) from the ν_6, ν_8, ν_{10}, and v_4, ν_6, ν_{10} vibrational modes of both EOMIP-CCSD and MCQDPT methods, respectively. The peaks corresponding to these modes are approximately $\sim 1080\ cm^{-1}$, $\sim 1236\ cm^{-1}$, and $\sim 756\ cm^{-1}$ ($\sim 1152\ cm^{-1}$, $\sim 771\ cm^{-1}$, and $\sim 722\ cm^{-1}$) in energy, respectively. The sixth vibronic band is attributed to the $\widetilde{E}\ ^2A'$ electronic states of $CH_2NHCH_2^+$, with the dominant excitation of ν_5, ν_6, and ν_7 vibrational modes in both the EOMIP-CCSD and MCQDPT methods. The corresponding peaks for these modes are spaced at approximately $\sim 1339\ cm^{-1}$, $\sim 1157\ cm^{-1}$, and $\sim 1094\ cm^{-1}$ ($\sim 1166\ cm^{-1}$, $\sim 1127\ cm^{-1}$, and $\sim 974\ cm^{-1}$) in energy, respectively. Tables C10 and C11 of Appendix C provide further details, indicating that in addition to the

fundamental vibrational progressions discussed above, overtones and numerous combination levels are also excited in the $\widetilde{X}\ ^2A'$, $\widetilde{A}\ ^2A'$, $\widetilde{B}\ ^2A''$, $\widetilde{C}\ ^2A''$, $\widetilde{D}\ ^2A'$, and $\widetilde{E}\ ^2A'$ bands.

The nodal patterns of the vibrational wave functions are further investigated to validate their excitation in the spectrum. These patterns are computed using a block improved-relaxation method implemented in the MCTDH program module [140, 152, 171, 172]. In Figs. C1 and C2 (a-i) of Appendix C, a couple of $\widetilde{X}\ ^2A'$ state vibrational eigenfunctions are displayed. In these figures, the probability density of the wave function is represented using appropriate dimensionless normal displacement coordinates. The results obtained from EOMIP-CCSD are shown in Fig. C1 panels (a–c), depicting the wave functions corresponding to the fundamental modes of ν_5, ν_6, and ν_9, respectively. The MCQDPT data results shown in Fig. C2 panels (a–c) of Appendix C display the fundamental wave functions of ν_4, ν_5, and ν_9. These figures demonstrate that the wave function acquires a node along the relevant normal coordinate. The wave functions for the initial overtone peaks of the excited vibrational modes (with two nodes along the respective modes) are shown in panels (d–f). Additionally, some of the combination peaks are depicted in Figs. C1 and C2 (g–i) of Appendix C. The vibrational wave functions for the other states ($\widetilde{A}\ ^2A'$, $\widetilde{B}\ ^2A''$, $\widetilde{C}\ ^2A''$, $\widetilde{D}\ ^2A'$, and $\widetilde{E}\ ^2A'$) are similarly displayed in Figs. C3-C12 of Appendix C, utilizing both the EOMIP-CCSD and MCQDPT methods.

5.2.2.2 Coupled two-states dynamics

In this section, various coupled two-states calculations are carried out to assess the influence of nonadiabatic coupling on the vibronic structure of individual states. The coupling between $\widetilde{X}\ ^2A'$-$\widetilde{A}\ ^2A'$, $\widetilde{A}\ ^2A'$-$\widetilde{B}\ ^2A''$, $\widetilde{B}\ ^2A''$-$\widetilde{C}\ ^2A''$, $\widetilde{C}\ ^2A''$-$\widetilde{D}\ ^2A'$, and $\widetilde{D}\ ^2A'$-$\widetilde{E}\ ^2A'$ states significantly impacts their vibronic structures. Despite the relatively substantial coupling between the $\widetilde{X}\ ^2A'$ state and the $\widetilde{A}\ ^2A'$, $\widetilde{B}\ ^2A''$, $\widetilde{C}\ ^2A''$, $\widetilde{D}\ ^2A'$, and $\widetilde{E}\ ^2A'$ electronic states, the spectrum of the $\widetilde{X}\ ^2A'$ state remains unaffected in the coupled states scenario (cf., Figs. C13-C14 (a) of Appendix C). This is primarily because the $\widetilde{X}\ ^2A'$ state is mostly isolated from the other electronic states, except for the $\widetilde{A}\ ^2A'$ state (cf., Table 5.3). Compared to the equilibrium minimum, the minimum energy of the intersection seam with them is higher in enrgy (cf., Table 5.6). Consequently, the WP generated on the $\widetilde{X}\ ^2A'$ state fails to reach the $\widetilde{X}\ ^2A'$-$\widetilde{A}\ ^2A'$ crossing seam, resulting in only modest electronic population migration to the $\widetilde{A}\ ^2A'$ state (cf., Figs. C15 and C16 (a) of Appendix C). The minimum energy of the intersection seam experiences approximately $\sim$1.94 ($\sim$1.72) eV and $\sim$0.00 ($\sim$0.01) eV higher than the minimum of the $\widetilde{X}\ ^2A'$ and $\widetilde{A}\ ^2A'$ states, respectively (cf., Table 5.6). The energies given in the with and without paranthesis are from the both MCQDPT and EOMIP-CCSD *ab initio* data in

the throughout the text. A significant portion of the population is transferred to the $\widetilde{X}$ $^2A'$ state when the WP is initially prepared on the $\widetilde{A}$ $^2A'$ state, as the minimum of the $\widetilde{A}$ $^2A'$ state is closer to the $\widetilde{X}$ $^2A'$-$\widetilde{A}$ $^2A'$ intersection seam (cf., Table 5.6). Approximately $\sim$70% of the population is transferred to the $\widetilde{A}$ $^2A'$ state within about $\sim$25 fs. Due to this a significant amount of population is transferred to the $\widetilde{X}$ $^2A'$ state, the vibronic spectrum of the $\widetilde{A}$ $^2A'$ state becomes broad and structureless due to a considerable increase in spectral line density (cf., Figs. C13-C14 (b) of Appendix C).

In the case of the $\widetilde{A}$ $^2A'$-$\widetilde{B}$ $^2A''$ and $\widetilde{B}$ $^2A''$-$\widetilde{C}$ $^2A''$ ($\widetilde{A}$ $^2A'$-$\widetilde{B}$ $^2A''$-$\widetilde{C}$ $^2A''$) coupled two-states, the equilibrium minimum energies of these states are close in energy compared to other electronic states (cf., Table 5.3). Additionally, the coupling between these ($\widetilde{A}$ $^2A'$-$\widetilde{B}$ $^2A''$-$\widetilde{C}$ $^2A''$) states is quite strong (cf., Tables C5-C7 of Appendix C). When the WP is initially prepared on the $\widetilde{A}$ $^2A'$ state, in the $\widetilde{A}$ $^2A'$-$\widetilde{B}$ $^2A''$ coupled states scenario, only a minimal amount of population migrates to the $\widetilde{B}$ $^2A''$ state (cf., Figs. C15 and C16 (c) of Appendix C). This is due to the fact that the minimum energy of the $\widetilde{A}$ $^2A'$-$\widetilde{B}$ $^2A''$ intersection seam occur at approximately $\sim$0.95 ($\sim$1.34) eV and $\sim$1.26 ($\sim$0.95) eV above the minima of the $\widetilde{A}$ $^2A'$ and $\widetilde{B}$ $^2A''$ electronic states, respectively (cf., Table 5.6). The band structure of the $\widetilde{A}$ $^2A'$ state in the $\widetilde{A}$ $^2A'$-$\widetilde{B}$ $^2A''$ coupled states scenario is depicted in Figs. C13-C14 (c) of Appendix C. However, despite the significant nonadiabatic interaction between the $\widetilde{A}$ $^2A'$-$\widetilde{B}$ $^2A''$ states (cf., Tables C5-C6 of Appendix C), it affects the electronic population dynamics (cf., Figs. C15 and C16 (d) of Appendix C) and the vibronic band structure of the $\widetilde{B}$ $^2A''$ state (cf., Figs. C13-C14 (d) of Appendix C). When the WP is initially prepared on the $\widetilde{B}$ $^2A''$ state, approximately $\sim$60% of the population is transferred to the $\widetilde{A}$ $^2A'$ state within about $\sim$20 fs (cf., Figs. C15 and C16 (d) of Appendix C).

In the $\widetilde{B}$ $^2A''$-$\widetilde{C}$ $^2A''$ coupled states case, the minimum energies of these two states are little far apart from each other (cf., Table 5.6). However, the coupling between them is moderate (cf., Table C7 of Appendix C), resulting in a broad spectrum band for these states (cf., Figs. C13-C14 (e) and (f) of Appendix C). When WP is initially generated on the $\widetilde{B}$ $^2A''$ state, approximately $\sim$20% of the population is transferred to the $\widetilde{C}$ $^2A''$ state within about $\sim$3 fs (cf., Figs. C15 and C16 (e) of Appendix C). Conversely, a large portion of the population (approximately $\sim$70%) is transferred to the $\widetilde{B}$ $^2A''$ state within the same timeframe when the WP is initially prepared on the $\widetilde{C}$ $^2A''$ state (cf., Figs. C15 and C16 (f) of Appendix C).

In the coupled $\widetilde{C}\,^2A''$-$\widetilde{D}\,^2A'$ and $\widetilde{D}\,^2A'$-$\widetilde{E}\,^2A'$ states, the population dynamics are influenced by the strength of coupling and the energy separation between the states. The coupling between the $\widetilde{C}\,^2A''$-$\widetilde{D}\,^2A'$ states is strong along the ν_{13}, ν_{14}, and ν_{15} vibrational modes (cf., Tables C5-C6 of Appendix C). However, due to the larger minimum energy separation between these states, when the WP is initially prepared on the $\widetilde{C}\,^2A''$ state, there is minimal population transfer to the $\widetilde{D}\,^2A'$ state (cf., Figs. C15 and C16 (g) of Appendix C). Conversely, when the WP is generated on the $\widetilde{D}\,^2A'$ state, a substantial portion of the population (approximately $\sim$90%) is transferred to the $\widetilde{C}\,^2A''$ state within about $\sim$15 fs (cf., Figs. C15 and C16 (h) of Appendix C). Regarding the $\widetilde{D}\,^2A'$-$\widetilde{E}\,^2A'$ coupled states situation, these two states are having the same symmetry terms, and the coupling between them is minimal (cf., Tables C7 of Appendix C). However, they are slightly close in energy at the FC geometry (cf., Table 5.3), which affects the vibronic band structure of the $\widetilde{D}\,^2A'$-$\widetilde{E}\,^2A'$ coupled states spectrum (cf., Figs. C13-C14 (g) and (h) of Appendix C). When the WP is initially prepared on the $\widetilde{D}\,^2A'$ state, only approximately $\sim$10% of the population is transferred to the $\widetilde{E}\,^2A'$ electronic state. Conversely, when the WP is initially prepared on the $\widetilde{E}\,^2A'$ state, approximately $\sim$50% of the population flows to the $\widetilde{D}\,^2A'$ state within a timescale of about $\sim$20 fs and these states populations are almost constant (cf., Figs. C15 and C16 (i) and (j) of Appendix C) at the longer times.

5.2.2.3 Coupled $\widetilde{X}\,^2A'$-$\widetilde{E}\,^2A'$ states dynamics and photoelectron spectrum of CH$_2$NHCH$_2$

The dynamical calculations for the coupled six-electronic states ($\widetilde{X}\,^2A'$-$\widetilde{A}\,^2A'$-$\widetilde{B}\,^2A''$-$\widetilde{C}\,^2A''$-$\widetilde{D}\,^2A'$-$\widetilde{E}\,^2A'$), inclusive of eighteen vibrational DOFs (ten with a' symmetry, ν_1-ν_{10}, and eight with a'' symmetry, ν_{11}-ν_{18}), were conducted using the model Hamiltonian (Eq. 5.3) as described in Sec. 5.1.2. The MCTDH program module [139, 152] is used for this purpose using the both EOMIP-CCSD and MCQDPT methods *ab initio* electronic structure data, for the determination of Hamiltonian parameters in the coupled state spectrum calculations. The analysis focused on calculating and examining the vibronic structure of the CH$_2$NHCH$_2$ photoelectron band. The TDSE was solved for the intended purpose, where the initial WP was independently generated for each of the six electronic states. Details regarding the combinations of vibrational modes and dimensions (sizes) of the basis functions can be found in Table C12 of Appendix C. In each electronic state calculation, the WP was propagated up to 200 fs. The photoionization band for all six electronic states ($\widetilde{X}\,^2A'$, $\widetilde{A}\,^2A'$, $\widetilde{B}\,^2A''$, $\widetilde{C}\,^2A''$, $\widetilde{D}\,^2A'$, and $\widetilde{E}\,^2A'$) was generated via Fourier transformation of the time autocorrelation function, $C(t)$, using a dephasing time of 33 fs. The composite theoretical band was created by

combining the results of six electronic states with equal weighting. The coupled state spectrum obtained from both EOMIP-CCSD and MCQDPT methods are illustrated in panels (b) and (c) of Fig. 5.6, respectively, with comparisons made to the experimental spectrum of Bieri *et al.*[47] (cf., Fig. 5.6(a)). The vibronic spectrum of $CH_2NHCH_2^+$ (cf., Fig. 5.6) reveals that the first band originates from the $\widetilde{X}\ ^2A'$ electronic state, while the second, third, and fourth bands are formed collectively by $\widetilde{A}\ ^2A'$, $\widetilde{B}\ ^2A''$, and $\widetilde{C}\ ^2A''$ electronic states, owing to their proximity in energy as indicated in Tables 5.3 and moderate coupling between them (cf., Tables C5-C7 of Appendix C). The remaining $\widetilde{D}\ ^2A'$ and $\widetilde{E}\ ^2A'$ electronic states, being relatively close in energy, contribute to the last two vibrionic bands (fifth and sixth). These computational findings, as depicted in Fig. 5.6, demonstrate good agreement between our computed photoelectron spectrum and the available experimental results.
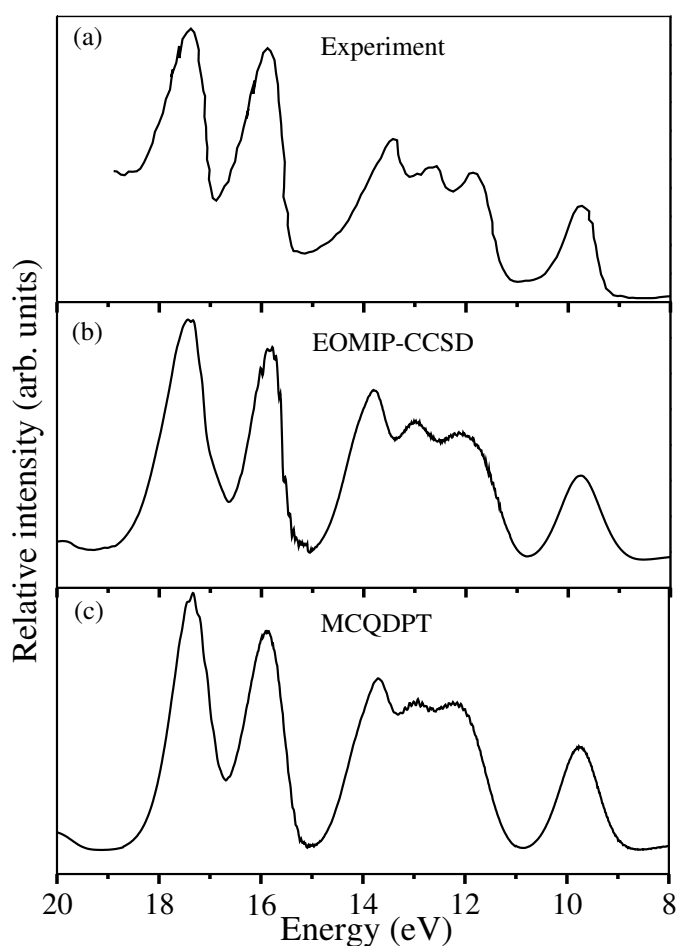
FIGURE 5.6: A comparison between the experimental [47] photo-ionization spectrum of the CH_2NHCH_2, shown in panel (a), and the theoretical spectra depicted in panels (b) and (c). The theoretical spectrum is obtained using six ($\widetilde{X}\ ^2A'$-$\widetilde{A}\ ^2A'$-$\widetilde{B}\ ^2A''$-$\widetilde{C}\ ^2A''$-$\widetilde{D}\ ^2A'$-$\widetilde{E}\ ^2A'$) coupled electronic states and eighteen vibrational modes, calculated by propagating wave packets using the MCTDH program modules (details provided in the text).

Additionally, we also calculated the spectral bands by incorporating bilinear coupling parameters (cf., Tables C8 of Appendix C) of both EOMIP-CCSD and MCQDPT methods. The resulting spectrum is illustrated in Fig. C17 of Appendix C. In panel (b), we present the results from the EOMIP-CCSD method, while in panel (c), those from the MCQDPT method are depicted. Output results are compared with an experiment in panel (a). From this figure, it is evident that the inclusion of bilinear coupling parameters does not significantly alter the photoelectron spectrum of CH_2NHCH_2.

5.3 Diabatic electronic population

To gain further insights into the photophysical characteristics of CH_2NHCH_2, we examined the time-dependent evolution of diabatic electronic populations of the coupled six electronic states ($\widetilde{X}\ ^2A'$-$\widetilde{E}\ ^2A'$) of $CH_2NHCH_2^+$. The results obtained using both the EOMIP-CCSD and MCQDPT methods are illustrated in panels (a-f) of Figs. 5.7 and 5.8, respectively. The $\widetilde{X}\ ^2A'$, $\widetilde{A}\ ^2A'$, $\widetilde{B}\ ^2A''$, $\widetilde{C}\ ^2A''$, $\widetilde{D}\ ^2A'$, and $\widetilde{E}\ ^2A'$ states population evolution is represented by distinct color lines (in online). In panel (a), it is observed that upon initially placing the WP on the $\widetilde{X}\ ^2A'$ state, approximately $\sim30\%$ of the population transitions to the $\widetilde{A}\ ^2A'$ electronic state. The reason for this is the strong nonadiabatic coupling between the $\widetilde{X}\ ^2A'$ and $\widetilde{A}\ ^2A'$ states (cf., Table C7 of Appendix C). A small fraction of the population also disperses to other excited states (cf., Figs. 5.7 and 5.8 (a)) due to the coupling of $\widetilde{X}\ ^2A'$ state with other excited states. The decay rate for the $\widetilde{X}\ ^2A'$ state is approximately ~29 fs (~23 fs). In contrast, a significant portion of the population transfers to the $\widetilde{X}\ ^2A'$ state when the WP is initially localized on the $\widetilde{A}\ ^2A'$ state (cf., panel (b) of Figs. 5.7 and 5.8). Analyzing the population curve of the $\widetilde{A}\ ^2A'$ state reveals an estimated decay rate of approximately ~32 fs (~61 fs). The proximity of the $\widetilde{A}\ ^2A'$ state minimum to the $\widetilde{X}\ ^2A'$-$\widetilde{A}\ ^2A'$ intersection seam further contributes to this behavior (cf., Table 5.6). Additionally, moderate coupling between the $\widetilde{X}\ ^2A'$ and $\widetilde{A}\ ^2A'$ states, particularly through the vibrational modes of a' symmetry, with strong coupling along the ν_6 vibrational mode (cf., Table C7 of Appendix C), enhances this phenomenon.

In the diabatic electronic populations of the $\widetilde{B}\ ^2A''$ state depicted in panel (c) of Figs. 5.7 and 5.8, it is evident that approximately $\sim40\%$ of the population transitions to the $\widetilde{X}\ ^2A'$ state, while approximately $\sim20\%$ and $\sim10\%$ of the population transfer to the $\widetilde{A}\ ^2A'$ and $\widetilde{B}\ ^2A''$ states, respectively, with a rapid decay rate of around ~20 fs. This phenomenon arises due to the strong coupling between the $\widetilde{X}\ ^2A'$-$\widetilde{B}\ ^2A''$ and $\widetilde{A}\ ^2A'$-$\widetilde{B}\ ^2A''$ states in the EOMIP-CCSD method (cf., Table C6). Conversely, in the case of the MCQDPT method, a different scenario unfolds, where around $\sim40\%$ of the population transfers
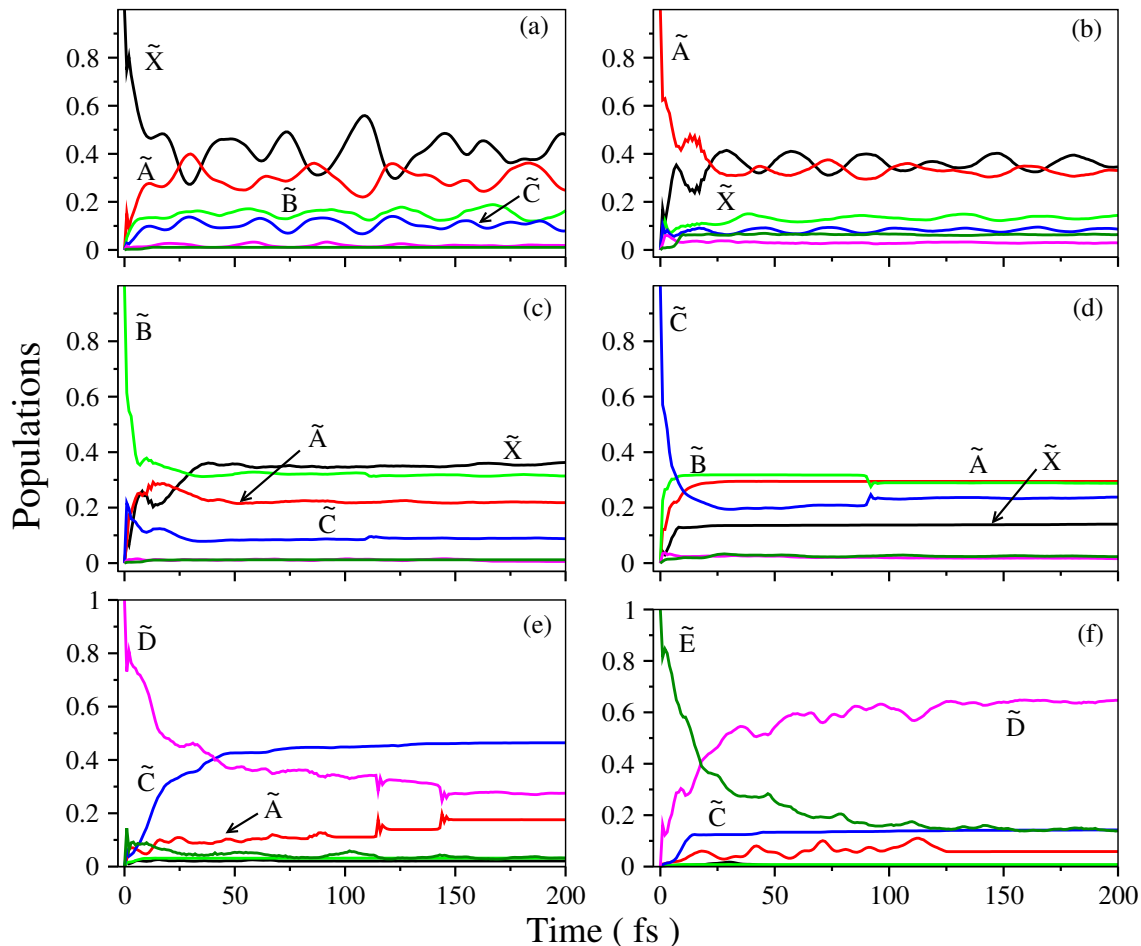
FIGURE 5.7: The electronic population dynamics within the coupled $\widetilde{X}\ ^2A'$-$\widetilde{A}\ ^2A'$-$\widetilde{B}\ ^2A''$-$\widetilde{C}\ ^2A''$-$\widetilde{D}\ ^2A'$-$\widetilde{E}\ ^2A'$ states of the $CH_2NHCH_2^+$ is calculated using EOMIP-CCSD data. Population diagrams are obtained by initially locating the WP separately on each of the $\widetilde{X}\ ^2A'$, $\widetilde{A}\ ^2A'$, $\widetilde{B}\ ^2A''$, $\widetilde{C}\ ^2A''$, $\widetilde{D}\ ^2A'$ and $\widetilde{E}\ ^2A'$ electronic states at t = 0, as depicted in panels (a)-(g) respectively.

to the $\widetilde{A}\ ^2A'$ state, while approximately ∼20% and ∼10% of the population transition to the $\widetilde{X}\ ^2A'$ and $\widetilde{C}\ ^2A''$ states, respectively, within the same timescale. This variation occur because of the strong coupling between the $\widetilde{X}\ ^2A'$-$\widetilde{B}\ ^2A''$ and $\widetilde{A}\ ^2A'$-$\widetilde{B}\ ^2A''$ states (cf., Table C6), as well as the proximity of the $\widetilde{B}\ ^2A''$ state minimum to the $\widetilde{X}\ ^2A'$-$\widetilde{B}\ ^2A''$ and $\widetilde{A}\ ^2A'$-$\widetilde{B}\ ^2A''$ intersection seams (cf., Table 5.6). Additionally, the electronic states $\widetilde{A}\ ^2A'$, $\widetilde{B}\ ^2A''$, and $\widetilde{C}\ ^2A''$ are close in energy, further contributing to this phenomenon.

Upon initial excitation to the $\widetilde{C}\ ^2A''$ state, the diabatic electronic populations depicted in Figs. 5.7 and 5.8 (d) reveal that approximately ∼30% and ∼20% of the populations transition to each of the $\widetilde{B}\ ^2A''$ and $\widetilde{A}\ ^2A'$ electronic states, respectively. Furthermore, around ∼10% of the population populates the $\widetilde{X}\ ^2A'$ electronic state within a timescale of approximately ∼15 fs. This population transfer occur because the minimum of the $\widetilde{C}\ ^2A''$ state is close to the $\widetilde{A}\ ^2A'$ and $\widetilde{B}\ ^2A''$ electronic states, and the three intersection

seams of $\widetilde{X}~^2A'$-$\widetilde{C}~^2A''$, $\widetilde{A}~^2A'$-$\widetilde{C}~^2A''$, and $\widetilde{B}~^2A''$-$\widetilde{C}~^2A''$ states are also in close proximity to the $\widetilde{C}~^2A''$ state minimum (cf., Table 5.6). Moreover, strong coupling exists between these three ($\widetilde{A}~^2A'$-$\widetilde{B}~^2A''$-$\widetilde{C}~^2A''$) electronic states, as indicated in Tables C5-C6.
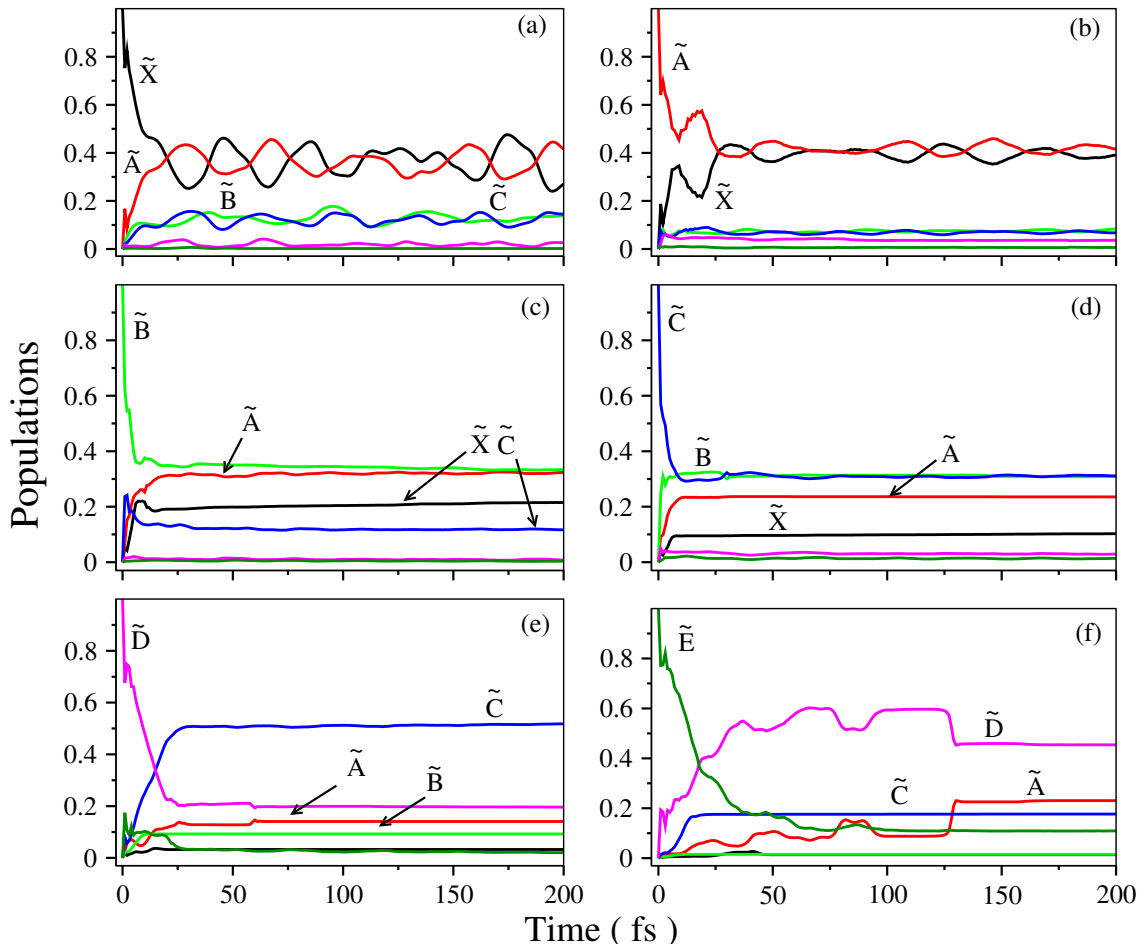
FIGURE 5.8: The electronic population dynamics within the coupled $\widetilde{X}~^2A'$-$\widetilde{A}~^2A'$-$\widetilde{B}~^2A''$-$\widetilde{C}~^2A''$-$\widetilde{D}~^2A'$-$\widetilde{E}~^2A'$ states of the $CH_2NHCH_2^+$ is calculated using MCQDPT data. Population diagrams are obtained by initially locating the WP separately on each of the $\widetilde{X}~^2A'$, $\widetilde{A}~^2A'$, $\widetilde{B}~^2A''$, $\widetilde{C}~^2A''$, $\widetilde{D}~^2A'$, and $\widetilde{E}~^2A'$ electronic states at t = 0, as depicted in panels (a)-(g) respectively.

In Figs. 5.7 and 5.8, panels (e) and (f) illustrate the electron population dynamics of the $\widetilde{D}~^2A'$ and $\widetilde{E}~^2A'$ electronic states, respectively, when the WP is initially prepared on these electronic states. When the WP is initially generated on the $\widetilde{D}~^2A'$ state, approximately ~50% and ~10% of the population migrate to the $\widetilde{C}~^2A''$ and $\widetilde{A}~^2A'$ electronic states, respectively. This population transfer occur due to the strong coupling between the $\widetilde{C}$-$\widetilde{D}$ states along a'' symmetry vibrational modes (cf., Tables C5-C6). Additionally, for a' symmetry vibrational modes, the $\widetilde{A}$-$\widetilde{D}$ coupling is also strong, thereby influencing the population dynamics of the $\widetilde{D}~^2A'$ electronic state (cf., Table C7). In the case of the $\widetilde{E}~^2A'$ electronic state, a larger proportion of the population (~60%) is transferred to

the $\widetilde{D}\ ^2A'$ state, while a minimal amount ($\sim$10%) moves to the $\widetilde{C}\ ^2A''$ electronic state. This phenomenon arises because the minimum of the $\widetilde{E}\ ^2A'$ electronic state is close to the minimum of the $\widetilde{D}\ ^2A'$ state, and the $\widetilde{D}\ ^2A'$-$\widetilde{E}\ ^2A'$ CI minimum is close to the $\widetilde{E}\ ^2A'$ state. Consequently, population leakage to the $\widetilde{D}\ ^2A'$ state occur through this CI, and coupling between these states is also strong (cf., Table C7). Furthermore, the $\widetilde{C}\ ^2A''$-$\widetilde{E}\ ^2A'$ states coupling is strongly influenced by the vibrational modes of a'' symmetry (cf., Tables C5-C6), which explains why some population is transferred to the $\widetilde{C}\ ^2A''$ electronic state.

Finally, we compared the present theoretical results with its isomer of both Acetaldehyde (CH_3CHO, Cs) and Oxirane (c-C_2H_4O ($C2v$)) molecules. That is, CH_2NHCH_2, CH_3CHO, and c-C_2H_4O are having the same number of electrons with different types of atoms, so their molecular geometries are also different from each other. Due to this, each of these isomers exhibit different number of DOFs. For example, both CH_3CHO and c-C_2H_4O are having the fifteen vibrational DOFs denoted as $\Gamma_{vib} = 10a' + 5a''$ and $\Gamma_{vib} = 5a_1 + 3b_1 + 4b_2 + 3a_2$, respectively. The aziridine, CH_2NHCH_2 encompasses a total of eighteen DOFs, outlined as $\Gamma_{vib} = 10a' + 8a''$. Recently, we have studied the photoelectron spectroscopy of both CH_3CHO [98] and c-C_2H_4O [195]. According to our theoretical calculations of all the three isomers, we concluded some of the major outcomes based on the topography of their PESs, coupling mechanism, and the corresponding nonadiabatic dynamics.

In the case of CH_3CHO isomer, it has C_s symmetry point group, and the electronic states are of both A' and A'' symmetry. The photoelectron spectrum has been computed using the first seven low-lying electronic states ($\widetilde{X}^2A'$, $\widetilde{A}^2A''$, $\widetilde{B}^2A'$, $\widetilde{C}^2A'$, $\widetilde{D}^2A''$, $\widetilde{E}^2A'$, and $\widetilde{F}^2A'$). Among them, we observed that both $\widetilde{X}$ and electronic states are well separated from the other electronic states at the FC geometry. Conversely, the remaining $\widetilde{A}^2A''$ to $\widetilde{E}^2A'$ states are very close in energy, and $\widetilde{C}^2A'$ and $\widetilde{D}^2A''$ states appearing as quasi-degenerate. These close energy states are strongly overlap and played major role in the nuclear dynamics and form the four vibronic broad band structures (cf., Fig. 4 of Ref. [98]). The time-dependence of the diabatic population of the coupled seven electronic states is very complex due to strong nonadiabatic couplings between them (cf., Fig. 5 of Ref. [98]). In addition to this, we have estimated the couplings between the same spatial symmetry states. On the other hand, the second isomer c-C_2H_4O has C_{2v} symmetry point group. The photoelectron spectrum of this isomer is calculated from the six low-lying electronic states (cf., Fig. 5 of Ref. [195]). Among the six electronic states, $\widetilde{X}\ ^2B_1$-$\widetilde{A}\ ^2A_1$, $\widetilde{B}\ ^2B_2$-$\widetilde{C}\ ^2A_2$, and $\widetilde{D}\ ^2A_1$-$\widetilde{E}\ ^2B_1$ states exhibit close energy proximity and significant nonadiabatic couplings between them. Due to these strong couplings, third

and fourth vibronic bands are contributed from the $\widetilde{B}\ ^2B_2$-$\widetilde{C}\ ^2A_2$ and $\widetilde{D}\ ^2A_1$-$\widetilde{E}\ ^2B_1$ electronic states, respectively. Also, due to the strong nonadibatic coupling between the $\widetilde{B}\ ^2B_2$ and $\widetilde{C}\ ^2A_2$ states, $\widetilde{B}\ ^2B_2$ state strongly repel from the $\widetilde{C}\ ^2A_2$ state and resulting to form a symmetric double-well potential topography (cf., Fig. 3 of Ref. [195]), this is called the PJT coupling in the literature. All together, in the present chapter we systematically studied the photoelectron spectrum of CH_2NHCH_2 molecule and compared with our previous theoretical results of both CH_3CHO, and c-C_2H_4O isomers. Based on these findings, we may conclude that these three isoelectronic molecules have diffrent molecular configurations and molecular symmetry, which affects their electronic state character, PES topography, and vibronic band structures.

5.4 Summary

This chapter presents a theoretical investigation into the photo-ionization spectroscopy of CH_2NHCH_2, focusing on multi-state and multi-mode vibrionic coupling and the roles played by the $\widetilde{X}\ ^2A'$, $\widetilde{A}\ ^2A'$, $\widetilde{B}\ ^2A''$, $\widetilde{C}\ ^2A''$, $\widetilde{D}\ ^2A'$, and $\widetilde{E}\ ^2A'$ electronic states. We construct potential energy surfaces for these six ($\widetilde{X}\ ^2A'$, $\widetilde{A}\ ^2A'$, $\widetilde{B}\ ^2A''$, $\widetilde{C}\ ^2A''$, $\widetilde{D}\ ^2A'$, and $\widetilde{E}\ ^2A'$) states and their potential couplings are calculated using the *ab initio* EOMIP-CCSD and MCQDPT methods. A standard vibronic coupling model Hamiltonian is developed for the six energetically low-lying electronic states of $CH_2NHCH_2^+$, based on a diabatic electronic basis and in terms of dimensionless normal displacement coordinates of the electronic ground state of CH_2NHCH_2 vibrational modes. We conduct nuclear dynamics calculations using time-independent matrix diagonalization and WP propagation methods. Finally, we compared our theoretical results with the available experimental results. Our theoretical results are in good agreement with the experimental results.

The electronic ground state of CH_2NHCH_2 was optimized using DFT with the B3LYP functional and the aug-cc-pVTZ basis set. Analysis of the electronic structure revealed that the $\widetilde{X}\ ^2A'$, $\widetilde{D}\ ^2A'$, and $\widetilde{E}\ ^2A'$ electronic states are energetically distant from the other $\widetilde{A}\ ^2A'$, $\widetilde{B}\ ^2A''$, and $\widetilde{C}\ ^2A''$ electronic states. However, these three ($\widetilde{A}\ ^2A'$-$\widetilde{B}\ ^2A''$-$\widetilde{C}\ ^2A''$) states are closely situated in the Franck-Condon region, indicating strong vibronic coupling among them, which significantly influences the nuclear dynamics. The coupling between the $\widetilde{X}\ ^2A'$ to $\widetilde{E}\ ^2A'$ electronic states was evaluated using basic vibronic coupling theory and symmetry selection rules. Nuclear dynamical calculations were performed to get the precise eigenvalue locations from the time-independent matrix diagonalization method and from the time-dependent approach we achieved the diabatic

electronic populations for coupled ($\widetilde{X}\ ^2A'$-$\widetilde{A}\ ^2A'$-$\widetilde{B}\ ^2A''$-$\widetilde{C}\ ^2A''$-$\widetilde{D}\ ^2A'$-$\widetilde{E}\ ^2A'$) electronic states. Additionally, the nodal pattern of vibrational wave functions was examined using the block-improved relaxation method for further confirm of the peak assignments. The theoretical results were found to be in good agreement with experimental data, with thorough examination of the vibronic band structures of $\widetilde{X}\ ^2A'$, $\widetilde{A}\ ^2A'$, $\widetilde{B}\ ^2A''$, $\widetilde{C}\ ^2A''$, $\widetilde{D}\ ^2A'$, and $\widetilde{E}\ ^2A'$ electronic states conducted in this study. These findings were compared with previous experimental results, showing excellent agreement. Notably, due to their energetic proximity of $\widetilde{A}\ ^2A'$, $\widetilde{B}\ ^2A''$, and $\widetilde{C}\ ^2A''$ electronic states collectively contribute to the overlapping second, third, and fourth vibronic bands of $CH_2NHCH_2^+$, while $\widetilde{X}\ ^2A'$, $\widetilde{D}\ ^2A'$, and $\widetilde{E}\ ^2A'$ electronic states form the first, fifth, and sixth separate vibronic bands. At the end, we compared these results with its isoelectronic molecules (i.e., Acetaldehyde and Oxirane) of photoelectron spectroscopy studies.

Chapter 6

Summary and outlook

This thesis presents theoretical explorations into the multi-state and multi-mode nonadiabatic dynamics of isoelectronic molecular systems. Specifically, we delve into the analysis of photoelectron spectra for molecules such as CH_3CHO, c-C_2H_4O and CH_2NHCH_2, employing advanced quantum dynamical methods and state-of-the-art *ab initio* initio quantum chemistry calculations. Our investigation demonstrated that vibronic coupling plays a significant role in controlling the dynamics of the low-lying electronic states. Theoretical vibronic band structures were calculated and compared with available experimental data, showing good agreement between theoretical predictions and experimental evidence. Additionally, we examined dominant vibrational progressions in each electronic state, electronic population transfer processes at conical intersections (CIs), and nonradiative decay rates in detail.

To address challenges posed by PESs crossings and avoid the singularity of the nuclear kinetic coupling term in the adiabatic electronic representation, we developed and implement a diabatic electronic representation. For electronic couplings between states of the same spatial symmetry, we utilized the fourfold-way diabatization scheme [116, 121–124] at the level of MCQDPT theory. The model vibronic Hamiltonian was constructed in this basis using elementary symmetry selection techniques, and crucial coupling parameters were extracted from *ab initio* initio electronic structure data.

Using the MCTDH program module, we solved both the time-independent and time-dependent Schrödinger equations to determine the vibronic bands. In the following subsection, we summarize the main conclusions of this thesis chapter by chapter.

Chapter 3:
(a) This chapter contain a theoretical exploration of multi-state and multi-mode vibronic coupling in the photo-ionization spectroscopy of CH_3CHO.

(b) We develop a standard vibronic coupling model Hamiltonian, encompassing seven energetically low-lying electronic states of $CH_3CHO^{.+}$, represented in a diabatic electronic basis and using dimensionless normal displacement coordinates of the electronic ground state of CH_3CHO.

(c) Optimization of the electronic ground state of CH_3CHO is conducted at the DFT level using the B3LYP functional and a 6-311++g(d,p) basis set. Extensive *ab initio* quantum chemistry calculations are performed with the EOMIP-CCSD method to parameterize the vibronic Hamiltonian.

(d) Analysis of the electronic structure reveals significant energy separation of the $\widetilde{X}$ and $\widetilde{F}$ states from the other states within the Franck-Condon zone. Conversely, the remaining ($\widetilde{A}$ to $\widetilde{E}$) electronic states are closely situated in energy, with $\widetilde{C}$ and $\widetilde{D}$ states appearing quasi-degenerate. This underscores the pivotal role of vibronic coupling in governing the nuclear dynamics.

(e) Theoretical evaluation of the coupling among the seven ($\widetilde{X}$ to $\widetilde{F}$) electronic states is conducted using standard vibronic coupling theory and elementary symmetry selection rules. Additionally, coupling between electronic states of the same spatial symmetry ($\widetilde{B}$-$\widetilde{C}$, $\widetilde{B}$-$\widetilde{E}$, and $\widetilde{C}$-$\widetilde{E}$) via a' vibrational modes is addressed.

(f) Nuclear dynamical calculations are performed using both time-independent and time-dependent quantum mechanical methods. Each vibronic band is meticulously analyzed, and the results are compared with available experimental findings. Notably, the theoretical results exhibit good agreement with experimental data, confirming the accuracy of the theoretical model.

Chapter 4:

In this chapter, we delve into a comprehensive theoretical examination of vibronic coupling in the photo-ionization spectroscopy of c-C_2H_4O. Here are the key points discussed:

(a) The study investigates multi-state multi-mode vibronic coupling within the first six energetically low- lying electronic states of c-$C_2H_4O^{.+}$.

(b) Electronic potential energy surfaces (PESs) are computed using extensive *ab initio* quantum chemistry calculations employing the EOMIP-CCSD method. The PESs for the $\widetilde{X}$ $^2B_1$, $\widetilde{A}$ $^2A_1$, $\widetilde{B}$ $^2B_2$, $\widetilde{C}$ $^2A_2$, $\widetilde{D}$ $^2A_1$, and $\widetilde{E}$ $^2B_1$ electronic states of c-C_2H_4O are plotted along dimensionless normal displacement coordinates.

(c) A vibronic model Hamiltonian is constructed for the coupled manifold of $\widetilde{X}$ $^2B_1$, $\widetilde{A}$ $^2A_1$, $\widetilde{B}$ $^2B_2$, $\widetilde{C}$ $^2A_2$, $\widetilde{D}$ $^2A_1$, and $\widetilde{E}$ $^2B_1$ electronic states in a diabatic electronic basis, employing standard vibronic coupling theory and elementary symmetry selection rules.

(d) Nuclear dynamics calculations are performed using the developed Hamiltonian parameters through both time-independent matrix diagonalization and time-dependent WP propagation quantum mechanical methods. All fifteen vibrational modes ($5a_1 + 3b_1 + 4b_2 + 3a_2$) are included in the nuclear dynamics calculations.

(e) The vibronic band structures of $\widetilde{X}$ $^2B_1$, $\widetilde{A}$ $^2A_1$, $\widetilde{B}$ $^2B_2$, $\widetilde{C}$ $^2A_2$, $\widetilde{D}$ $^2A_1$, and $\widetilde{E}$ $^2B_1$ electronic states are thoroughly examined and assigned. The vibrational modes responsible for specific band structures are identified.

(f) The impact of nonadiabatic coupling between $\widetilde{X}$ $^2B_1$-$\widetilde{A}$ $^2A_1$, $\widetilde{B}$ $^2B_2$-$\widetilde{C}$ $^2A_2$, and $\widetilde{D}$ $^2A_1$-$\widetilde{E}$ $^2B_1$ states is found to be significantly stronger compared to other possible electronic state combinations.

(g) Decay rates of the $\widetilde{X}$ $^2B_1$, $\widetilde{A}$ $^2A_1$, $\widetilde{B}$ $^2B_2$, $\widetilde{C}$ $^2A_2$, $\widetilde{D}$ $^2A_1$, and $\widetilde{E}$ $^2B_1$ states are calculated, providing insights into their dynamical behavior.

(h) Notably, the coupling between $\widetilde{X}$ $^2B_1$-$\widetilde{A}$ $^2A_1$, $\widetilde{B}$ $^2B_2$-$\widetilde{C}$ $^2A_2$, and $\widetilde{D}$ $^2A_1$-$\widetilde{E}$ $^2B_1$ states exerts a significant influence on the vibronic structure of the second, third, and fourth vibronic bands, as depicted in Fig. 3.4.

(i) It is observed that the $\widetilde{B}$ $^2B_2$ and $\widetilde{C}$ $^2A_2$ electronic states experience the pseudo-Jahn-Teller (PJT) effect along the b_1 symmetry vibrational mode. This results in the lower adiabatic $\widetilde{B}$ $^2B_2$ state exhibiting a symmetric double-well potential landscape, with its minimum at a distorted geometry compared to the Franck-Condon (FC) geometry ($Q = 0$).

(j) Among the three b_1-symmetry vibrational modes (ν_6, ν_7, ν_8), the ν_7 mode demonstrates strong coupling between the $\widetilde{B}$ $^2B_2$ and $\widetilde{C}$ $^2A_2$ states, while coupling along the ν_6 and ν_8 modes is moderate.

(k) In summary, the $\widetilde{X}$ $^2B_1$-$\widetilde{A}$ $^2A_1$, $\widetilde{B}$ $^2B_2$-$\widetilde{C}$ $^2A_2$, and $\widetilde{D}$ $^2A_1$-$\widetilde{E}$ $^2B_1$ electronic states exhibit close energy proximity and significant nonadiabatic coupling among them, playing pivotal roles in the nuclear dynamics. The theoretical calculations align well with available experimental results. Additionally, intriguing findings regarding c-C_2H_4O are compared with acetaldehyde isomer as necessary.

Chapter 5:

To illuminate the photo-ionization spectroscopy of CH_2NHCH_2, this chapter focuses into a theoretical exploration of multi-state and multi-mode vibrionic coupling involving the $\tilde{X}^2A'$, $\tilde{A}^2A'$, $\tilde{B}^2A''$, $\tilde{C}^2A''$, $\tilde{D}^2A'$, and $\tilde{E}^2A'$ electronic states. Here's a breakdown of the key points discussed:

(a) PESs for the six electronic states of CH_2NHCH_2 are meticulously constructed, and their possible couplings are computed using *ab initio* methods such as EOMIP-CCSD and MCQDPT. Vibronic coupling model Hamiltonians are established for these six electronic states in a diabatic electronic basis, accounting for dimensionless normal displacement coordinates of the electronic ground state's vibrational modes.

(b) The electronic ground state of CH_2NHCH_2 is optimized via DFT with the B3LYP functional and the aug-cc-pVTZ basis set. Analysis of the electronic structure reveals that $\tilde{X}^2A'$, $\tilde{D}^2A'$, and $\tilde{E}^2A'$ electronic states exhibit slight energy separation from $\tilde{A}^2A'$, $\tilde{B}^2A''$, and $\tilde{C}^2A''$ states. However, the latter trio is closely situated within the Franck-Condon zone, indicating strong vibronic coupling among them, which significantly influences the nuclear dynamics. The coupling between $\tilde{X}^2A'$ to $\tilde{E}^2A'$ electronic states is evaluated using basic vibronic coupling theory and symmetry selection rules.

(c) Nuclear dynamical calculations, encompassing both time-independent matrix diagonalization and time-dependent WP propagation methods, reveal precise eigenvalue locations and diabatic electronic populations for coupled states. Thorough examination of the vibronic band structures for each electronic state is conducted and compared with previous experimental findings. Remarkably, the theoretical results align remarkably well with recent experimental recordings. The vibronic bands formed by $\tilde{A}^2A'$, $\tilde{B}^2A''$, and $\tilde{C}^2A''$ electronic states overlap, while those originating from $\tilde{X}^2A'$, $\tilde{D}^2A'$, and $\tilde{E}^2A'$ states remain distinct. Peaks' assignment is further confirmed through the block-improved relaxation method, validating the theoretical findings against experimental data.

Future challenges:
The expertise gained from my PhD work has inspired me to broaden my research scope. Building on my background in electronic structure and nonadiabatic quantum dynamics, I plan to address the following challenges in my future research:

(1) While my previous focus has primarily been on small organic molecules and their photoelectron spectroscopy properties, I aim to expand my research to encompass larger molecular systems and highly symmetric metal complexes and organic materials.

(2) In recent years, there has been growing interest in understanding organic photovoltaics and optoelectronics due to their potential to enhance the efficiency of solar cells and other photonic devices. Exploring projects related to Singlet-Fission processes, where one singlet exciton splits into two triplet excitons, will provide valuable insights

into practical applications.

(3) Additionally, I am keen on investigating Polaritonic Chemistry, which involves manipulating chemistry using hybrid light-matter states known as Polaritons. This emerging field offers exciting opportunities to explore novel chemical reactions and phenomena.

Appendix A

Supplementary material for Chapter 3
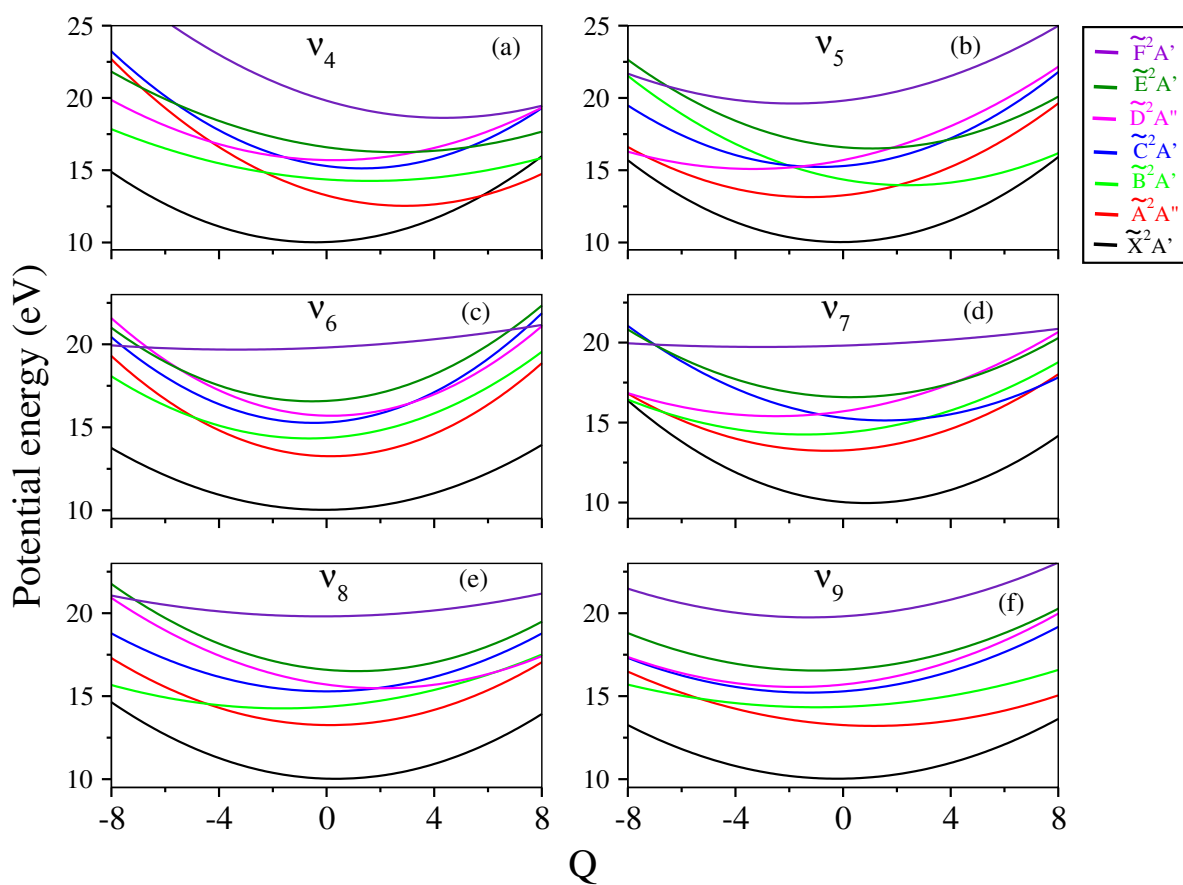
FIGURE A1: The diabatic PESs of the first seven low-lying $\widetilde{X}^2 A^{'}$ to $\widetilde{F}^2 A^{'}$ electronic states of the $CH_3COH^{\cdot+}$ plotted along the dimensionless normal displacement coordinates of the $a^{'}$ vibrational modes, ν_4-ν_9.

TABLE A1: *Ab initio* calculated linear (κ_i) and quadratic (γ_i) coupling parameters for the $\widetilde{X}^2A'$, $\widetilde{A}^2A''$, $\widetilde{B}^2A'$, $\widetilde{C}^2A'$, $\widetilde{D}^2A''$, $\widetilde{E}^2A'$ and $\widetilde{F}^2A'$ electronic states of $CH_3COH^{\cdot+}$. All quantities are in eV and the dimensionless Poisson parameters $\left(\kappa_i{}^2/2\omega_i{}^2\right)$ are given in the parentheses.

Mode	$\widetilde{X}^2A'$		$\widetilde{A}^2A''$		$\widetilde{B}^2A'$	
	κ_i	γ_i	κ_i	γ_i	κ_i	γ_i
a'						
ν_1	0.0083 (0.0002)	0.0052	0.0611(0.0123)	0.0013	-0.2349 (0.1826)	-0.0634
ν_2	-0.0061 (0.0001)	0.0031	0.1375(0.0674)	-0.0177	0.2288 (0.1866)	-0.0163
ν_3	-0.0306 (0.0037)	-0.0057	0.0565(0.0126)	0.0168	-0.0811 (0.0259)	-0.0113
ν_4	0.0139 (0.0019)	-0.0521	-0.3905(1.5168)	-0.0515	-0.0912 (0.0827)	-0.0526
ν_5	-0.0074 (0.0008)	-0.0106	0.1877(0.5371)	-0.0592	-0.3205 (1.5660)	-0.1182
ν_6	-0.0534 (0.0460)	-0.0608	-0.0446(0.0321)	-0.0017	0.0626 (0.0632)	-0.0391
ν_7	-0.1029 (0.1815)	-0.0084	0.0974(0.1626)	-0.0586	0.1253 (0.2691)	-0.0799
ν_8	-0.0279 (0.0199)	-0.0221	-0.0298(0.0227)	-0.0259	0.1461 (0.5461)	-0.0923
ν_9	-0.0134 (0.0074)	-0.0056	-0.1062(0.4677)	-0.0272	0.0385 (0.0615)	-0.0642
ν_{10}	0.0039 (0.0019)	-0.0175	-0.0291(0.1057)	-0.0327	-0.0602 (0.4522)	-0.0429
a''						
ν_{11}	-	0.0058	-	-0.0418	-	-0.0058
ν_{12}	-	-0.0072	-	-0.1678	-	-0.1183
ν_{13}	-	-0.0212	-	-0.0514	-	-0.0235
ν_{14}	-	-0.0048	-	-0.0417	-	-0.0877
ν_{15}	-	0.0026	-	-0.1642	-	-0.2171

Mode	$\widetilde{C}^2A'$		$\widetilde{D}^2A''$	
	κ_i	γ_i	κ_i	γ_i
ν_1	-0.1061(0.0372)	0.0439	0.1453 (0.0699)	0.0173
ν_2	0.0561(0.0112)	0.0047	0.3098 (0.3421)	0.0475
ν_3	0.0431(0.0073)	0.0211	0.0587 (0.0136)	0.0118
ν_4	-0.1314(0.1717)	0.0795	-0.0075 (0.0005)	0.1025
ν_5	0.1078(0.1772)	0.0063	0.3254 (1.6142)	-0.0383
ν_6	0.1043(0.1754)	0.0045	-0.0484 (0.0378)	0.0041
ν_7	-0.1892(0.6135)	-0.0163	0.2112 (0.7645)	-0.0336
ν_8	-0.0224(0.0128)	0.0089	-0.1823 (0.8502)	-0.0098
ν_9	0.1228(0.6254)	0.0089	0.1527 (0.9670)	-0.0024
ν_{10}	-0.0696(0.6045)	-0.0221	0.0028 (0.0010)	-0.0337
ν_{11}	-	-0.0025	-	-0.0099
ν_{12}	-	-0.0629	-	0.1671
ν_{13}	-	-0.0242	-	-0.0084
ν_{14}	-	-0.0137	-	0.0063
ν_{15}	-	-0.1087	-	-0.1524
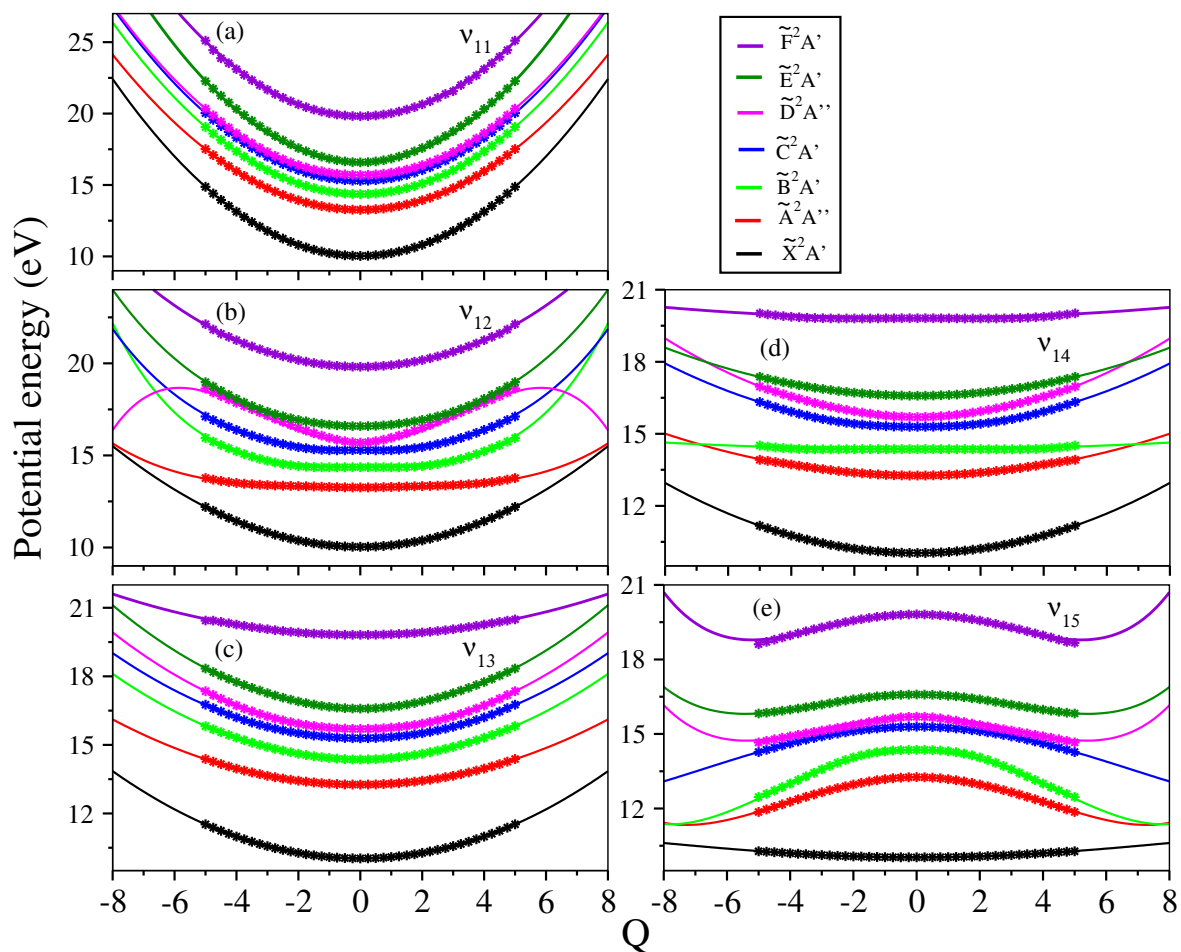
FIGURE A2: The adiabatic PESs of the lowest electronic state $\widetilde{X}^2A'$, $\widetilde{A}^2A''$, $\widetilde{B}^2A'$, $\widetilde{C}^2A'$, $\widetilde{D}^2A''$, $\widetilde{E}^2A'$ and $\widetilde{F}^2A'$ of $CH_3COH^{.+}$ plotted along the normal displacement coordinate of the a'' vibrational modes, ν_{11}-ν_{15}. The solid lines are obtained from the theoretical model and the calculated *ab initio* potential energies are shown by the asterisks.

Table A1: Continued

| Sym. | Mode | $\widetilde{E}^2 A'$ | | $\widetilde{F}^2 A'$ | |
		κ_i	γ_i	κ_i	γ_i
a'	ν_1	0.0197 (0.0013)	0.0035	-0.0689(0.0157)	0.0392
	ν_2	0.1444 (0.0743)	0.0221	0.1504(0.0806)	-0.0065
	ν_3	-0.0367 (0.0053)	-0.0075	-0.5248(1.0866)	0.0636
	ν_4	-0.1327 (0.1752)	0.0463	0.1006(0.1007)	-0.0059
	ν_5	-0.2001 (0.6104)	0.0519	0.0325(0.0161)	-0.0109
	ν_6	0.1287 (0.2670)	0.0168	-0.0603(0.0586)	-0.0808
	ν_7	-0.1215 (0.2530)	0.0021	-0.1714(0.5035)	0.0082
	ν_8	-0.1456 (0.5423)	0.0255	0.0436(0.0486)	-0.0095
	ν_9	0.0877 (0.3190)	0.0067	-0.0383(0.0608)	-0.0162
	ν_{10}	0.0681 (0.5787)	-0.0099	0.0476(0.2827)	-0.0054
a''	ν_{11}	-	0.0748	-	0.0381
	ν_{12}	-	-0.0133	-	-0.0057
	ν_{13}	-	0.0009	-	-0.0846
	ν_{14}	-	-0.0336	-	-0.0821
	ν_{15}	-	-0.1246	-	-0.1706

TABLE A2: *Ab initio* calculated cubic (ρ_i) and quartic (ξ_i) coupling parameters (in eV) for the $\widetilde{X}^2A'$, $\widetilde{A}^2A''$, $\widetilde{B}^2A'$, $\widetilde{C}^2A'$, $\widetilde{D}^2A''$, $\widetilde{E}^2A'$, and $\widetilde{F}^2A'$ electronic states of $CH_3COH^{\cdot+}$.

Sym.	Mode	$\widetilde{X}^2A'$ ρ_i	ξ_i	$\widetilde{A}^2A''$ ρ_i	ξ_i	$\widetilde{B}^2A'$ ρ_i	ξ_i
a'	ν_1	-	-	-	-	-	-
	ν_2	-	-	-	-	-	-
	ν_3	-	-	-	-	-	-
	ν_4	0.0076	-	0.0314	-	-0.0062	-
	ν_5	-0.0022	-	0.0092	-	0.0204	-
	ν_6	-0.0056	-	0.0015	-	0.0047	-
	ν_7	0.0067	-	0.0097	-	-0.0108	-
	ν_8	-	-	-	-	-	-
	ν_9	-0.0021	-	-0.0014	-	-0.0023	-
	ν_{10}	-0.0073	-	-0.0004	-	-0.0032	-
a''	ν_{11}	-	-	-	-	-	-
	ν_{12}	-	-0.0007	-	0.0113	-	0.0337
	ν_{13}	-	-	-	-	-	-
	ν_{14}	-	-	-	-	-	-
	ν_{15}	-	-0.0006	-	0.0165	-	0.0197

Sym.	Mode	$\widetilde{C}^2A'$ ρ_i	ξ_i	$\widetilde{D}^2A''$ ρ_i	ξ_i
a'	ν_1	-	-	-	-
	ν_2	-	-	-	-
	ν_3	-	-	-	-
	ν_4	0.0031	-	-0.0393	-
	ν_5	-0.0119	-	-0.0233	-
	ν_6	-0.0025	-	-0.0005	-
	ν_7	0.0151	-	-0.0199	-
	ν_8	-	-	-	-
	ν_9	-0.0093	-	0.0047	-
	ν_{10}	0.0087	-	-0.0002	-
a''	ν_{11}	-	-	-	-
	ν_{12}	-	0.0162	-	-0.0615
	ν_{13}	-	-	-	-
	ν_{14}	-	-	-	-
	ν_{15}	-	0.0038	-	0.0277

TABLE A2: Continued.

Sym.	Mode	$\widetilde{E}^2A'$		$\widetilde{F}^2A'$	
		ρ_i	ξ_i	ρ_i	ξ_i
a'	ν_1	-	-	-	-
	ν_2	-	-	-	-
	ν_3	-	-	-	-
	ν_4	-0.0095	-	-0.0074	-
	ν_5	0.0096	-	-0.0034	-
	ν_6	-0.0064	-	0.0112	-
	ν_7	0.0053	-	0.0072	-
	ν_8	-	-	-	-
	ν_9	0.0024	-	-0.0002	-
	ν_{10}	-0.0033	-	0.0038	-
a''	ν_{11}	-	-	-	-
	ν_{12}	-	0.0117	-	0.0028
	ν_{13}	-	-	-	-
	ν_{14}	-	-	-	-
	ν_{15}	-	0.0216	-	0.0337

TABLE A3: Linear (λ_i^{nm}), quadratic (γ_i^{nm}), cubic (β_i^{nm}) and fifth (η_i^{nm}) order inter-state coupling constants (in eV) between the n and m electronic states of the $CH_3COH^{\cdot+}$ (Eq. 3.2) estimated from the *ab initio* electronic structure results (see the text for details). Dimensionless Poisson parameters $\left(\lambda_i^2/2\omega_i^2\right)$ are given in the parentheses.

	$\widetilde{X}$-$\widetilde{A}$			$\widetilde{X}$-$\widetilde{D}$		
Mode	λ_i	β_i		λ_i	β_i	η_i
a''						
ν_{11}	0.2084(0.1493)	-0.0009		0.2811(0.2717)	-0.0097	0.0002
ν_{12}	0.3405(1.7468)	-0.0022		0.7188(7.7818)	-0.0351	0.0009
ν_{13}	0.1672(0.7080)	0.0007		-	-	-
ν_{14}	0.1522(1.2508)	0.0006		0.2569(3.5667)	-0.0119	0.0003
ν_{15}	0.3686(192.2656)	-0.0036		0.1204(20.5202)	-0.0122	0.0005

	$\widetilde{A}$-$\widetilde{B}$			$\widetilde{A}$-$\widetilde{C}$		
Mode	λ_i	β_i		λ_i	β_i	η_i
a''						
ν_{11}	0.0995(0.0340)	-0.0004		0.1443(0.0716)	0.0002	-
ν_{12}	0.1454(0.3184)	-0.0216		0.1025(0.1584)	0.0161	-0.0004
ν_{13}	0.1115(0.3147)	0.0007		0.1108(0.3113)	-0.0005	-
ν_{14}	0.1337(0.9655)	-0.0016		0.0478(0.1235)	0.0034	-
ν_{15}	0.1501(31.8601)	-0.0344		0.1824(47.0574)	-0.0022	-

	$\widetilde{A}$-$\widetilde{E}$				$\widetilde{A}$-$\widetilde{F}$	
Mode	λ_i	β_i	η_i		λ_i	β_i
a''						
ν_{11}	0.3864 (0.5135)	-0.0019	-		0.3641 (0.4559)	-0.00059
ν_{12}	0.3387 (1.7279)	0.0028	-		0.5062 (3.8597)	-0.00002
ν_{13}	0.2519 (1.6080)	-0.0015	-		-	-
ν_{14}	0.0564 (0.1718)	-0.0021	0.00014		0.3475 (6.5255)	-0.00423
ν_{15}	0.2234 (70.5830)	-0.0035	0.00013		0.1968 (54.7865)	0.00138

	$\widetilde{B}$-$\widetilde{D}$				$\widetilde{C}$-$\widetilde{D}$	
Mode	λ_i	β_i	η_i		λ_i	β_i
a''						
ν_{11}	0.1107(0.0422)	-0.0053	0.0001		0.0644 (0.0143)	-0.0029
ν_{12}	0.4501(3.0508)	-0.0134	0.0002		0.2724 (1.1172)	-0.0074
ν_{13}	-	-	-		0.0211 (0.0112)	0.0021
ν_{14}	0.2151(2.5003)	-0.0003	-		0.0918 (0.4556)	-0.0025
ν_{15}	-	-	-		0.1204 (20.5202)	-0.0122

TABLE A3: Continued

	$\widetilde{D}$-$\widetilde{E}$			$\widetilde{D}$-$\widetilde{F}$		
Mode	λ_i	β_i	η_i	λ_i	β_i	η_i
a''						
ν_{11}	0.2065 (0.1467)	-0.0015	-	0.2925 (0.2942)	0.0066	-0.00013
ν_{12}	0.2933 (1.2953)	-0.0301	0.0015	0.5943 (5.3197)	-0.0331	0.00091
ν_{13}	0.1031 (0.2693)	-0.0024	-	0.2567 (1.6689)	-0.0004	-
ν_{14}	0.1221 (0.8048)	-0.0027	0.00004	0.3691 (7.3575)	-0.0038	-
ν_{15}	0.1855 (48.6780)	-0.0157	0.0006	0.3345 (158.2742)	-0.0326	0.00061

	$\widetilde{B}$-$\widetilde{C}$	$\widetilde{B}$-$\widetilde{E}$		$\widetilde{C}$-$\widetilde{E}$	
Mode	λ_i	λ_i	γ_i	λ_i	γ_i
a'					
ν_3	0.0413 (0.0067)	0.0846 (0.0282)	0.0339	0.0060 (0.0001)	-0.0105
ν_4	-0.1281 (0.1632)	0.2002 (0.3987)	-	-0.0531 (0.0280)	-
ν_5	-0.1146 (0.2002)	-0.3428 (1.7915)	-	0.0066 (0.0007)	-0.0037
ν_6	-0.1231 (0.2443)	0.0603 (0.0586)	0.0251	0.1625 (0.4257)	-
ν_7	-0.0695 (0.0828)	0.0767 (0.1008)	-0.0308	-0.1106 (0.2096)	-
ν_8	-0.1810 (0.8381)	-0.1421 (0.5166)	-	-0.0729 (0.1359)	-
ν_9	-0.1167 (0.5648)	0.0757 (0.2377)	-0.0075	-0.0211 (0.0185)	0.0121
ν_{10}	0.0731 (0.6668)	0.0086 (0.0092)	0.0100	0.0385 (0.1850)	0.0291

TABLE A4: Diagonal bilinear γ_{ij}^n parameters (in eV) along the totally symmetric vibrational modes ν_4, ν_5, ν_7, ν_8, ν_9 and ν_{10} of the lowest seven electronic states of $CH_3COH^{\cdot+}$.

γ_{ij}	$\widetilde{X}^2A'$	$\widetilde{A}^2A''$	$\widetilde{B}^2A'$	$\widetilde{C}^2A'$	$\widetilde{D}^2A''$	$\widetilde{E}^2A'$	$\widetilde{F}^2A'$
γ_{45}	-0.0016	-0.0881	0.0189	0.0132	0.0689	-0.053	-0.0010
γ_{47}	0.0229	-0.0806	-0.0588	0.0653	0.0701	-0.0325	-0.0227
γ_{48}	-0.0069	0.0627	-0.0344	0.0497	-0.0586	-0.0442	0.0043
γ_{49}	-0.0216	-0.0285	-0.0858	0.0611	0.0071	0.0202	0.0119
γ_{410}	-0.0185	0.0179	0.0527	-0.0323	-0.0108	0.0081	-0.0209
γ_{57}	-0.0198	-0.0702	0.1035	0.0027	0.0038	-0.0312	-0.0082
γ_{58}	0.0040	0.0693	-0.1266	-0.0102	0.0275	0.0936	-0.0111
γ_{59}	0.0059	0.0268	-0.0605	0.0297	0.0407	-0.0017	0.0113
γ_{510}	-0.0182	-0.0135	0.0839	-0.0111	-0.0416	0.0068	0.0039
γ_{78}	-0.0308	-0.0027	0.0229	0.0650	-0.0546	-0.0169	0.0270
γ_{79}	0.0249	-0.0272	0.0009	0.0591	-0.0442	-0.0335	0.0245
γ_{710}	0.0044	0.0488	-0.0431	-0.0256	0.0501	-0.0336	0.0019
γ_{89}	0.0065	-0.0132	-0.0825	0.0467	-0.0513	-0.0202	-0.0181
γ_{810}	-0.0609	-0.0018	0.1199	-0.0243	0.0362	-0.0238	0.0283
γ_{910}	-0.0239	0.0247	0.0962	-0.0141	0.0521	-0.0092	0.0344

TABLE A5: The number of harmonic oscillator (HO) basis functions along the totally symmetric vibrational modes and the dimension of the secular matrix used in the calculation of the stick vibrational spectrum of the uncoupled electronic states of $CH_3COH^{\cdot+}$ shown in Fig. 3.3.

Electronic state	Normal modes	Primitive basis	Dimension of secular matrix
$\widetilde{X}^2A'$	$\nu_3, \nu_4, \nu_5, \nu_6$ $\nu_7, \nu_8, \nu_9, \nu_{10}$	(6,6,4,10) (12,8,6,6)	4980580
$\widetilde{A}^2A''$	$\nu_3, \nu_4, \nu_5, \nu_6$ $\nu_7, \nu_8, \nu_9, \nu_{10}$	(6,14,12,6) (10,6,12,10)	43545600
$\widetilde{B}^2A'$	ν_3, ν_4, ν_5 $\nu_6, \nu_7, \nu_8, \nu_9$	(6,10,16) (10,12,20,12)	27648000
$\widetilde{C}^2A'$	$\nu_3, \nu_4, \nu_5, \nu_6$ $\nu_7, \nu_8, \nu_9, \nu_{10}$	(6,14,14,14) (16,10,16,16)	674365440
$\widetilde{D}^2A''$	$\nu_3, \nu_4, \nu_5, \nu_6$ $\nu_7, \nu_8, \nu_9, \nu_{10}$	(8,4,12,8) (10,10,12,6)	22120000
$\widetilde{E}^2A'$	$\nu_3, \nu_4, \nu_5, \nu_6$ $\nu_7, \nu_8, \nu_9, \nu_{10}$	(4,6,8,6) (6,8,6,8)	2654208
$\widetilde{F}^2A'$	$\nu_3, \nu_4, \nu_5, \nu_6$ $\nu_7, \nu_8, \nu_9, \nu_{10}$	(12,8,6,6) (10,6,6,10)	12440000

TABLE A6: Energetically low-lying vibrational levels (in cm^{-1}) of the $\widetilde{X}$, $\widetilde{A}$, $\widetilde{B}$, $\widetilde{C}$, $\widetilde{D}$, $\widetilde{E}$ and $\widetilde{F}$ electronic states of $CH_3COH^{.+}$ obtained from the uncoupled state calculations. The assignment of the levels carried out by examining the nodal pattern of the wave functions is included in the table.

$\widetilde{X}^2A'$		Expt. [37]	$\widetilde{A}^2A''$		$\widetilde{B}^2A'$		$\widetilde{C}^2A'$	
Energy	Assignment	Energy	Energy	Assignment	Energy	Assignment	Assignment	Energy
0	0_0^0		0	0_0^0	0	0_0^0	0	0_0^0
434	$\nu_{10_0}^1$		357	$\nu_{10_0}^1$	582	$\nu_{9_0}^1$	468	$\nu_{10_0}^1$
861	$\nu_{9_0}^1$	700	729	$\nu_{10_0}^2$	668	$\nu_{8_0}^1$	934	$\nu_{10_0}^2$
869	$\nu_{10_0}^2$		760	$\nu_{9_0}^1$	1076	$\nu_{7_0}^1$	955	$\nu_{9_0}^1$
1034	$\nu_{8_0}^1$	1100	1017	$\nu_{8_0}^1$	1164	$\nu_{9_0}^2$	1162	$\nu_{8_0}^1$
1135	$\nu_{6_0}^1$		1074	$\nu_{7_0}^1$	1242	$\nu_{6_0}^1$	1380	$\nu_{7_0}^1$
1295	$\nu_{9_0}^1+\nu_{10_0}^1$		1117	$\nu_{9_0}^1+\nu_{10_0}^1$	1250	$\nu_{8_0}^1+\nu_{9_0}^1$	1397	$\nu_{10_0}^3$
1309	$\nu_{10_0}^3$		1117	$\nu_{5_0}^1$	1268	$\nu_{5_0}^1$	1424	$\nu_{9_0}^1+\nu_{10_0}^1$
1360	$\nu_{7_0}^1$	1260	1375	$\nu_{8_0}^1+\nu_{10_0}^1$	1372	$\nu_{8_0}^2$	1444	$\nu_{6_0}^1$
1416	$\nu_{5_0}^1$		1415	$\nu_{6_0}^1$	1566	$\nu_{4_0}^1$	1511	$\nu_{5_0}^1$
1468	$\nu_{8_0}^1+\nu_{10_0}^1$		1432	$\nu_{7_0}^1+\nu_{10_0}^1$	1658	$\nu_{7_0}^1+\nu_{9_0}^1$	1849	$\nu_{7_0}^1+\nu_{10_0}^1$
1569	$\nu_{6_0}^1+\nu_{10_0}^1$		1489	$\nu_{5_0}^1+\nu_{10_0}^1$	1744	$\nu_{7_0}^1+\nu_{8_0}^1$	1889	$\nu_{9_0}^1+\nu_{10_0}^2$
1580	$\nu_{4_0}^1$		1525	$\nu_{9_0}^2$	1749	$\nu_{9_0}^3$	1909	$\nu_{9_0}^2$
1722	$\nu_{9_0}^2$		1772	$\nu_{6_0}^1+\nu_{10_0}^1$	1824	$\nu_{6_0}^1+\nu_{9_0}^1$	1912	$\nu_{6_0}^1+\nu_{10_0}^1$
1730	$\nu_{9_0}^1+\nu_{10_0}^2$		1777	$\nu_{8_0}^1+\nu_{9_0}^2$	1832	$\nu_{8_0}^1+\nu_{9_0}^2$	1980	$\nu_{5_0}^1+\nu_{10_0}^1$
1794	$\nu_{7_0}^2+\nu_{10_0}^1$		1834	$\nu_{7_0}^2+\nu_{9_0}^1$	1850	$\nu_{5_0}^1+\nu_{9_0}^1$	2109	$\nu_{4_0}^1$
1851	$\nu_{5_0}^1+\nu_{10_0}^1$		1837	$\nu_{4_0}^1$	1910	$\nu_{8_0}^2+\nu_{9_0}^1$	2314	$\nu_{7_0}^1+\nu_{10_0}^2$
1896	$\nu_{8_0}^1+\nu_{9_0}^1$		1883	$\nu_{5_0}^1+\nu_{9_0}^1$	1936	$\nu_{5_0}^1+\nu_{8_0}^1$	2335	$\nu_{7_0}^1+\nu_{9_0}^1$
1996	$\nu_{6_0}^2+\nu_{9_0}^1$		2036	$\nu_{8_0}^2$	1954	$\nu_{8_0}^3$	2352	$\nu_{9_0}^1+\nu_{10_0}^3$
2015	$\nu_{4_0}^1+\nu_{10_0}^2$		2092	$\nu_{7_0}^1+\nu_{8_0}^1$	2148	$\nu_{4_0}^1+\nu_{9_0}^1$	2378	$\nu_{9_0}^2+\nu_{10_0}^1$
2069	$\nu_{8_0}^2$		2135	$\nu_{7_0}^2$	2149	$\nu_{7_0}^2$	2378	$\nu_{6_0}^1+\nu_{10_0}^2$
2169	$\nu_{6_0}^1+\nu_{8_0}^1$		2144	$\nu_{5_0}^1+\nu_{8_0}^1$	2234	$\nu_{4_0}^1+\nu_{8_0}^1$	2399	$\nu_{6_0}^1+\nu_{9_0}^1$
2221	$\nu_{7_0}^1+\nu_{9_0}^1$		2175	$\nu_{6_0}^1+\nu_{9_0}^1$	2417	$\nu_{7_0}^1+\nu_{8_0}^2$	2466	$\nu_{5_0}^1+\nu_{9_0}^1$
2270	$\nu_{6_0}^2$		2192	$\nu_{5_0}^1+\nu_{7_0}^1$	2536	$\nu_{5_0}^2$	2578	$\nu_{4_0}^1+\nu_{10_0}^1$
2278	$\nu_{5_0}^1+\nu_{9_0}^1$		2192	$\nu_{4_0}^1+\nu_{10_0}^1$			2758	$\nu_{7_0}^2$
2394	$\nu_{7_0}^1+\nu_{8_0}^1$		2255	$\nu_{5_0}^2$			2777	$\nu_{4_0}^2+\nu_{10_0}^1$
2442	$\nu_{4_0}^1+\nu_{9_0}^1$		2432	$\nu_{6_0}^1+\nu_{8_0}^1$			2824	$\nu_{6_0}^1+\nu_{7_0}^1$
2451	$\nu_{5_0}^1+\nu_{8_0}^1$		2489	$\nu_{6_0}^1+\nu_{7_0}^1$			2843	$\nu_{9_0}^2+\nu_{10_0}^2$
2495	$\nu_{6_0}^1+\nu_{7_0}^1$		2532	$\nu_{5_0}^1+\nu_{6_0}^1$			2862	$\nu_{9_0}^3$
2552	$\nu_{5_0}^1+\nu_{6_0}^1$		2597	$\nu_{4_0}^1+\nu_{9_0}^1$			2888	$\nu_{6_0}^2$
2585	$\nu_{9_0}^3$		2627	$\nu_{5_0}^1+\nu_{9_0}^2$			2891	$\nu_{5_0}^1+\nu_{7_0}^1$
2615	$\nu_{4_0}^1+\nu_{8_0}^1$		2829	$\nu_{6_0}^2$			2955	$\nu_{4_0}^1+\nu_{5_0}^1$
2719	$\nu_{7_0}^2$		2855	$\nu_{4_0}^1+\nu_{8_0}^1$			3021	$\nu_{5_0}^2$
2552	$\nu_{5_0}^1+\nu_{7_0}^1$		2911	$\nu_{4_0}^1+\nu_{7_0}^1$				
2837	$\nu_{5_0}^2$		2938	$\nu_{3_0}^1$				
2848	$\nu_{3_0}^1$							
2940	$\nu_{4_0}^1+\nu_{7_0}^1$							
2997	$\nu_{4_0}^1+\nu_{5_0}^1$							

TABLE A6: Continued

$\widetilde{D}$ Energy	$\widetilde{D}$ Assignment	$\widetilde{E}$ Energy	$\widetilde{E}$ Assignment	$\widetilde{F}$ Energy	$\widetilde{F}$ Assignment
0	0_0^0	0	0_0^0	0	0_0^0
349	$\nu_{10_0}^1$	470	$\nu_{10_0}^1$	488	$\nu_{10_0}^1$
707	$\nu_{10_0}^2$	905	$\nu_{9_0}^1$	817	$\nu_{9_0}^1$
846	$\nu_{9_0}^1$	952	$\nu_{10_0}^2$	976	$\nu_{10_0}^2$
1087	$\nu_{8_0}^1$	1226	$\nu_{8_0}^1$	1082	$\nu_{6_0}^1$
1196	$\nu_{9_0}^1+\nu_{10_0}^1$	1375	$\nu_{9_0}^1+\nu_{10_0}^1$	1088	$\nu_{8_0}^1$
1350	$\nu_{7_0}^1$	1400	$\nu_{7_0}^1$	1305	$\nu_{9_0}^1+\nu_{10_0}^1$
1436	$\nu_{6_0}^1$	1479	$\nu_{10_0}^3$	1418	$\nu_{5_0}^1$
1436	$\nu_{8_0}^1+\nu_{10_0}^1$	1502	$\nu_{6_0}^1$	1436	$\nu_{7_0}^1$
1486	$\nu_{5_0}^1$	1684	$\nu_{5_0}^1$	1464	$\nu_{10_0}^3$
1553	$\nu_{9_0}^1+ \nu_{10_0}^2$	1696	$\nu_{8_0}^1+ \nu_{10_0}^1$	1570	$\nu_{6_0}^1+\nu_{10_0}^1$
1693	$\nu_{9_0}^2$	1816	$\nu_{9_0}^2$	1576	$\nu_{8_0}^1+\nu_{10_0}^1$
1693	$\nu_{7_0}^1+\nu_{10_0}^1$	1857	$\nu_{9_0}^1+\nu_{10_0}^2$	1636	$\nu_{9_0}^2$
1786	$\nu_{6_0}^1+\nu_{10_0}^1$	1870	$\nu_{7_0}^1+\nu_{10_0}^1$	1793	$\nu_{9_0}^1+\nu_{10_0}^2$
1794	$\nu_{8_0}^2+\nu_{10_0}^2$	1870	$\nu_{10_0}^4$	1797	$\nu_{4_0}^1$
1836	$\nu_{5_0}^1+\nu_{10_0}^1$	1972	$\nu_{6_0}^1+\nu_{10_0}^1$	1905	$\nu_{8_0}^1+\nu_{9_0}^1$
1934	$\nu_{8_0}^1+\nu_{9_0}^1$	2131	$\nu_{8_0}^1+\nu_{9_0}^1$	1906	$\nu_{5_0}^1+ \nu_{10_0}^1$
2057	$\nu_{7_0}^1+\nu_{10_0}^2$	2155	$\nu_{5_0}^1+\nu_{10_0}^1$	1924	$\nu_{7_0}^1+ \nu_{10_0}^1$
2143	$\nu_{6_0}^1+\nu_{10_0}^2$	2178	$\nu_{8_0}^1+\nu_{10_0}^2$	1955	$\nu_{10_0}^4$
2177	$\nu_{8_0}^2$	2305	$\nu_{7_0}^1+\nu_{9_0}^1$	2059	$\nu_{6_0}^1+\nu_{10_0}^2$
2187	$\nu_{4_0}^1$	2353	$\nu_{7_0}^1+\nu_{10_0}^2$	2065	$\nu_{8_0}^1+\nu_{10_0}^2$
2196	$\nu_{7_0}^1+\nu_{9_0}^1$	2353	$\nu_{10_0}^5$	2171	$\nu_{6_0}^1+\nu_{8_0}^1$
2283	$\nu_{6_0}^1+\nu_{9_0}^1$	2407	$\nu_{6_0}^1+\nu_{9_0}^1$	2177	$\nu_{8_0}^2$
2332	$\nu_{5_0}^1+\nu_{9_0}^1$	2452	$\nu_{6_0}^1+\nu_{10_0}^2$	2235	$\nu_{5_0}^1+\nu_{9_0}^1$
2523	$\nu_{4_0}^1+\nu_{10_0}^1$	2452	$\nu_{8_0}^2$	2253	$\nu_{7_0}^1+\nu_{9_0}^1$
2523	$\nu_{6_0}^1+\nu_{8_0}^1$	2590	$\nu_{5_0}^1+\nu_{9_0}^1$	2286	$\nu_{4_0}^1+\nu_{10_0}^1$
2573	$\nu_{5_0}^1+\nu_{8_0}^1$	2626	$\nu_{7_0}^1+\nu_{8_0}^1$	2395	$\nu_{5_0}^1+\nu_{10_0}^2$
2695	$\nu_{7_0}^2$	2637	$\nu_{5_0}^1+\nu_{10_0}^2$	2412	$\nu_{7_0}^1+\nu_{10_0}^2$
2786	$\nu_{6_0}^1+\nu_{7_0}^1$	2728	$\nu_{6_0}^1+\nu_{8_0}^1$	2457	$\nu_{9_0}^3$
2836	$\nu_{5_0}^1+\nu_{7_0}^1$	2801	$\nu_{7_0}^2$	2501	$\nu_{5_0}^1+\nu_{6_0}^1$
2872	$\nu_{6_0}^2$	2873	$\nu_{3_0}^1$	2507	$\nu_{5_0}^1+\nu_{8_0}^1$
2918	$\nu_{3_0}^1$	2911	$\nu_{5_0}^1+\nu_{8_0}^1$	2518	$\nu_{7_0}^1+\nu_{8_0}^1$
2968	$\nu_{5_0}^2$	3343	$\nu_{3_0}^1+\nu_{10_0}^1$	2524	$\nu_{6_0}^1+\nu_{7_0}^1$
3034	$\nu_{4_0}^1+\nu_{9_0}^1$			2615	$\nu_{4_0}^1+\nu_{9_0}^1$
3261	$\nu_{4_0}^1+\nu_{8_0}^1$			2774	$\nu_{4_0}^1+\nu_{10_0}^2$
3272	$\nu_{3_0}^1+\nu_{10_0}^1$			2837	$\nu_{5_0}^2$
				2854	$\nu_{5_0}^1+\nu_{7_0}^2$
				2872	$\nu_{7_0}^2$
				3117	$\nu_{3_0}^1$

TABLE A7: Normal mode combination, sizes of the primitive and single particle functions (SPFs) used in the coupled states dynamics calculations of $CH_3COH^{\cdot+}$ using MCTDH suite of programmes. [a] The primitive basis is the number of Harmonic oscillator DVR functions for the relevant mode. The primitive basis for each particle is the product of the one-dimensional bases. [b] The SPF basis is the number of single-particle functions used. The vibronic spectrum of the coupled electronic states of $CH_3COH^{\cdot+}$ is shown in Fig. 3.4 see in the text.

Electronic state	Normal modes	Primitive basis[a]	SPF basis[b]
	ν_3	(10)	[8,8,8,8,8,8,8]
	$\nu_4, \nu_5, \nu_6, \nu_7, \nu_{12}$	(12,14,8,10,12)	[10,10,8,10,8,8,8]
$\widetilde{X}$-$\widetilde{A}$-$\widetilde{B}$-$\widetilde{C}$-$\widetilde{D}$-$\widetilde{E}$-$\widetilde{F}$	ν_9, ν_{14}	(12,12)	[8,8,8,10,10,10,8]
	ν_8, ν_{13}	(12,10)	[8,8,10,8,10,10,8]
	ν_{10}, ν_{15}	(8,14)	[8,8,10,10,6,10,8]

(a) 1360 cm^{-1}

(b) 1135 cm^{-1}

(c) 1034 cm^{-1}

(d) 2719 cm^{-1}

(e) 2270 cm^{-1}

(f) 2069 cm^{-1}

(g) 2495 cm^{-1}

(h) 2394 cm^{-1}

(i) 2169 cm^{-1}
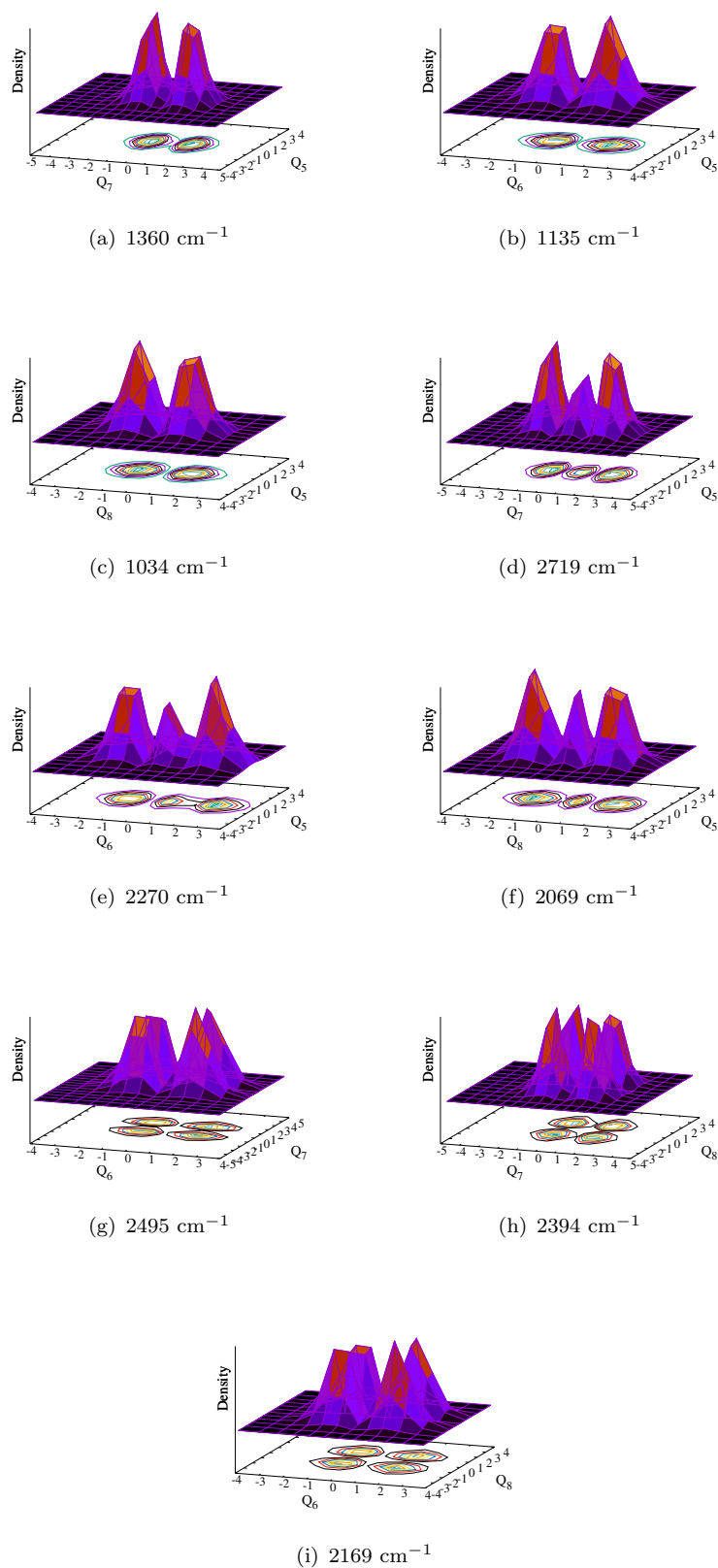
FIGURE A3: Probability density of vibronic wave functions of the $\widetilde{X}^2 A^{'}$ electronic state of $CH_3COH^{\cdot+}$ as a function of nuclear coordinate. Panels a, b and c represent the fundamentals ν_{70}^1, ν_{60}^1 and ν_{80}^1 and panels d, e and f represent the first overtone ν_{70}^2, ν_{60}^2 and ν_{80}^2, respectively. The wave functions in panels g, h and i represent the combination peaks $\nu_{60}^1 + \nu_{70}^1$, $\nu_{70}^1 + \nu_{80}^1$ and $\nu_{60}^1 + \nu_{80}^1$, respectively.

(a) 1837 cm^{-1}

(b) 1119 cm^{-1}

(c) 759 cm^{-1}

(d) 2233 cm^{-1}

(e) 2136 cm^{-1}

(f) 1519 cm^{-1}

(g) 1878 cm^{-1}

(h) 2596 cm^{-1}

(i) 2638 cm^{-1}
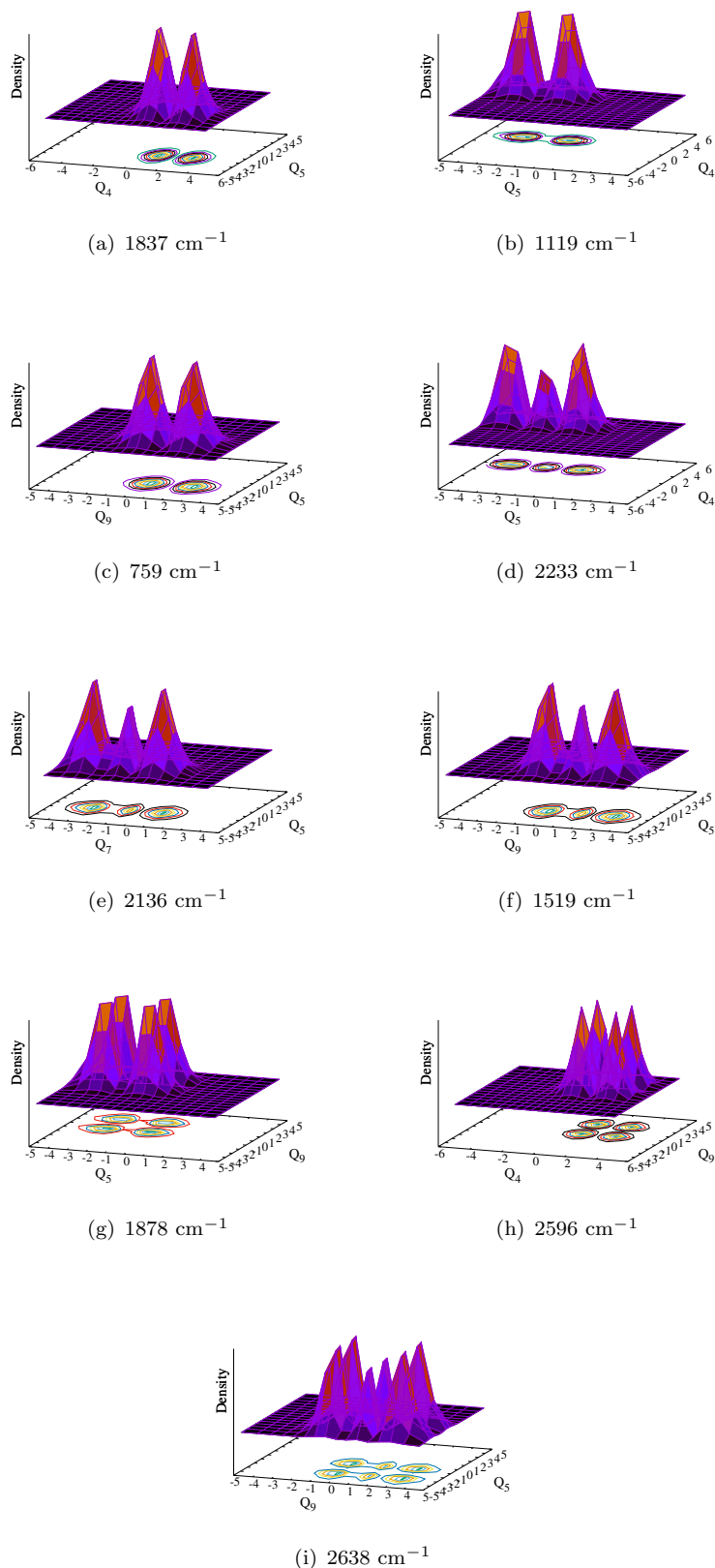
FIGURE A4: Probability density of vibronic wave functions of the $\widetilde{A}^2A''$ electronic state of $CH_3COH^{\cdot+}$ as a function of nuclear coordinate. Panels a, b and c represent the fundamentals ν_{40}^1, ν_{50}^1 and ν_{90}^1 and panels d, e and f represent the first overtone ν_{50}^2, ν_{70}^2 and ν_{90}^2, respectively. The wave functions in panels g, h and i represent the combination peaks $\nu_{50}^1+\nu_{90}^1$, $\nu_{40}^1+\nu_{90}^1$ and $\nu_{90}^1+\nu_{50}^1$, respectively.

(a) 1234 cm^{-1}

(b) 1076 cm^{-1}

(c) 683 cm^{-1}

(d) 2471 cm^{-1}

(e) 2148 cm^{-1}

(f) 1425 cm^{-1}

(g) 1918 cm^{-1}

(h) 1759 cm^{-1}

(i) 2501 cm^{-1}
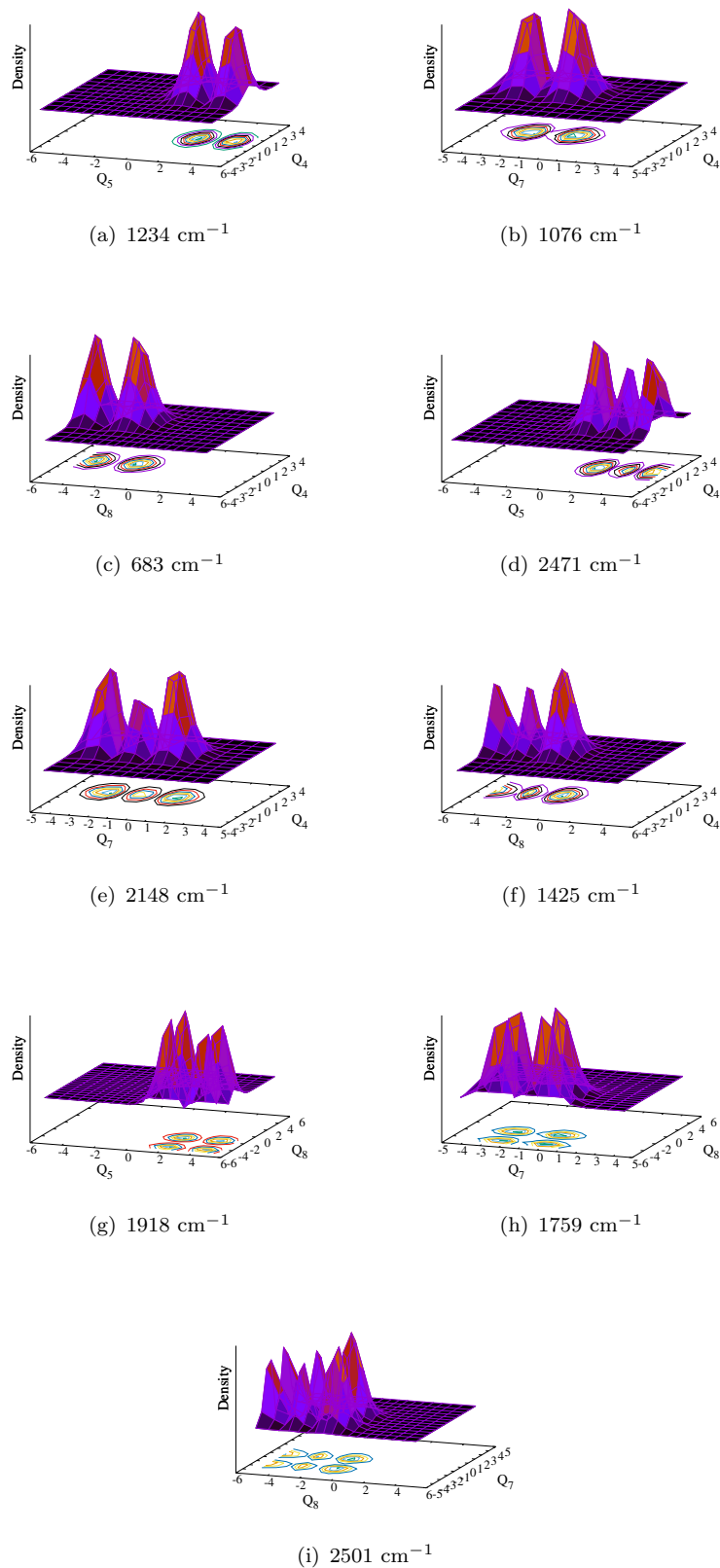
FIGURE A5: Probability density of vibronic wave functions of the $\widetilde{B}^2 A'$ electronic state of $CH_3COH^{·+}$ as a function of nuclear coordinate. Panels a, b and c represent the fundamentals ν_{50}^1, ν_{70}^1 and ν_{80}^1 and panels d, e and f represent the first overtone ν_{50}^2, ν_{70}^2 and ν_{80}^2, respectively. The wave functions in panels g, h and i represent the combination peaks $\nu_{50}^1 + \nu_{80}^1$, $\nu_{70}^1 + \nu_{80}^1$ and $\nu_{70}^1 + \nu_{80}^2$, respectively.

(a) 1380 cm^{-1}

(b) 955 cm^{-1}

(c) 468 cm^{-1}

(d) 2758 cm^{-1}

(e) 1909 cm^{-1}

(f) 934 cm^{-1}

(g) 2335 cm^{-1}

(h) 1848 cm^{-1}

(i) 1423 cm^{-1}
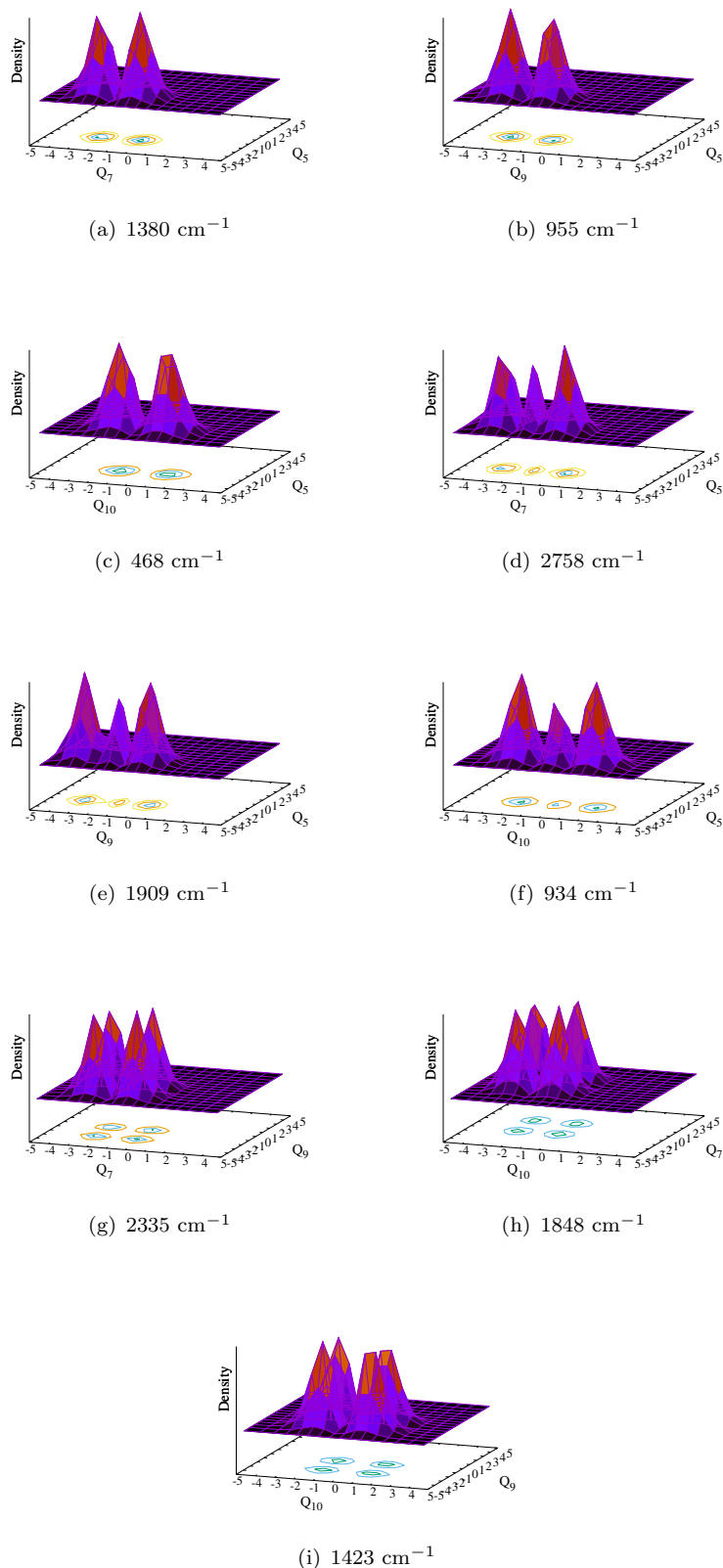
FIGURE A6: Probability density of vibronic wave functions of the $\widetilde{C}^2 A^{'}$ electronic state of $CH_3COH^{\cdot+}$ as a function of nuclear coordinate. Panels a, b and c represent the fundamentals ν_{70}^1, ν_{90}^1 and ν_{100}^1 and panels d, e and f represent the first overtone ν_{70}^2, ν_{90}^2 and ν_{100}^2, respectively. The wave functions in panels g, h and i represent the combination peaks $\nu_{70}^1 + \nu_{90}^1$, $\nu_{70}^1 + \nu_{100}^1$ and $\nu_{90}^1 + \nu_{100}^1$, respectively.

(a) 1486 cm^{-1}

(b) 1087 cm^{-1}

(c) 846 cm^{-1}

(d) 2967 cm^{-1}

(e) 2174 cm^{-1}

(f) 1693 cm^{-1}

(g) 2573 cm^{-1}

(h) 2332 cm^{-1}

(i) 1934 cm^{-1}
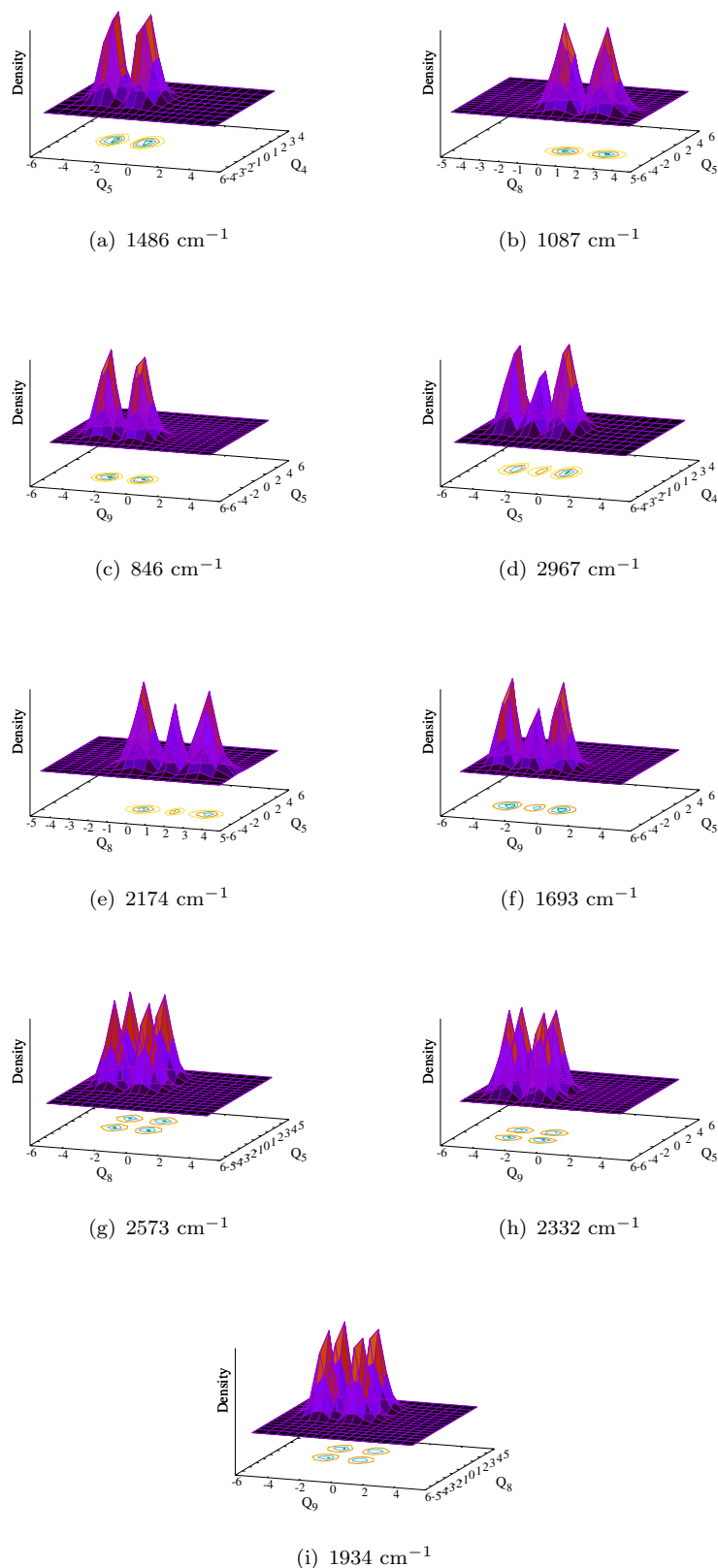
FIGURE A7: Probability density of vibronic wave functions of the $\widetilde{D}^2 A^{''}$ electronic state of $CH_3COH^{.+}$ as a function of nuclear coordinate. Panels a, b and c represent the fundamentals ν_{50}^1, ν_{80}^1 and ν_{90}^1 and panels d, e and f represent the first overtone ν_{50}^2, ν_{80}^2 and ν_{90}^2, respectively. The wave functions in panels g, h and i represent the combination peaks $\nu_{50}^1+\nu_{80}^1$, $\nu_{50}^1+\nu_{90}^1$ and $\nu_{90}^1+\nu_{80}^1$, respectively.

(a) 1684 cm^{-1}

(b) 1226 cm^{-1}

(c) 468 cm^{-1}

(d) 2452 cm^{-1}

(e) 2163 cm^{-1}

(f) 937 cm^{-1}

(g) 2911 cm^{-1}

(h) 2153 cm^{-1}

(i) 1695 cm^{-1}
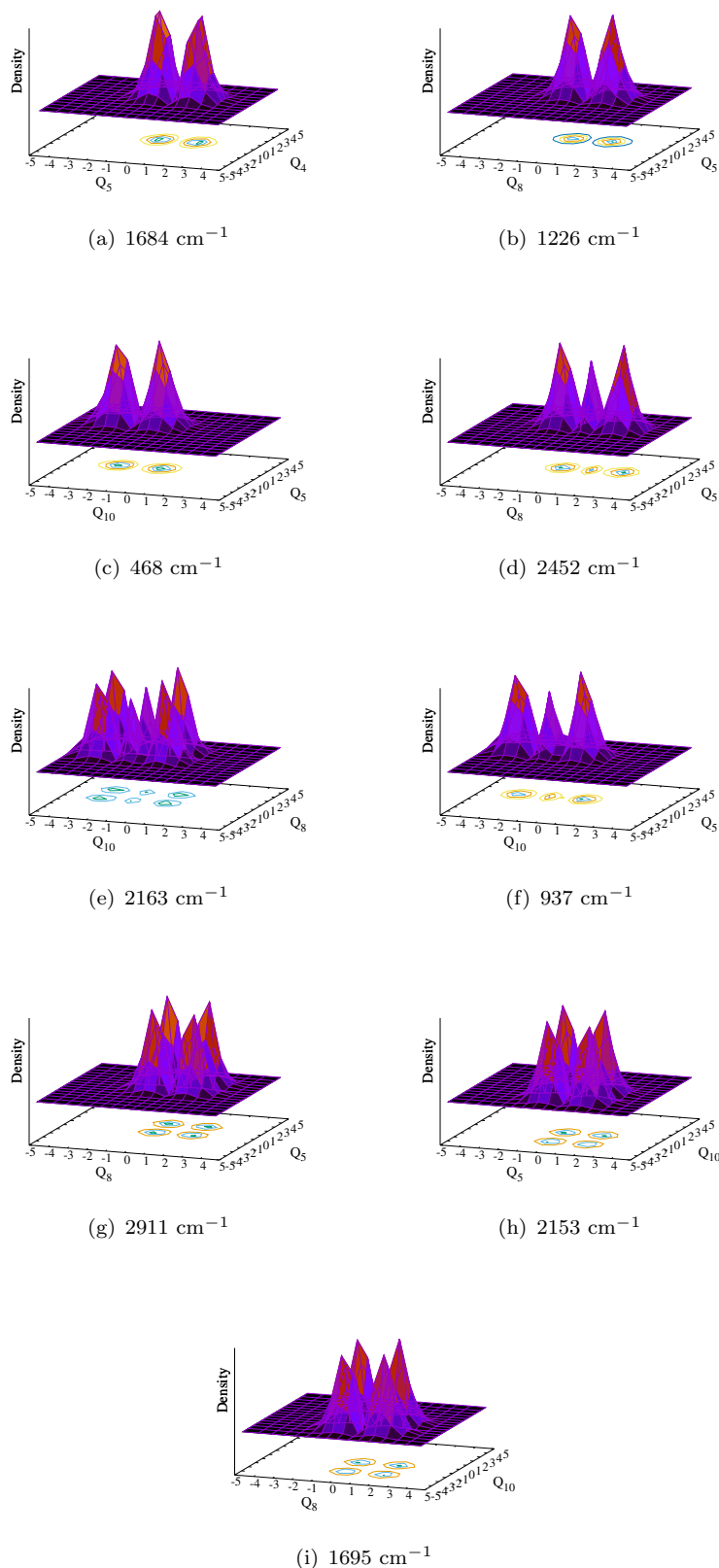
FIGURE A8: Probability density of vibronic wave functions of the $\widetilde{E}^2 A^{'}$ electronic state of CH$_3$COH$^{·+}$ as a function of nuclear coordinate. Panels a, b and c represent the fundamentals ν_{50}^1, ν_{80}^1 and ν_{100}^1 and panels d, e and f represent the first overtone ν_{80}^2, $\nu_{100}^2 + \nu_{80}^1$ and ν_{100}^2, respectively. The wave function in panels g, h and i represent the combination peaks $\nu_{50}^1 + \nu_{80}^1$, $\nu_{50}^1 + \nu_{100}^1$ and $\nu_{80}^1 + \nu_{100}^1$, respectively.

(a) 3117 cm^{-1}

(b) 1436 cm^{-1}

(c) 488 cm^{-1}

(d) 976 cm^{-1}

(e) 1464 cm^{-1}

(f) 1953 cm^{-1}

(g) 2872 cm^{-1}

(h) 2286 cm^{-1}

(i) 2774 cm^{-1}

FIGURE A9: Probability density of vibronic wave functions of the $\widetilde{F}^2 A'$ electronic state of $CH_3COH^{\cdot+}$ as a function of nuclear coordinate. Panels a, b and c represent the fundamentals ν_{30}^1, ν_{70}^1 and ν_{100}^1 and panels d, e and f represent the first, second and third overtones of ν_{10} mode. The wave functions in panels g, h and i represent the overtones, combination peaks ν_{70}^2, $\nu_{40}^1 + \nu_{100}^1$ and $\nu_{40}^1 + \nu_{100}^2$, respectively.
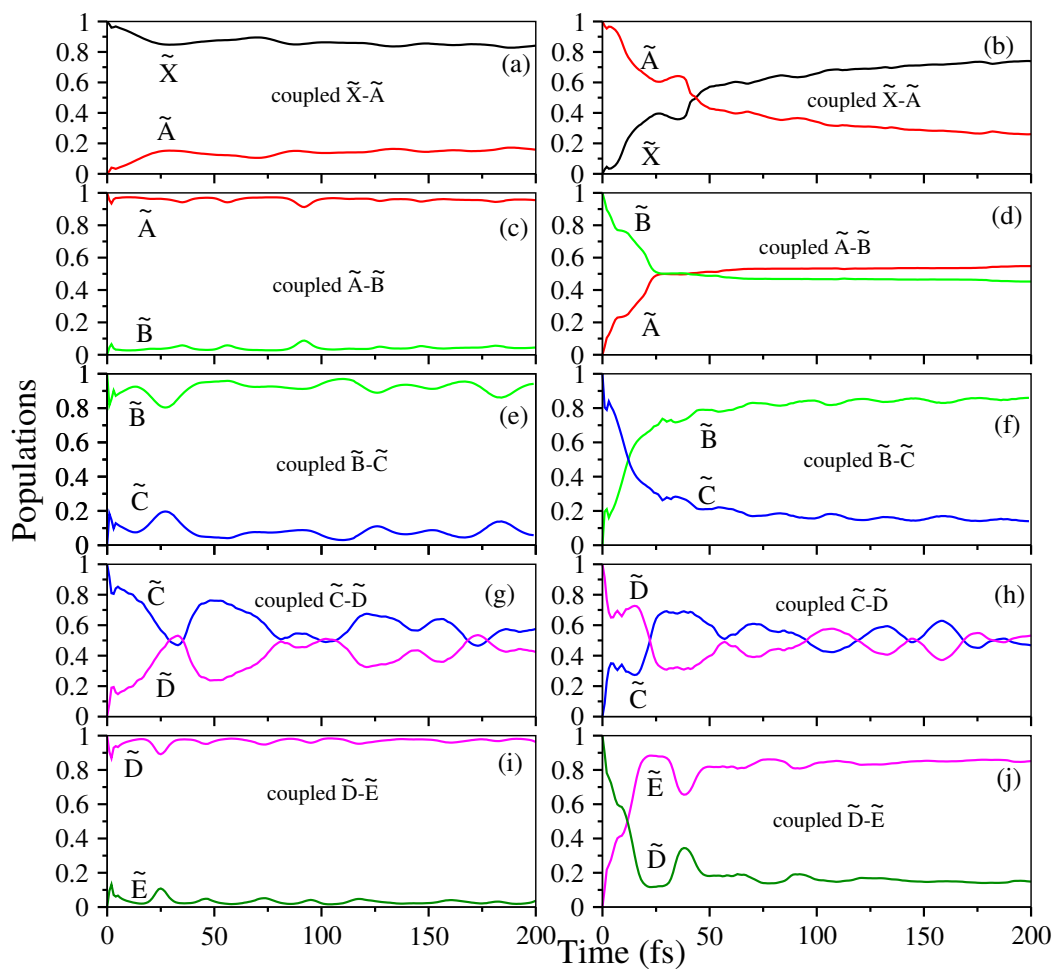
FIGURE A10: Time-dependence of diabatic electronic populations obtained in the coupled two states, $\widetilde{X}$-$\widetilde{A}$, $\widetilde{A}$-$\widetilde{B}$, $\widetilde{B}$-$\widetilde{C}$, $\widetilde{C}$-$\widetilde{D}$ and $\widetilde{D}$-$\widetilde{E}$ dynamics are shown in the panels (a)–(j), respectively (see text for details).

Appendix B

Supplementary material for Chapter 4

TABLE B1: *Ab initio* calculated cubic (ρ_i) and quartic (δ_i) coupling parameters for the $\widetilde{X}$ ^{2}B$_1$, $\widetilde{A}$ ^{2}A$_1$, $\widetilde{B}$ ^{2}B$_2$, $\widetilde{C}$ ^{2}A$_2$, $\widetilde{D}$ ^{2}A$_1$ and $\widetilde{E}$ ^{2}B$_1$ electronic states of c-C$_2$H$_4$O$^{\cdot+}$. All quantities are in eV.

Sym.	Mode	$\widetilde{X}$ ρ_i	$\widetilde{A}$ ρ_i	$\widetilde{B}$ ρ_i
	ν_1	-	-	-
a_1	ν_2	-0.0078	-	-0.0028
	ν_3	-	-	-
	ν_4	-0.0050	0.0082	-0.0131
	ν_5	-	-	-

Sym.	Mode	$\widetilde{C}$ ρ_i	$\widetilde{D}$ ρ_i	$\widetilde{E}$ ρ_i	δ_i
	ν_1	-	-	-	-
a_1	ν_2	0.0077	-0.0080	0.0134	-
	ν_3	-	-	-	-
	ν_4	0.0002	-	0.0036	0.0224
	ν_5	-	-	-	-

TABLE B2: *ab initio* calculated quadratic (γ_i) and quartic (δ_i) coupling parameters for the $\widetilde{X}$ $^2\text{B}_1$, $\widetilde{A}$ $^2\text{A}_1$, $\widetilde{B}$ $^2\text{B}_2$, $\widetilde{C}$ $^2\text{A}_2$, $\widetilde{D}$ $^2\text{A}_1$ and $\widetilde{E}$ $^2\text{B}_1$ electronic states of c-$\text{C}_2\text{H}_4\text{O}^{\cdot+}$. All quantities are in eV.

Sym.	Mode	$\widetilde{X}$ $^2\text{B}_1$		$\widetilde{A}$ $^2\text{A}_1$		$\widetilde{B}$ $^2\text{B}_2$	
		γ_i	δ_i	γ_i	δ_i	γ_i	δ_i
b_1	ν_6	0.0062	-0.0003	0.0115	-	-0.1990	0.1815
	ν_7	-0.0446	0.0031	0.0101	-0.0023	-0.3737	0.3331
	ν_8	-0.0764	0.0198	0.0840	-0.0146	-0.1017	-0.0055
b_2	ν_9	-0.0040	-	0.0053	-	-0.0023	-
	ν_{10}	-0.0297	-	-0.0034	-	-0.0212	-
	ν_{11}	-0.0101	-0.0019	0.0075	-0.0008	-0.0097	-0.0014
	ν_{12}	-0.0301	0.0005	-0.0994	0.0158	0.1266	-0.0308
a_2	ν_{13}	0.0041	-	0.0036	-	0.0123	-0.0003
	ν_{14}	-0.0083	-0.0002	-0.0805	-0.0023	-0.0034	-0.0003
	ν_{15}	-0.0339	0.0009	-0.0765	0.0077	0.0029	-0.0003

Sym.	Mode	$\widetilde{C}$ $^2\text{A}_2$		$\widetilde{D}$ $^2\text{A}_1$		$\widetilde{E}$ $^2\text{B}_1$	
		γ_i	δ_i	γ_i	δ_i	γ_i	δ_i
b_1	ν_6	0.1820	-0.1791	-0.0548	0.0087	0.0541	-0.0079
	ν_7	0.2885	-0.3310	-0.0165	0.0010	-0.0372	0.0022
	ν_8	-0.0536	0.0211	-0.0299	0.0053	-0.0319	-0.0018
b_2	ν_9	-0.0353	0.0046	-0.0096	-	0.0888	-
	ν_{10}	-0.1635	0.0200	-0.0063	-	0.0299	-0.0103
	ν_{11}	-0.1021	0.0078	-0.0130	-	-0.0656	0.0051
	ν_{12}	0.0350	-0.0006	0.0053	0.0006	0.0069	0.0009
a_2	ν_{13}	-0.0580	0.0086	0.0887	-0.0096	-0.0519	0.0072
	ν_{14}	-0.0927	0.0322	0.0388	-0.0115	-0.0321	0.0021
	ν_{15}	-0.0119	-0.0045	-0.0300	0.0022	-0.0466	0.0021

TABLE B3: *Ab initio* calculated sixth (σ_i) and eighth (ξ_i) coupling parameters for the $\widetilde{B}\ ^2B_2$ and $\widetilde{C}\ ^2A_2$ electronic states of c-$C_2H_4O^{\cdot+}$. All quantities are in eV.

Sym.	Mode	$\widetilde{B}\ ^2B_2$		$\widetilde{C}\ ^2A_2$	
		σ_i	ξ_i	σ_i	ξ_i
b_1	ν_6	-0.2457	0.2283	0.2435	-0.2255
	ν_7	-0.4585	0.4292	0.4591	-0.4303
	ν_8	-	-	-0.0119	-
b_2	ν_9	-	-	-	-
	ν_{10}	-	-	-	-
	ν_{11}	-	-	-	-
	ν_{12}	0.0126	-	-0.0003	-
a_2	ν_{13}	-	-	-	-
	ν_{14}	-0.00008	-	-0.0127	-
	ν_{15}	-	-	-	-

TABLE B4: Linear inter-state coupling parameter and the corresponding excitation strength (in eV) ($\frac{1}{2}\left(\frac{\lambda^{nm}}{\omega_i}\right)^2$) (given in the parentheses) between the n and m states (λ^{nm}) of c-$C_2H_4O^{\cdot+}$ molecule.

Symmetry	Mode	λ^{nm}	λ^{nm}	λ^{nm}
		$\widetilde{X}$-$\widetilde{A}$	$\widetilde{X}$-$\widetilde{D}$	$\widetilde{A}$-$\widetilde{E}$
b_1	ν_6	0.2139(0.1400)	-	0.2431(0.2431)
	ν_7	0.0981(0.2289)	0.6137(8.9588)	-
	ν_8	0.1628(1.2722)	0.2106(2.1290)	-
		$\widetilde{B}$-$\widetilde{C}$	$\widetilde{D}$-$\widetilde{E}$	
b_1	ν_6	0.1953(0.1167)	0.1770(0.0958)	
	ν_7	0.3437(2.8099)	-	
	ν_8	0.0622(0.1857)	-	
		$\widetilde{X}$-$\widetilde{C}$	$\widetilde{A}$-$\widetilde{B}$	$\widetilde{B}$-$\widetilde{D}$
b_2	ν_9	-	-	0.2979(0.2910)
	ν_{10}	-	-	0.3369(1.6075)
	ν_{11}	-	-	1.7871(76.6764)
	ν_{12}	0.1732(1.3635)	0.2509(2.8613)	-
		$\widetilde{C}$-$\widetilde{E}$		
b_2	ν_9	0.2248(0.1657)		
	ν_{10}	0.2821(1.1271)		
	ν_{11}	0.0825(0.1634)		
	ν_{12}	-		
		$\widetilde{X}$-$\widetilde{B}$	$\widetilde{A}$-$\widetilde{C}$	$\widetilde{C}$-$\widetilde{D}$
a_2	ν_{13}	0.3569(0.3930)	-	0.4916(0.7457)
	ν_{14}	0.0401(0.0376)	-	0.4908(5.6379)
	ν_{15}	0.0891(0.2332)	0.1415(0.5882)	-

TABLE B5: The number of harmonic oscillator (HO) basis functions along the totally symmetric vibrational modes and the dimension of the secular matrix used in the calculation of the stick vibrational spectra of the uncoupled electronic states of c-$C_2H_4O^{\cdot+}$ is shown in Fig. 4.4

Electronic state	Normal modes	Primitive basis	Dimension of secular matrix
$\widetilde{X}\ ^2B_1$	$\nu_1,\ \nu_2$ $\nu_3,\ \nu_4,\ \nu_5$	(16,26) (24,28,24)	6709248
$\widetilde{A}\ ^2A_1$	$\nu_1,\ \nu_2$ $\nu_3,\ \nu_4,\ \nu_5$	(16,24) (26,32,28)	8945664
$\widetilde{B}\ ^2B_2$	$\nu_1,\ \nu_2$ $\nu_3,\ \nu_4,\ \nu_5$	(16,28) (22,30,30)	8870400
$\widetilde{C}\ ^2A_2$	$\nu_1,\ \nu_2$ $\nu_3,\ \nu_4,\ \nu_5$	(26,28) (20,20,26)	7571200
$\widetilde{D}\ ^2A_1$	$\nu_1,\ \nu_2$ $\nu_3,\ \nu_4,\ \nu_5$	(22,30) (28,22,26)	10570560
$\widetilde{E}\ ^2B_1$	$\nu_1,\ \nu_2$ $\nu_3,\ \nu_4,\ \nu_5$	(22,24) (26,24,20)	6589440

TABLE B6: A few vibrational energy levels (in cm^{-1}) of the $\widetilde{X}$ ^{2}B$_1$, $\widetilde{A}$ ^{2}A$_1$, $\widetilde{B}$ ^{2}B$_2$, $\widetilde{C}$ ^{2}A$_2$, $\widetilde{D}$ ^{2}A$_1$ and $\widetilde{E}$ ^{2}B$_1$ electronic states of c-C$_2$H$_4$O$^{\cdot+}$ obtained from the uncoupled state calculations. The assignment of the levels carried out by examining the nodal pattern of the wavefunctions are included in the table.

$\widetilde{X}$ ^{2}B$_1$		Expt. [86]	$\widetilde{A}$ ^{2}A$_1$		$\widetilde{B}$ ^{2}B$_2$		$\widetilde{C}$ ^{2}A$_2$	
Energy	Assignment	Energy	Energy	Assignment	Energy	Assignment	Energy	Assignment
0	0_0^0		0	0_0^0	0	0_0^0	0	0_0^0
856	ν_{50}^1	700-800	832	ν_{50}^1	923	ν_{50}^1	671	ν_{40}^1
1172	ν_{40}^1		1136	ν_{40}^1	1152	ν_{40}^1	877	ν_{50}^1
1292	ν_{30}^1	1120	1366	ν_{30}^1	1248	ν_{30}^1	1177	ν_{30}^1
1446	ν_{20}^1		1576	ν_{20}^1	1620	ν_{20}^1	1267	ν_{20}^1
1712	ν_{50}^2		1664	ν_{50}^2	1846	ν_{50}^2	1342	ν_{40}^2
2028	$\nu_{40}^1+\nu_{50}^1$		1968	$\nu_{40}^1+\nu_{50}^1$	2076	$\nu_{40}^1+\nu_{50}^1$	1548	$\nu_{40}^1+\nu_{50}^1$
2147	$\nu_{30}^1+\nu_{50}^1$		2199	$\nu_{30}^1+\nu_{50}^1$	2171	$\nu_{30}^1+\nu_{50}^1$	1754	ν_{50}^2
2301	$\nu_{20}^1+\nu_{50}^1$		2271	ν_{40}^2	2305	ν_{40}^2	1849	$\nu_{30}^1+\nu_{40}^1$
2344	ν_{40}^2		2408	$\nu_{20}^1+\nu_{50}^1$	2400	$\nu_{30}^1+\nu_{40}^1$	1938	$\nu_{20}^1+\nu_{40}^1$
2464	$\nu_{30}^1+\nu_{40}^1$		2496	ν_{50}^3	2496	ν_{30}^2	2013	ν_{40}^3
2567	ν_{50}^3		2503	$\nu_{30}^1+\nu_{40}^1$	2544	$\nu_{20}^1+\nu_{50}^1$	2054	$\nu_{30}^1+\nu_{50}^1$
2583	ν_{30}^2		2712	$\nu_{20}^1+\nu_{40}^1$	2770	ν_{50}^3	2144	$\nu_{20}^1+\nu_{50}^1$
2618	$\nu_{20}^1+\nu_{40}^1$		2733	ν_{30}^3	2773	$\nu_{20}^1+\nu_{40}^1$	2355	ν_{30}^2
2737	$\nu_{20}^1+\nu_{30}^1$		2943	$\nu_{20}^1+\nu_{30}^1$	2868	$\nu_{30}^1+\nu_{20}^1$	2425	$\nu_{40}^1+\nu_{50}^2$
2891	ν_{20}^2		3152	ν_{20}^2	3149	ν_{10}^1	2532	ν_{20}^2
3170	ν_{10}^1		3184	ν_{10}^1	3239	ν_{20}^2	2631	ν_{50}^3
3439	ν_{40}^3		3240	ν_{40}^3	3458	ν_{40}^3	3021	$\nu_{20}^1+\nu_{50}^2$
3875	ν_{30}^3		4016	$\nu_{10}^1+\nu_{50}^1$	3696	ν_{50}^4	3260	ν_{10}^1
4026	$\nu_{10}^1+\nu_{50}^1$		4100	ν_{30}^3	3744	ν_{30}^3	3533	ν_{30}^3
4335	ν_{20}^3		4288	$\nu_{10}^1+\nu_{40}^1$	4073	$\nu_{10}^1+\nu_{50}^1$	3931	$\nu_{10}^1+\nu_{40}^1$
4343	$\nu_{10}^1+\nu_{40}^1$		4551	$\nu_{10}^1+\nu_{30}^1$	4302	$\nu_{10}^1+\nu_{40}^1$	4137	$\nu_{10}^1+\nu_{50}^1$
4462	$\nu_{10}^1+\nu_{30}^1$		4760	$\nu_{10}^1+\nu_{20}^1$	4397	$\nu_{10}^1+\nu_{30}^1$		
					4476	$\nu_{10}^1+\nu_{20}^1$		

TABLE B6: Continued

$\widetilde{D}\ ^2A_1$		$\widetilde{E}\ ^2B_1$	
Energy	Assignment	Energy	Assignment
0	0_0^0	0	0_0^0
1000	ν_{50}^1	1006	ν_{40}^1
1248	ν_{40}^1	1019	ν_{50}^1
1305	ν_{30}^1	1347	ν_{30}^1
1590	ν_{20}^1	1524	ν_{20}^1
2000	ν_{50}^2	2015	ν_{40}^2
2248	$\nu_{40}^1+\nu_{50}^1$	2025	$\nu_{40}^1+\nu_{50}^1$
2305	$\nu_{30}^1+\nu_{50}^1$	2039	ν_{50}^2
2496	ν_{40}^2	2353	$\nu_{30}^1+\nu_{40}^1$
2554	$\nu_{30}^1+\nu_{40}^1$	2366	$\nu_{30}^1+\nu_{50}^1$
2590	$\nu_{20}^1+\nu_{50}^1$	2530	$\nu_{30}^1+\nu_{40}^1$
2611	ν_{30}^2	2544	$\nu_{20}^1+\nu_{50}^1$
2837	$\nu_{20}^1+\nu_{40}^1$	2694	ν_{30}^2
2895	$\nu_{20}^1+\nu_{30}^1$	2871	$\nu_{20}^1+\nu_{30}^1$
3000	ν_{50}^3	3032	ν_{40}^3
3126	ν_{10}^1	3047	ν_{20}^2
3179	ν_{20}^2	3058	ν_{50}^3
3745	ν_{40}^3	3267	ν_{10}^1
3916	ν_{30}^3	4041	ν_{30}^3
4126	$\nu_{10}^1+\nu_{50}^1$	4273	$\nu_{10}^1+\nu_{40}^1$
4374	$\nu_{10}^1+\nu_{40}^1$	4287	$\nu_{10}^1+\nu_{50}^1$
4431	$\nu_{10}^1+\nu_{30}^1$	4614	$\nu_{10}^1+\nu_{30}^1$
4715	$\nu_{10}^1+\nu_{20}^1$	4792	$\nu_{10}^1+\nu_{20}^1$

TABLE B7: Normal mode combination, sizes of the primitive and single particle functions (SPFs) used in the coupled states dynamics calculations of c-$C_2H_4O^{\cdot+}$ using the MCTDH suite of programs. ^{a} The primitive basis is the number of Harmonic oscillator DVR functions for the relevant mode. The primitive basis for each particle is the product of the one-dimensional bases. ^{b} The SPF basis is the number of single-particle functions used. The vibronic spectrum of the coupled electronic states of the c-$C_2H_4O^{\cdot+}$ is shown in Fig. 4.5.

Electronic state	Normal modes	Primitive basis^a	SPF basis^b
$\widetilde{X}\ ^2B_1$-$\widetilde{A}\ ^2A_1$-$\widetilde{B}\ ^2B_2$ -$\widetilde{C}\ ^2A_2$-$\widetilde{D}\ ^2A_1$-$\widetilde{E}\ ^2B_1$	$\nu_1,\ \nu_6,\ \nu_9,\ \nu_{13}$	(10,10,10,10)	[8,8,8,10,10,10]
	$\nu_2,\ \nu_3,\ \nu_{10}$	(16,18,12)	[10,10,8,10,10,10]
	$\nu_4,\ \nu_7,\ \nu_{11},\ \nu_{14},\ \nu_{15}$	(18,10,12,10,10)	[8,8,8,12,12,10]
	$\nu_5,\ \nu_8,\ \nu_{12}$	(18,14,10)	[8,8,10,10,12,10]

(a) 1446 cm^{-1}

(b) 1172 cm^{-1}

(c) 856 cm^{-1}

(d) 2891 cm^{-1}

(e) 2344 cm^{-1}

(f) 1712 cm^{-1}

(g) 2618 cm^{-1}

(h) 2301 cm^{-1}

(i) 2028 cm^{-1}
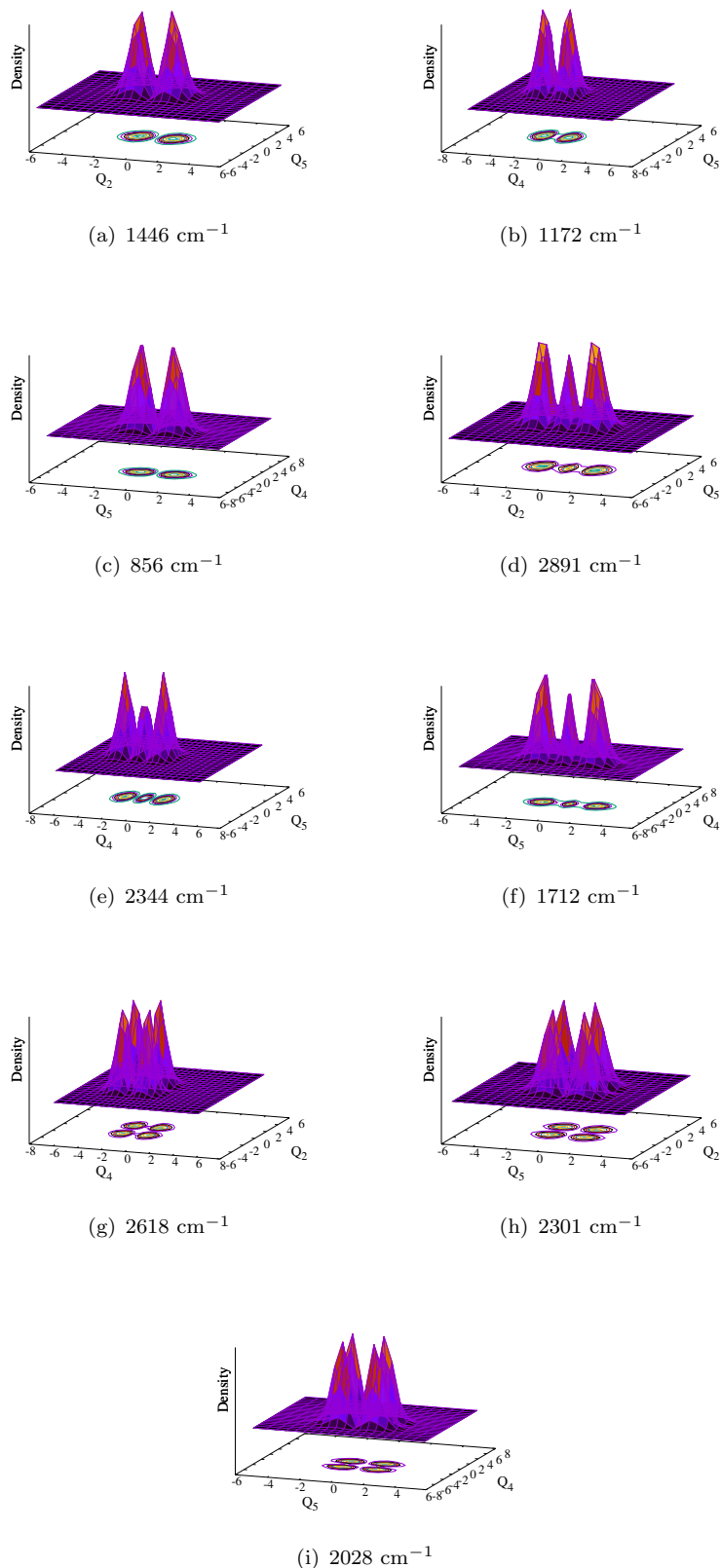
FIGURE B1: Probability density of vibronic wave functions of the $\widetilde{X}$ ^{2}B$_1$ electronic state of c-C$_2$H$_4$O$^{\cdot+}$ as a function of nuclear coordinate. Panels a, b and c represent the fundamental of ν_{20}^1, ν_{40}^1 and ν_{50}^1 and first overtone of ν_{20}^2, ν_{40}^2 and ν_{50}^2 modes, the wavefunction in panels g, h and i represent the combination peak of $\nu_{40}^1+\nu_{20}^1$, $\nu_{50}^1+\nu_{20}^1$ and $\nu_{50}^1+\nu_{40}^1$.

(a) 1366 cm^{-1}
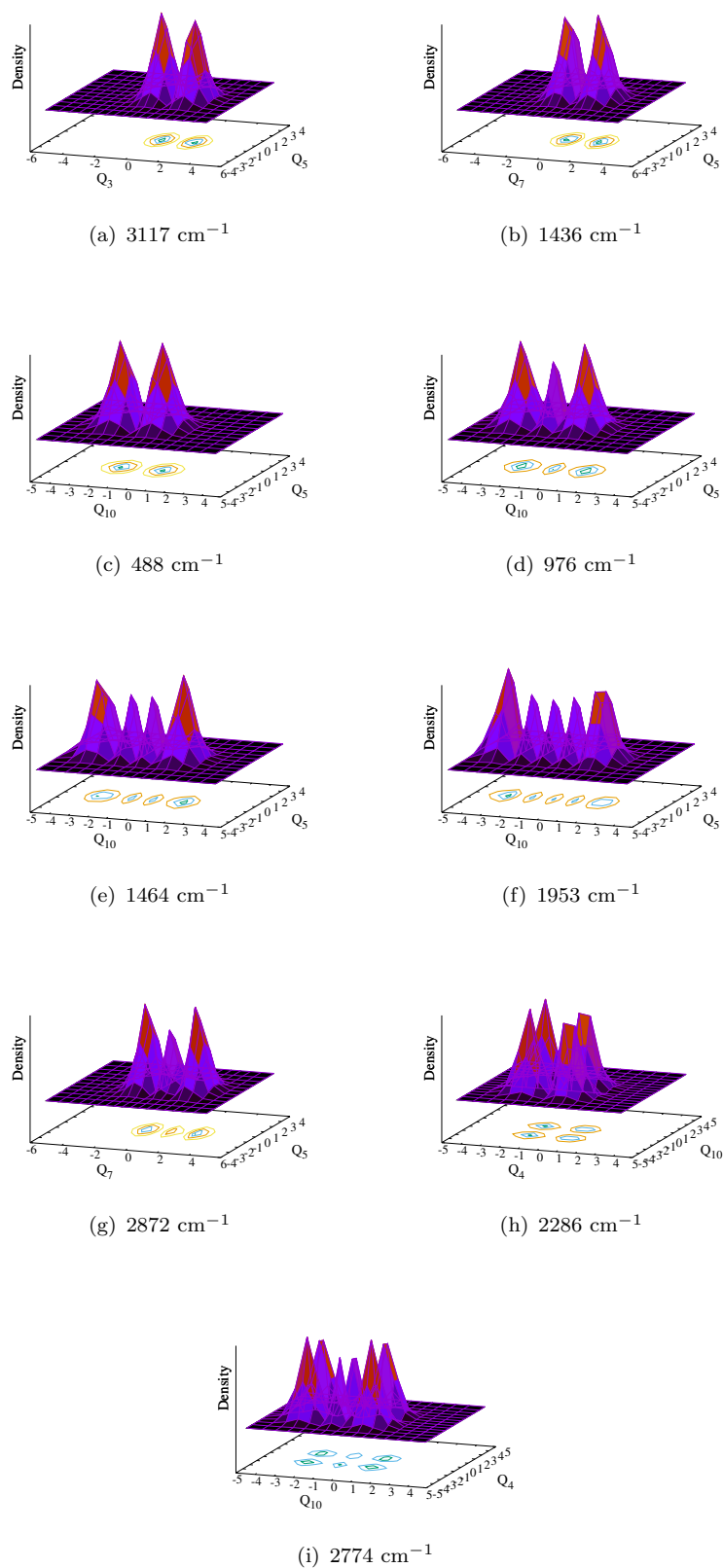

(b) 1136 cm^{-1}

(c) 832 cm^{-1}

(d) 2733 cm^{-1}

(e) 2271 cm^{-1}

(f) 1664 cm^{-1}

(g) 2503 cm^{-1}

(h) 2199 cm^{-1}

(i) 1968 cm^{-1}
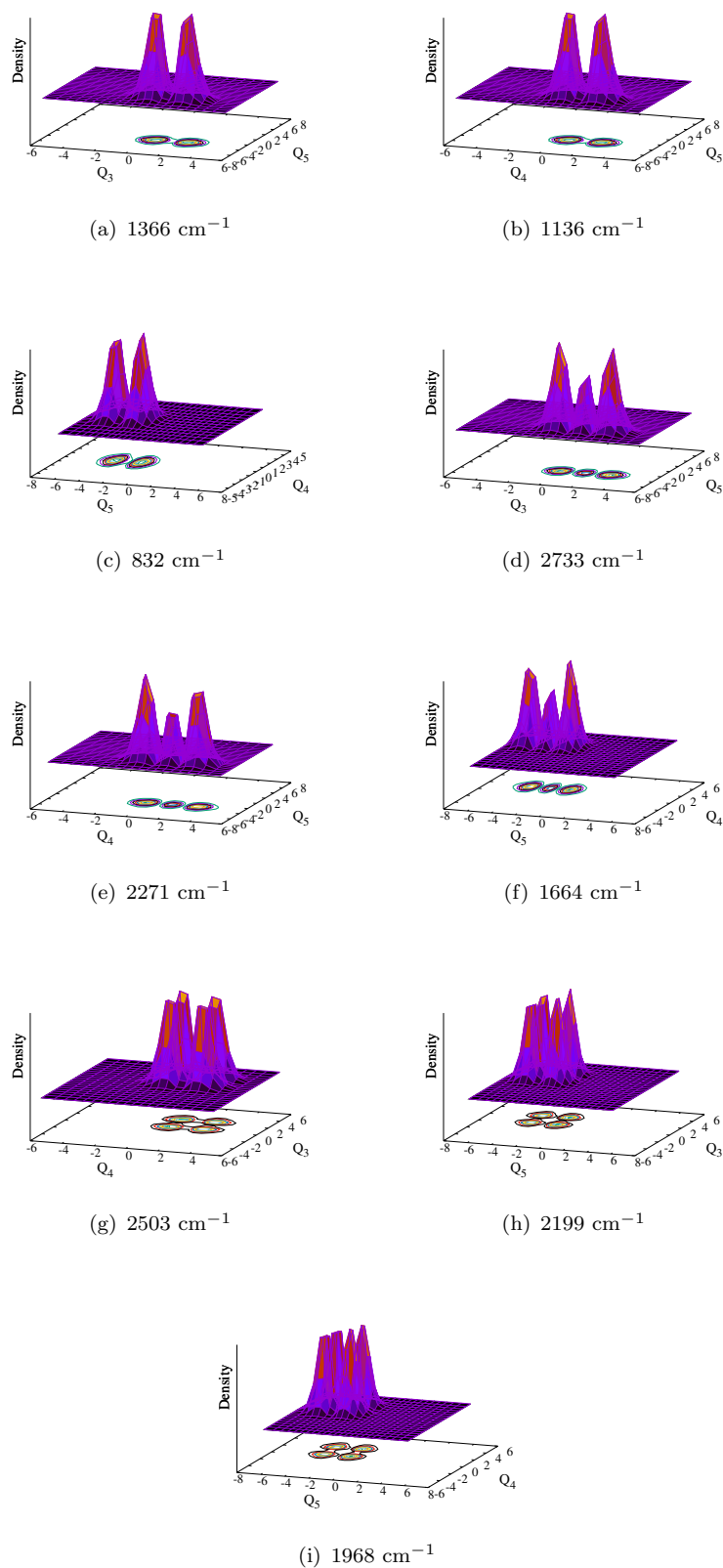
FIGURE B2: Probability density of vibronic wave functions of the $\widetilde{A}\ ^2A_1$ electronic state of c-$C_2H_4O^{\cdot+}$ as a function of nuclear coordinate. Panels a, b and c represent the fundamental of ν_{30}^1, ν_{40}^1 and ν_{50}^1 and first overtone of ν_{30}^2, ν_{40}^2 and ν_{50}^2 modes, the wavefunction in panels g, h and i represent the combination peak of $\nu_{40}^1+\nu_{30}^1$, $\nu_{50}^1+\nu_{30}^1$ and $\nu_{50}^1+\nu_{40}^1$.

(a) 1620 cm^{-1}

(b) 1152 cm^{-1}

(c) 923 cm^{-1}

(d) 3239 cm^{-1}

(e) 2305 cm^{-1}

(f) 1846 cm^{-1}

(g) 2773 cm^{-1}

(h) 2544 cm^{-1}

(i) 2076 cm^{-1}
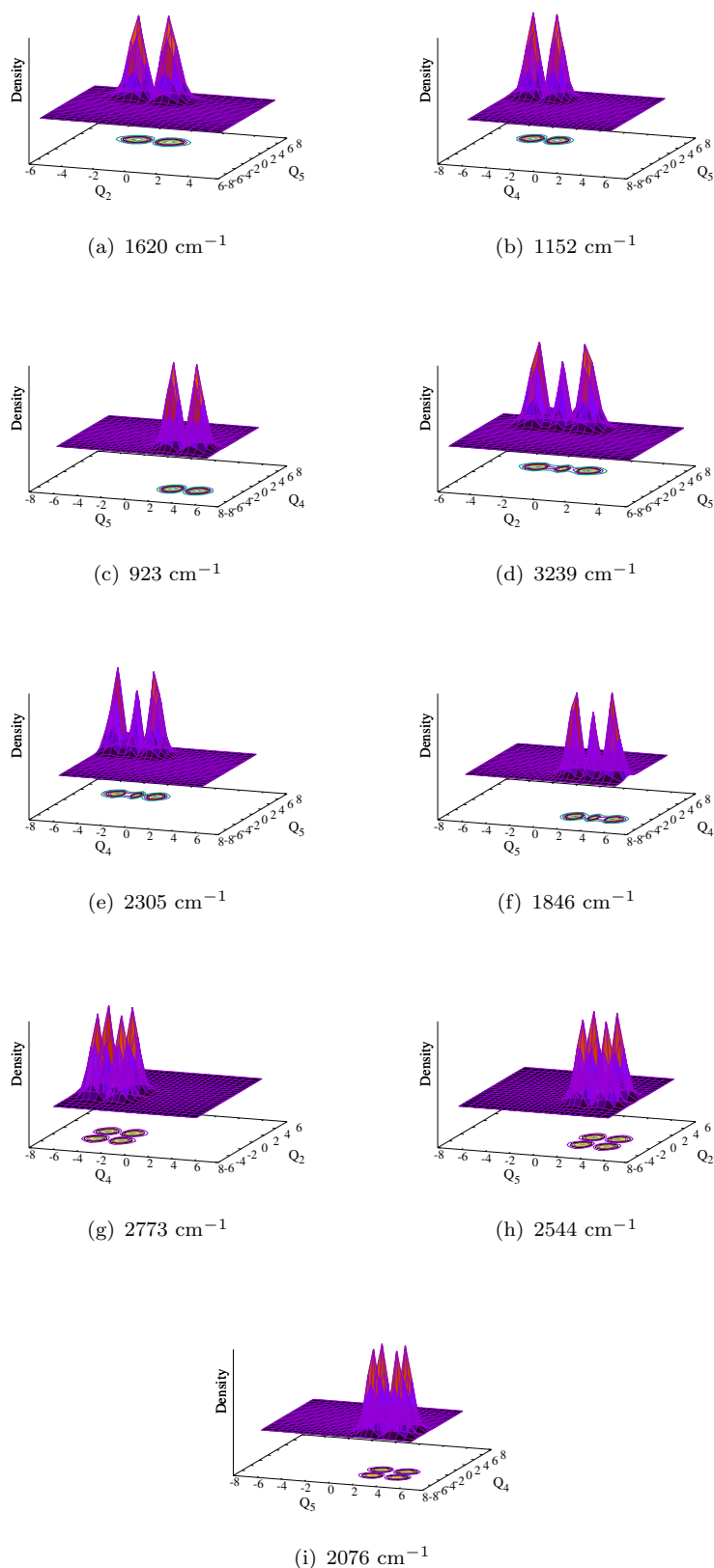
FIGURE B3: Probability density of vibronic wave functions of the $\widetilde{B}$ $^2B_2$ electronic state of c-C$_2$H$_4$O$^{\cdot+}$ as a function of nuclear coordinate. Panels a, b and c represent the fundamental of ν_{20}^1, ν_{40}^1 and ν_{50}^1 and first overtone of ν_{20}^2, ν_{40}^2 and ν_{50}^2 modes, the wavefunction in panels g, h and i represent the combination peak of $\nu_{40}^1+\nu_{20}^1$, $\nu_{50}^1+\nu_{20}^1$ and $\nu_{50}^1+\nu_{40}^2$.

(a) 3260 cm^{-1}

(b) 1267 cm^{-1}

(c) 877 cm^{-1}

(d) 2533 cm^{-1}

(e) 1548 cm^{-1}

(f) 2631 cm^{-1}

(g) 4137 cm^{-1}

(h) 2144 cm^{-1}

(i) 3021 cm^{-1}
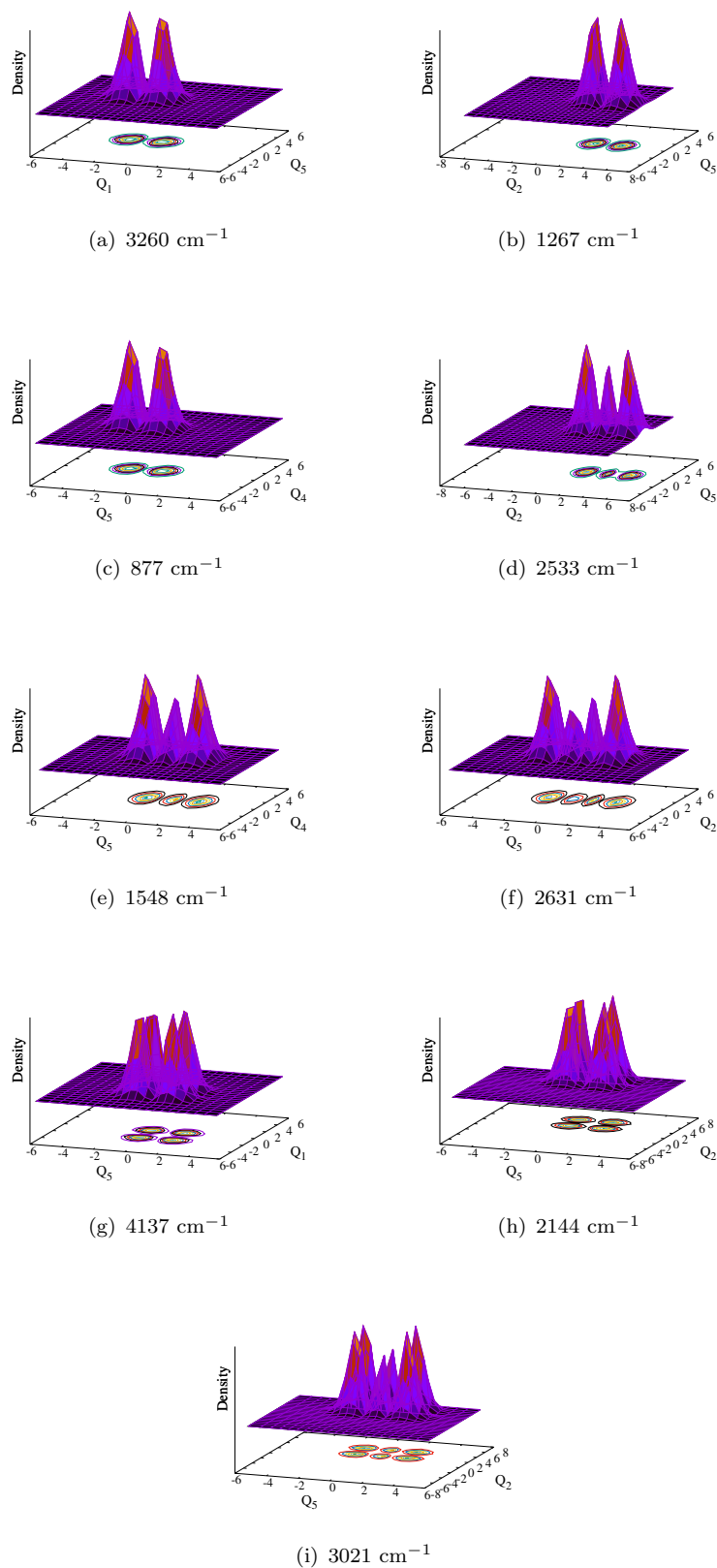
FIGURE B4: Probability density of vibronic wave functions of the $\widetilde{C}\ ^2A_2$ electronic state of c-$C_2H_4O^{\cdot+}$ as a function of nuclear coordinate. Panels a, b and c represent the fundamental of ν_{10}^1, ν_{20}^1 and ν_{50}^1 and first overtone and second overtone of ν_{20}^2, ν_{50}^2 and ν_{50}^3 modes, the wavefunction in panels g, h and i represent the combination peak of $\nu_{50}^1+\nu_{10}^1$, $\nu_{50}^1+\nu_{20}^1$ and $\nu_{50}^2+\nu_{20}^1$.

(a) 1590 cm^{-1}

(b) 1305 cm^{-1}

(c) 1000 cm^{-1}

(d) 3179 cm^{-1}

(e) 2611 cm^{-1}

(f) 2000 cm^{-1}

(g) 2895 cm^{-1}

(h) 2590 cm^{-1}

(i) 2305 cm^{-1}
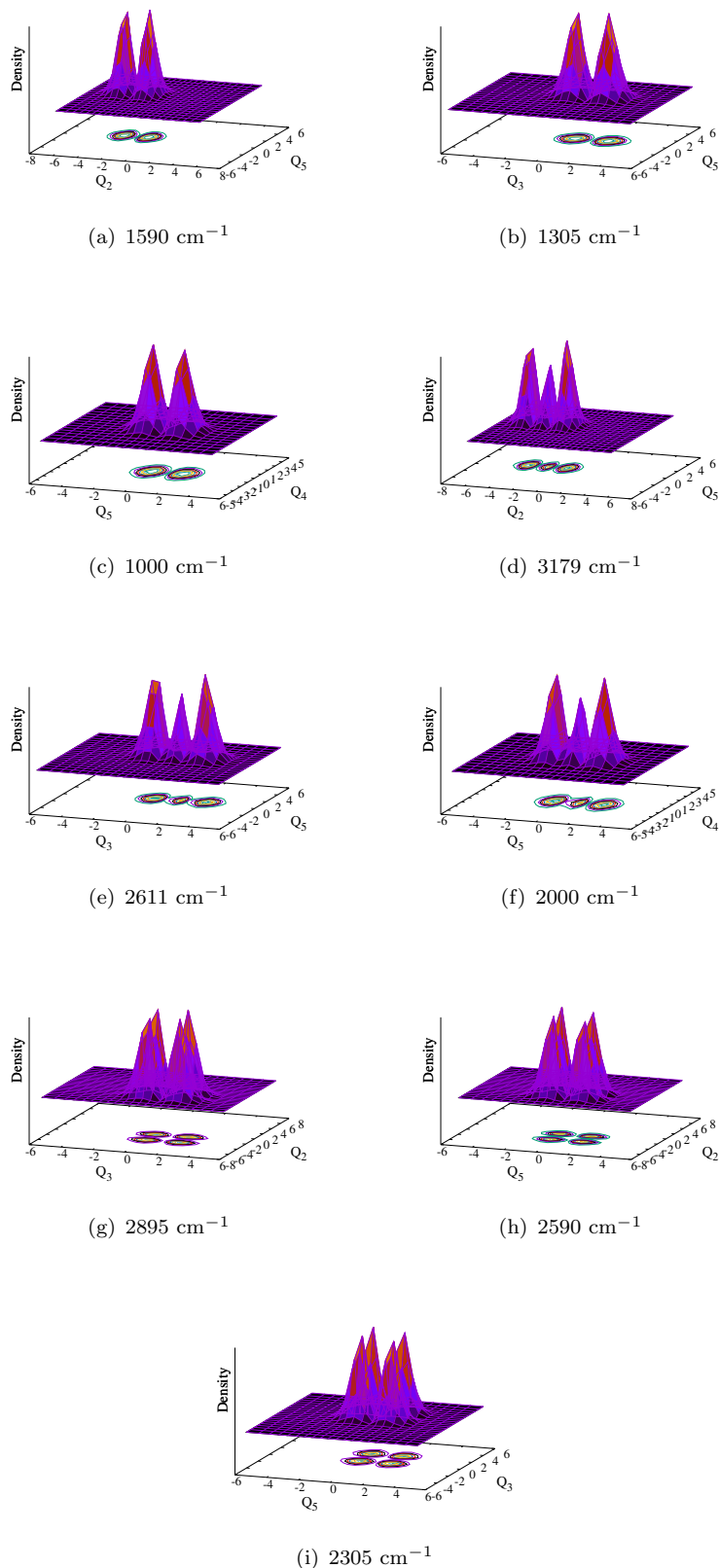
FIGURE B5: Probability density of vibronic wave functions of the $\widetilde{D}$ $^2A_1$ electronic state of c-$C_2H_4O^{\cdot+}$ as a function of nuclear coordinate. Panels a, b and c represent the fundamental of ν_{20}^1, ν_{30}^1 and ν_{50}^1 and first overtone of ν_{20}^2, ν_{30}^2 and ν_{50}^2 modes, the wavefunction in panels g, h and i represent the combination peak of $\nu_{30}^1+\nu_{20}^1$, $\nu_{50}^1+\nu_{20}^1$ and $\nu_{50}^1+\nu_{30}^2$.

(a) 1524 cm^{-1}

(b) 1347 cm^{-1}

(c) 1006 cm^{-1}

(d) 3047 cm^{-1}

(e) 2694 cm^{-1}

(f) 2015 cm^{-1}

(g) 2871 cm^{-1}

(h) 2530 cm^{-1}

(i) 2353 cm^{-1}
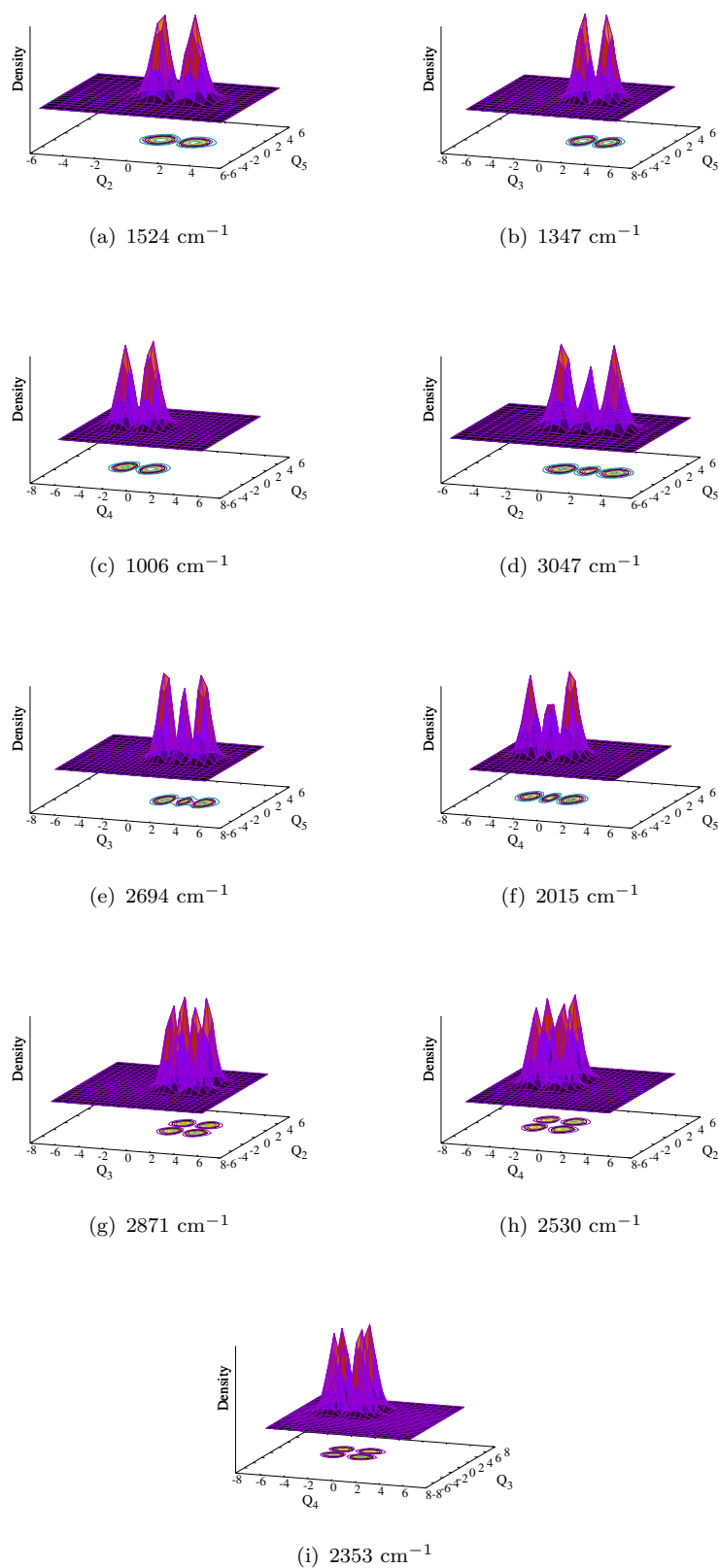
FIGURE B6: Probability density of vibronic wave functions of the $\widetilde{E}\ ^2B_1$ electronic state of c-C$_2$H$_4$O$^{\cdot+}$ as a function of nuclear coordinate. Panels a, b and c represent the fundamental of ν_{20}^1, ν_{30}^1 and ν_{40}^1 and first overtone of ν_{20}^2, ν_{30}^2 and ν_{40}^2 modes, the wavefunction in panels g, h and i represent the combination peak of $\nu_{30}^1 + \nu_{20}^1$, $\nu_{40}^1 + \nu_{20}^1$ and $\nu_{40}^1 + \nu_{30}^2$.
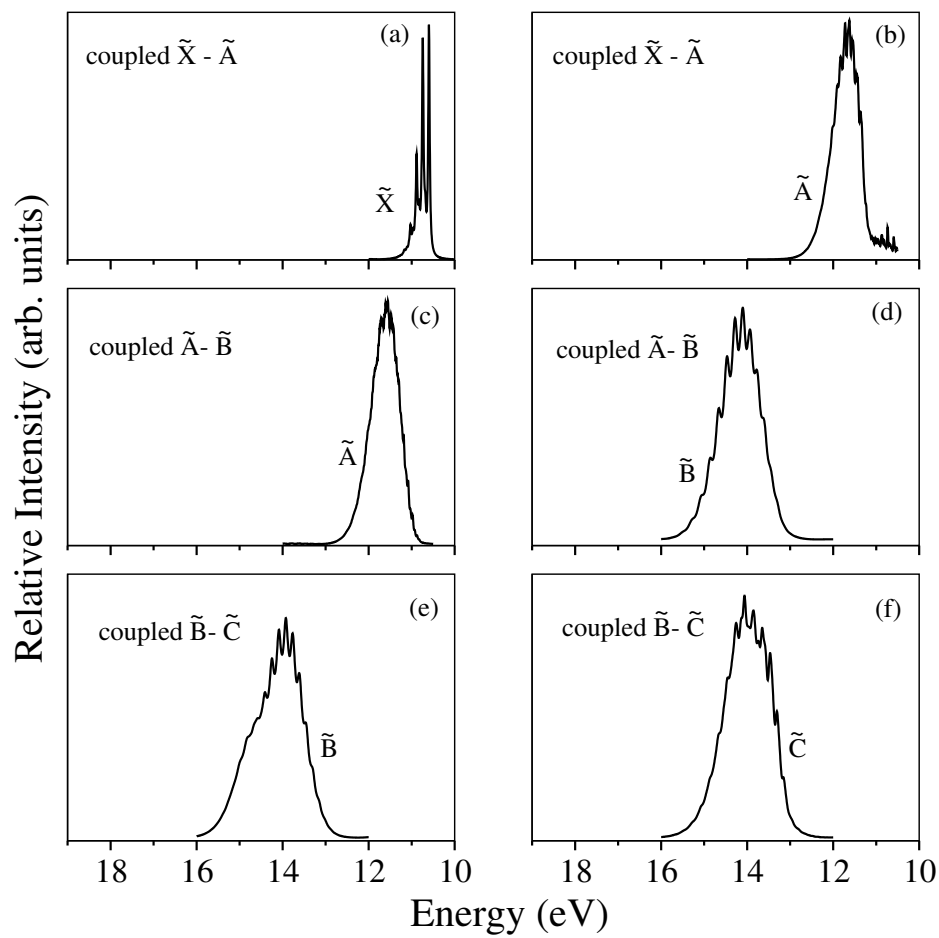
FIGURE B7: Composite vibronic band structure of the coupled $\widetilde{X}$ $^2B_1$-$\widetilde{A}$ $^2A_1$, $\widetilde{A}$ $^2A_1$-$\widetilde{B}$ $^2B_2$, $\widetilde{B}$ $^2B_2$-$\widetilde{C}$ $^2A_2$, $\widetilde{C}$ $^2A_2$-$\widetilde{D}$ $^2A_1$ and $\widetilde{D}$ $^2A_1$-$\widetilde{E}$ $^2B_1$ states of c-$C_2H_4O^{.+}$ are shown in the panels (a)–(j), respectively.
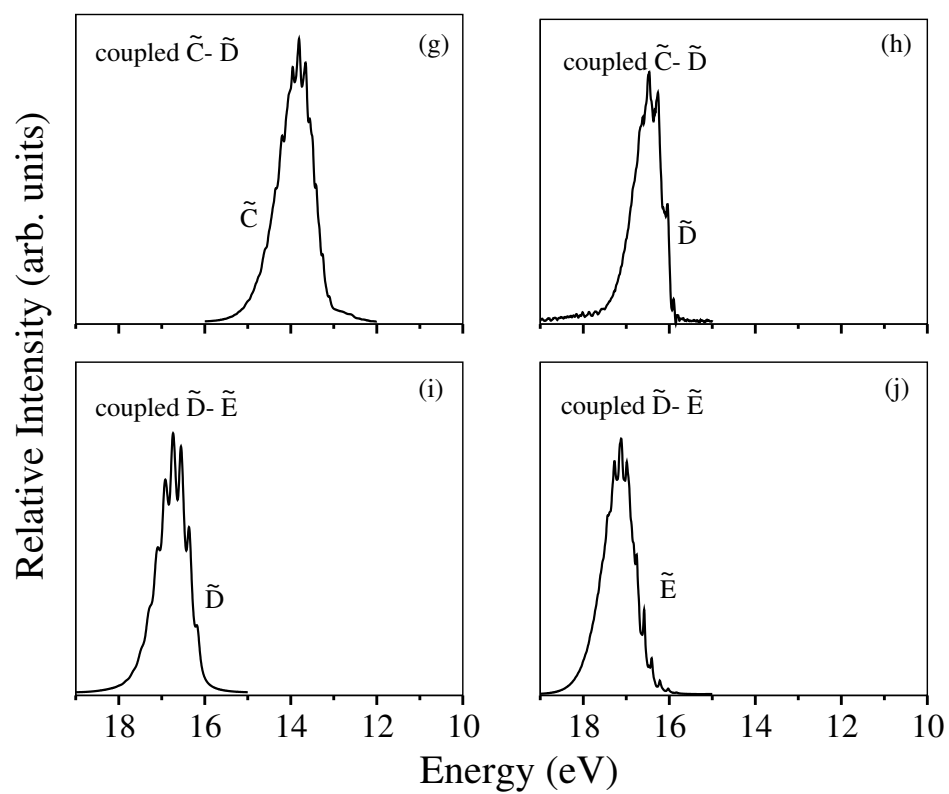
FIGURE B7: Continued
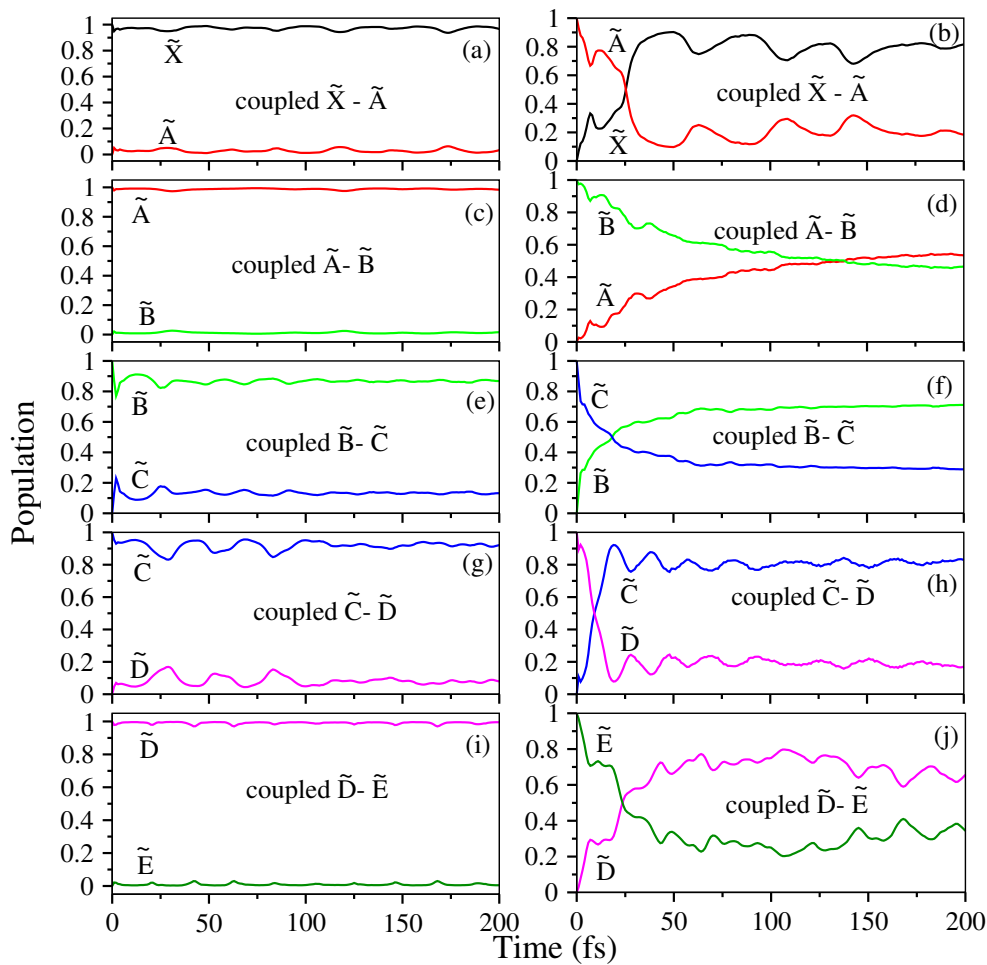
FIGURE B8: Time-dependence of the diabatic electronic populations in the coupled $\widetilde{X}$ $^2B_1$-$\widetilde{A}$ $^2A_1$, $\widetilde{A}$ $^2A_1$-$\widetilde{B}$ $^2B_2$, $\widetilde{B}$ $^2B_2$-$\widetilde{C}$ $^2A_2$, $\widetilde{C}$ $^2A_2$-$\widetilde{D}$ $^2A_1$ and $\widetilde{D}$ $^2A_1$-$\widetilde{E}$ $^2B_1$ states dynamics obtained by locating an initial WP on each electronic state separately is shown in the panels (a)–(j), respectively (see text for details).

Appendix C

Supplementary material for Chapter 5

TABLE C1: The *ab initio* calculated cubic (η_i) and quartic (γ_i) coupling parameters for the $\widetilde{X}\ ^2A'$, $\widetilde{A}\ ^2A'$, $\widetilde{B}\ ^2A''$, $\widetilde{C}\ ^2A''$, $\widetilde{D}\ ^2A'$ and $\widetilde{E}\ ^2A'$ electronic states of the $CH_2NHCH_2^+$ are determined using the EOMIP-CCSD method. These parameters are given in eV.

Symm.	Modes	$\widetilde{X}\ ^2A'$ η_i	δ_i	$\widetilde{A}\ ^2A'$ η_i	δ_i	$\widetilde{B}\ ^2A''$ η_i	δ_i
a'	ν_1	-0.0017	-	-	-	-0.0016	-
	ν_2	-0.0001	-	-	-	-0.0009	-
	ν_3	-0.0004	-	-0.0008	-	0.0103	0.0068
	ν_4	-0.0067	-0.0014	-0.0029	-	-0.0038	-
	ν_5	-0.0076	-	-0.0051	-	-0.0056	0.0061
	ν_6	-0.0086	-	0.0098	-	0.0047	-
	ν_7	0.0002	-	0.0099	-	-0.0865	-0.0798
	ν_8	-0.0028	-	-0.0139	-	0.0057	-
	ν_9	-	-	-	-	0.0030	-0.0126
	ν_{10}	-0.0176	-0.0066	0.0297	0.0069	-0.0211	-0.0117
a''	ν_{11}	-	-	-	0.0135	-	-0.0165
	ν_{12}	-	-	-	0.0038	-	-0.0091
	ν_{13}	-	-0.0019	-	0.0237	-	-0.0580
	ν_{14}	-	-	-	0.3455	-	-0.3574
	ν_{15}	-	-0.0023	-	0.2275	-	-0.2765
	ν_{16}	-	-0.0009	-	0.0035	-	-0.0303
	ν_{17}	-	-	-	0.0192	-	-0.0171
	ν_{18}	-	-	-	0.4473	-	-0.4805

Symm.	Modes	$\widetilde{C}\ ^2A''$ η_i	δ_i	$\widetilde{D}\ ^2A'$ η_i	δ_i	$\widetilde{E}\ ^2A'$ η_i	δ_i
a'	ν_1	-0.0007	-	-0.0018	-	-0.0076	-
	ν_2	0.0016	-	-0.0158	-0.0494	0.0137	0.0495
	ν_3	0.0071	0.0074	-	-	-	-
	ν_4	0.0100	-	0.0015	0.0213	0.0067	-0.0166
	ν_5	0.0054	-0.0057	0.0120	0.0063	0.0027	-
	ν_6	-0.0026	-	0.0009	-	-0.0000131	-
	ν_7	0.0814	0.0820	-0.0007	0.0028	0.0030	-
	ν_8	-0.0032	-	0.0030	-	0.0104	-
	ν_9	-0.0027	0.0117	0.0031	-	-0.0076	-
	ν_{10}	0.0202	0.0123	-0.0105	-	-0.0005	-
a''	ν_{11}	-	0.0125	-	-0.0231	-	0.0229
	ν_{12}	-	0.0065	-	-0.0114	-	0.0084
	ν_{13}	-	0.0694	-	-0.0172	-	-0.0042
	ν_{14}	-	0.0320	-	-0.0024	-	0.0020
	ν_{15}	-	-0.0551	-	0.0032	-	6.5115
	ν_{16}	-	0.0111	-	-0.0002	-	0.0063
	ν_{17}	-	0.0020	-	0.0019	-	0.0016
	ν_{18}	-	0.0099	-	0.0002	-	-0.0004

TABLE C2: The *ab initio* calculated cubic (η_i) and quartic (δ_i) coupling parameters for the $\widetilde{X}\,^2A'$, $\widetilde{A}\,^2A'$, $\widetilde{B}\,^2A''$, $\widetilde{C}\,^2A''$, $\widetilde{D}\,^2A'$ and $\widetilde{E}\,^2A'$ electronic states of the $CH_2NHCH_2^+$ are determined using the MCQDPT method. These parameters are given in eV.

Symm.	Modes	$\widetilde{X}\,^2A'$		$\widetilde{A}\,^2A'$		$\widetilde{B}\,^2A''$	
		η_i	δ_i	η_i	δ_i	η_i	δ_i
a'	ν_1	0.0004	-	-0.0019	-	0.00004	-
	ν_2	0.0327	0.0389	0.0327	0.0386	0.0327	0.0366
	ν_3	-0.0065	0.0002	-0.0046	-0.0001	-0.0053	-0.0004
	ν_4	0.0093	-	0.0091	-	0.0084	-
	ν_5	-0.0084	-	-0.0004	-	-0.0007	0.0062
	ν_6	-0.0050	0.0042	-0.0002	0.0044	-0.0027	0.0078
	ν_7	0.0046	0.0053	0.0029	0.0049	-0.0115	0.0010
	ν_8	-0.0048	0.00005	-0.0053	0.0069	0.0150	0.0044
	ν_9	0.0076	-	0.0065	-0.0034	0.0034	-
	ν_{10}	0.0026	0.0096	0.0181	-	0.0047	0.0100
a''	ν_{11}	-	-0.0011	-	0.0055	-	-0.0145
	ν_{12}	-	-0.0004	-	0.0022	-	-0.0080
	ν_{13}	-	0.0031	-	0.0085	-	-0.0736
	ν_{14}	-	0.0009	-	0.1439	-	-0.3135
	ν_{15}	-	0.0145	-	0.1310	-	-0.1441
	ν_{16}	-	0.0028	-	0.0022	-	-0.0080
	ν_{17}	-	-0.0007	-	0.0065	-	-0.0214
	ν_{18}	-	-0.0416	-	0.4014	-	-0.4724

Symm.	Modes	$\widetilde{C}\,^2A''$		$\widetilde{D}\,^2A'$		$\widetilde{E}\,^2A'$	
		η_i	δ_i	η_i	δ_i	η_i	δ_i
a'	ν_1	0.00107	-	-0.0026	-	0.0020	-
	ν_2	0.03369	0.0419	0.0554	0.0376	0.0467	0.0381
	ν_3	-0.00426	0.0001	-0.0044	-0.0003	-0.0039	0.0005
	ν_4	0.01996	-	0.0082	-	0.0147	-
	ν_5	0.00010	0.0088	0.0014	-0.0002	0.0023	0.0020
	ν_6	-0.00164	0.0105	-0.0014	0.0047	-0.0035	0.0063
	ν_7	0.00210	0.0088	0.0039	0.0103	0.0034	0.0069
	ν_8	0.01351	0.0086	0.0143	0.0061	0.0070	0.0109
	ν_9	0.01210	-0.0047	0.0030	-0.0049	0.0011	-0.0015
	ν_{10}	0.00976	0.0111	-0.0091	0.0109	0.0019	0.0129
a''	ν_{11}	-	0.0125	-	-0.0191	-	0.0177
	ν_{12}	-	0.0012	-	-0.0207	-	0.0078
	ν_{13}	-	0.1058	-	-0.0192	-	-0.0006
	ν_{14}	-	0.0387	-	0.0011	-	0.0023
	ν_{15}	-	-0.0682	-	0.0024	-	-0.0030
	ν_{16}	-	0.0127	-	0.0009	-	0.0054
	ν_{17}	-	0.0013	-	0.0019	-	0.0011
	ν_{18}	-	0.0019	-	0.0198	-	0.0917

TABLE C3: The *ab initio* calculated fifth (α_i), sixth (ζ_i), seventh (β_i), and eighth (μ_i) coupling parameters (in eV) for the $\widetilde{X}\ ^2A'$, $\widetilde{A}\ ^2A'$, $\widetilde{B}\ ^2A''$, $\widetilde{C}\ ^2A''$, $\widetilde{D}\ ^2A'$ and $\widetilde{E}\ ^2A'$ electronic states of $CH_2NHCH_2^+$ with using EOMIP-CCSD method.

| Symm. | Mode | $\widetilde{A}\ ^2A'$ | | | $\widetilde{B}\ ^2A''$ | | | | $\widetilde{C}\ ^2A''$ | |
		ζ_i	μ_i		α_i	ζ_i	μ_i		α_i	ζ_i
a'	ν_3	-	-		-0.0156	-0.0166	-		-	-
	ν_7	-	-		0.0299	0.0619	-		-0.0320	-0.0607
	ν_9	-	-		-0.0125	-	-		0.0127	-
a''	ν_{11}	-0.0076	-		-	0.0067	-		-	-0.0024
	ν_{12}	-	-		-	0.0043	-		-	-0.0019
	ν_{13}	-0.0185	-		-	0.0264	-		-	-0.0184
	ν_{14}	-0.4714	0.4431		-	0.4695	-0.4274		-	-0.0157
	ν_{15}	-0.2891	0.2660		-	0.6897	-1.4798		-	0.0255
	ν_{16}	-	-		-	0.0376	-0.0370		-	-
	ν_{17}	-0.0102	-		-	0.0089	-		-	0.0003
	ν_{18}	-0.6179	0.5786		-	0.6318	-0.5711		-	-

| Sym. | Mode | $\widetilde{D}\ ^2A'$ | | | | $\widetilde{E}\ ^2A'$ | | |
		α_i	ζ_i	β_i		α_i	ζ_i	β_i
a'	ν_2	0.0879	0.0254	-0.0955		-0.0873	-0.0264	0.0946
a''	ν_{11}	-	0.0098	-		-	-0.0100	-
	ν_{13}	-	0.0084	-		-	-	-

TABLE C4: The *ab initio* calculated fifth (α_i), sixth (ζ_i) and eighth (μ_i) coupling parameters (in eV) for the $\widetilde{X}\ ^2A'$, $\widetilde{A}\ ^2A'$, $\widetilde{B}\ ^2A''$, $\widetilde{C}\ ^2A''$, $\widetilde{D}\ ^2A'$ and $\widetilde{E}\ ^2A'$ electronic states of $CH_2NHCH_2^+$ with using MCQDPT method.

Symm.	Mode	$\widetilde{X}\ ^2A'$		$\widetilde{A}\ ^2A'$			$\widetilde{B}\ ^2A''$		
		α_i	ζ_i	α_i	ζ_i	μ_i	α_i	ζ_i	μ_i
a'	ν_2	0.0132	-	0.0131	-	-	-	-	-
	ν_3	0.0012	-	0.0009	-	-	0.0132	-	-
	ν_8	-	-	-	-	-	-0.0064	-	-
a''	ν_{11}	-	-	-	-0.0030	-	-	0.0053	-
	ν_{12}	-	-	-	-	-	-	0.0037	-
	ν_{13}	-	-0.0043	-	-0.0093	-	-	0.0416	-
	ν_{14}	-	-	-	-0.0813	-	-	0.3911	-0.3397
	ν_{15}	-	-0.0154	-	-0.0768	-	-	0.2402	-0.2629
	ν_{16}	-	-0.0019	-	-	-	-	-0.0005	-
	ν_{17}	-	-	-	-	-	-	0.0239	-0.0000005
	ν_{18}	-	0.0673	-	-0.5350	0.4917	-	0.6317	-0.5777

Symm.	Mode	$\widetilde{C}\ ^2A''$		$\widetilde{D}\ ^2A'$		$\widetilde{E}\ ^2A'$
		α_i	ζ_i	α_i	ζ_i	ζ_i
a'	ν_2	0.0131	-	-	-	-
	ν_8	-0.0067	-	-0.0074	-	-
a''	ν_{11}	-	-0.0027	-	0.0091	-0.0088
	ν_{12}	-	0.0008	-	0.0064	-
	ν_{13}	-	-0.0456	-	0.0087	-0.0015
	ν_{14}	-	-0.0222	-	-0.0014	-
	ν_{15}	-	0.0345	-	-	-
	ν_{16}	-	-	-	-	-
	ν_{17}	-	-	-	-	-
	ν_{18}	-	-	-	-0.0446	-0.2564

TABLE C5: Linear $(\lambda_i^{(1)})$, cubic $(\lambda_i^{(3)})$, fifth $(\lambda_i^{(5)})$ and seventh $(\lambda_i^{(7)})$ order inter-state coupling constants (in eV) between the n and m electronic states of the $CH_2NHCH_2^+$ with using EOMIP-CCSD method (Eq. 5.9) are estimated from the *ab initio* electronic structure results (see the text for details). Dimensionless Poisson parameters $\left(\lambda_i{}^2/2\omega_i{}^2\right)$ are given in the parentheses.

| | $\widetilde{X}\ ^2A'$-$\widetilde{B}\ ^2A''$ | | | | | $\widetilde{X}\ ^2A'$-$\widetilde{C}\ ^2A''$ | | |
Mode	$\lambda_i^{(1)}$	$\lambda_i^{(3)}$	$\lambda_i^{(5)}$	$\lambda_i^{(7)}$		$\lambda_i^{(1)}$	$\lambda_i^{(3)}$	$\lambda_i^{(5)}$
a''								
ν_{11}	0.1434(0.0661)	-0.0218	0.0038	-		-	-	
ν_{12}	0.1042(0.0366)	-0.0202	0.0058	-		-	-	
ν_{13}	0.2256(0.7382)	-0.0967	0.1186	-0.1877		-	-	
ν_{14}	0.5481(6.0842)	-0.2236	0.2151	-0.1613		0.0507(0.0520)	0.0707	-0.0279
ν_{15}	0.3242(2.5628)	-0.1814	0.1944	-0.1458		0.3560(3.0902)	-0.0211	
ν_{16}	0.1057(0.2879)	-0.0271	-0.0080	-		-	-	
ν_{17}	0.2076(1.6614)	-0.0169	0.0073	-		-	-	
ν_{18}	0.6763(20.4976)	-0.2617	0.2642	-0.2004		0.2255(2.2789)	0.0174	

| | $\widetilde{A}\ ^2A'$-$\widetilde{B}\ ^2A''$ | | | | $\widetilde{A}\ ^2A'$-$\widetilde{C}\ ^2A''$ | | | |
Mode	$\lambda_i^{(1)}$	$\lambda_i^{(3)}$	$\lambda_i^{(5)}$		$\lambda_i^{(1)}$	$\lambda_i^{(3)}$	$\lambda_i^{(5)}$	$\lambda_i^{(7)}$
a''								-
ν_{11}	0.0592(0.0113)	-0.0022	-		-	-	-	-
ν_{12}	0.0496(0.0083)	-	-		0.0632(0.0135)	-	-	-
ν_{13}	0.0885(0.1137)	-0.0018	-0.0049		-	-	-	-
ν_{14}	0.2828(1.6197)	-0.0260	-		0.3986(3.2178)	-0.1577	0.1765	-0.1393
ν_{15}	0.1810(0.7988)	-	-		0.3997(3.8954)	-0.0172	-	-
ν_{16}	0.0649(0.1085)	-	-		-	-	-	-
ν_{17}	0.0843(0.2739)	0.0061	-		0.1220(0.5738)	-0.0379	0.0356	-0.0254
ν_{18}	0.3856(6.6634)	-0.0179	-		0.5048(11.420)	-0.1737	0.2108	-0.1702

| | $\widetilde{C}\ ^2A''$-$\widetilde{D}\ ^2A'$ | | | | | $\widetilde{C}\ ^2A''$-$\widetilde{E}\ ^2A'$ | |
Mode	$\lambda_i^{(1)}$	$\lambda_i^{(3)}$	$\lambda_i^{(5)}$	$\lambda_i^{(7)}$		$\lambda_i^{(1)}$	$\lambda_i^{(3)}$
a''							
ν_{11}	0.2290(0.1685)	-0.0217	-	-		0.1960(0.1234)	0.0059
ν_{12}	0.1985(0.1329)	-0.0183	-	-		0.2022(0.1379)	0.0077
ν_{13}	0.3662(1.9450)	-0.0327	-	-		0.4388(2.7926)	-0.0376
ν_{14}	0.1567(0.4973)	-0.0107	-0.0296	0.0230		-	-
ν_{16}	0.2193(1.2393)	-0.0072	-	-		0.1929(0.9589)	-0.0047
ν_{17}	0.0619(0.1477)	0.0009	-	-		0.0842(0.2733)	-0.0015

| | $\widetilde{B}\ ^2A''$-$\widetilde{D}\ ^2A'$ | | |
Mode	$\lambda_i^{(1)}$	$\lambda_i^{(3)}$	$\lambda_i^{(5)}$
a''			
ν_{12}	0.1343(0.0608)	-0.0078	-0.0062

TABLE C6: Linear $(\lambda_i^{(1)})$, cubic $(\lambda_i^{(3)})$, fifth $(\lambda_i^{(5)})$ and seventh $(\lambda_i^{(7)})$ order inter-state coupling constants (in eV) between the n and m electronic states of the $CH_2NHCH_2^+$ with using MCQDPT method (Eq. 5.9) are estimated from the *ab initio* electronic structure results (see the text for details). Dimensionless Poisson parameters $(\lambda_i{}^2/2\omega_i{}^2)$ are given in the parentheses.

Mode	$\widetilde{X}\ ^2A'$-$\widetilde{B}\ ^2A''$				$\widetilde{X}\ ^2A'$-$\widetilde{C}\ ^2A''$		
	$\lambda_i^{(1)}$	$\lambda_i^{(3)}$	$\lambda_i^{(5)}$	$\lambda_i^{(7)}$	$\lambda_i^{(1)}$	$\lambda_i^{(3)}$	$\lambda_i^{(5)}$
a''							-
ν_{11}	0.1206 (0.0467)	-0.0162	-	-	-	-	-
ν_{12}	0.1055 (0.0375)	-0.0226	0.0079	-	-	-	-
ν_{13}	0.2349 (0.8000)	-0.1281	0.2038	-0.3986	-	-	-
ν_{14}	0.5121 (5.3123)	-0.1898	0.1645	-0.1172	0.1484(0.4462)	0.0361	-0.0117
ν_{15}	0.3109 (2.3573)	-0.1707	0.1927	-0.1586	0.3976(3.8550)	-0.0471	0.0152
ν_{16}	0.1040 (0.2790)	-0.0283	0.0133	-0.0513	-	-	-
ν_{17}	0.2032 (1.5922)	-0.0127	0.0054	-	-	-	-
ν_{18}	0.5315 (12.6605)	-0.1302	0.0875	-0.0478	0.3119(4.3598)	-0.0067	-

Mode	$\widetilde{A}\ ^2A'$-$\widetilde{B}\ ^2A''$			$\widetilde{A}\ ^2A'$-$\widetilde{C}\ ^2A''$			
	$\lambda_i^{(1)}$	$\lambda_i^{(3)}$	$\lambda_i^{(5)}$	$\lambda_i^{(1)}$	$\lambda_i^{(3)}$	$\lambda_i^{(5)}$	$\lambda_i^{(7)}$
a''							
ν_{11}	0.0601(0.0116)	-0.0023	-	-	-	-	-
ν_{12}	0.0519(0.0091)	-	-	0.0707(0.0168)	-0.0003	-	-
ν_{13}	0.1040(0.1568)	-0.0154	0.0056	-	-	-	-
ν_{14}	0.2819(1.6099)	-0.0361	0.0057	0.3193(2.0647)	-0.0523	0.0243	-
ν_{15}	0.2021(0.9959)	-0.0035	-	0.3922(3.7510)	-0.0147	-	-
ν_{16}	0.0720(0.1338)	-0.0002	-	-	-	-	-
ν_{17}	0.0944(0.3435)	0.0054	-	0.1170(0.5276)	-0.0356	0.0362	-0.0277
ν_{18}	0.3756(6.3229)	-0.0184	-	0.5298(12.5805)	-0.2039	0.2510	-0.2090

Mode	$\widetilde{C}\ ^2A''$-$\widetilde{D}\ ^2A'$			$\widetilde{C}\ ^2A''$-$\widetilde{E}\ ^2A'$			
	$\lambda_i^{(1)}$	$\lambda_i^{(3)}$	$\lambda_i^{(5)}$	$\lambda_i^{(1)}$	$\lambda_i^{(3)}$	$\lambda_i^{(5)}$	$\lambda_i^{(7)}$
a''							
ν_{11}	0.1985(0.1266)	-0.0252	-	0.2158(0.1496)	-	-	-
ν_{12}	0.2033(0.1393)	-0.0158	-	0.1427(0.0687)	0.0126	-	-
ν_{13}	0.3835(2.1332)	-0.0422	-	0.4393(2.7985)	-0.0487	-	-
ν_{14}	0.0841(0.1432)	0.0471	-0.1638	-	-	-	-
ν_{15}	-	-	-	-	-	-	-
ν_{16}	0.1917(0.9474)	0.0033	-0.0079	0.1689(0.7356)	0.0045	-0.0096	-
ν_{17}	0.0527(0.1069)	0.00003	-	0.0245(0.0232)	-0.0127	0.0318	-0.0989
ν_{18}	-	-	-	-	-	-	-

Mode	$\widetilde{B}\ ^2A''$-$\widetilde{D}\ ^2A'$	
	$\lambda_i^{(1)}$	$\lambda_i^{(3)}$
a''		
ν_{12}	0.1836(0.1137)	-0.0148

TABLE C7: Linear $(\lambda_i^{'(1)})$, quadratic $(\lambda_i^{'(2)})$ and cubic $(\lambda_i^{'(3)})$ order intra-state coupling constants (in eV) between the n and m electronic states of same symmetry of the $CH_2NHCH_2^+$ with using MCQDPT method (Eq. 5.10) are estimated from the *ab initio* electronic structure results (see the text for details). Dimensionless Poisson parameters $\left(\lambda_i^{'(1)^2}/2\omega_i^2\right)$ are given in the parentheses.

Mode	$\tilde{X}$-$\tilde{A}$ $\lambda_i^{'(1)}$	$\lambda_i^{'(2)}$	$\lambda_i^{'(3)}$	$\tilde{X}$-$\tilde{D}$ $\lambda_i^{'(1)}$	$\lambda_i^{'(2)}$	$\lambda_i^{'(3)}$	$\tilde{X}$-$\tilde{E}$ $\lambda_i^{'(1)}$	$\lambda_i^{'(2)}$	$\lambda_i^{'(3)}$
a'									
ν_1	-0.0017 (0.000008)	-0.0002	0.0014	0.0181 (0.0009)	0.0033	-	-0.0093 (0.00022)	0.0042	-
ν_2	0.0125 (0.0005)	-0.0005	-	-0.0832 (0.0220)	-0.0014	-	0.0109 (0.00047)	-0.0073	-
ν_3	-0.0208 (0.0014)	-	-	-0.0752 (0.0190)	-	-	-0.0594 (0.01196)	0.0040	-
ν_4	-0.0513 (0.0368)	-0.0111	-	-0.0316 (0.0140)	-0.0107	-	-0.1076 (0.16216)	-0.0178	-
ν_5	0.1845 (0.6598)	-	-	0.0239 (0.0111)	-0.0073	-	-0.0171 (0.00576)	-0.0085	-0.0020
ν_6	0.2796 (1.6611)	-0.0126	-	0.0517 (0.0568)	-0.0141	-	0.0108 (0.00257)	-0.0070	-
ν_7	0.1879 (0.9247)	-0.0071	-	-0.1132 (0.3356)	-0.0213	0.0068	-0.0820 (0.17610)	-0.0132	0.0045
ν_8	0.1119 (0.4022)	-0.0193	-0.0124	0.2387 (1.8302)	-0.0416	-0.0161	-0.2781 (2.48425)	-0.0111	0.0113
ν_9	0.0543 (0.1272)	0.0052	-	-0.1437 (0.8907)	-0.0111	-	-0.1681 (1.21883)	-0.0070	-
ν_{10}	-0.0811 (0.3526)	-0.0296	0.0072	0.0288 (0.0445)	-0.0067	-	0.1251 (0.83894)	-0.0069	-0.0093

Mode	$\tilde{A}$-$\tilde{D}$ $\lambda_i^{'(1)}$	$\lambda_i^{'(2)}$	$\lambda_i^{'(3)}$	$\tilde{A}$-$\tilde{E}$ $\lambda_i^{'(1)}$	$\lambda_i^{'(2)}$	$\lambda_i^{'(3)}$	$\tilde{B}$-$\tilde{C}$ $\lambda_i^{'(1)}$	$\lambda_i^{'(2)}$	$\lambda_i^{'(3)}$
a'									
ν_1	0.1671 (0.0739)	-	-	-0.0982 (0.0255)	0.0204	-	0.0130 (0.0004)	-0.0007	-
ν_2	-0.0525 (0.0088)	-0.0037	-	0.0914 (0.0266)	-0.0045	-	-0.1569 (0.0784)	-0.0017	-
ν_3	-0.0198 (0.0013)	0.0052	-	-0.1310 (0.0577)	-	-	0.00003 (0.0000)	0.0009	-
ν_4	-0.1906 (0.5085)	-0.0096	-	-0.0709 (0.0704)	-0.0232	-	-0.0255 (0.0091)	-	-
ν_5	-0.2192 (0.9313)	-0.0436	-	-0.1181 (0.2703)	0.0110	-	-0.1936 (0.7265)	-0.0084	-
ν_6	-0.0030 (0.0002)	-0.0056	-0.0005	-0.0530 (0.0597)	-0.0110	0.0034	-0.0894 (0.1698)	0.0129	-0.0068
ν_7	0.2314 (1.4023)	-0.0111	-0.0105	-0.0864 (0.1955)	-0.0221	-	0.1396 (0.5104)	-0.0257	-
ν_8	-0.1311 (0.5521)	-0.0403	-	0.0237 (0.0180)	0.0057	-	0.1837 (1.0839)	0.0121	-
ν_9	-0.0103 (0.0046)	-0.0227	-0.0019	0.0313 (0.0422)	0.0137	-0.0031	0.0067 (0.0019)	-0.0049	-0.0015
ν_{10}	-0.0464 (0.1154)	-0.0283	-	-0.2310 (2.8605)	-0.0142	0.0138	-0.1050 (0.5910)	0.0109	0.0109

Mode	$\tilde{D}$-$\tilde{E}$ $\lambda_i^{'(1)}$	$\lambda_i^{'(2)}$	$\lambda_i^{'(3)}$
a'			
ν_1	-0.1114 (0.0328)	0.0209	-
ν_2	-0.0853 (0.0232)	-0.0212	-
ν_3	-0.0675 (0.0153)	0.0134	-
ν_4	-0.2828 (1.1195)	-0.0111	-
ν_5	0.1026 (0.2040)	0.0201	-
ν_6	-0.0233 (0.0115)	0.0156	-
ν_7	-0.0024 (0.0000)	-0.0252	0.0020
ν_8	0.0466 (0.0697)	0.0169	-0.0086
ν_9	-0.1208 (0.6294)	-	-
ν_{10}	-0.0442 (0.1047)	-0.0008	-0.0059

TABLE C8: Diagonal bilinear coupling (γ_{ij}^n) parameters (in eV) along the totally symmetric vibrational modes ν_4, ν_5, ν_6, ν_7, ν_9 and ν_{10} of the lowest seven electronic states of $CH_2NHCH_2^+$ calculated using EOMIP-CCSD method.

γ_{ij}	$\tilde{X}^2A'$	$\tilde{A}^2A''$	$\tilde{B}^2A'$	$\tilde{C}^2A'$	$\tilde{D}^2A''$	$\tilde{E}^2A'$
γ_{45}	0.0124	-0.0696	-0.0346	0.0636	0.1820	-0.1280
γ_{46}	0.0108	-0.0569	-0.0312	0.0074	0.0055	-0.0426
γ_{47}	0.0044	0.0187	-0.0697	0.1086	-0.0655	0.0291
γ_{49}	-0.0022	-0.0200	-0.0221	0.0634	-0.0402	0.0597
γ_{410}	-0.0003	0.0044	-0.0613	0.0838	-0.0827	0.0804
γ_{56}	-0.0394	0.0193	-0.0398	0.0398	-0.0198	-0.0578
γ_{57}	-0.0473	0.0634	0.0861	-0.0508	-0.0066	-0.0063
γ_{59}	-0.0479	0.0383	-0.0037	0.0143	0.0321	-0.0164
γ_{510}	0.0140	-0.0161	-0.0621	0.0528	0.0499	-0.0123
γ_{67}	-0.0495	0.0864	0.0360	-0.0772	-0.0352	-0.0278
γ_{69}	-0.0189	0.0643	-0.0176	-0.0015	-0.0108	0.0469
γ_{610}	0.0418	-0.0233	-0.0384	0.0181	0.0493	-0.0245
γ_{79}	-0.0530	0.0502	-0.0041	0.0552	-0.0021	0.0241
γ_{710}	0.0519	-0.0650	0.0295	-0.0302	0.0624	-0.0306
γ_{910}	0.0235	-0.0730	0.0083	0.0885	0.0206	0.0251

TABLE C9: The number of the harmonic oscillator (HO) basis functions along the totally symmetric vibrational modes and the dimension of the secular matrix used in the calculation of the stick vibrational spectra of the uncoupled electronic states of $CH_2NHCH_2^+$ is shown in Fig. 5.5.

EOMIP-CCSD				
Electronic state	Normal modes	Primitive basis	Dimension of secular matrix	Figure(s)
$\widetilde{X}$	$\nu_4, \nu_5, \nu_6, \nu_7$ ν_8, ν_9, ν_{10}	(4,14,12,4) (12,16,4)	2064384	Fig. 5.5 (a)
$\widetilde{A}$	$\nu_4, \nu_5, \nu_6, \nu_7$ ν_8, ν_9, ν_{10}	(12,4,12,10) (12,10,14)	9676800	Fig. 5.5 (a)
$\widetilde{B}$	$\nu_4, \nu_5, \nu_6, \nu_7$ ν_8, ν_9, ν_{10}	(14,10,10,16) (10,14,14)	43904000	Fig. 5.5 (a)
$\widetilde{C}$	$\nu_3, \nu_4, \nu_5, \nu_6, \nu_7$ ν_8, ν_9, ν_{10}	(12,14,4,4,10) (10,12,4)	12902400	Fig. 5.5 (a)
$\widetilde{D}$	ν_2, ν_3, ν_4 $\nu_6, \nu_7, \nu_8, \nu_{10}$	(12,10,8) (14,8,10,14)	15052800	Fig. 5.5 (a)
$\widetilde{E}$	ν_1, ν_3, ν_5 $\nu_6, \nu_7, \nu_9, \nu_{10}$	(10,10,14) (14,12,8,10)	18816000	Fig. 5.5 (a)
MCQDPT				
$\widetilde{X}$	$\nu_2, \nu_4, \nu_5, \nu_7$ ν_8, ν_9, ν_{10}	(10,16,10,10) (10,18,10)	28800000	Fig. 5.5 (b)
$\widetilde{A}$	$\nu_1, \nu_2, \nu_4, \nu_6$ $\nu_7, \nu_8, \nu_9, \nu_{10}$	(8,8,10,6) (10,10,10,12)	46080000	Fig. 5.5 (b)
$\widetilde{B}$	$\nu_2, \nu_4, \nu_5, \nu_6$ $\nu_7, \nu_8, \nu_9, \nu_{10}$	(6,10,8,6) (12,8,12,10)	33177600	Fig. 5.5 (b)
$\widetilde{C}$	$\nu_2, \nu_3, \nu_4, \nu_5$ ν_8, ν_9, ν_{10}	(10,12,14,10) (14,14,10)	32928000	Fig. 5.5 (b)
$\widetilde{D}$	$\nu_1, \nu_2, \nu_4, \nu_5$ $\nu_6, \nu_7, \nu_8, \nu_{10}$	(8.10,10,10) (12,8,10,10)	76800000	Fig. 5.5 (b)
$\widetilde{E}$	$\nu_1, \nu_2, \nu_3, \nu_5$ $\nu_6, \nu_7, \nu_9, \nu_{10}$	(8,8,10,12) (12,10,8,10)	73728000	Fig. 5.5 (b)

TABLE C10: A few vibrational energy levels (in cm^{-1}) of the $\widetilde{X}$, $\widetilde{A}$, $\widetilde{B}$, $\widetilde{C}$, $\widetilde{D}$ and $\widetilde{E}$ electronic states of CH$_2$NHCH$_2^+$ calculated with using EOMIP-CCSD method obtained from the uncoupled state calculations. The assignment of the levels carried out by examining the nodal pattern of the wavefunctions are included in the table.

$\widetilde{X}$ Energy	Assignment	Expt. [86] Energy	$\widetilde{A}$ Energy	Assignment	$\widetilde{B}$ Energy	Assignment	$\widetilde{C}$ Energy	Assignment
0	0_0^0		0	0_0^0	0	0_0^0	0	0_0^0
815	$\nu_9{}_0^1$	800-650	864	$\nu_8{}_0^1$	720	$\nu_{10}{}_0^1$	341	$\nu_{10}{}_0^1$
839	$\nu_{10}{}_0^1$		871	$\nu_9{}_0^1$	767	$\nu_8{}_0^1$	661	$\nu_{10}{}_0^2$
962	$\nu_8{}_0^1$		1098	$\nu_{10}{}_0^1$	900	$\nu_9{}_0^1$	721	$\nu_9{}_0^1$
1012	$\nu_7{}_0^1$		1100	$\nu_5{}_0^1$	1041	$\nu_5{}_0^1$	1004	$\nu_8{}_0^1$
1127	$\nu_6{}_0^1$		1172	$\nu_7{}_0^1$	1048	$\nu_7{}_0^1$	1018	$\nu_{10}{}_0^3$
1288	$\nu_5{}_0^1$		1449	$\nu_4{}_0^1$	1125	$\nu_6{}_0^1$	1035	$\nu_7{}_0^1$
1488	$\nu_4{}_0^1$		1450	$\nu_6{}_0^1$	1424	$\nu_{10}{}_0^2$	1063	$\nu_9{}_0^1+\nu_{10}{}_0^1$
1636	$\nu_9{}_0^2$		1724	$\nu_8{}_0^2$	1487	$\nu_8{}_0^1+\nu_{10}{}_0^1$	1166	$\nu_6{}_0^1$
1655	$\nu_9{}_0^1+\nu_{10}{}_0^1$		1735	$\nu_8{}_0^1+\nu_9{}_0^1$	1533	$\nu_8{}_0^2$	1289	$\nu_4{}_0^1$
1667	$\nu_{10}{}_0^2$		1742	$\nu_9{}_0^2$	1544	$\nu_4{}_0^1$	1346	$\nu_8{}_0^1+\nu_{10}{}_0^1$
1777	$\nu_8{}_0^1+\nu_9{}_0^1$		1963	$\nu_8{}_0^1+\nu_{10}{}_0^1$	1620	$\nu_9{}_0^1+\nu_{10}{}_0^1$	1377	$\nu_7{}_0^1+\nu_{10}{}_0^1$
1801	$\nu_8{}_0^1+\nu_{10}{}_0^1$		1964	$\nu_5{}_0^1+\nu_8{}_0^1$	1667	$\nu_8{}_0^1+\nu_9{}_0^1$	1382	$\nu_9{}_0^1+\nu_{10}{}_0^2$
1827	$\nu_7{}_0^1+\nu_9{}_0^1$		1969	$\nu_9{}_0^1+\nu_{10}{}_0^1$	1761	$\nu_5{}_0^1+\nu_{10}{}_0^1$	1428	$\nu_5{}_0^1$
1852	$\nu_7{}_0^1+\nu_{10}{}_0^1$		1971	$\nu_5{}_0^1+\nu_9{}_0^1$	1767	$\nu_7{}_0^1+\nu_{10}{}_0^1$	1441	$\nu_9{}_0^2$
1923	$\nu_8{}_0^2$		2037	$\nu_7{}_0^1+\nu_8{}_0^1$	1807	$\nu_5{}_0^1+\nu_8{}_0^1$	1507	$\nu_6{}_0^1+\nu_{10}{}_0^1$
1943	$\nu_6{}_0^1+\nu_9{}_0^1$		2190	$\nu_{10}{}_0^2$	1816	$\nu_7{}_0^1+\nu_8{}_0^1$	1631	$\nu_4{}_0^1+\nu_{10}{}_0^1$
1967	$\nu_6{}_0^1+\nu_{10}{}_0^1$		2198	$\nu_5{}_0^1+\nu_{10}{}_0^1$	1818	$\nu_9{}_0^2$	1665	$\nu_7{}_0^1+\nu_{10}{}_0^2$
1974	$\nu_7{}_0^1+\nu_8{}_0^1$		2199	$\nu_5{}_0^2$	1846	$\nu_6{}_0^1+\nu_{10}{}_0^1$	1696	$\nu_4{}_0^1+\nu_{10}{}_0^1$
2051	$\nu_7{}_0^2$		2271	$\nu_7{}_0^1+\nu_{10}{}_0^1$	1893	$\nu_6{}_0^1+\nu_8{}_0^1$	1725	$\nu_8{}_0^1+\nu_9{}_0^1$
2089	$\nu_6{}_0^1+\nu_8{}_0^1$		2272	$\nu_5{}_0^1+\nu_7{}_0^1$	1941	$\nu_5{}_0^1+\nu_9{}_0^1$	1756	$\nu_7{}_0^1+\nu_9{}_0^1$
2103	$\nu_5{}_0^1+\nu_9{}_0^1$		2313	$\nu_4{}_0^1+\nu_8{}_0^1$	1948	$\nu_7{}_0^1+\nu_9{}_0^1$	1769	$\nu_5{}_0^1+\nu_{10}{}_0^1$
2127	$\nu_5{}_0^1+\nu_{10}{}_0^1$		2314	$\nu_6{}_0^1+\nu_8{}_0^1$	2025	$\nu_6{}_0^1+\nu_9{}_0^1$	1783	$\nu_9{}_0^2+\nu_{10}{}_0^1$
2140	$\nu_6{}_0^1+\nu_7{}_0^1$		2320	$\nu_4{}_0^1+\nu_9{}_0^1$	2090	$\nu_5{}_0^2$	1827	$\nu_6{}_0^1+\nu_{10}{}_0^2$
2250	$\nu_5{}_0^1+\nu_8{}_0^1$		2321	$\nu_6{}_0^1+\nu_9{}_0^1$	2091	$\nu_5{}_0^1+\nu_7{}_0^1$	1887	$\nu_6{}_0^1+\nu_9{}_0^1$
2254	$\nu_6{}_0^2$		2344	$\nu_7{}_0^2$	2114	$\nu_{10}{}_0^3$	1950	$\nu_8{}_0^2$
2300	$\nu_5{}_0^1+\nu_7{}_0^1$		2547	$\nu_4{}_0^1+\nu_{10}{}_0^1$	2167	$\nu_5{}_0^1+\nu_6{}_0^1$	2018	$\nu_7{}_0^2$
2303	$\nu_4{}_0^1+\nu_9{}_0^1$		2548	$\nu_6{}_0^1+\nu_{10}{}_0^1$	2174	$\nu_6{}_0^1+\nu_7{}_0^1$	2022	$\nu_4{}_0^1+\nu_{10}{}_0^2$
2327	$\nu_4{}_0^1+\nu_{10}{}_0^1$		2549	$\nu_5{}_0^1+\nu_6{}_0^1$	2182	$\nu_7{}_0^2$	2067	$\nu_5{}_0^1+\nu_{10}{}_0^2$
2415	$\nu_5{}_0^1+\nu_6{}_0^1$		2550	$\nu_4{}_0^1+\nu_5{}_0^1$	2191	$\nu_8{}_0^1+\nu_{10}{}_0^2$	2089	$\nu_4{}_0^1+\nu_9{}_0^1$
2450	$\nu_4{}_0^1+\nu_8{}_0^1$		2595	$\nu_8{}_0^3$	2251	$\nu_6{}_0^2$	2149	$\nu_5{}_0^1+\nu_9{}_0^1$
2500	$\nu_4{}_0^1+\nu_7{}_0^1$		2606	$\nu_8{}_0^1+\nu_9{}_0^2$	2253	$\nu_8{}_0^2+\nu_{10}{}_0^1$	2160	$\nu_9{}_0^3$
2575	$\nu_5{}_0^2$		2613	$\nu_9{}_0^3$	2264	$\nu_4{}_0^1+\nu_{10}{}_0^1$	2170	$\nu_6{}_0^1+\nu_8{}_0^1$
2615	$\nu_4{}_0^1+\nu_6{}_0^1$		2621	$\nu_4{}_0^1+\nu_7{}_0^1$	2298	$\nu_8{}_0^3$	2201	$\nu_6{}_0^1+\nu_7{}_0^1$
2676	$\nu_7{}_0^1+\nu_{10}{}_0^2$		2622	$\nu_6{}_0^1+\nu_7{}_0^1$	2312	$\nu_4{}_0^1+\nu_8{}_0^1$	2293	$\nu_4{}_0^1+\nu_8{}_0^1$
2792	$\nu_6{}_0^1+\nu_{10}{}_0^2$		2822	$\nu_8{}_0^2+\nu_{10}{}_0^1$	2433	$\nu_8{}_0^2+\nu_9{}_0^1$	2421	$\nu_5{}_0^1+\nu_8{}_0^1$
2867	$\nu_7{}_0^2+\nu_{10}{}_0^1$		2824	$\nu_5{}_0^1+\nu_8{}_0^2$	2444	$\nu_4{}_0^1+\nu_9{}_0^1$	2445	$\nu_8{}_0^1+\nu_9{}_0^2$
2885	$\nu_8{}_0^3$		2896	$\nu_7{}_0^1+\nu_8{}_0^2$	2465	$\nu_5{}_0^1+\nu_{10}{}_0^2$	2455	$\nu_4{}_0^1+\nu_6{}_0^1$
2934	$\nu_7{}_0^1+\nu_8{}_0^2$		2897	$\nu_4{}_0^1+\nu_6{}_0^1$	2472	$\nu_7{}_0^1+\nu_{10}{}_0^2$	2462	$\nu_5{}_0^1+\nu_7{}_0^1$
2955	$\nu_5{}_0^1+\nu_{10}{}_0^2$		2898	$\nu_6{}_0^2$	2536	$\nu_9{}_0^2+\nu_{10}{}_0^1$	2582	$\nu_3{}_0^1$
2979	$\nu_4{}_0^2$		2899	$\nu_4{}_0^2$	2549	$\nu_6{}_0^1+\nu_{10}{}_0^2$	2586	$\nu_4{}_0^2$
3051	$\nu_6{}_0^1+\nu_8{}_0^2$		2914	$\nu_7{}_0^1+\nu_9{}_0^2$	2576	$\nu_5{}_0^1+\nu_8{}_0^2$	2593	$\nu_5{}_0^1+\nu_6{}_0^1$
3069	$\nu_6{}_0^2+\nu_9{}_0^1$		3054	$\nu_8{}_0^1+\nu_{10}{}_0^2$	2585	$\nu_4{}_0^1+\nu_5{}_0^1$		
3148	$\nu_6{}_0^1+\nu_7{}_0^2$		3062	$\nu_9{}_0^1+\nu_{10}{}_0^2$	2586	$\nu_8{}_0^1+\nu_9{}_0^2$		
3155	$\nu_4{}_0^1+\nu_{10}{}_0^2$		3064	$\nu_5{}_0^2+\nu_8{}_0^1$	2593	$\nu_7{}_0^1+\nu_4{}_0^1$		
3212	$\nu_5{}_0^1+\nu_8{}_0^2$		3070	$\nu_5{}_0^2+\nu_9{}_0^1$	2659	$\nu_6{}_0^1+\nu_8{}_0^2$		
			3173	$\nu_4{}_0^1+\nu_8{}_0^2$	2670	$\nu_4{}_0^1+\nu_6{}_0^1$		
			3174	$\nu_6{}_0^1+\nu_8{}_0^2$	2709	$\nu_5{}_0^1+\nu_9{}_0^1$		
			3191	$\nu_4{}_0^1+\nu_9{}_0^2$	2810	$\nu_5{}_0^2+\nu_{10}{}_0^1$		
			3192	$\nu_6{}_0^1+\nu_9{}_0^2$	2857	$\nu_5{}_0^2+\nu_8{}_0^1$		
			3208	$\nu_8{}_0^1+\nu_7{}_0^2$	2857	$\nu_5{}_0^1+\nu_9{}_0^2$		
			3215	$\nu_7{}_0^2+\nu_9{}_0^1$	2866	$\nu_7{}_0^1+\nu_9{}_0^2$		
			3290	$\nu_5{}_0^1+\nu_{10}{}_0^2$	2902	$\nu_7{}_0^2+\nu_{10}{}_0^1$		
			3297	$\nu_5{}_0^3$	2943	$\nu_6{}_0^1+\nu_9{}_0^2$		
			3362	$\nu_7{}_0^1+\nu_{10}{}_0^2$	2957	$\nu_7{}_0^2+\nu_8{}_0^1$		
			3372	$\nu_5{}_0^2+\nu_7{}_0^1$	2968	$\nu_4{}_0^1+\nu_{10}{}_0^2$		

TABLE C10: Continued

$\widetilde{D}$		$\widetilde{E}$	
Energy	Assignment	Energy	Assignment
0	0_0^0	0	0_0^0
756	$\nu_{10_0^1}$	626	$\nu_{10_0^1}$
927	$\nu_{7_0^1}$	899	$\nu_{9_0^1}$
935	$\nu_{8_0^1}$	1094	$\nu_{7_0^1}$
1080	$\nu_{4_0^1}$	1157	$\nu_{6_0^1}$
1236	$\nu_{6_0^1}$	1252	$\nu_{10_0^2}$
1510	$\nu_{10_0^2}$	1339	$\nu_{5_0^1}$
1683	$\nu_{7_0^1}+\nu_{10_0^1}$	1525	$\nu_{9_0^1}+\nu_{10_0^1}$
1691	$\nu_{8_0^1}+\nu_{10_0^1}$	1720	$\nu_{7_0^1}+\nu_{10_0^1}$
1836	$\nu_{4_0^1}+\nu_{10_0^1}$	1783	$\nu_{6_0^1}+\nu_{10_0^1}$
1859	$\nu_{7_0^2}$	1797	$\nu_{9_0^2}$
1862	$\nu_{7_0^1}+\nu_{8_0^1}$	1878	$\nu_{10_0^3}$
1869	$\nu_{8_0^2}$	1964	$\nu_{5_0^1}+\nu_{10_0^1}$
1992	$\nu_{6_0^1}+\nu_{10_0^1}$	1993	$\nu_{7_0^1}+\nu_{9_0^1}$
2007	$\nu_{4_0^1}+\nu_{7_0^1}$	2057	$\nu_{6_0^1}+\nu_{9_0^1}$
2015	$\nu_{4_0^1}+\nu_{8_0^1}$	2151	$\nu_{9_0^1}+\nu_{10_0^2}$
2163	$\nu_{6_0^1}+\nu_{7_0^1}$	2188	$\nu_{7_0^2}$
2171	$\nu_{6_0^1}+\nu_{8_0^1}$	2238	$\nu_{5_0^1}+\nu_{9_0^1}$
2193	$\nu_{4_0^2}$	2251	$\nu_{6_0^1}+\nu_{7_0^1}$
2261	$\nu_{10_0^3}$	2315	$\nu_{6_0^2}$
2316	$\nu_{4_0^1}+\nu_{6_0^1}$	2346	$\nu_{7_0^1}+\nu_{10_0^2}$
2437	$\nu_{7_0^1}+\nu_{10_0^2}$	2409	$\nu_{6_0^1}+\nu_{10_0^2}$
2444	$\nu_{8_0^1}+\nu_{10_0^2}$	2423	$\nu_{9_0^2}+\nu_{10_0^1}$
2471	$\nu_{6_0^2}$	2432	$\nu_{5_0^1}+\nu_{7_0^1}$
2590	$\nu_{4_0^1}+\nu_{10_0^2}$	2496	$\nu_{5_0^1}+\nu_{6_0^1}$
2615	$\nu_{7_0^2}+\nu_{10_0^1}$	2590	$\nu_{5_0^1}+\nu_{10_0^2}$
2625	$\nu_{8_0^2}+\nu_{10_0^1}$	2677	$\nu_{5_0^2}$
2746	$\nu_{6_0^1}+\nu_{10_0^2}$	2941	$\nu_{6_0^2}+\nu_{10_0^1}$
2752	$\nu_{7_0^3}$	3136	$\nu_{5_0^1}+\nu_{9_0^2}$
2794	$\nu_{8_0^3}$	3187	$\nu_{3_0^1}$
2795	$\nu_{7_0^2}+\nu_{8_0^1}$	3214	$\nu_{6_0^2}+\nu_{9_0^1}$
2797	$\nu_{7_0^1}+\nu_{8_0^2}$	3303	$\nu_{5_0^2}+\nu_{10_0^1}$
2939	$\nu_{4_0^1}+\nu_{7_0^2}$	3409	$\nu_{6_0^2}+\nu_{7_0^1}$
2949	$\nu_{4_0^1}+\nu_{8_0^2}$	3526	$\nu_{5_0^1}+\nu_{7_0^2}$
2949	$\nu_{4_0^2}+\nu_{10_0^1}$	3529	$\nu_{1_0^1}$
3100	$\nu_{3_0^1}$	3576	$\nu_{5_0^2}+\nu_{9_0^1}$
3239	$\nu_{2_0^1}$	3771	$\nu_{5_0^2}+\nu_{7_0^1}$
		3813	$\nu_{3_0^1}+\nu_{10_0^1}$
		3840	$\nu_{5_0^2}+\nu_{6_0^1}$
		4086	$\nu_{3_0^1}+\nu_{9_0^1}$
		4155	$\nu_{1_0^1}+\nu_{10_0^1}$
		4281	$\nu_{3_0^1}+\nu_{7_0^1}$

TABLE C11: A few vibrational energy levels (in cm^{-1}) of the $\widetilde{X}$, $\widetilde{A}$, $\widetilde{B}$, $\widetilde{C}$, $\widetilde{D}$ and $\widetilde{E}$ electronic states of $CH_2NHCH_2^+$ calculated using MCQDPT method obtained from the uncoupled state calculations. The assignment of the levels carried out by examining the nodal pattern of the wavefunctions are included in the table.

$\widetilde{X}$		Expt. [86]	$\widetilde{A}$		$\widetilde{B}$		$\widetilde{C}$	
Energy	Assignment	Energy	Energy	Assignment	Energy	Assignment	Energy	Assignment
0	0_0^0		0	0_0^0	0	0_0^0	0	0_0^0
820	ν_9^1	800-650	758	ν_9^1	504	ν_9^1	600	ν_8^1
838	ν_{10}^1		791	ν_8^1	698	ν_{10}^1	607	ν_{10}^1
1058	ν_8^1		948	ν_{10}^1	958	ν_8^1	939	ν_5^1
1088	ν_7^1		1109	ν_7^1	1013	ν_9^2	1112	ν_{10}^2
1174	ν_5^1		1161	ν_6^1	1056	ν_6^1	1206	$\nu_8^1+\nu_{10}^1$
1341	ν_4^1		1321	ν_4^1	1118	ν_5^1	1231	ν_8^2
1639	ν_9^2		1512	ν_9^2	1202	$\nu_9^1+\nu_{10}^1$	1252	ν_4^1
1659	$\nu_9^1+\nu_{10}^1$		1550	$\nu_8^1+\nu_9^1$	1203	ν_7^1	1480	$\nu_5^1+\nu_8^1$
1685	ν_{10}^2		1588	ν_8^2	1307	ν_4^1	1539	$\nu_5^1+\nu_{10}^1$
1878	$\nu_8^1+\nu_9^1$		1706	$\nu_9^1+\nu_{10}^1$	1401	ν_{10}^2	1711	$\nu_8^1+\nu_{10}^2$
1897	$\nu_8^1+\nu_{10}^1$		1739	$\nu_8^1+\nu_{10}^1$	1462	$\nu_8^1+\nu_9^1$	1837	$\nu_8^2+\nu_{10}^1$
1908	$\nu_7^1+\nu_9^1$		1867	$\nu_7^1+\nu_9^1$	1545	ν_9^3	1851	$\nu_4^1+\nu_8^1$
1926	$\nu_7^1+\nu_{10}^1$		1893	ν_{10}^2	1560	$\nu_6^1+\nu_9^1$	1858	$\nu_4^1+\nu_{10}^1$
1995	$\nu_5^1+\nu_9^1$		1900	$\nu_7^1+\nu_8^1$	1622	$\nu_5^1+\nu_9^1$	1891	ν_5^2
2013	$\nu_5^1+\nu_{10}^1$		1919	$\nu_6^1+\nu_9^1$	1657	$\nu_8^1+\nu_{10}^1$	2064	$\nu_5^1+\nu_{10}^2$
2116	ν_8^2		1952	$\nu_6^1+\nu_8^1$	1707	$\nu_7^1+\nu_9^1$	2175	$\nu_5^1+\nu_8^2$
2146	$\nu_7^1+\nu_8^1$		2057	$\nu_7^1+\nu_{10}^1$	1712	$\nu_9^2+\nu_{10}^1$	2191	$\nu_4^1+\nu_5^1$
2161	$\nu_4^1+\nu_9^1$		2079	$\nu_4^1+\nu_9^1$	1754	$\nu_6^1+\nu_{10}^1$	2363	$\nu_4^1+\nu_{10}^2$
2180	$\nu_4^1+\nu_{10}^1$		2109	$\nu_6^1+\nu_{10}^1$	1811	$\nu_4^1+\nu_9^1$	2482	$\nu_4^1+\nu_8^2$
2181	ν_7^2		2112	$\nu_4^1+\nu_8^1$	1817	$\nu_5^1+\nu_{10}^1$	2512	ν_4^2
2232	$\nu_5^1+\nu_8^1$		2222	ν_7^2	1901	$\nu_7^1+\nu_{10}^1$	3089	$\nu_8^1+\nu_4^2$
2262	$\nu_5^1+\nu_7^1$		2268	$\nu_6^1+\nu_7^1$	1905	$\nu_9^1+\nu_{10}^2$	3199	ν_3^1
2350	ν_5^2		2269	ν_9^3	1914	ν_8^2	3798	$\nu_3^1+\nu_8^1$
2399	$\nu_4^1+\nu_8^1$		2304	$\nu_8^1+\nu_9^2$	1972	$\nu_8^1+\nu_9^2$	4448	$\nu_3^1+\nu_4^1$
2429	$\nu_4^1+\nu_7^1$		2325	ν_6^2	2006	$\nu_4^1+\nu_{10}^1$	6398	ν_3^2
2459	ν_9^3		2347	$\nu_8^2+\nu_9^1$	2014	$\nu_6^1+\nu_8^1$		
2478	$\nu_9^2+\nu_{10}^1$		2429	$\nu_4^1+\nu_6^1$	2069	$\nu_6^1+\nu_9^2$		
2505	$\nu_9^1+\nu_{10}^2$		2481	$\nu_9^2+\nu_{10}^1$	2076	$\nu_5^1+\nu_8^1$		
2515	$\nu_4^1+\nu_5^1$		2621	$\nu_7^1+\nu_9^2$	2109	ν_{10}^3		
2680	ν_4^2		2640	ν_4^2	2122	ν_6^2		
2728	$\nu_7^1+\nu_9^2$		2697	$\nu_7^1+\nu_8^2$	2132	$\nu_5^1+\nu_9^2$		
2746	$\nu_8^1+\nu_{10}^2$		2749	$\nu_6^1+\nu_8^2$	2161	$\nu_7^1+\nu_8^1$		
2773	$\nu_7^1+\nu_{10}^2$		2833	$\nu_4^1+\nu_9^2$	2174	$\nu_5^1+\nu_6^1$		
2814	$\nu_5^1+\nu_9^2$		2848	ν_{10}^3	2216	$\nu_7^1+\nu_9^2$		
2860	$\nu_5^1+\nu_{10}^2$		2909	$\nu_4^1+\nu_8^2$	2244	ν_5^2		
2980	$\nu_4^1+\nu_9^2$		3028	ν_9^4	2258	$\nu_6^1+\nu_7^1$		
3026	$\nu_4^1+\nu_{10}^2$		3340	ν_7^3	2259	$\nu_4^1+\nu_8^1$		
3170	ν_8^3		3495	ν_6^3	2265	$\nu_8^1+\nu_{10}^2$		
3268	ν_7^3				2320	$\nu_5^1+\nu_7^1$		
3280	ν_9^4				2321	$\nu_4^1+\nu_9^2$		
3354	ν_{10}^4				2363	$\nu_4^1+\nu_6^1$		
3522	ν_5^3				2405	ν_7^2		
					2457	$\nu_6^1+\nu_{10}^2$		
					2519	$\nu_5^1+\nu_{10}^2$		
					2604	$\nu_7^1+\nu_{10}^2$		
					2708	$\nu_4^1+\nu_{10}^2$		
					2820	ν_{10}^4		
					2872	ν_8^3		
					3165	ν_6^3		
					3355	ν_5^3		

TABLE C11: Continued

$\widetilde{D}$		$\widetilde{E}$	
Energy	Assignment	Energy	Assignment
0	0_0^0	0	0_0^0
722	$\nu10_0^1$	360	$\nu10_0^1$
763	$\nu7_0^1$	606	$\nu9_0^1$
771	$\nu8_0^1$	757	$\nu10_0^2$
984	$\nu5_0^1$	967	$\nu9_0^1+\nu10_0^1$
1152	$\nu6_0^1$	974	$\nu7_0^1$
1199	$\nu4_0^1$	1127	$\nu6_0^1$
1437	$\nu10_0^2$	1166	$\nu5_0^1$
1485	$\nu7_0^1+\nu10_0^1$	1189	$\nu10_0^3$
1493	$\nu8_0^1+\nu10_0^1$	1210	$\nu9_0^2$
1529	$\nu8_0^2$	1364	$\nu9_0^1+\nu10_0^2$
1533	$\nu7_0^1+\nu8_0^1$	1526	$\nu5_0^1+\nu10_0^1$
1706	$\nu5_0^1+\nu10_0^1$	1581	$\nu7_0^1+\nu9_0^1$
1747	$\nu5_0^1+\nu7_0^1$	1732	$\nu7_0^1+\nu10_0^2$
1755	$\nu5_0^1+\nu8_0^1$	1733	$\nu6_0^1+\nu9_0^1$
1874	$\nu6_0^1+\nu10_0^1$	1772	$\nu5_0^1+\nu9_0^1$
1915	$\nu6_0^1+\nu7_0^1$	1810	$\nu9_0^3$
1921	$\nu4_0^1+\nu10_0^1$	1884	$\nu6_0^1+\nu10_0^2$
1923	$\nu6_0^1+\nu8_0^1$	1923	$\nu5_0^1+\nu10_0^2$
1961	$\nu4_0^1+\nu7_0^1$	1956	$\nu7_0^2$
1968	$\nu5_0^2$	1967	$\nu9_0^2+\nu10_0^2$
1969	$\nu4_0^1+\nu8_0^1$	2101	$\nu6_0^1+\nu7_0^1$
2136	$\nu5_0^1+\nu6_0^1$	2140	$\nu5_0^1+\nu7_0^1$
2147	$\nu10_0^3$	2259	$\nu6_0^2$
2208	$\nu8_0^1+\nu10_0^2$	2316	$\nu5_0^1+\nu6_0^1$
2307	$\nu6_0^2$	2333	$\nu5_0^2$
2316	$\nu7_0^2+\nu8_0^1$	2399	$\nu9_0^2+\nu10_0^3$
2348	$\nu4_0^1+\nu6_0^1$	2409	$\nu9_0^4$
2390	$\nu4_0^2$		
2421	$\nu5_0^1+\nu10_0^2$		
2513	$\nu5_0^1+\nu7_0^2$		
2589	$\nu6_0^1+\nu10_0^2$		
2636	$\nu4_0^1+\nu10_0^2$		
2682	$\nu6_0^1+\nu7_0^2$		
2728	$\nu4_0^1+\nu7_0^2$		
2858	$\nu5_0^1+\nu10_0^1$		

TABLE C12: The normal mode combination and sizes of the primitive and single-particle functions (SPFs) utilized in the coupled states dynamics calculations of the $CH_2NHCH_2^+$ using the MCTDH suite of programs are presented. [a] The primitive basis denotes the number of Harmonic oscillator DVR functions for the relevant mode, with the primitive basis for each particle being the product of the one-dimensional bases. [b] The SPF basis represents the number of single-particle functions used. The vibronic spectrum of the coupled electronic states of the $CH_2NHCH_2^+$ is depicted in Fig. 5.6.

Electronic state	Normal modes	Primitive basis[a]	SPF basis[b]	method
$\widetilde{X}$-$\widetilde{A}$-$\widetilde{B}$ -$\widetilde{C}$-$\widetilde{D}$-$\widetilde{E}$	$\nu_1, \nu_2, \nu_3, \nu_{11}, \nu_{12}$ ν_4, ν_{13} ν_5, ν_6, ν_{14} $\nu_7, \nu_8, \nu_{15}, \nu_{16}$ $\nu_9, \nu_{10}, \nu_{17}, \nu_{18}$	(8,10,12,8,8) (16,12) (14,14,16) (8,10,16,10) (18,20,10,20)	[8,10,10,10,8,8] [8,10,10,10,8,8] [8,10,10,10,8,8] [8,10,10,10,8,8] [8,10,10,10,8,8]	EOMIP-CCSD
$\widetilde{X}$-$\widetilde{A}$-$\widetilde{B}$ -$\widetilde{C}$-$\widetilde{D}$-$\widetilde{E}$	$\nu_1, \nu_2, \nu_3, \nu_{11}, \nu_{12}$ ν_4, ν_{13} ν_5, ν_6, ν_{14} $\nu_7, \nu_8, \nu_{15}, \nu_{16}$ $\nu_9, \nu_{10}, \nu_{17}, \nu_{18}$	(8,10,10,8,8) (12,14) (14,16,16) (10,12,12,10) (16,16,16,16)	[8,10,10,10,8,8] [8,10,10,10,8,8] [8,10,10,10,8,8] [8,10,10,10,8,8] [8,10,10,10,8,8]	MCQDPT

(a) 1288 cm^{-1}

(b) 1127 cm^{-1}

(c) 815 cm^{-1}

(d) 2575 cm^{-1}

(e) 2254 cm^{-1}

(f) 1636 cm^{-1}

(g) 2415 cm^{-1}

(h) 2103 cm^{-1}

(i) 1943 cm^{-1}
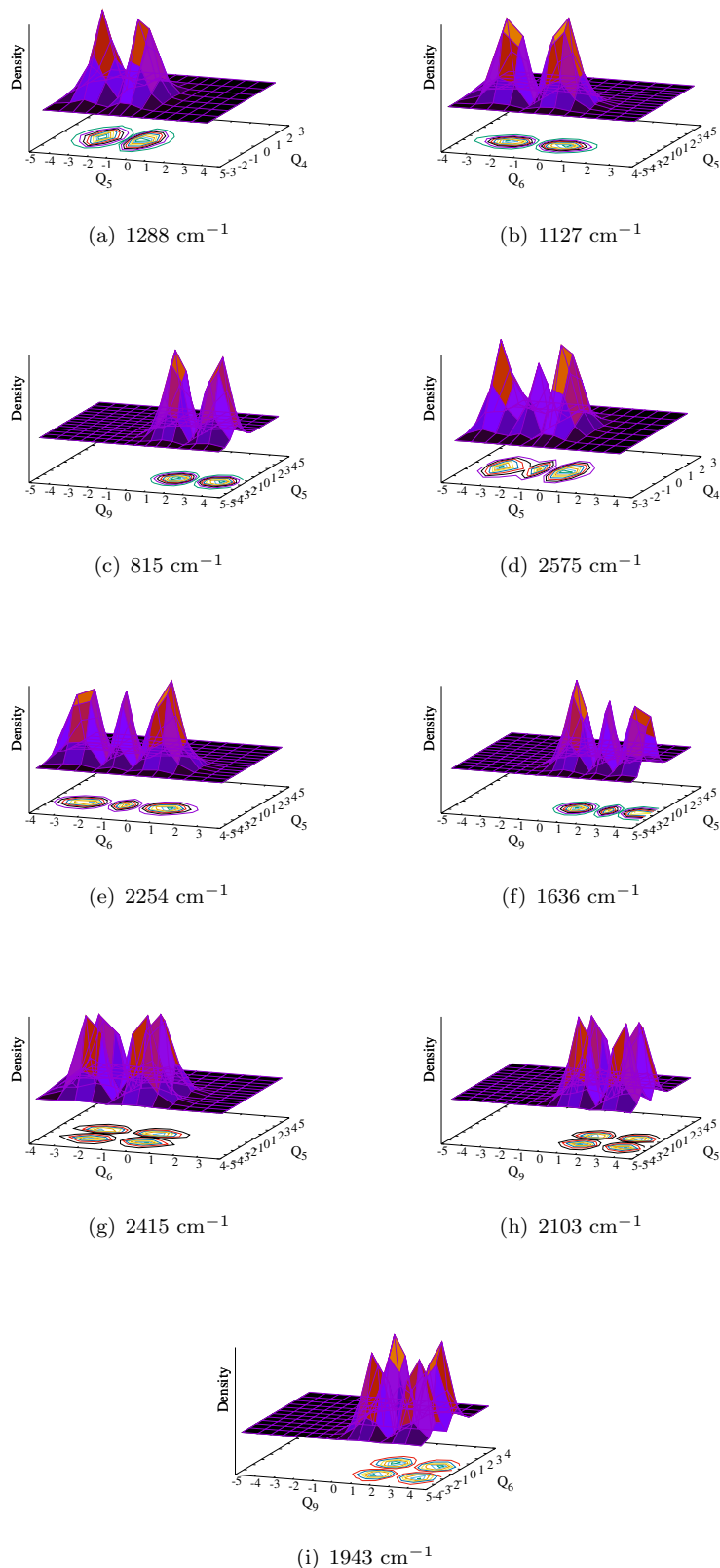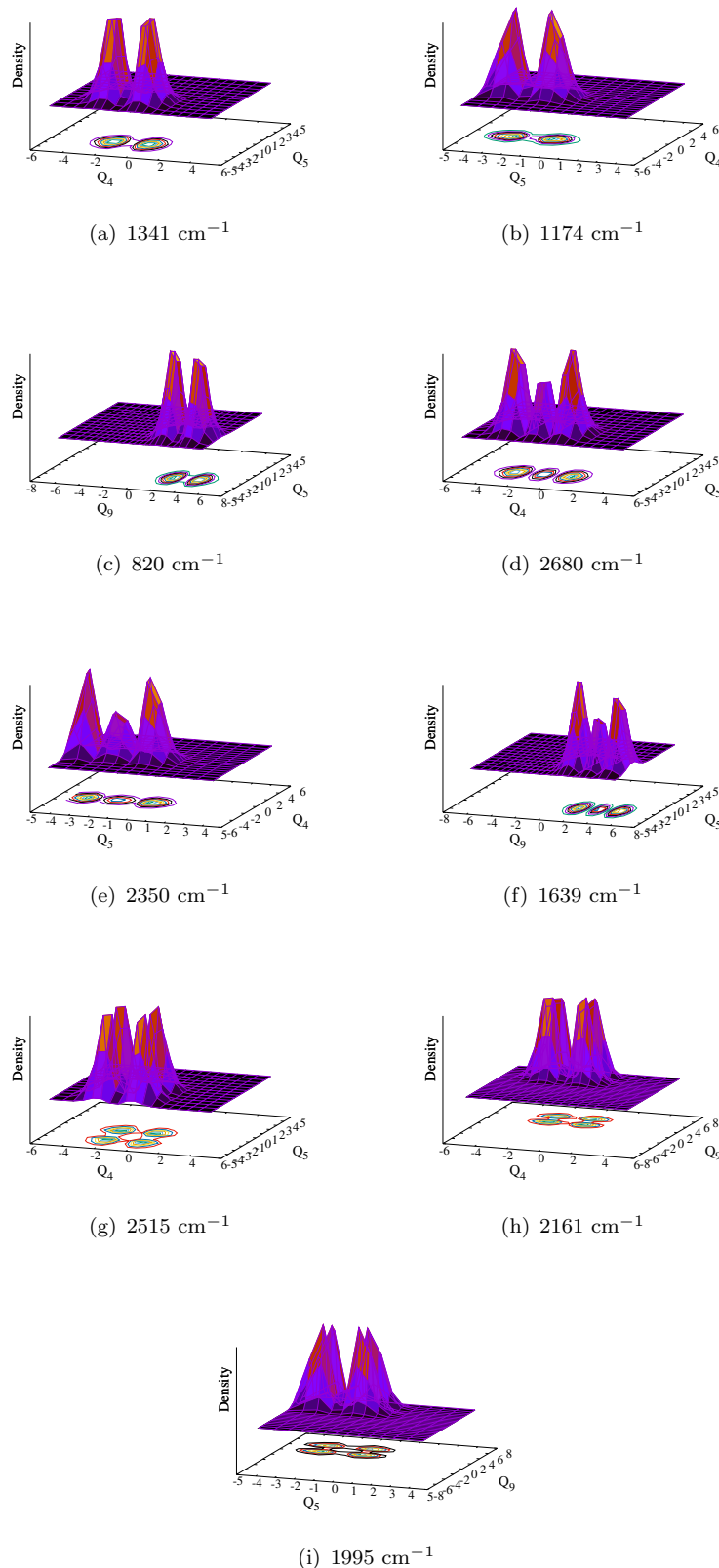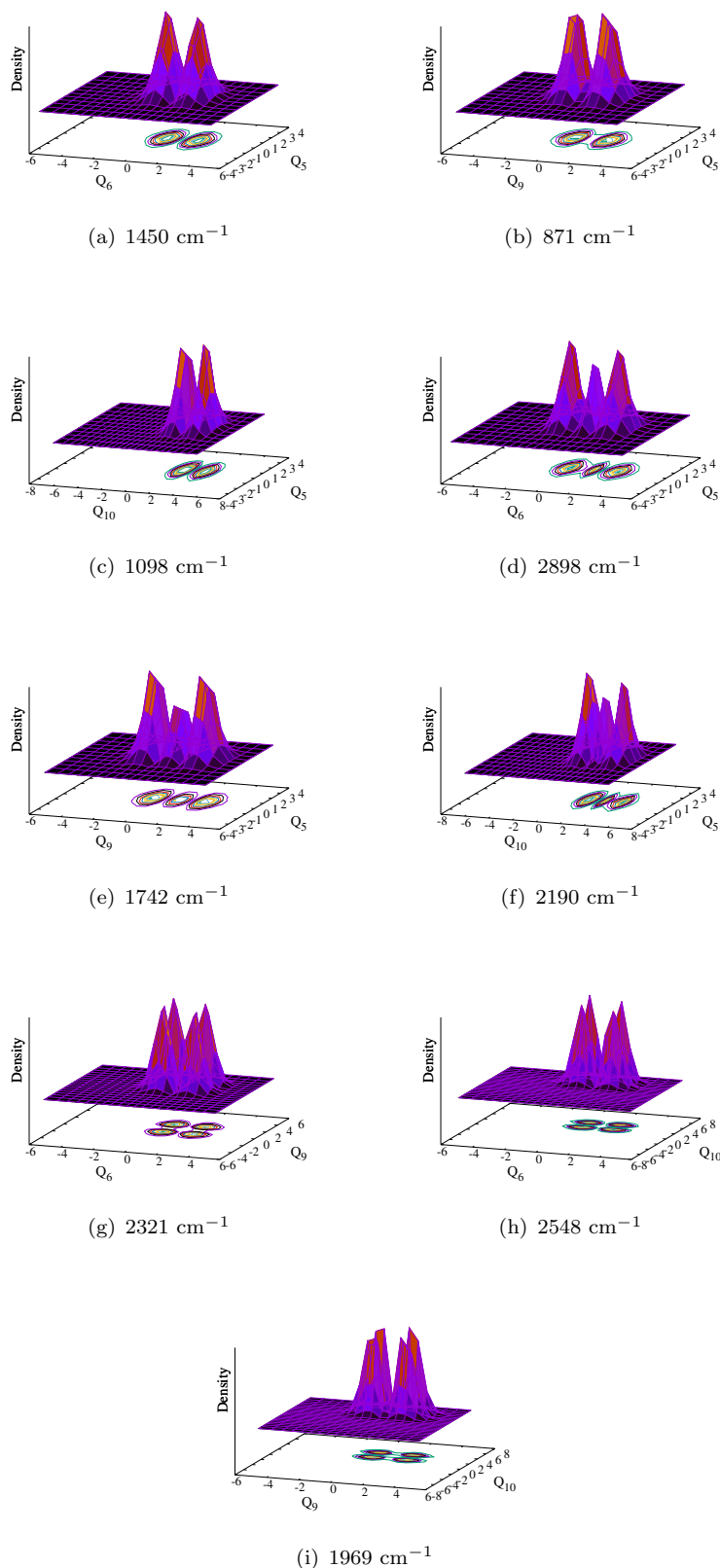
FIGURE C1: Probability density of vibronic wave functions of the $\widetilde{X}$ electronic state of $CH_2NHCH_2^+$ with using EOMIP-CCSD data as a function of nuclear coordinate. Panels a, b and c represent the fundamental of ν_{50}^1, ν_{60}^1 and ν_{90}^1 and first overtone of ν_{50}^2, ν_{60}^2 and ν_{90}^2 modes, the wavefunction in panels g, h and i represent the combination peak of $\nu_{50}^1+\nu_{60}^1$, $\nu_{50}^1+\nu_{90}^1$ and $\nu_{60}^1+\nu_{90}^1$.

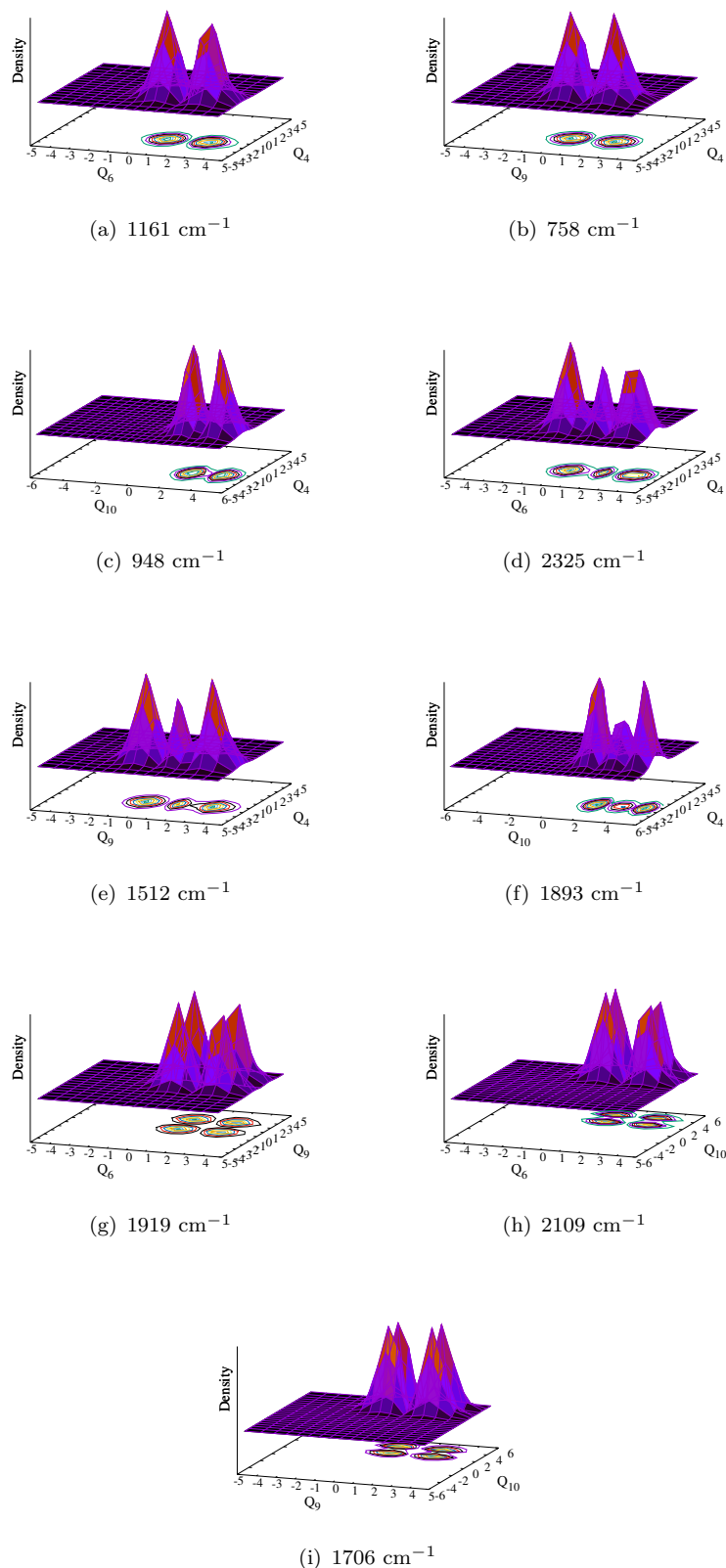(a) 1341 cm^{-1}

(b) 1174 cm^{-1}

(c) 820 cm^{-1}

(d) 2680 cm^{-1}

(e) 2350 cm^{-1}

(f) 1639 cm^{-1}

(g) 2515 cm^{-1}

(h) 2161 cm^{-1}

(i) 1995 cm^{-1}

FIGURE C2: Probability density of vibronic wave functions of the $\widetilde{X}$ electronic state of $CH_2NHCH_2^+$ with using MCQDPT data as a function of nuclear coordinate. Panels a, b and c represent the fundamental of ν_{40}^1, ν_{50}^1 and ν_{90}^1 and first overtone of ν_{40}^2, ν_{50}^2 and ν_{90}^2 modes, the wavefunction in panels g, h and i represent the combination peak of $\nu_{40}^1 + \nu_{50}^1$, $\nu_{40}^1 + \nu_{90}^1$ and $\nu_{50}^1 + \nu_{90}^1$.
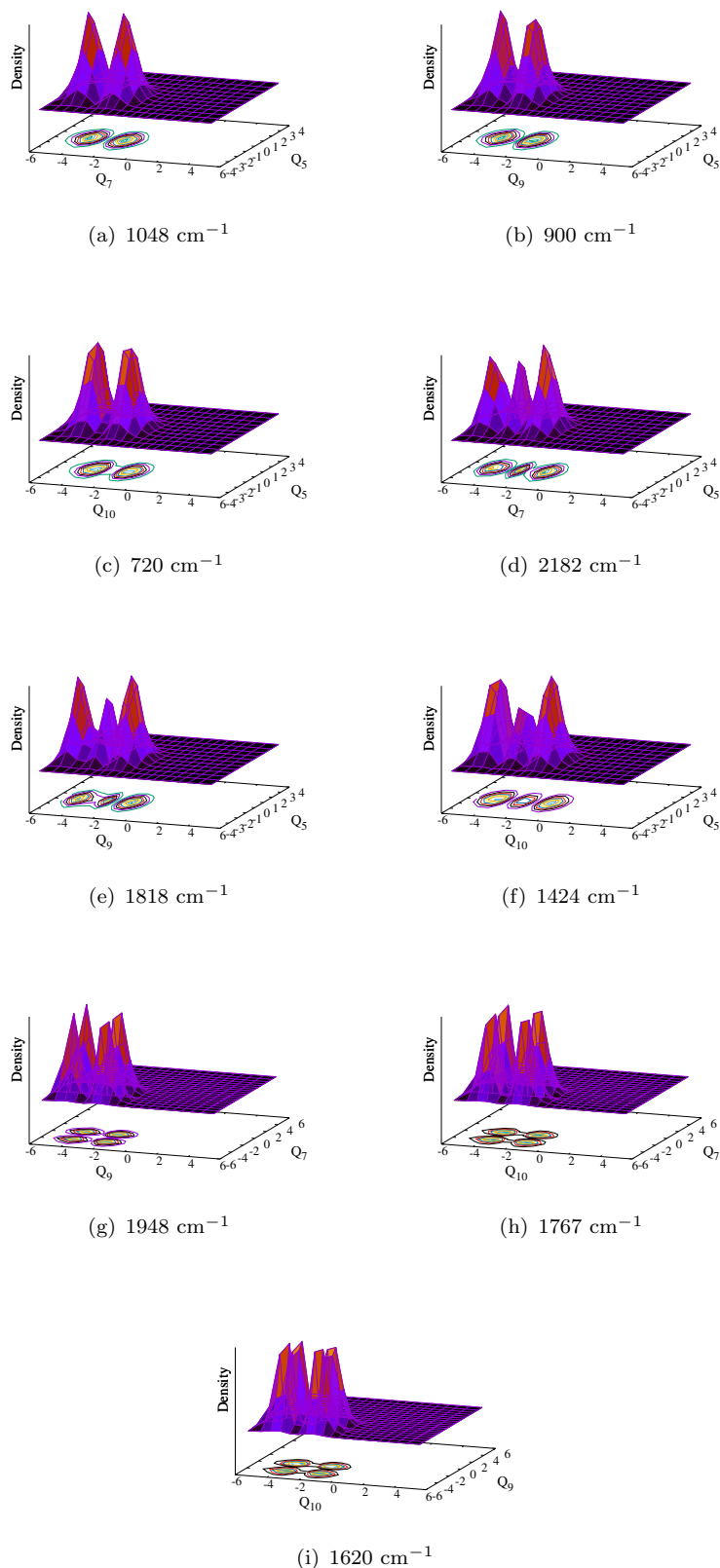
(a) 1450 cm^{-1}

(b) 871 cm^{-1}

(c) 1098 cm^{-1}

(d) 2898 cm^{-1}

(e) 1742 cm^{-1}

(f) 2190 cm^{-1}

(g) 2321 cm^{-1}

(h) 2548 cm^{-1}

(i) 1969 cm^{-1}

FIGURE C3: Probability density of vibronic wave functions of the $\widetilde{A}$ electronic state of $CH_2NHCH_2^+$ with using EOMIP-CCSD data as a function of nuclear coordinate. Panels a, b and c represent the fundamental of ν_{60}^1, ν_{90}^1 and ν_{100}^1 and first overtone of ν_{60}^2, ν_{90}^2 and ν_{100}^2 modes, the wavefunction in panels g, h and i represent the combination peak of $\nu_{60}^1 + \nu_{90}^1$, $\nu_{60}^1 + \nu_{100}^1$ and $\nu_{90}^1 + \nu_{100}^1$.

(a) 1161 cm^{-1}

(b) 758 cm^{-1}

(c) 948 cm^{-1}

(d) 2325 cm^{-1}

(e) 1512 cm^{-1}

(f) 1893 cm^{-1}

(g) 1919 cm^{-1}

(h) 2109 cm^{-1}

(i) 1706 cm^{-1}
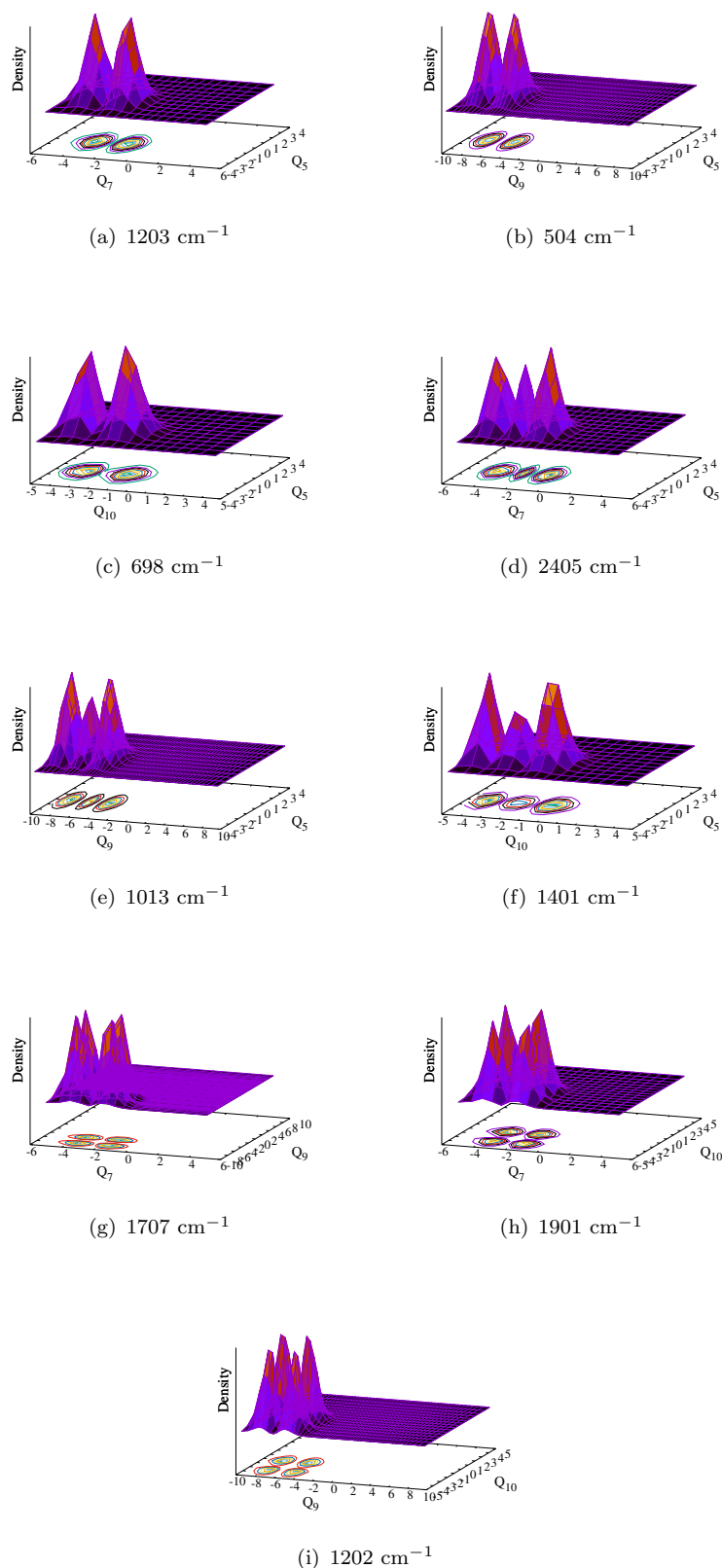
FIGURE C4: Probability density of vibronic wave functions of the $\widetilde{A}$ electronic state of $CH_2NHCH_2^+$ with using MCQDPT data as a function of nuclear coordinate. Panels a, b and c represent the fundamental of ν_{60}^1, ν_{90}^1 and ν_{100}^1 and first overtone of ν_{60}^2, ν_{90}^2 and ν_{100}^2 modes, the wavefunction in panels g, h and i represent the combination peak of $\nu_{60}^1 + \nu_{90}^1$, $\nu_{60}^1 + \nu_{100}^1$ and $\nu_{90}^1 + \nu_{100}^1$.

(a) 1048 cm^{-1}

(b) 900 cm^{-1}

(c) 720 cm^{-1}

(d) 2182 cm^{-1}

(e) 1818 cm^{-1}

(f) 1424 cm^{-1}
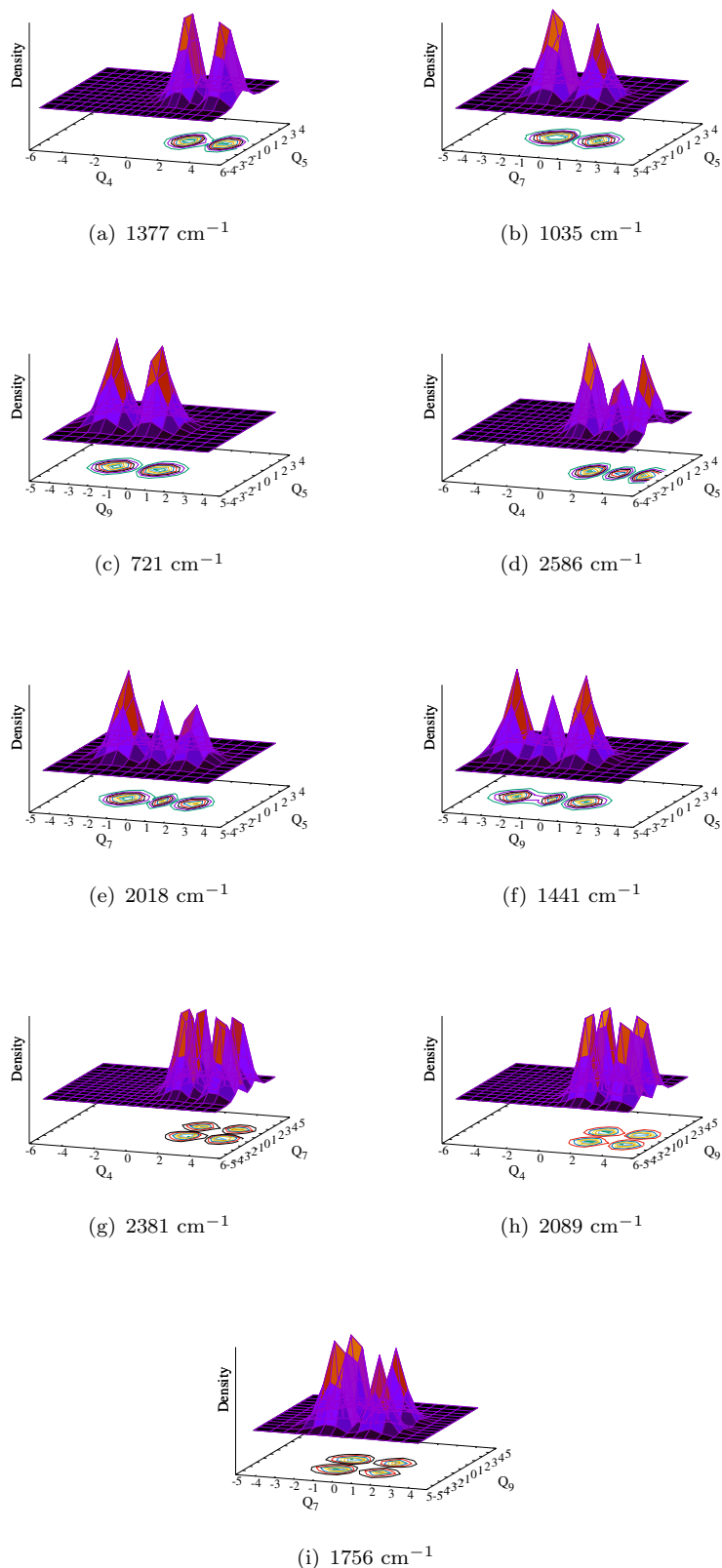
(g) 1948 cm^{-1}

(h) 1767 cm^{-1}

(i) 1620 cm^{-1}

FIGURE C5: Probability density of vibronic wave functions of the $\widetilde{B}$ electronic state of $CH_2NHCH_2^+$ with using EOMIP-CCSD data as a function of nuclear coordinate. Panels a, b and c represent the fundamental of ν_{70}^1, ν_{90}^1 and ν_{100}^1 and first overtone of ν_{70}^2, ν_{90}^2 and ν_{100}^2 modes, the wavefunction in panels g, h and i represent the combination peak of $\nu_{70}^1+\nu_{90}^1$, $\nu_{70}^1+\nu_{100}^1$ and $\nu_{90}^1+\nu_{100}^1$.
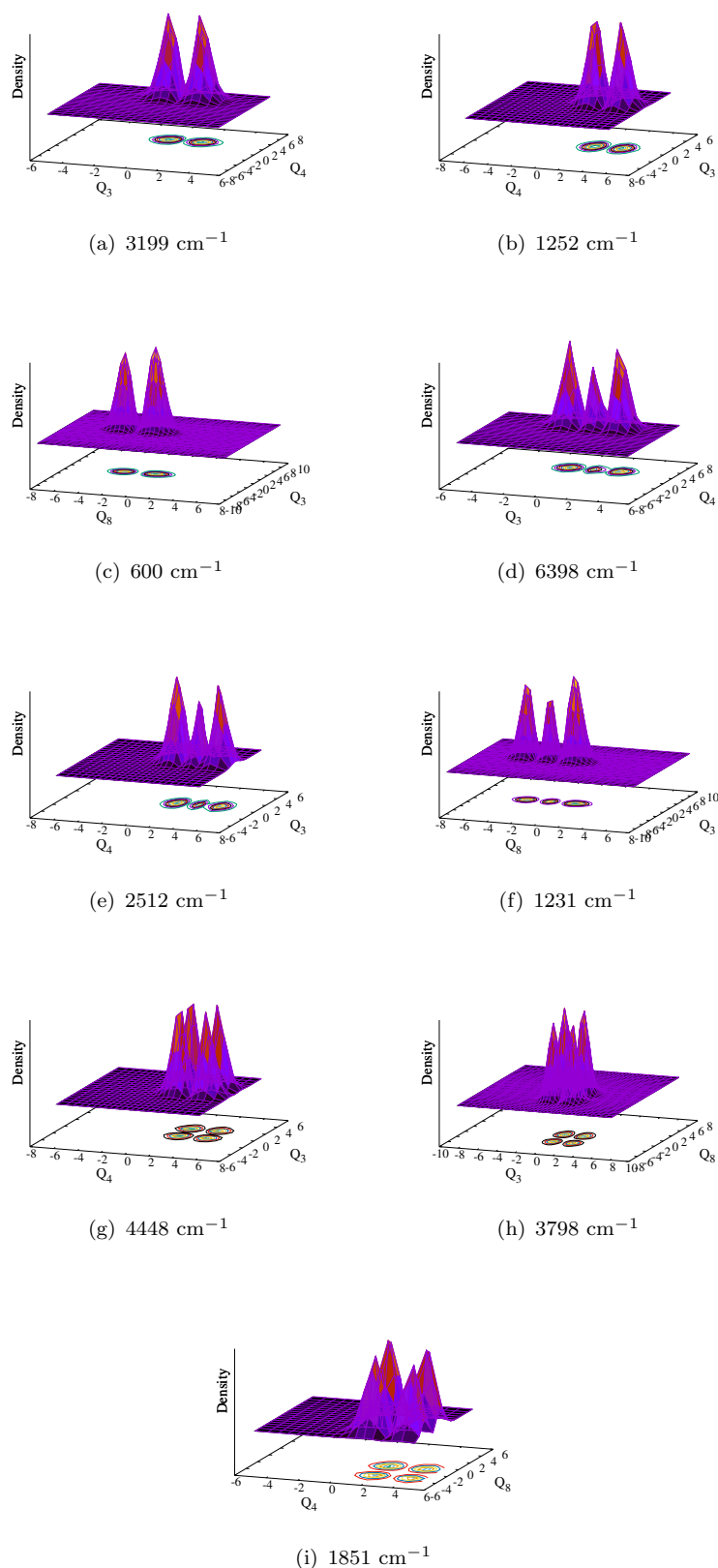
(a) 1203 cm^{-1}

(b) 504 cm^{-1}

(c) 698 cm^{-1}

(d) 2405 cm^{-1}

(e) 1013 cm^{-1}

(f) 1401 cm^{-1}

(g) 1707 cm^{-1}

(h) 1901 cm^{-1}

(i) 1202 cm^{-1}

FIGURE C6: Probability density of vibronic wave functions of the $\widetilde{B}$ electronic state of $CH_2NHCH_2^+$ with using MCQDPT data as a function of nuclear coordinate. Panels a, b and c represent the fundamental of ν_{70}^1, ν_{90}^1 and ν_{100}^1 and first overtone of ν_{70}^2, ν_{90}^2 and ν_{100}^2 modes, the wavefunction in panels g, h and i represent the combination peak of $\nu_{70}^1 + \nu_{90}^1$, $\nu_{70}^1 + \nu_{100}^1$ and $\nu_{90}^1 + \nu_{100}^1$.
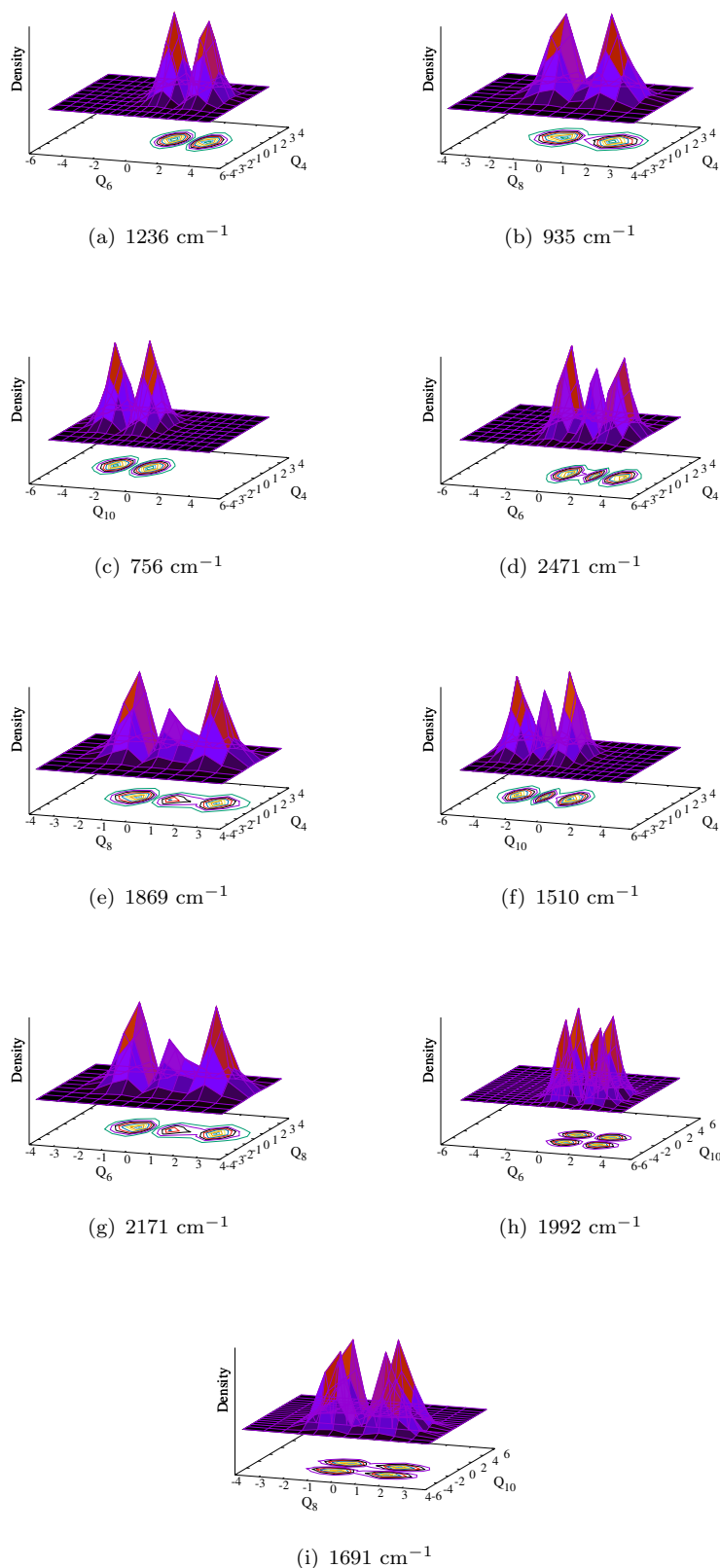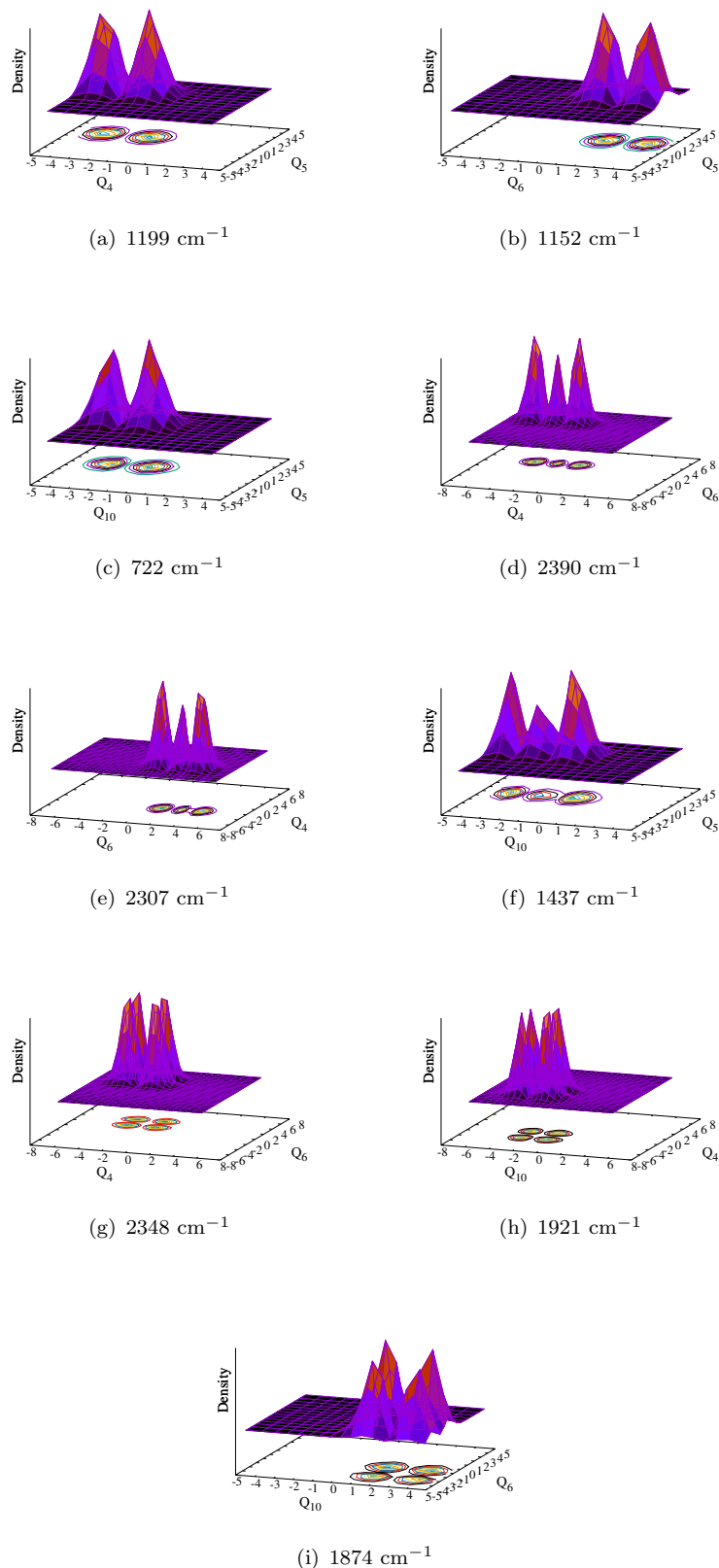
(a) 1377 cm^{-1}

(b) 1035 cm^{-1}

(c) 721 cm^{-1}

(d) 2586 cm^{-1}

(e) 2018 cm^{-1}

(f) 1441 cm^{-1}

(g) 2381 cm^{-1}

(h) 2089 cm^{-1}

(i) 1756 cm^{-1}

FIGURE C7: Probability density of vibronic wave functions of the $\widetilde{C}$ electronic state of $CH_2NHCH_2^+$ with using EOMIP-CCSD data as a function of nuclear coordinate. Panels a, b and c represent the fundamental of ν_{40}^1, ν_{70}^1 and ν_{90}^1 and first overtone and second overtone of ν_{40}^2, ν_{70}^2 and ν_{90}^3 modes, the wavefunction in panels g, h and i represent the combination peak of $\nu_{40}^1+\nu_{70}^1$, $\nu_{40}^1+\nu_{90}^1$ and $\nu_{70}^1+\nu_{90}^1$.

(a) 3199 cm^{-1}

(b) 1252 cm^{-1}

(c) 600 cm^{-1}

(d) 6398 cm^{-1}

(e) 2512 cm^{-1}

(f) 1231 cm^{-1}

(g) 4448 cm^{-1}

(h) 3798 cm^{-1}

(i) 1851 cm^{-1}

FIGURE C8: Probability density of vibronic wave functions of the $\widetilde{C}$ electronic state of $CH_2NHCH_2^+$ with using MCQDPT data as a function of nuclear coordinate. Panels a, b and c represent the fundamental of ν_{30}^1, ν_{40}^1 and ν_{80}^1 and first overtone and second overtone of ν_{30}^2, ν_{40}^2 and ν_{80}^3 modes, the wavefunction in panels g, h and i represent the combination peak of $\nu_{30}^1+\nu_{40}^1$, $\nu_{30}^1+\nu_{80}^1$ and $\nu_{40}^1+\nu_{80}^1$.
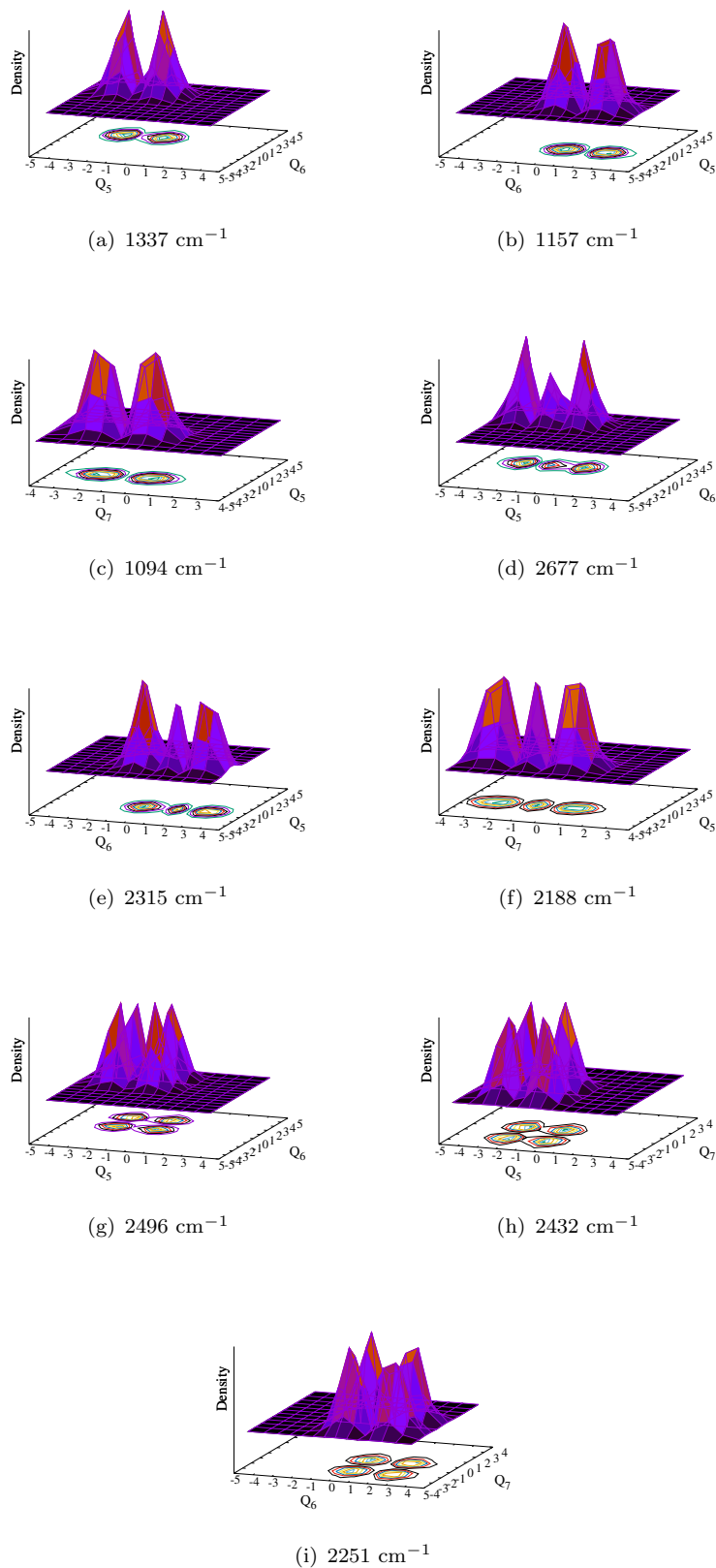
(a) 1236 cm^{-1}

(b) 935 cm^{-1}

(c) 756 cm^{-1}

(d) 2471 cm^{-1}

(e) 1869 cm^{-1}

(f) 1510 cm^{-1}

(g) 2171 cm^{-1}

(h) 1992 cm^{-1}

(i) 1691 cm^{-1}

FIGURE C9: Probability density of vibronic wave functions of the $\widetilde{D}$ electronic state of $CH_2NHCH_2^+$ with using EOMIP-CCSD data as a function of nuclear coordinate. Panels a, b and c represent the fundamental of ν_{60}^1, ν_{80}^1 and ν_{100}^1 and first overtone of ν_{60}^2, ν_{80}^2 and ν_{100}^2 modes, the wavefunction in panels g, h and i represent the combination peak of $\nu_{60}^1 + \nu_{80}^1$, $\nu_{60}^1 + \nu_{100}^1$ and $\nu_{80}^1 + \nu_{100}^1$.
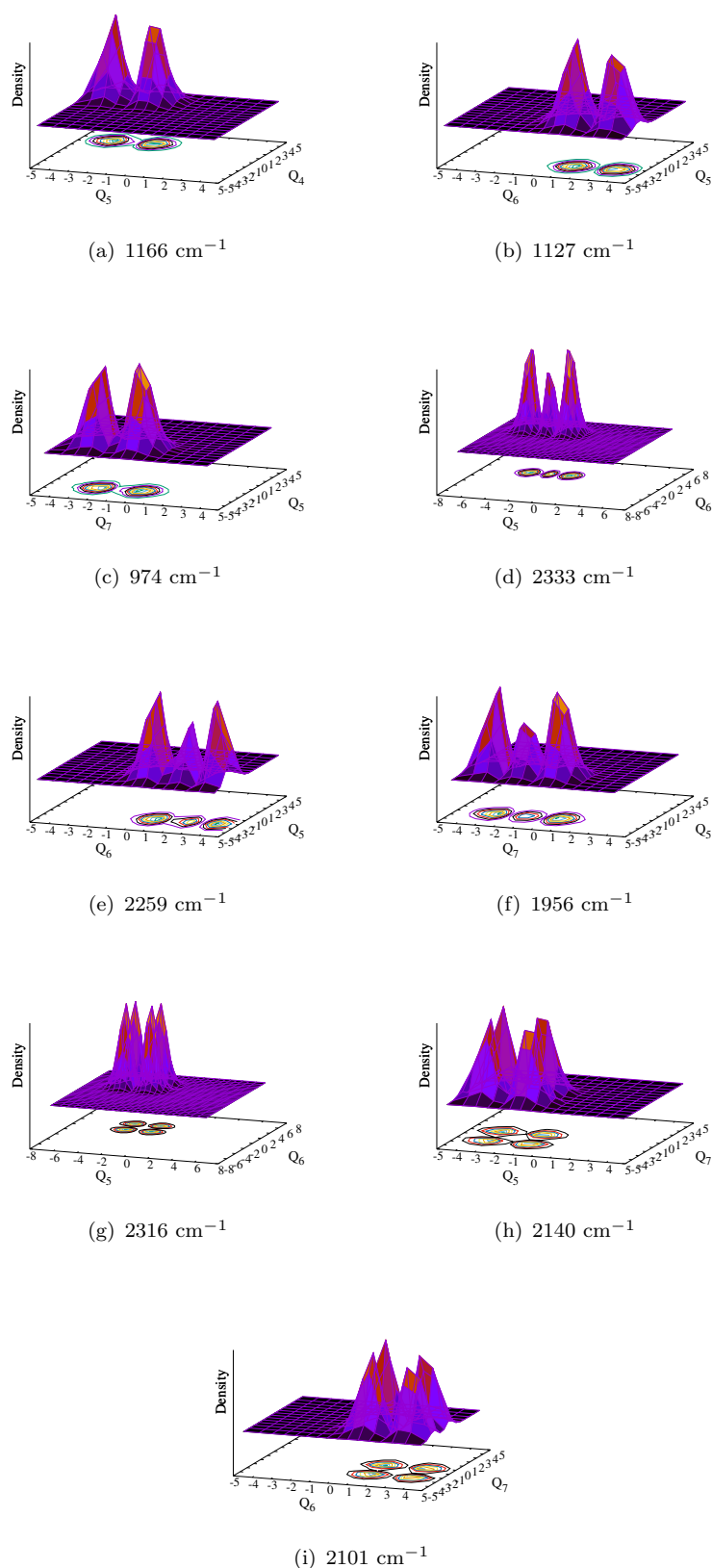
(a) 1199 cm^{-1}

(b) 1152 cm^{-1}

(c) 722 cm^{-1}

(d) 2390 cm^{-1}

(e) 2307 cm^{-1}

(f) 1437 cm^{-1}

(g) 2348 cm^{-1}

(h) 1921 cm^{-1}

(i) 1874 cm^{-1}

FIGURE C10: Probability density of vibronic wave functions of the $\widetilde{D}$ electronic state of $CH_2NHCH_2^+$ with using MCQDPT data as a function of nuclear coordinate. Panels a, b and c represent the fundamental of ν_{60}^1, ν_{40}^1 and ν_{100}^1 and first overtone of ν_{60}^2, ν_{40}^2 and ν_{100}^2 modes, the wavefunction in panels g, h and i represent the combination peak of $\nu_{40}^1 + \nu_{60}^1$, $\nu_{40}^1 + \nu_{100}^1$ and $\nu_{60}^1 + \nu_{100}^1$.

(a) 1337 cm^{-1}

(b) 1157 cm^{-1}

(c) 1094 cm^{-1}

(d) 2677 cm^{-1}

(e) 2315 cm^{-1}

(f) 2188 cm^{-1}

(g) 2496 cm^{-1}

(h) 2432 cm^{-1}

(i) 2251 cm^{-1}

FIGURE C11: Probability density of vibronic wave functions of the $\widetilde{E}$ electronic state of $CH_2NHCH_2^+$ with using EOMIP-CCSD data as a function of nuclear coordinate. Panels a, b and c represent the fundamental of ν_{50}^1, ν_{60}^1 and ν_{70}^1 and first overtone of ν_{50}^2, ν_{60}^2 and ν_{70}^2 modes, the wavefunction in panels g, h and i represent the combination peak of $\nu_{50}^1 + \nu_{60}^1$, $\nu_{50}^1 + \nu_{70}^1$ and $\nu_{60}^1 + \nu_{70}^1$.

(a) 1166 cm^{-1}

(b) 1127 cm^{-1}

(c) 974 cm^{-1}

(d) 2333 cm^{-1}

(e) 2259 cm^{-1}

(f) 1956 cm^{-1}

(g) 2316 cm^{-1}

(h) 2140 cm^{-1}

(i) 2101 cm^{-1}

FIGURE C12: Probability density of vibronic wave functions of the $\widetilde{E}$ electronic state of $CH_2NHCH_2^+$ with using MCQDPT data as a function of nuclear coordinate. Panels a, b and c represent the fundamental of ν_{50}^1, ν_{60}^1 and ν_{70}^1 and first overtone of ν_{50}^2, ν_{60}^2 and ν_{70}^2 modes, the wavefunction in panels g, h and i represent the combination peak of $\nu_{50}^1+\nu_{60}^1$, $\nu_{50}^1+\nu_{70}^1$ and $\nu_{60}^1+\nu_{70}^1$.
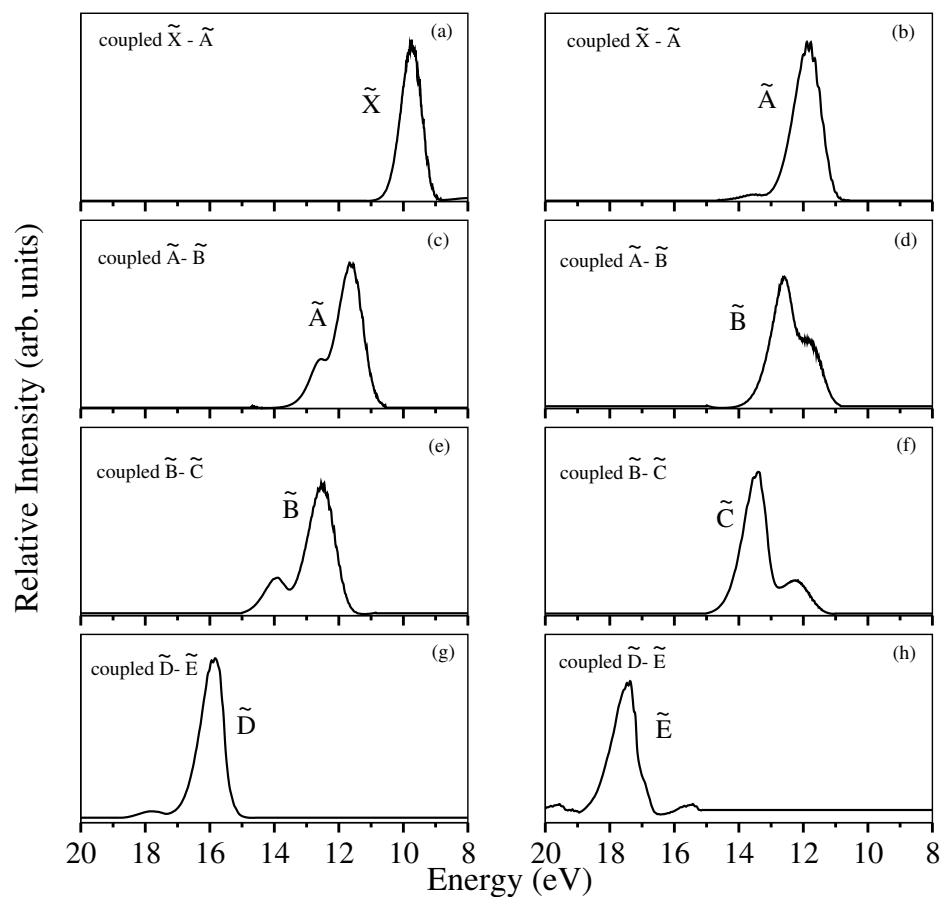
FIGURE C13: The composite vibronic band structure of the coupled $\widetilde{X}$-$\widetilde{A}$, $\widetilde{A}$-$\widetilde{B}$, $\widetilde{B}$-$\widetilde{C}$ and $\widetilde{D}$-$\widetilde{E}$ states of $CH_2NHCH_2^+$ are depicted in panels (a)-(h) respectively. These band structures are calculated utilizing the Hamiltonian parameters derived from the EOMIP-CCSD energy data.
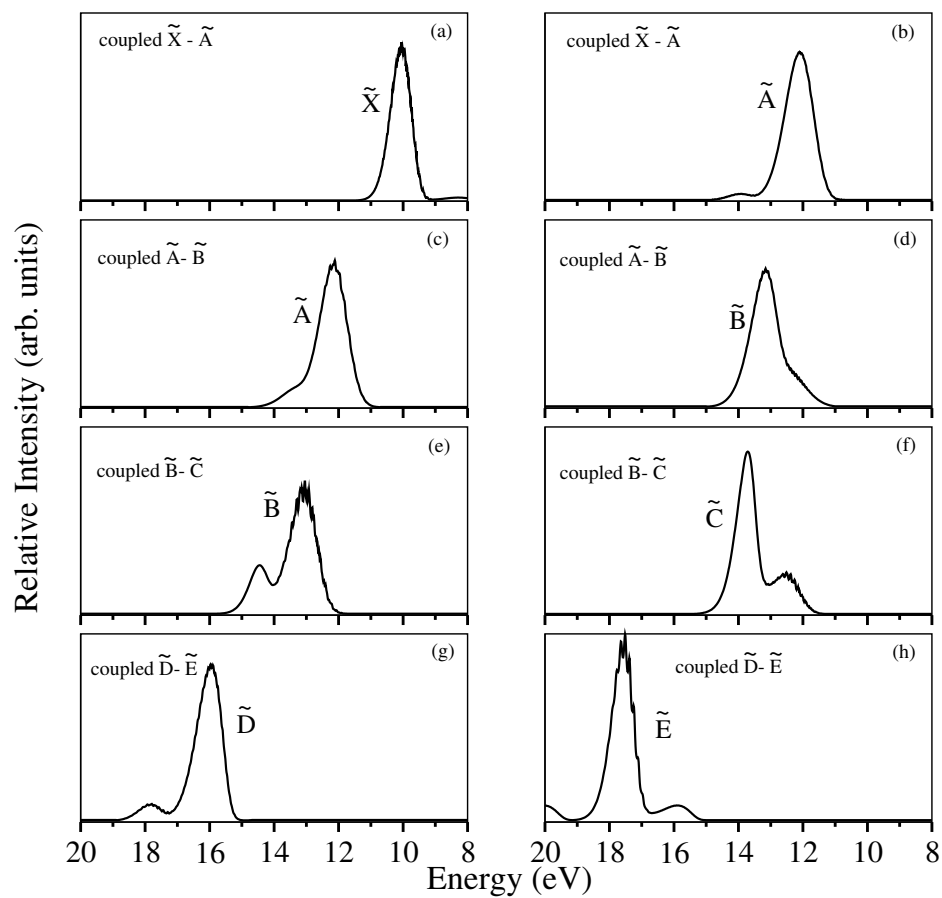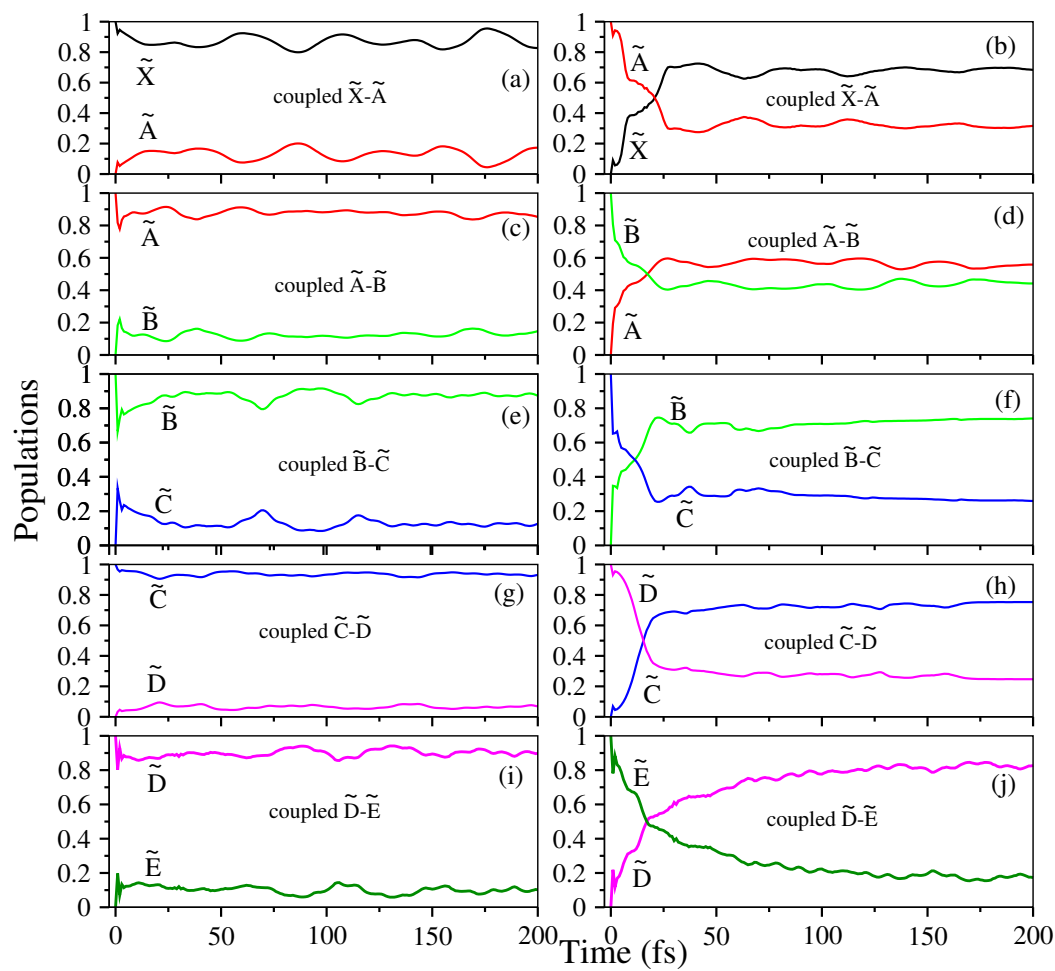
FIGURE C14: The composite vibronic band structure of the coupled $\widetilde{X}$-$\widetilde{A}$, $\widetilde{A}$-$\widetilde{B}$, $\widetilde{B}$-$\widetilde{C}$ and $\widetilde{D}$-$\widetilde{E}$ states of $CH_2NHCH_2^+$ are depicted in panels (a)-(h), respectively. These band structures are calculated utilizing the Hamiltonian parameters derived from the MCQDPT energy data.

FIGURE C15: The electronic population dynamics for the coupled $\widetilde{X}$-$\widetilde{A}$, $\widetilde{A}$-$\widetilde{B}$, $\widetilde{B}$-$\widetilde{C}$, $\widetilde{C}$-$\widetilde{D}$ and $\widetilde{D}$-$\widetilde{E}$ states of the $CH_2NHCH_2^+$ calculated with using EOMIP-CCSD data are shown in the panels (a)–(j), respectively.
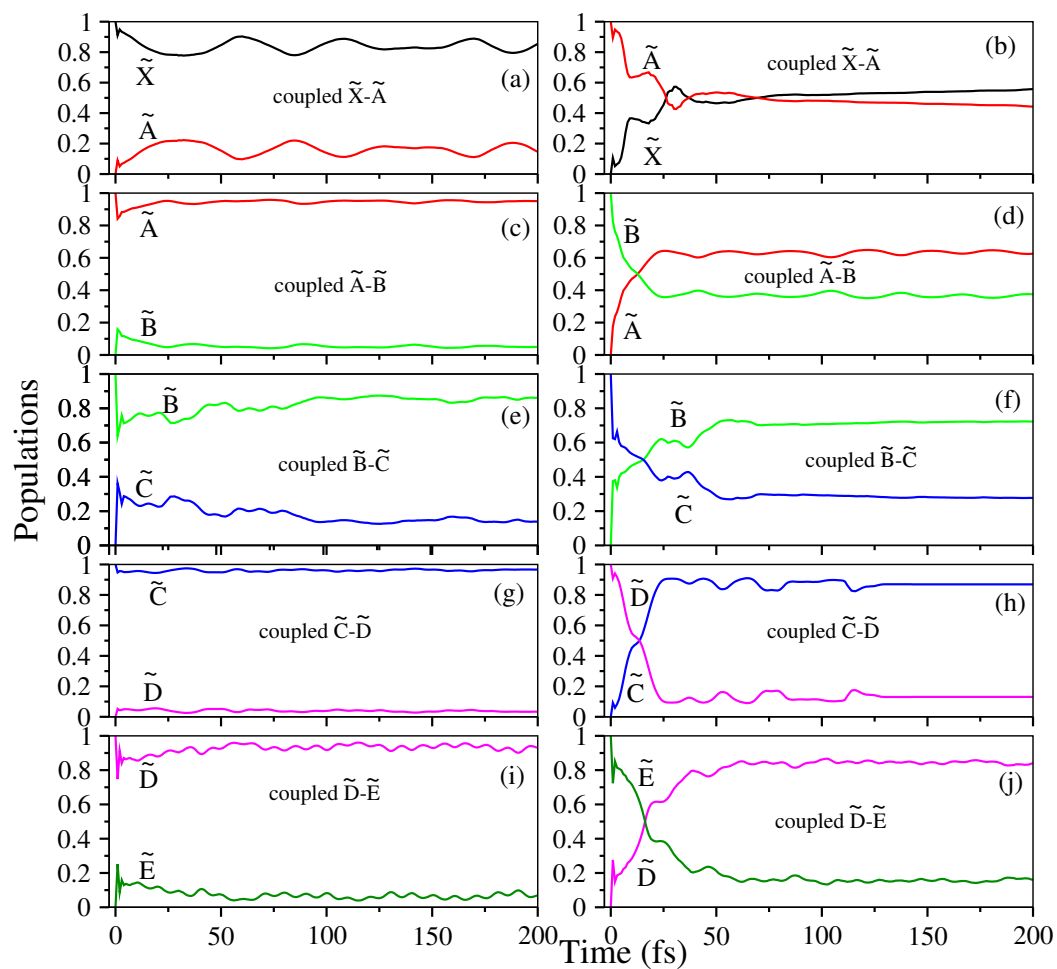
FIGURE C16: The electronic population dynamics for the coupled $\widetilde{X}$-$\widetilde{A}$, $\widetilde{A}$-$\widetilde{B}$, $\widetilde{B}$-$\widetilde{C}$, $\widetilde{C}$-$\widetilde{D}$ and $\widetilde{D}$-$\widetilde{E}$ states of the $CH_2NHCH_2^+$ calculated with using MCQDPT data are shown in the panels (a)–(j), respectively.
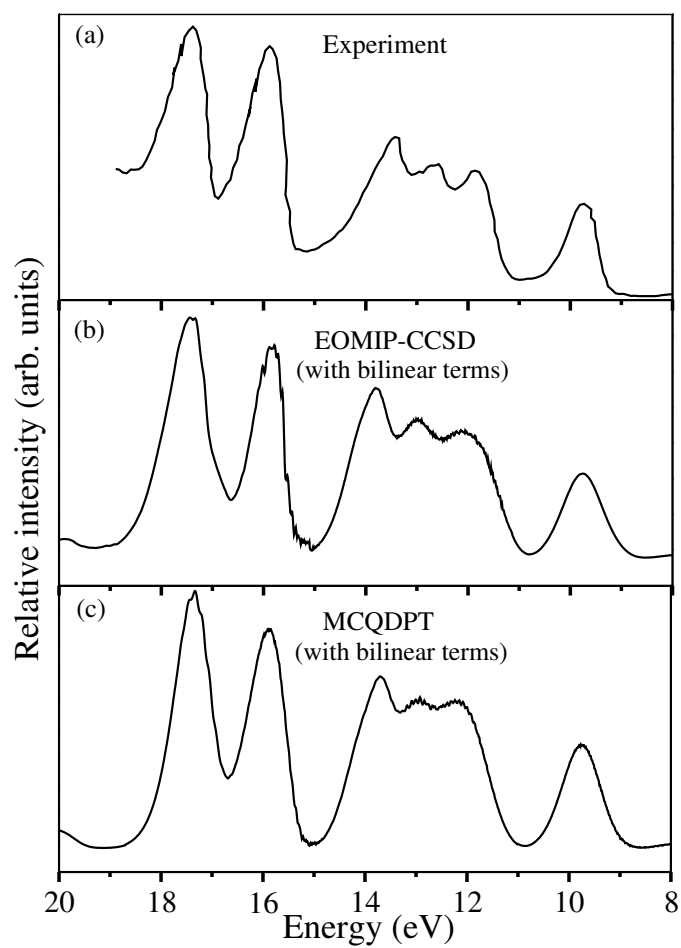
FIGURE C17: A comparison between the experimental [47] photo-ionization spectrum of the CH_2NHCH_2, shown in panel (a), and the theoretical spectra depicted in panels (b) and (c). This theoretical spectrum is obtained after including the bilinear coupling parameters (details provided in the text).

Bibliography

[1] M. Born and R. Oppenheimer, Ann. Phys. **389**, 457 (1927).

[2] H. Köppel, W. Domcke, and L. S. Cederbaum, Adv. Chem. Phys. **57**, 59 (1984).

[3] W. Domcke, D. R. Yarkony, and H. Köppel, *Conical Intersections*, 2004.

[4] E. Teller, J. Phys. Chem. **41**, 109 (1937).

[5] G. Herzberg and H. C. Longuet-Higgins, Discuss. Faraday Soc. **35**, 77 (1963).

[6] T. Carrington, Faraday Discuss. Chem. Soc. **53**, 27 (1972).

[7] D. R. Yarkony, Acc. Chem. Res. **31**, 511 (1998).

[8] F. Bernardi, M. Olivucci, and M. A. Robb, Chem. Soc. Rev. **25**, 321 (1996).

[9] S. Mahapatra, Acc. Chem. Res. **42**, 1004 (2009).

[10] I. Prigogine and S. A. Rice, *The role of degenerate states in chemistry*, volume 150, John Wiley & Sons, 2003.

[11] B. M. Wong, M. Piacenza, and F. Della Sala, Phys. Chem. Chem. Phys. **11**, 4498 (2009).

[12] O. Tagit and N. Hildebrandt, ACS Sensors **2**, 31 (2017), PMID: 28722447.

[13] S. Perun, A. L. Sobolewski, and W. Domcke, Chem. Phys. **313**, 107 (2005).

[14] S. Perun, A. L. Sobolewski, and W. Domcke, J. Am. Chem. Soc. **127**, 6257 (2005).

[15] D. Zhong, Ann. Rev. Phys. Chem. **66**, 691 (2015), PMID: 25830375.

[16] H. Wang, X. Chen, and W. Fang, Phys. Chem. Chem. Phys. **16**, 25432 (2014).

[17] S. Hahn and G. Stock, J. Phys. Chem. B **104**, 1146 (2000).

[18] T. V. Tscherbul and P. Brumer, J. Phys. Chem. A **118**, 3100 (2014), PMID: 24684415.

[19] M. Hariharan and P. Kamat, ACS Energy Lett. **7**, 2114 (2022).

[20] M. Chattoraj, B. A. King, G. U. Bublitz, and S. G. Boxer, Proc. Natl. Acad. Sci. **93**, 8362 (1996).

[21] D. Stoner-Ma et al., J. Am. Chem. Soc. **127**, 2864 (2005).

[22] X. Shu et al., Protein Sci. **16**, 2703 (2007).

[23] A. Szabo and N. S. Ostlund, *Modern quantum chemistry: introduction to advanced electronic structure theory*, Courier Corporation, 2012.

[24] P. Ehrenfreund and S. B. Charnley, ARAA **38**, 427 (2000).

[25] T. J. Millar, Plasma Sources Sci. Technol. **24**, 043001 (2015).

[26] S. Petrie and D. K. Bohme, Mass Spectrom. Rev. **26**, 258 (2007).

[27] R. C. Henry, Astrophys. J. **570**, 697 (2002).

[28] S. Cazaux et al., Astrophys. J. **593**, L51 (2003).

[29] A. A. Jaber, C. Ceccarelli, C. Kahane, and E. Caux, Astrophys. J. **791**, 29 (2014).

[30] Requena-Torres, M. A. et al., A&A **455**, 971 (2006).

[31] B. E. Turner, R. Terzieva, and E. Herbst, Astrophys. J. **518**, 699 (1999).

[32] Crovisier, J. et al., A&A **418**, 1141 (2004).

[33] A. WALSH, Proc. R. Soc. Med. **185**, 176 (1946).

[34] D. J. Knowles and A. J. C. Nicholson, J. Chem. Phys. **60**, 1180 (1974).

[35] M. J. Dewar and S. Worley, J. Chem. Phys. **50**, 654 (1969).

[36] B. J. Cocksey, J. H. D. Eland, and C. J. Danby, J. Chem. Soc. B , 790 (1971).

[37] D. Chadwick and A. Katrib, J. Electron Spectrosc. Relat. Phenom. **3**, 39 (1974).

[38] W.-C. Tam, D. Yee, and C. Brion, J. Electron Spectrosc. Relat. Phenom. **4**, 77 (1974).

[39] K. Kimura, S. Katsumata, T. Yamazaki, and H. Wakabayashi, J. Electron Spectrosc. Relat. Phenom. **6**, 41 (1975).

[40] S. McGlynn and J. Meeks, J. Electron Spectrosc. Relat. Phenom. **6**, 269 (1975).

[41] J. L. Meeks, J. Arnett, D. Larson, and S. McGlynn, Chem. Phys. Lett. **30**, 190 (1975).

[42] R. Hernandez, P. Masclet, and G. Mouvier, J. Electron Spectrosc. Relat. Phenom. **10**, 333 (1977).

[43] F. M. Benoit and A. G. Harrison, J. Am. Chem. Soc. **99**, 3980 (1977).

[44] K. Kimura, *Handbook of HeI photoelectron spectra of fundamental organic molecules*, Halsted Press, 1981.

[45] K. Johnson, I. Powis, and C. Danby, Chem. Phys. **70**, 329 (1982).

[46] A. Potts, T. Williams, and W. Price, Faraday Discuss. Chem. Soc. **54**, 104 (1972).

[47] G. Bieri, L. Åsbrink, and W. von Niessen, J. Electron Spectrosc. Relat. Phenom. **27**, 129 (1982).

[48] H. Hurzeler, M. G. Inghram, and J. D. Morrison, J. Chem. Phys. **28**, 76 (1958).

[49] K. M. Kapnas, L. M. McCaslin, and C. Murray, Phys. Chem. Chem. Phys. **21**, 14214 (2019).

[50] H. Jochims, W. Lohr, and H. Baumgärtel, Chem. Phys. Lett. **54**, 594 (1978).

[51] K. Głuch, J. Cytawa, and L. Michalak, Int. J. Mass Spectrom. **273**, 20 (2008).

[52] A. Golovin, Y. Sergeev, M. Akopyan, and F. Vilesov, Theo. Expe. Chem. **13**, 580 (1978).

[53] R. Bombach, J.-P. Stadelmann, and J. Vogt, Chem. Phys. **60**, 293 (1981).

[54] A. J. Yencha, M. R. Siggel-King, G. C. King, A. E. Malins, and M. Eypper, J. Electron Spectrosc. Relat. Phenom. **187**, 65 (2013).

[55] H. Köppel, L. Cederbaum, and W. Domcke, Chem. Phys. **69**, 175 (1982).

[56] B. Nikoobakht and H. Köppel, Mol. Phys. **119**, e1958019 (2021).

[57] B. Nikoobakht and H. Köppel, Phys. Chem. Chem. Phys. **24**, 12433 (2022).

[58] Y.-J. Kuan et al., Adv. Space Res. **33**, 31 (2004).

[59] I. Cleaves and J. Henderson, Monatshefte für Chemie/Chemical Monthly **134**, 585 (2003).

[60] S. L. Miller and G. Schlesinger, J. Mol. Evol. **36**, 302 (1993).

[61] Å. Hjalmarson, P. Bergman, and A. Nummelin, Progress in searches for prebiotic interstellar olecules, in *Exo-Astro-Biology*, edited by P. Ehrenfreund, O. Angerer, and B. Battrick, volume 496 of *ESA Special Publication*, pages 263–266, 2001.

[62] E. Tapavicza, I. Tavernelli, U. Rothlisberger, C. Filippi, and M. E. Casida, J. Chem. Phys **129**, 124108 (2008).

[63] M. Kawasaki, T. Ibuki, M. Iwasaki, and Y. Takezaki, J. Chem. Phys **59**, 2076 (1973).

[64] R. Gomer and W. A. Noyes, J. Am. Chem. Soc. **72**, 101 (1950).

[65] B. C. Roquitte, J. Phys. Chem. **70**, 2699 (1966).

[66] R. Cvetanović, Can. J. Chem. **33**, 1684 (1955).

[67] X. Bin et al., Int. J. Quantum Chem. **119**, e25957 (2019).

[68] C. J. Bennett, Y. Osamura, M. D. Lebar, and R. I. Kaiser, Astrophys. J. **634**, 698 (2005).

[69] S. Charnley, Adv. Space Res. **33**, 23 (2004).

[70] W. M. Irvine et al., Astrophys. J. **342**, 871 (1989).

[71] B. E. Turner and A. J. Apponi, Astrophys. J. **561**, L207 (2001).

[72] F. J. Lovas, D. R. Johnson, D. Buhl, and L. E. Snyder, Astrophys. J. **209**, 770 (1976).

[73] E. N. Rodriguez Kuiper, T. B. H. Kuiper, B. Zuckerman, and R. K. Kakar, Astrophys. J. **214**, 394 (1977).

[74] J. M. Hollis, L. E. Snyder, R. D. Suenram, and F. J. Lovas, Astrophys. J. **241**, 1001 (1977).

[75] M. Ikeda et al., Astrophys. J. **571**, 560 (2002).

[76] M. Ikeda et al., Astrophys. J. **560**, 792 (2001).

[77] J. E. Dickens et al., Astrophys. J. **489**, 753 (1997).

[78] P. Coll, J.-M. Bernard, R. Navarro-Gonzalez, and F. Raulin, Astrophys. J. **598**, 700 (2003).

[79] A. Occhiogrosso, S. Viti, M. D. Ward, and S. D. Price, Mon. Notices Royal Astron. Soc. **427**, 2450 (2012).

[80] A. Occhiogrosso et al., Astron. Astrophys. **564**, A123 (2014).

[81] L. Johansson et al., Astronomy and Astrophysics (ISSN 0004-6361), vol. 130, no. 2, Jan. 1984, p. 227-256. **130**, 227 (1984).

[82] B. Turner, Astrophys. J. Supplement Series **76**, 617 – 686 (1991), Cited by: 352.

[83] E. Herbst and E. F. van Dishoeck, Annu. Rev. Astron. Astrophys. **47**, 427 (2009).

[84] C. Fridh, J. Chem. Soc., Faraday Trans. 2 **75**, 993 (1979).

[85] A. Komornicki, F. Pauzat, and Y. Ellinger, J. Phys. Chem. **87**, 3847 (1983).

[86] H. Basch, M. B. Robin, N. A. Kuebler, C. Baker, and D. W. Turner, J. Chem. Phys **51**, 52 (1969).

[87] A. Schweig and W. Thiel, Chem. Phys. Lett **21**, 541 (1973).

[88] R. R. Corderman, P. R. LeBreton, S. E. Buttrill, A. D. Williamson, and J. L. Beauchamp, J. Chem. Phys **65**, 4929 (1976).

[89] D. H. Aue et al., J. Am. Chem. Soc. **102**, 5151 (1980).

[90] K. Kimura, *Handbook of HeI photoelectron spectra of fundamental organic molecules*, Halsted Press, 1981.

[91] W. von Niessen, L. S. Cederbaum, and W. P. Kraemer, Theor. Chem. Acc **44**, 85 (1977).

[92] E. D. Simandiras et al., J. Am. Chem. Soc. **110**, 1388 (1988).

[93] R. Bonaccorsi, E. Scrocco, and J. Tomasi, J. Chem. Phys. **52**, 5270 (1970).

[94] P. Lavvas, A. Coustenis, and I. Vardavas, Planet. Space Sci. **56**, 67 (2008).

[95] J. Dickens et al., Spectrochim. Acta - A: Mol. Biomol. Spectrosc. **57**, 643 (2001).

[96] E. F. van Dishoeck and G. A. Blake, Annu. Rev. Astron. Astrophys. **36**, 317 (1998).

[97] P. Myers, P. Thaddeus, and R. A. Linke, Astrophys. J. **241**, 155 (1980).

[98] V. J. Rani, A. K. Kanakati, and S. Mahapatra, J. Phys. Chem. A **126**, 6581 (2022).

[99] E. B. Wilson, J. C. Decius, and P. C. Cross, *Molecular Vibrations*, McGraw-Hill, New York, 1955.

[100] B. H. Lengsfield III and D. R. Yarkony, *Nonadiabatic Interactions Between Potential Energy Surfaces: Theory and Applications*, pages 1–71, John Wiley & Sons, Ltd, 1992.

[101] M. Born and K. Huang, *Dynamical theory of crystal lattices*, Oxford University press, New York, 1954.

[102] W. Pauli jr, Ann. Phys. **373**, 177 (1922).

[103] Güttinger P., Z. Phys. **73**, 169 (1932).

[104] Hellmann H., Z. Phys. **85**, 180 (1933).

[105] R. P. Feynman, Phys. Rev. **56**, 340 (1939).

[106] R. Englman, *The Jahn-Teller effect in Molecules and Crystals*, Wiley-Interscience, New York, 1972.

[107] W. Lichten, Phys. Rev. **164**, 131 (1967).

[108] F. T. Smith, Phys. Rev. **179**, 111 (1969).

[109] T. F. O'Malley, Adv. At. Mol. Phys. **7**, 223 (1971).

[110] M. Baer, Chem. Phys. **15**, 49 (1976).

[111] M. Baer, Chem. Phys. Lett. **35**, 112 (1975).

[112] M. Baer, Mol. Phys. **40**, 1011 (1980).

[113] Z. H. Top and M. Baer, J. Chem. Phys. **66**, 1363–1371 (1977).

[114] J. von Neumann and E. Wigner, Physik. Z. **30**, 467 (1929).

[115] H. A. Jahn and E. Teller, Pro. R. Soc. London. Ser. A **161**, 220 (1937).

[116] H. Nakamura and D. G. Truhlar, J. Chem. Phys. **115**, 10353 (2001).

[117] D. Simah, B. Hartke, and H.-J. Werner, J. Chem. Phys. **111**, 4523 (1999).

[118] T. Pacher, L. S. Cederbaum, and H. Köppel, Adv. Chem. Phys. **84**, 293 (1993).

[119] H. Köppel, J. Gronki, and S. Mahapatra, J. Chem. Phys. **115**, 2377 (2001).

[120] H. Köppel and B. Schubert, Mol. Phys. **104**, 1069 (2006).

[121] H. Nakamura and D. G. Truhlar, J. Chem. Phys. **117**, 5576 (2002).

[122] H. Nakamura and D. G. Truhlar, J. Chem. Phys. **118**, 6816 (2003).

[123] K. R. Yang, X. Xu, J. Zheng, and D. G. Truhlar, Chem. Sci. **5**, 4661 (2014).

[124] Y. Shu, Z. Varga, S. Kanchanakungwankul, L. Zhang, and D. G. Truhlar, J. Phys. Chem. A **126**, 992 (2022).

[125] H. Nakano, J. Chem. Phys. **99**, 7983 (1993).

[126] H. Nakano, Chem. Phys. Lett. **207**, 372 (1993).

[127] A. A. Granovsky, J. Chem. Phys. **134**, 214113 (2011).

[128] M. W. Schmidt et al., J. Comput. Chem. **14**, 1347 (1993).

[129] J. C. Tully, J. Chem. Phys. **93**, 1061 (1990).

[130] H.-D. Meyer, U. Manthe, and L. S. Cederbaum, Chem. Phys. Lett. **165**, 73 (1990).

[131] E. J. Heller, J. Chem. Phys. **68**, 3891 (1978).

[132] W. Domcke, H. Köppel, and L. S. Cederbaum, Mol. Phys. **43**, 851 (1981).

[133] J. Cullum and R. A. Willoughby, *Lanczos Algorithms for Large Symmetric Eigenvalue Computations*, Vol. I and II, Birkhäuser Boston, 1985.

[134] H. Köppel and W. Domcke, *Encyclopedia in Computational Chemistry*, edited by P. von Ragué (Wiley, New York, 1998), p. 3166.

[135] P. A. M. Dirac, Note on exchange phenomena in the thomas atom, volume 26, pages 376–385, 1930.

[136] J. Frenkel, *Waves Mechanics: Advanced General Theory*, volume 18, Clarendon Press, Oxford, 1934, 1934.

[137] J. Kucar, H.-D. Meyer, and L. Cederbaum, Chem. Phys. Lett. **140**, 525 (1987).

[138] U. Manthe, H. Meyer, and L. S. Cederbaum, J. Chem. Phys. **97**, 3199 (1992).

[139] M. H. Beck, A. Jäckle, G. A. Worth, and H.-D. Meyer, Phys. Rep. **324**, 1 (2000).

[140] H.-D. Meyer and G. A. Worth, Theor. Chem. Acc. **109**, 251 (2003).

[141] H.-D. Meyer, F. Gatti, and G. A. Worth, *Multidimensional Quantum Dynamics: MCTDH Theory and Applications*, Wiley-VCH, Weinheim, 2009.

[142] G. A. Worth, M. H. Beck, A. Jackle, and H.-D. Meyer, The MCTDH package, version 8.2, (2000), University of Heidelberg, Heidelberg, Germany. H.-D. Meyer, version 8.3 (2002), version 8.4 (2007). O. Vendrell and H.-D. Meyer, version 8.5 (2011)., See http://mctdh.uni-hd.de.

[143] R. Sarkar and S. Mahapatra, J. Chem. Phys. **147**, 194305 (2017).

[144] B. F. Gherman, R. A. Friesner, T.-H. Wong, Z. Min, and R. Bersohn, J. Chem. Phys. **114**, 6128 (2001).

[145] H.-T. Kim and S. L. Anderson, J. Chem. Phys. **114**, 3018 (2001).

[146] V. Galasso, J. Chem. Phys. **92**, 2495 (1990).

[147] J. S. Crighton and S. Bell, J. Mol. Spectrosc. **112**, 285 (1985).

[148] T.-K. Ha and L. S. Keller, J. Mol. Struct. **27**, 225 (1975).

[149] B. J. M. MARTELL, H. YU, and J. D. GODDARD, Mol. Phys. **92**, 497 (1997).

[150] M. Musiał, S. A. Kucharski, and R. J. Bartlett, J. Chem. Phys. **118**, 1128 (2003).

[151] Y. J. Bomble et al., J. Chem. Phys. **122**, 154107 (2005).

[152] G. A. Worth, M. H. Beck, A. Jackle, and H.-D. Meyer, The MCTDH package, version 8.2, (2000), University of Heidelberg, Heidelberg, Germany. H.-D. Meyer, version 8.3 (2002), version 8.4 (2007). O. Vendrell and H.-D. Meyer, version 8.5 (2011)., See http://mctdh.uni-hd.de.

[153] H.-D. Meyer, U. Manthe, and L. Cederbaum, Chem. Phys. Lett. **165**, 73 (1990).

[154] U. Manthe, H.-D. Meyer, and L. S. Cederbaum, J. Chem. Phys. **97**, 3199 (1992).

[155] M. J. Frisch et al., Gaussian 09 Revision E.01, Gaussian Inc. Wallingford CT 2009.

[156] R. W. Kilb, C. C. Lin, and E. B. Wilson, J. Chem. Phys. **26**, 1695 (1957).

[157] T. Shimanouchi, H. Matsuura, Y. Ogawa, and I. Harada, J. Phys. Chem. Ref. Data **7**, 1323 (1978).

[158] H. Hollenstein and H. Günthard, Spectrochim. Acta A Mol. Spectrosc. **27**, 2027 (1971).

[159] K. B. Wiberg, Y. Thiel, L. Goodman, and J. Leszczynski, J. Phys. Chem. **99**, 13850 (1995).

[160] J. F. Stanton et al., Cfour, coupled-cluster techniques for computational chemistry, a quantum-chemical program package, With contributions from A.A. Auer, R.J. Bartlett, U. Benedikt, C. Berger, D.E. Bernholdt, Y.J. Bomble, O. Christiansen, F. Engel, R. Faber, M. Heckert, O. Heun, M. Hilgenberg, C. Huber, T.-C. Jagau, D. Jonsson, J. Jusélius, T. Kirsch, K. Klein, W.J. Lauderdale, F. Lipparini, T. Metzroth, L.A. Mück, D.P. O'Neill, D.R. Price, E. Prochnow, C. Puzzarini, K. Ruud, F. Schiffmann, W. Schwalbach, C. Simmons, S. Stopkowicz, A. Tajti, J. Vázquez, F. Wang, J.D. Watts and the integral packages MOLECULE (J. Almlöf and P.R. Taylor), PROPS (P.R. Taylor), ABACUS (T. Helgaker, H.J. Aa. Jensen, P. Jørgensen, and J. Olsen), and ECP routines by A. V. Mitin and C. van Wüllen. For the current version, see http://www.cfour.de.

[161] L. S. Cederbaum and W. Domcke, Adv. Chem. Phys. **36**, 205 (2007).

[162] H. Werner and P. J. Knowles, J. Chem. Phys. **82**, 5053 (1985).

[163] P. J. Knowles and H.-J. Werner, Chem. Phys. Lett. **115**, 259 (1985).

[164] H. Werner and P. J. Knowles, J. Chem. Phys. **89**, 5803 (1988).

[165] P. J. Knowles and H.-J. Werner, Theor. Chim. Acta. **84**, 95 (1992).

[166] W. von Niessen, G. Bieri, and L. Åsbrink, J. Electron Spectrosc. Relat. Phenom. **21**, 175 (1980).

[167] H. Köppel, W. Domcke, and L. S. Cederbaum, Adv. Chem. Phys. **57**, 59 (1984).

[168] H. A. Witek, Y.-K. Choe, J. P. Finley, and K. Hirao, J. Comput. Chem. **23**, 957 (2002).

[169] M. O. Toolbox, Matlab optimization toolbox, version 9.8.0.1323502 (R2020a), The MathWorks, Natick, MA, USA.

[170] Wolfram Research Inc., Mathematica Version 11.1, Champaign, Illinois, 2017.

[171] H.-D. Meyer, F. L. Quéré, and C. Léonard, Chem. Phys. **329**, 179 (2006).

[172] L. J. Doriol, F. Gatti, C. Iung, and H.-D. Meyer, J. Chem. Phys. **129**, 224109 (2008).

[173] T. H. Dunning, J. Chem. Phys. **90**, 1007 (1989).

[174] G. L. Cunningham, A. W. Boyd, R. J. Myers, W. D. Gwinn, and W. I. Le Van, J. Chem. Phys **19**, 676 (1951).

[175] T. Nakanaga, J. Chem. Phys **73**, 5451 (1980).

[176] N. Cant and W. Armstead, Spectrochim. Acta A Mol. Spectrosc. **31**, 839 (1975).

[177] W. von Niessen, J. Schirmer, and L. Cederbaum, Comput. Phys. Rep. **1**, 57 (1984).

[178] I. B. Bersuker, Chem. Rev. **113**, 1351 (2013), PMID: 23301718.

[179] H. Koppel, W. Domcke, and L. Cederbaum, Adv. Chem. Phys. **57**, 59 (1984).

[180] D. W. Turner and W. C. Price, Proc. R. Soc. London. Math. Phys. Sci. **307**, 15 (1968).

[181] P. Rademacher, G. Irsch, W. Sicking, and E.-U. Würthwein, J. Mol. Struct. **197**, 291 (1989).

[182] W. Potts, Spectrochim. Acta **21**, 511 (1965).

[183] R. Mitchell, J. Burr, and J. Merritt, Spectrochim. Acta - A: Mol. Spectrosc. **23**, 195 (1967).

[184] C. Coulombeau and H. Jobic, J. Mol. Struct. **216**, 161 (1990).

[185] M. Ngom et al., Mol. Phys. **109**, 2153 (2011).

[186] E. D. Simandiras et al., J. Am. Chem. Soc. **110**, 1388 (1988).

[187] I. M. Nielsen, J. Phys. Chem. A **102**, 3193 (1998).

[188] R. Bonaccorsi, E. Scrocco, and J. Tomasi, J. Chem. Phys. **52**, 5270 (2003).

[189] A. G. Császár, J. Demaison, and H. D. Rudolph, J. Phys. Chem. A **119**, 1731 (2015).

[190] M. Beck, A. Jäckle, G. Worth, and H.-D. Meyer, Phys. Rep. **324**, 1 (2000).

[191] T. H. Dunning, J. Chem. Phys. **90**, 1007 (1989).

[192] B. Bak and S. Skaarup, J. Mol. Struct. **10**, 385 (1971).

[193] C. Fridh, J. Chem. Soc., Faraday Trans. 2 **75**, 993 (1979).

[194] W. von Niessen, L. S. Cederbaum, and W. P. Kraemer, Theor. Chim. Acta **44**, 85 (1977).

[195] J. R. Vadala, A. K. Kanakati, and S. Mahapatra, to be submitted .

List of publications

[1] Arun Kumar Kanakati, **V. Jhansi Rani**, R. Sarkar and S. Mahapatra, "*Elucidation of vibronic structure and dynamics of first eight excited electronic states of Pentafluorobenzene*", J. Chem. Phys. **157**, 204304 (2022).

[2] **V. Jhansi Rani**†, Arun Kumar Kanakati† and S. Mahapatra, "*Multi-state and multi-mode vibronic coupling effects in the photo-ionization spectroscopy of acetaldehyde*", J. Phys. Chem. A **126**, 6581 (2022)(† equal contribution).

[3] Arun Kumar Kanakati, **V. Jhansi Rani** and S. Mahapatra, "*Impact of Jahn-Teller and pseudo-Jahn-Teller effect in Propyne radical cation*", Phys. Chem. Chem. Phys. **24**, 16522 (2022).

[4] **V. Jhansi Rani**, Arun Kumar Kanakati and S. Mahapatra, "*Vibronic coupling effects in the six low-lying electronic states of oxirane radical cation: Theoretical photoelectron spectrum of oxirane*", (manuscript under preparation).

[5] **V. Jhansi Rani**, Arun Kumar Kanakati and S. Mahapatra, "*Photoionization of Aziridine: Nonadiabatic Dynamics of the first six low-lying electronic states of the Aziridine radical cation*", (manuscript under review).

[6] Swathi Thangalipalli, Siddarama Goud Bandalla, **V. Jhansi Rani** and Chandra Kiran Neella, "*Preparation, Isolation and Structural Characterization of Transient Species of DBU. Their Application as Green Reagents*", (manuscript accepted for publication (in Journal of Molecular Structure)).

Posters and Oral presentations in conferences/Symposia

[1] Poster presented in "Current Trends in Theoretical Chemistry (CTTC-2021), 23-25 September, 2021, organised by Bhabha Atomic Research center (BARC), mumbai, India (National).".

[2] Poster presented in "17th Indian Theoretical Chemistry Symposium (TCS-2021), 11-14 December, 2021, at Indian Institute of Science Education and Research (IISER) Kolkata, India (National).".

[3] Poster presented in "National Conference on Molecular Modelling and Simulations (NCMMS 2022), from February 28-March 02, 2022, at VIT Bhopal University, Bhopal, India (National).".

[4] Poster presented in " Structure and Dynamics: Spectroscopy and Scattering (SDSS-2023), 5th-8th October, 2023, IACS, Kolkata, India (International).".

[5] Poster presented in "18th Indian Theoretical Chemistry Symposium (TCS-2023), 07-10 December, 2023, at Indian Institute Of Technology (IIT) Madras (National).".

[6] Oral presentation in "Chemfest 2022 an in-house symposium held at School of Chemistry, University of Hyderabad, India".

Proposed contents of the Thesis

[1] **Chapter 1 :** Introduction

[2] **Chapter 2 :** Theoretical methodology

[3] **Chapter 3 :** Multi-state and multi-mode vibronic coupling effects in the photo-ionization spectroscopy of acetaldehyde

[4] **Chapter 4 :** Vibronic coupling effects in the six low-lying electronic states of oxirane radical cation: Theoretical photoelectron spectrum of oxirane

[5] **Chapter 5 :** Photoionization of Aziridine: Nonadiabatic Dynamics of the first six low-lying electronic states of the Aziridine radical cation

[6] **Chapter 6 :** Summary and outlook

Theoretical studies of multi-state and multi-mode nonadiabatic dynamics of isoelectronic molecular systems

by Jhansi vadala

Theoretical studies of multi-state and multi-mode nonadiabatic dynamics of isoelectronic molecular systems

Refs. 1, 2, 3 & 8 are our own papers.

SMahapatra

6   Xiangkun Wu, Manman Wu, Xiaofeng Tang, Xiaoguo Zhou, Shilin Liu, Fuyi Liu, Liusi Sheng. " Cl-Loss Dynamics of Vinyl Chloride Cations in the B A″ State: Role of the C A′ State ", The Journal of Physical Chemistry A, 2017
Publication   <1%

7   physiolgenomics.physiology.org
Internet Source   <1%

8   Arun Kumar Kanakati, Vadala Jhansi Rani, Susanta Mahapatra. "The Jahn-Teller and pseudo-Jahn-Teller effects in propyne radical cation", Physical Chemistry Chemical Physics, 2022
Publication   <1%

9   Lee, Edmond P.F., Mok, Daniel K.W., Chau, Foo-tim, Dyke, John M.. "Ab initio calculations on SF2 and its low-lying cationic states: Anharmonic Franck-Condon simulation of the uv photoelectron spectrum of SF2", 'AIP Publishing', 2006
Internet Source   <1%

10   A. Occhiogrosso, A. Vasyunin, E. Herbst, S. Viti, M. D. Ward, S. D. Price, W. A. Brown. "Ethylene oxide and acetaldehyde in hot cores", Astronomy & Astrophysics, 2014
Publication   <1%

11   www.ices.ro
Internet Source

12	hdl.handle.net Internet Source	<1%

13	I C Walker. "The electronic states of ethylene oxide studied by photoabsorption and *ab initio* multireference configuration interaction calculations", Journal of Physics B Atomic Molecular and Optical Physics, 06/14/2008 Publication	<1%

14	Mamilwar Rani, Arun Kumar Kanakati, Susanta Mahapatra. "Photoionization Bands of Cyanogen: Multi-Mode Vibronic Coupling and Renner-Teller Effects", ChemPhysChem, 2023 Publication	<1%

15	Rudraditya Sarkar, Daradi Baishya, S. Mahapatra. " Photodetachment spectroscopy of carbon doped anionic boron cluster, : A theoretical study ", Chemical Physics, 2018 Publication	<1%

16	Chris J. Bennett. "Laboratory Studies on the Formation of Three C_2H_4O Isomers—Acetaldehyde (CH_3CHO), Ethylene Oxide (c-C_2H_4O), and Vinyl Alcohol (CH_2CHOH)—in Interstellar and Cometary Ices", The Astrophysical Journal, 11/20/2005	<1%

Publication

17 Rudraditya Sarkar, Marie-Catherine Heitz, Martial Boggio-Pasqua. "Absorption band structure of the photochromic dimethyldihydropyrene/metacyclophanediene couple. Insight from vibronic coupling theory", The Journal of Chemical Physics, 2022
Publication
<1 %

18 mediatum.ub.tum.de
Internet Source
<1 %

19 V. Sivaranjana Reddy, Samala Nagaprasad Reddy, S. Mahapatra. "Ultrafast dynamics of electronically excited diborane radical cation", Theoretical Chemistry Accounts, 2015
Publication
<1 %

20 www.science.gov
Internet Source
<1 %

21 Arun Kumar Kanakati, Vadala Jhansi Rani, Rudraditya Sarkar, Susanta Mahapatra. "Elucidation of vibronic structure and dynamics of first eight excited electronic states of pentafluorobenzene", The Journal of Chemical Physics, 2022
Publication
<1 %

22 Aurore Bacmann, Alexandre Faure, Joanna Berteaud. "Cold and Yet Complex: Detection
<1 %

of Ethylene Oxide in a Prestellar Core", ACS Earth and Space Chemistry, 2019
Publication

23 Arpita Ghosh, Karunamoy Rajak, Arun Kumar Kanakati, S. Mahapatra. "Renner-Teller and pseudo-Renner-Teller interactions in the electronic ground and excited states of the dicyanoacetylene radical cation: Assignment of vibronic spectrum and elucidation of nonradiative and radiative decay mechanisms", Computational and Theoretical Chemistry, 2019
Publication

<1 %

24 T. Mondal, S. Mahapatra. "Complex Dynamics at Conical Intersections: Vibronic Spectra and Ultrafast Decay of Electronically Excited Trifluoroacetonitrile Radical Cation", The Journal of Physical Chemistry A, 2008
Publication

<1 %

25 nssdcftp.gsfc.nasa.gov
Internet Source

<1 %

26 Karunamoy Rajak, Arpita Ghosh, S. Mahapatra. "Vibronic Coupling in the First Five Electronic States of Dicyanodiacetylene Radical Cation", The Journal of Physical Chemistry A, 2018
Publication

<1 %

27 V. Sivaranjana Reddy, T. S. Venkatesan, S. Mahapatra. "Vibronic interactions in the photodetachment spectroscopy of phenide anion", The Journal of Chemical Physics, 2007
Publication

<1 %

28 lab409.chem.ccu.edu.tw
Internet Source

<1 %

29 www.ehr.nsf.gov
Internet Source

<1 %

30 Rudraditya Sarkar, S. Mahapatra. " Theoretical study of photodetachment spectroscopy of hydrogenated boron cluster anion H B7− and its deuterated isotopomer ", The Journal of Chemical Physics, 2017
Publication

<1 %

31 Susanta Ghanta. "Jahn-Teller and pseudo-Jahn-Teller effects in trifluoromethane radical cation", Journal of Molecular Structure, 2016
Publication

<1 %

32 Arun Kumar Kanakati, Vadala Jhansi Rani, S. Mahapatra. "The Jahn–Teller and pseudo-Jahn–Teller effects in the propyne radical cation", Physical Chemistry Chemical Physics, 2022
Publication

<1 %

33 swisher.counterstrike-server.info
Internet Source

<1 %

34 N. Sathyamurthy, Susanta Mahapatra. "Time-dependent quantum mechanical wave packet dynamics", Physical Chemistry Chemical Physics, 2020
Publication

<1 %

35 link.springer.com
Internet Source

<1 %

36 www.researchgate.net
Internet Source

<1 %

37 Hoch, Constantin. "Tetrelide, Tetrelate und Tetrelid-Tetrelate der schweren Alkalimetalle - Synthese, Charakterisierung und Kristallchemie", Universität Freiburg, 2003.
Publication

<1 %

38 Karunamoy Rajak, Arpita Ghosh, Susanta Mahapatra. "Vibronic Coupling in the First Five Electronic States of Dicyanodiacetylene Radical Cation", The Journal of Physical Chemistry A, 2018
Publication

<1 %

39 baadalsg.inflibnet.ac.in
Internet Source

<1 %

40 www.csus.edu
Internet Source

<1 %

41 T. Mondal, A. J. C. Varandas. "Silane Radical Cation: A Theoretical Account on the Jahn–

Teller Effect at a Triple Degeneracy", The Journal of Physical Chemistry A, 2013
Publication

42   "The Jahn-Teller Effect", Springer Science and Business Media LLC, 2009   <1%
Publication

43   Janet E. Del Bene, Ibon Alkorta, José Elguero. " Carbenes as Electron-Pair Donors To CO for C···C Tetrel Bonds and C–C Covalent Bonds ", The Journal of Physical Chemistry A, 2017   <1%
Publication

44   Samala Nagaprasad Reddy, S. Mahapatra. "Theoretical Study on Molecules of Interstellar Interest. I. Radical Cation of Noncompact Polycyclic Aromatic Hydrocarbons", The Journal of Physical Chemistry A, 2013   <1%
Publication

45   pubs.rsc.org
Internet Source   <1%

46   ftp-mhf.desy.de
Internet Source   <1%

47   Volkhard May, Oliver Kühn. "Charge and Energy Transfer Dynamics in Molecular Systems", Wiley, 2003   <1%
Publication

48   ntrs.nasa.gov

Internet Source <1%

49 Gindensperger, E.. "Multi-state vibronic interactions in the fluorobenzene radical cation: The importance of quadratic coupling terms", Chemical Physics, 20070925
Publication
<1%

50 S. Ghanta, V. Sivaranjana Reddy, S. Mahapatra. "Theoretical study of electronically excited radical cations of naphthalene and anthracene as archetypal models for astrophysical observations. Part I. Static aspects", Physical Chemistry Chemical Physics, 2011
Publication
<1%

51 Screttas, Constantinos G., and Maria Micha-Screttas. "Paramagnetic solvent nuclear magnetic resonance shifts in radical anion solutions. 4. Carbon-13 contact shifts and mechanism of spin density and/or electron transfer to substrate", The Journal of Physical Chemistry, 1983.
Publication
<1%

52 Roman I. Ovsyannikov, Tsuneo Hirano, Per Jensen. " The Renner Effect in the X̃ A″ and Ã A′ Electronic States of HSO/HOS ", The Journal of Physical Chemistry A, 2013
Publication
<1%

53 Rudraditya Sarkar, S. Mahapatra. " Vibronic Dynamics of Electronic Ground State of CH F and Its Deuterated Isotopomer ", The Journal of Physical Chemistry A, 2016
Publication

54 S. Rajagopala Reddy, Arpita Ghosh, S. Mahapatra. " Electronic spectroscopy of carbon chains (C , = 7–10) of astrophysical importance. I. Quantum chemistry ", The Journal of Chemical Physics, 2019
Publication

55 Susanta Mahapatra *. "Quantum non-adiabatic dynamics through conical intersections: Spectroscopy to reactive scattering", International Reviews in Physical Chemistry, 2004
Publication

56 T. S. Venkatesan, S. Mahapatra, H.-D. Meyer, H. Köppel, L. S. Cederbaum. "Multimode Jahn–Teller and Pseudo-Jahn–Teller Interactions in the Cyclopropane Radical Cation: Complex Vibronic Spectra and Nonradiative Decay Dynamics", The Journal of Physical Chemistry A, 2007
Publication

57 backend.orbit.dtu.dk
Internet Source

<1 %

<1 %

<1 %

<1 %

<1 %

58 Susanta Mahapatra. "Structure and dynamics of electronically excited molecular systems", WIREs Computational Molecular Science, 2021
Publication

<1%

59 Venkatesan, T. S., S. Mahapatra, H.-D. Meyer, H. Köppel, and L. S. Cederbaum. "Multimode Jahn–Teller and Pseudo-Jahn–Teller Interactions in the Cyclopropane Radical Cation: Complex Vibronic Spectra and Nonradiative Decay Dynamics", The Journal of Physical Chemistry A, 2007.
Publication

<1%

60 H. Kuppel. "Multimode Molecular Dynamics Beyond the Born-Oppenheimer Approximation", Advances in Chemical Physics, 01/01/1984
Publication

<1%

61 Kaja Pae, Vladimir Hizhnyakov. "Time-dependent Jahn-Teller problem: Phonon-induced relaxation through conical intersection", The Journal of Chemical Physics, 2014
Publication

<1%

62 S. Rajagopala Reddy, S. Mahapatra. "Theoretical study of photodetachment processes of anionic boron cluster. III. B7–", The Journal of Chemical Physics, 2014

<1%

Publication

63 T. Mondal, S. Rajagopala Reddy, S. Mahapatra. "Photophysics of fluorinated benzene. III. Hexafluorobenzene", The Journal of Chemical Physics, 2012
Publication

<1%

64 ia600104.us.archive.org
Internet Source

<1%

65 "Quantum Mechanical Electronic Structure Calculations with Chemical Accuracy", Springer Nature, 1995
Publication

<1%

66 Reinhard Schinke. "Photodissociation Dynamics", Wiley, 2002
Publication

<1%

67 aip.scitation.org
Internet Source

<1%

68 Qingyong Meng, Shirin Faraji, Oriol Vendrell, Hans-Dieter Meyer. "Full dimensional quantum-mechanical simulations for the vibronic dynamics of difluorobenzene radical cation isomers using the multilayer multiconfiguration time-dependent Hartree method", The Journal of Chemical Physics, 2012
Publication

<1%

69 V. Sivaranjana Reddy, S. Ghanta, S. Mahapatra. "First Principles Quantum Dynamical Investigation Provides Evidence for the Role of Polycyclic Aromatic Hydrocarbon Radical Cations in Interstellar Physics", Physical Review Letters, 2010
Publication

<1 %

70 Submitted to University of South Florida
Student Paper

<1 %

71 V. Sivaranjana Reddy. "Electronic nonadiabatic interactions and ultrafast internal conversion in phenylacetylene radical cation", The Journal of Chemical Physics, 2009
Publication

<1 %

72 Abhishek Kumar, Shweta Agrawal, T. Rajagopala Rao, Rudraditya Sarkar. " Rationalization of photo-detachment spectra of the indenyl anion (C H) from the perspective of vibronic coupling theory ", Physical Chemistry Chemical Physics, 2019
Publication

<1 %

73 S. Rajagopala Reddy, S. Mahapatra. "Theoretical study of photodetachment processes of anionic boron clusters. II. Dynamics", The Journal of Chemical Physics, 2012
Publication

<1 %

74 U. Priyanka, Aishwarya Paul, T. Mondal. "Vibronic coupling and ultrafast relaxation dynamics in the first five excited singlet electronic states of bithiophene", The Journal of Chemical Physics, 2024

Publication

<1 %

Exclude quotes	On	Exclude matches	< 14 words
Exclude bibliography	On		